Tectonics of the eastern Tethyan Himalaya

Amos B. Aikman

Thesis submitted for the degree of Doctor of Philosophy

THE AUSTRALIAN NATIONAL UNIVERSITY

Declaration

The work presented in this thesis is my own except where otherwise acknowledged.

Amos B. Aikman

Acknowledgments

First and foremost, I would like to thank my supervisor Prof. Mark Harrison, for accepting me as a student and for guiding me through my time at ANU. His teachings on what constitutes 'good science', attention to detail and rationale in argument have been second to none. He has afforded me opportunities far beyond my expectations, through which I have been able to develop greatly as a person. I would also like to thank my advisors Joerg Hermann, Jean Braun, and Gordon Lister. Their diverse and insightful opinions have been a constant source of perspective and inspiration for my work.

I am grateful to the many people with whom I have collaborated - in particular Frederic Herman and Julien Célérier, whose willingness to exchange ideas fostered development of this project. Simon Richards is gratefully acknowledged for contributing regional tomographic interpretations, and Ding Lin, An Yin, Frederic Herman and members of the Chinese Academy of Sciences are thanked for insightful discussions and fieldwork assistance.

I would like to thank other members of the RSES academic, technical and administrative staff. In particular, Trevor Ireland and Peter Holden for their assistance with SHRIMP analyses, and Vivien Gleeson for her tireless efforts in keeping her many charges out of trouble.

During my time at RSES I have greatly enjoyed the friendship of many fellow students and postdocs. Nicole is thanked for equal blondness, Fred for his entertaining 'good moods' and Dave for a number of things that seem hard to encapsulate. Cal and Jules openly welcomed me to Australia. Their presence at many of the more colourful episodes of the past few years, as well as their enduring friendships,

have been some of the most memorable aspects of my time here. I also continue to greatly enjoy and appreciate the friendship of many others too numerous to mention - the Canberra massive, the Sydney Crew, that lot in Melbourne, and many more overseas - you know who you are.

Finally, I would like to thank my family. Although they may at times may feel neglected, their love and support transcend distance, making everything possible.

Abstract

The Himalaya have been considered a type example of collisional orogenesis for over a hundred years. Ongoing research has furnished a good understanding of the first order geology of this region, however, many aspects of its assembly remain poorly understood. Arguably, two persistent barriers to the realisation of a unifying model, have been a poor understanding of the orogen's early history, and over-reliance on results extrapolated along strike from central and western parts of the main Himalayan Arc.

The Himalayan Fold and Thrust Belt is characterised by a series of broadly E-W trending tectonometamorphic slices separated by predominantly N-dipping regional movement zones. The vast majority of these units represent components of the Indian foreland sequences dissected during the Tertiary episode of Himalayan orogenesis. Results of this and other studies indicate that, in the eastern Himalaya, the present day distribution of lithologies and their mutual relationships are broadly comparable to those described elsewhere along the main Himalayan Arc. However, several key aspects of their evolution appear to differ. These and other factors impact upon our understanding of the early stages of Himalayan orogenesis, and the usefulness of several evolutionary models.

The Tethyan Himalayan Sequences (THS) are the structurally highest and inferred earliest accreted unit of the HFTB. As such, they are uniquely placed to retain information regarding the formative stages of Himalayan orogenesis. Structural studies indicate that the dominant thickening phase in the THS metasediments along the length of the main Himalayan Arc occurred during the Eohimalayan episode of orogenesis. This deformation may have begun as early as the Paleocene, but was effectively complete by 44.1±1.2 Ma - the crystallisation age of the undeformed Dala

Granitoids. At this time, the THS were most likely positioned in the hanging wall of a major decollement that led to burial of the Greater Himalayan Crystalline (GHC) sequences. This structure may correspond to the incipient STFS.

Eohimalayan orogenesis (as documented in the central and western Himalaya) has traditionally been equated with crustal thickening and high pressure metamorphism. In the eastern Himalaya, however, it was contemporaneous with a major phase of arc-magmatism in the Eurasian Gangdese Batholith. Moreover, similar arc magmas appear to have mixed with components of the GHC sequence, giving rise to the Dala Granitoids that were emplaced within the Indian Tethyan Himalaya. Formation of these bodies was also associated with high temperature metamorphism of structurally deeper parts of the eastern THS metasediments - locally sufficient to induce partial melting and genesis of the Yala-Xiangbo Granitoids (42.3±4.9 Ma). Collectively, these data indicate that the record of magmatism and high temperature metamorphism in the eastern Himalaya extends significantly further into the geological past, and invokes processes quite unlike those that have so far been documented elsewhere.

The record of Neohimalayan orogenesis preserved in the eastern Himalaya appears to be broadly comparable with that described elsewhere along the main Himalayan Arc. Data from the Arunachal Himalaya and southern Tibet support the MCT as the dominant structure controlling on the formation of the High Himalayan Leucogranites. However, application of the newly calibrated Ti-in-zircon thermometer combined with conventional U-Pb dating, indicates that although the majority of the HHL may have been derived from fluid-absent melting, pockets of “wet” melting were present close to the Arunachal MCT. These bodies likely formed by partial melting of material incorporated into lower parts of the Arunachal crystalline

sequence from the Lesser Himalaya. The origins of the North Himalayan Granites (NHG) remain in dispute. However, data presented in this study support a structural control on formation of the North Himalayan Domes that is independent of the NHG.

The results of this study indicate that the record of Eohimalayan orogenesis preserved in the eastern Himalaya differs substantially from that which has been described elsewhere. This scenario is not easily accommodated by the present gamut of evolutionary models, which are leveraged towards data from the Neohimalayan episode and largely neglect heterogeneity along the length of the main Himalayan Arc. Recent tomography has revealed a slow seismic velocity anomaly beneath the eastern Himalaya, extending southwards into the Bay of Bengal co-incident with the Ninety East Ridge. It is suggested that this feature represents a lithosphere-scale discontinuity that has played a pivotal role in localising magmatism and heat flow into the eastern paleo-HFTB. The effects of this discontinuity may have persisted into the Neohimalayan.

Contents

Acronyms

HFTB	Himalayan Fold and Thrust Belt
THS	Tethyan Himalayan Sequences
GHC	Greater Himalayan Crystallines
LHS	Lesser Himalayan Sequences
Sw	Siwalik Molasse
STFS	South Tibetan Fault System
MCT	Main Central Thrust
MBT	Main Boundary Thrust
MFT	Main Frontal Thrust
MHT	Main Himalayan Thrust
GCT	Great Counter Thrust
RZT	Renbu Zedong Thrust
GB	Gangdese Batholith
HHL	High Himalayan Leucogranites
NHG	North Himalayan Granites
NHD	North Himalayan Domes
YX_D	Yala-Xiangbo Dome
YX_G	Yala-Xiangbo Granitoids
DG	Dala Granitoids
AL	Arunachal Leucogranites
TL	Tsona Leucogranites
AC	Arunachal Crystallines

Preface

This thesis discusses the results of roughly three and a half years of research at the Australian National University. It comprises seven chapters, their structure having been chosen to facilitate easy publication. As such, the introductions of some chapters may partially overlap with those preceding. The conclusions for *Chapter 3* to *Chapter 5* stop short of discussing wider tectonic interpretations, which are presented in the synthesis *Chapter 6*.

Many of the results of this study pertain to samples collected during fieldwork in the eastern Himalaya. These trips experienced all the usual constraints and obstacles familiar to anyone who has visited this or orther similar regions. However, large portions of the study area are also subject to additional scrutiny by the police and military authorities, due to their proximity to the Himalayan border regions. These and other factors periodically conspired to severely inhibit the progress research. As such, certain areas of this work might undoubtedly benefit from additional field based constraints unavailable at the time of writing.

Nomenclature conventions for the most part follow the established literature. The term *Himalayan*, when applied to geologic features (*e.g. Himalayan granitoids*), provides reference exclusively to those features with temporal association to the Tertiary episode of Himalayan orogenesis. The term *Himalayan Fold and Thrust Belt* refers only to crustal materials actively involved in Himalayan deformation, whereas *Himalayan orogen* encompasses all aspects of the Indo-Asia collision zone south of the ITS, including the mantle lithosphere.

In addition to the work discussed in this thesis, I have been involved in a number of collaborative projects, aspects of which are presented in Celerier (2007).

Chapter 1

Introduction

Orogeny, derived from Greek, is the collective term for the processes by which mountains are formed. Since the pioneering work of geologists such as James Hutton and Eduard Suess, our knowledge of orogenic zones has evolved to reveal their importance, not just in generating topography and localizing natural resources, but also influencing ocean and atmospheric circulation, and biological activity (*e.g.* Crowley and Burke, 1998). Although most commonly appreciated as generating large-scale topographic relief, orogenesis is intimately associated with many geological and geochemical processes on a broad range of time and spatial scales, and as such, provides a framework in which to study many aspects of the natural world. The advent of plate tectonic theory, combined with modern geochronological techniques, have permitted great intellectual advances in our understanding of orogeny over the past *ca.* 30 years. Nevertheless, many aspects remain poorly understood.

Stretching for over 2000 km from Pakistan to Burma, the Himalaya form one part of the Alpine-Himalayan chain; the topographic expression world's largest active orogenic belt. The Himalayan orogen has been considered a type example of collisional orogenesis for over a hundred years (e.g., Suess, 1875; Argand, 1924).

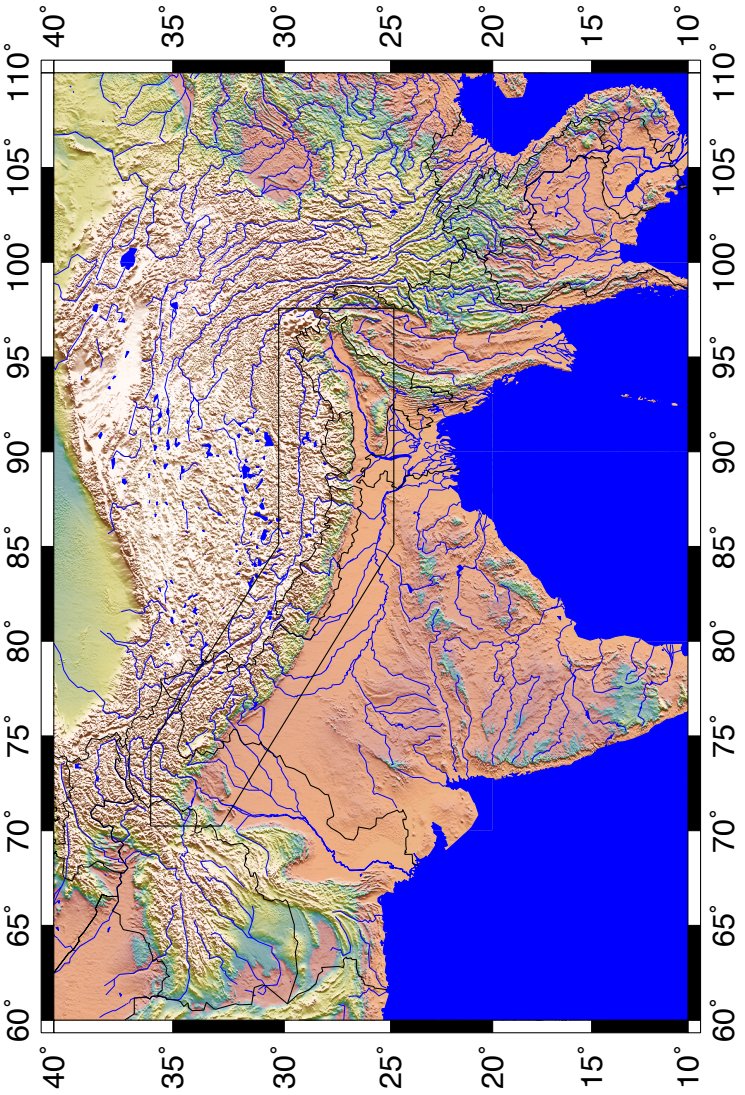

Figure 1.1: Digital elevation model of the Indo-Asia collision zone constructed from the ETOPO2 dataset. Box shows the location of *Figure 1.2.*

Since the initiation of continent-continent collision between India and Eurasia in the late Cretaceous (Yin and Harrison, 2000), the dominant process controlling the first order morphology of the Himalaya, has been the accommodation of >500 km of N-S convergence (Johnson, 2002). This deformation has largely been expressed through dissection of the Indian continental margin sequences into a series of shear-bounded tectono-metamorphic slices that comprise the Himalayan Fold and Thrust Belt (HFTB) today (Yin and Harrison, 2000).

To date, the vast majority of studies seeking to unravel the formation of the Himalayan orogen have restricted themselves to the frontal Himalaya, comprising only a small proportion of the total surface outcrop area, and concentrated on the past *ca.* 25 Ma of the orogen's history. This study attempts to provide fresh insight by considering a new transect through the eastern Himalaya, which focuses on the evolution of the structurally highest and inferred earliest accreted units of the HFTB.

1.1 Regional geology

The HFTB is commonly divided into four litho-tectonic units separated by broadly east-west trending regional movement zones, which outcrop sub-parallel to the trace of the main Himalayan Arc (LeFort, 1975, 1996; Yin and Harrison, 2000, *Figure 1.2*). The timing of movement on these structures is generally considered to decrease towards the foreland (*e.g.* LeFort, 1975, 1996; Yin and Harrison, 2000). From south to north, proportional to increasing structural height, the principal lithotectonic units are the Siwalik molasse, the Lesser Himalayan Series (LHS), the Greater Himalayan Crsytallines (GHC), and the Tethyan Himalayan Series (THS) (*Figure 1.2*). The Siwalik molasse comprise foreland basin deposits incorporated into the foreland fold and thrust belt in the hanging wall of the Main Frontal Thrust (Gansser, 1964), a Quaternary structure that is active today (Larson et al., 1999). The LHS com-

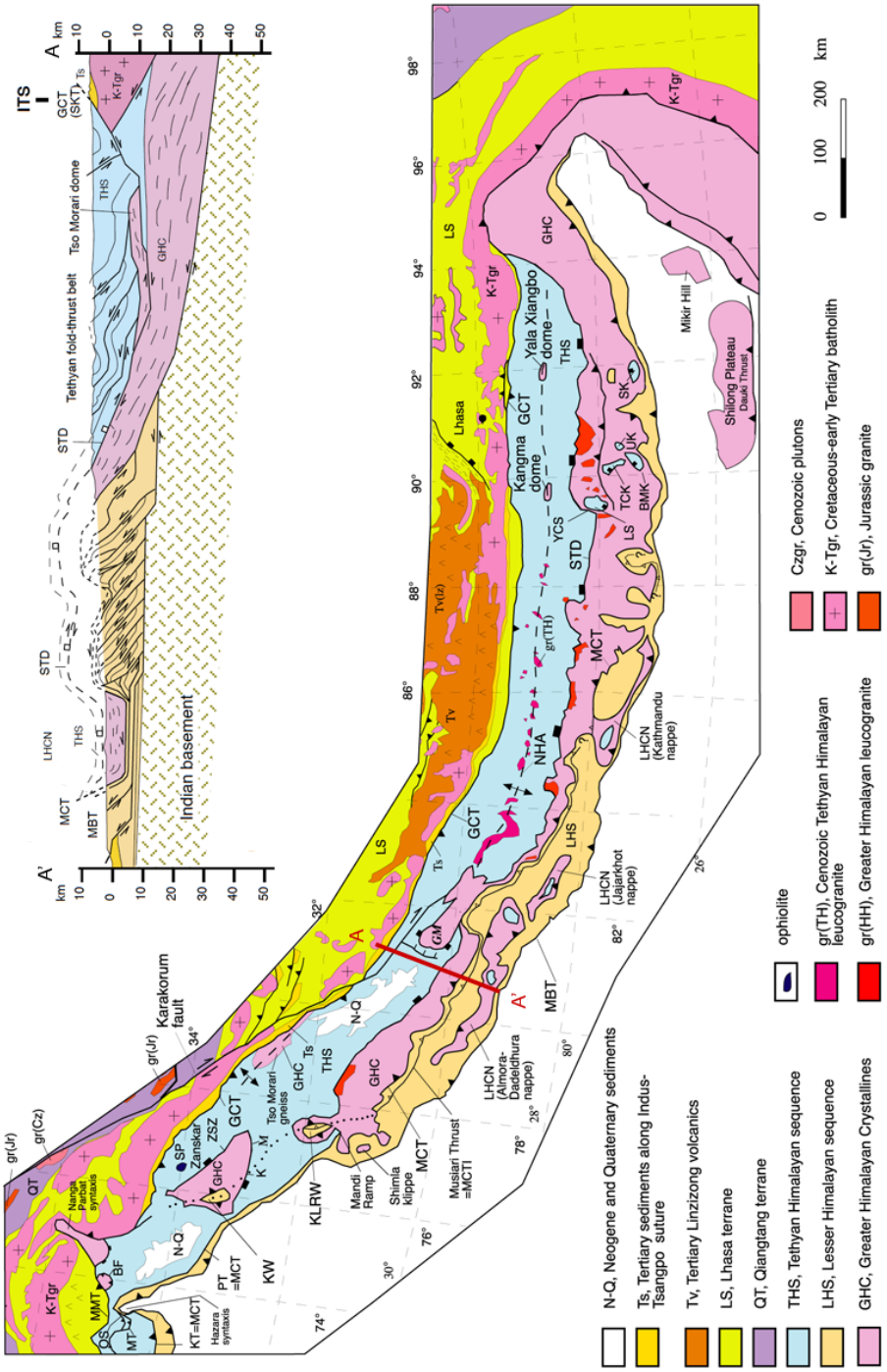

Figure 1.2: Regional geological map of the Himalayan orogen (An Yin *pers. comm.*, modified from Yin (2006)).

prise a sequence of dominantly siliciclastic rocks, ranging from lower greenschist to mid-amphibolite grade, separated from the underlying Siwalik molasse by the south vergent Main Boundary Thrust (Heim and Gansser, 1939; LeFort, 1975). The age of the Main Boundary Thrust is poorly constrained. However, it is suggested that the structure initiated at either *ca.* 11 Ma (Meigs et al., 1995), or <5 Ma (DeCelles et al., 1998). Structurally above the LHS are the GHC, the highest grade surface-outcropping unit of the HFTB. This sequence of paragneisses and migmatitic gneisses has been exhumed between the reverse sense Main Central Thrust (MCT) and the normal sense South Tibetan Fault System (STFS, *Figure 1.2*) (LeFort, 1996). Most workers agree that the MCT and STFS experienced a main phase of slip around 24-19 Ma, however, locally there is evidence that activity on both shear zones continued further into the Miocene (see discussions in Yin, 2006; Murphy and Harrison, 1999). Furthermore, studies of monazite inclusions in garnet indicate that components of the MCT system were active between 8-4 Ma, accounting for its present day outcrop at the base of the main topographic break (Harrison et al., 1997b; Catlos et al., 2001, 2002). In the upper portions of the GHC (*Figure 1.2*), a suite of leucogranite sheets and dykes and laccolithic bodies (the High Himalayan Leucogranites, HHL) are emplaced sub-parallel to the principal foliation (LeFort et al., 1987; Inger and Harris, 1993). These muscovite and tourmaline bearing bodies are thought to have formed by partial melting of the underlying sequences during the Miocene motion on the MCT (LeFort et al., 1987; Inger and Harris, 1993; Harrison et al., 1998b).

The THS comprise the structurally highest and most northerly unit of the HFTB (*Figure 1.2*). They are a Paleoproterozoic to Eocene sequence of predominantly low grade meta-sediments (Brookfield, 1993; Liu and Ensele, 1994, *Figure 1.4*) bounded to the south by the north-dipping STFS, and to the north by the south-dipping

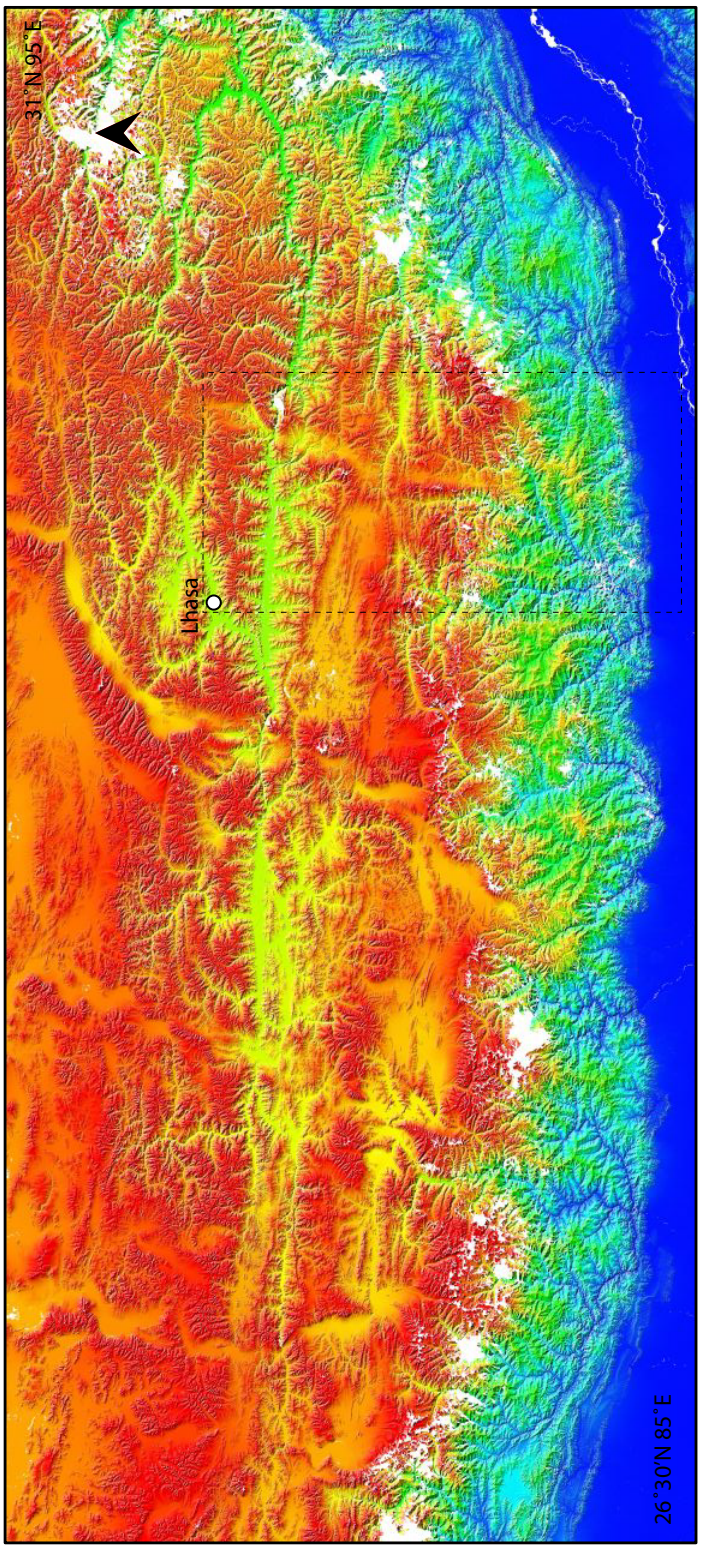

Figure 1.3: Digital elevation model showing the eastern half of the Himalayan Arc and southern Tibet. Area approximately equivalent to rectangular portion of *Figure 1.2*. Box shows the location of *Figure 1.5*.

Great Counter Thrust (GCT) adjacent and parallel to the Indus Tsangpo Suture (ITS, *Figure 1.2*), which marks the surface boundary between rocks of Indian and Eurasian continental affinity (Heim and Gansser, 1939; Yin and Harrison, 2000). The sequence is commonly subdivided into (1) Proterozoic to Devonian pre-rift deposits, (2) lower Carboniferous to Jurassic flysch-dominated syn- and post-rift deposits related to separation of the Lhasa terrane from northern India and opening of the Neo-Tethys, (3) Jurassic to Cretaceous passive continental margin deposits, primarily comprising marine carbonate and clastic sediments, and (4) latest Cretaceous to Eocene syn-collisional deposits, which include carbonate platform and proximal clastic sediments related to closure of the Tethyan basin (Liu and Ensele, 1994; Garzanti, 1999). In the eastern Himalaya (>90°E), the surface outcrop of THS lithologies is composed almost entirely of Mesozoic sequences, whereas further west, variable amounts of Paleozoic and older deposits are also found (Pan et al., 2004). In the Zedong window (*ca.* 92°E), the GCT (locally known as the Renbu-Zedong Thrust, RZT) is thought to have experienced a main phase of slip between 19-11 Ma, and may link at depth with the STFS fault system (Yin et al., 1994; Quidelleur et al., 1997; Yin et al., 1999; Harrison et al., 2000; Yin, 2006).

Metamorphic grade as defined by index minerals generally increases across the LHS from sub-greenschist to lower-amphibolite facies proportional to increasing structural height, thereby defining an inverted progression of metamorphic isograds (see review in Harrison et al., 1999c). The LHS and THS are generally agreed to have originated as continental margin deposits on the northern margin of the Indian shield prior to closure of the Tethys Ocean (*e.g.* Myrow et al., 2003). The GHC, however, are variably assigned as part of the same sequence (Yin, 2006, and refs. therein), an exotic terrane accreted prior to or during the early stages of the Indo-Asia collision (DeCelles et al., 2000), a structural high between two sedimentary

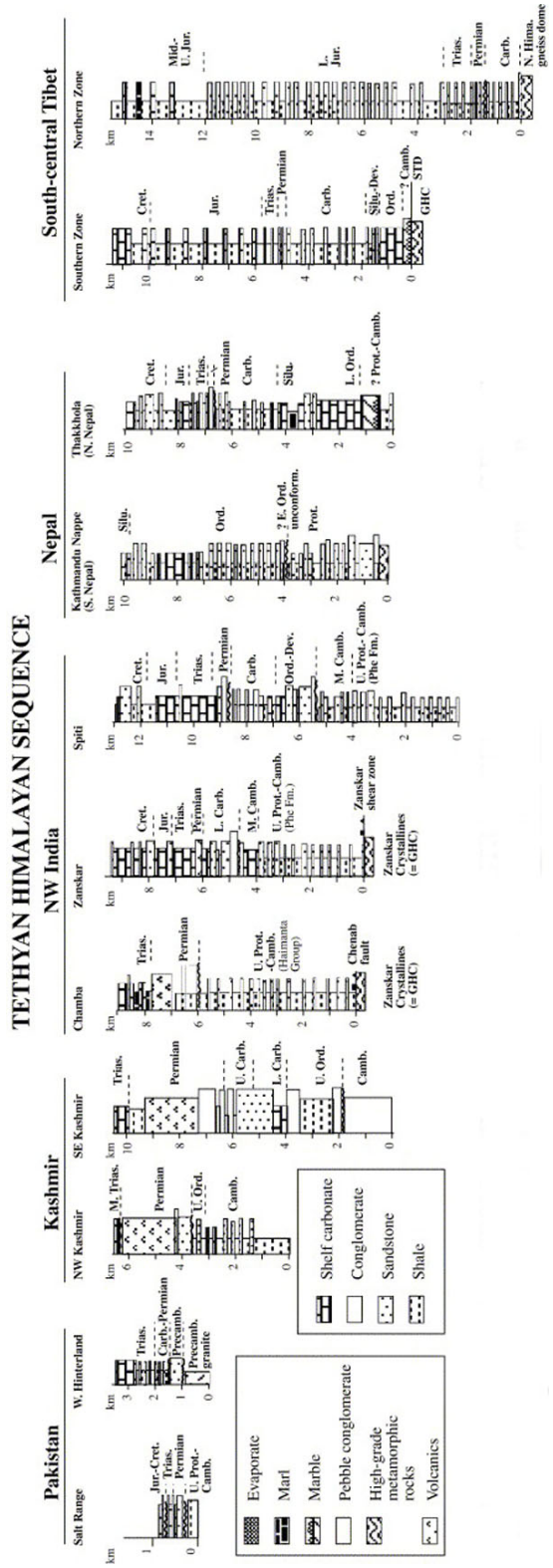

Figure 1.4: Generalised stratigraphic sections for several locations in the Tethyan Himalayan Sequence (Yin, 2006, and refs. therein)

basins (Saxena, 1971), or as Indian material exhumed from beneath the Tibetan Plateau by ductile flow (Nelson et al., 1996).

In the central THS, a series of gneiss and granite cored dome structures (the North Himalayan Domes, NHD) define a curvilinear trend parallel to the main Himalayan Arc, which is commonly referred to as the North Himalayan Antiform (NHA) (Hauck et al., 1998). These structures are thought to represent zones of focussed exhumation that were active during the Miocene, coincident with movement on the STFS-GCT fault system (Maluski et al., 1988; Chen et al., 1990; Lee et al., 2000). Peraluminous granitoids (the North Himalayan Granites) found in association with many NHD are poorly studied, however they are generally thought to be dominated by muscovite-biotite bearing assemblages, predominantly emplaced during the Miocene (Harrison et al., 1997a; Zhang et al., 2004a).

Metamorphism in the HFTB has traditionally been separated into two phases, an early (*ca.* 40 Ma), poorly documented Eohimalayan phase, followed by a Neohimalayan episode associated with coaxial deformation prior to exhumation and unroofing of the high-grade units (LeFort, 1996). Many workers have used thermobarometric techniques to constrain the peak metamorphic conditions preserved in the GHC. While no clear consensus has been reached, it is generally agreed that pressures adjacent to the MCT are *ca.* 8 kbar, decreasing to 3-4 kbar close to the STFS (see review in Harrison et al., 1999c). Peak temperatures across the GHC are typically around 650-700°C (Harrison et al., 1999c).

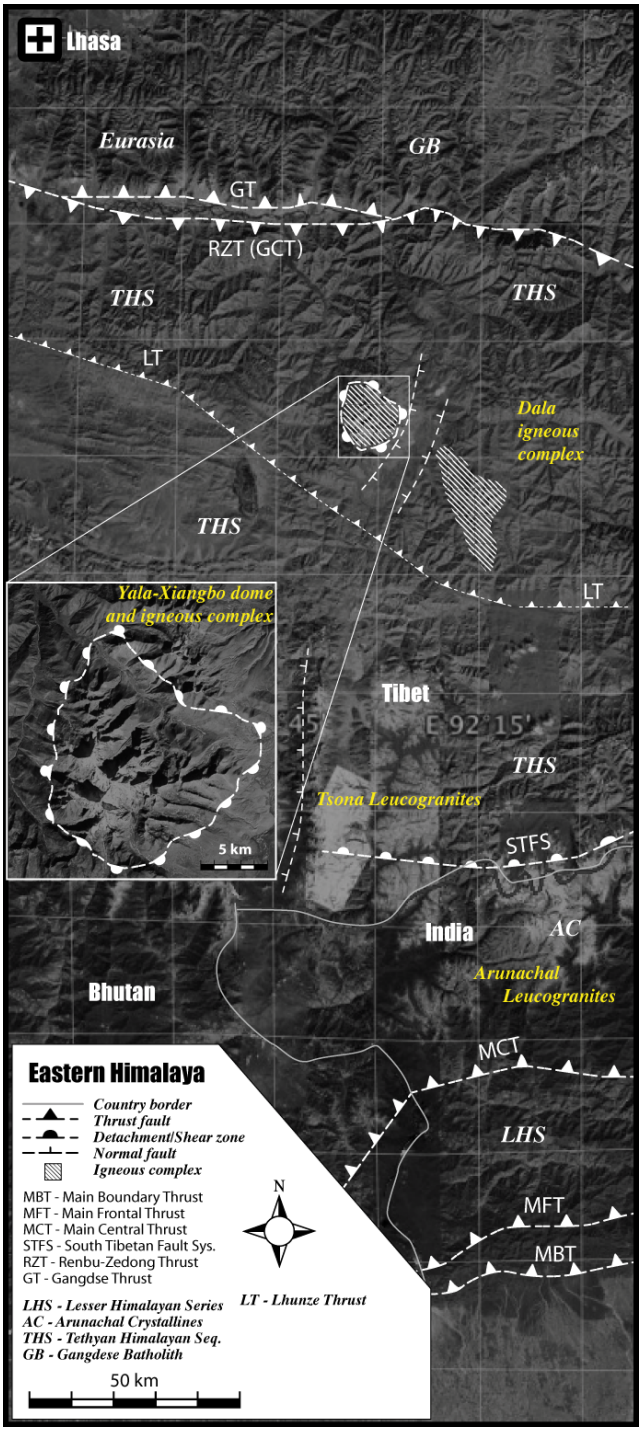

Figure 1.5: Simplified map and digital elevation model of the eastern Himalaya at *ca.* 92°E (Compiled from Pan et al., 2004; Yin et al., 2006, Google Earth, this study). This study primarily focuses on the region between the STFS and the RZT.

1.2 The eastern Himalaya

The eastern Himalaya (*ca.* 92°E) have received relatively little attention relative to many other parts of the HFTB and hence do not feature strongly in existing Himalayan evolutionary models. The structure of the Tethyan Himalaya is discussed in detail in *Chapter 2*. However, recent studies in Arunachal Himalaya (region between the MFT and STFS in the Indian state of Arunachal, *Figure 1.5*) are relevant to discussions in the several of the following chapters and therefore are briefly summarised below.

The first-order stratigraphic and structural relationships in the Arunachal Himalaya are broadly comparable to those described above (*Figure 1.5*); however, several important differences have also been found (Yin et al., 2006; Yin, 2007). Structural observations have shown that in this region, the MCT places kyanite-bearing schists over phyllite, quartzite and metavolcanic rocks that are ascribed to the LHS formations (Yin et al., 2006; Yin, 2007, this study). The MCT slip zone itself is narrow (1–200 m) and shows comparatively little evidence of the pervasive ductile deformation (*e.g.* thick mylonitic sequence) that is considered characteristic of the MCT zone in central Nepal and NW India (Heim and Gansser, 1939; LeFort, 1975; Catlos et al., 2001; Yin et al., 2006, this study). This may indicate that the Arunachal MCT was active at lower temperatures than elsewhere along the Himalayan Arc (An Yin *pers. comm.*, this study).

The units outcropping between the Arunachal MCT and the STFS are termed the Arunachal Crystallines, which are tectono-stratigraphically equivalent to the GHC as defined in northern Nepal (LeFort, 1975). The majority of the Arunachal Crystalline sequence comprises amphibolite grade pelites similar to those described in central Nepal (Yin et al., 2006; Yin, 2007, this study). However, gneissic units

are also found that are interpreted to be correlative with components of the Indian basement outcropping in the Shillong Plateau (Yin, 2007). Leucogranites appear to be more widespread in the Arunachal Crystalline sequences than elsewhere along the main Himalayan Arc (An Yin *pers. comm.*, this study). Abundant centimetre to meters sized leucosomes are found just above the Arunachal MCT (Yin et al., 2006). These bodies increase in size and abundance up section (tens to hundreds of meter sheet/dyke and laccolithic forms) through the pelitic sequences (Yin et al., 2006; Yin, 2007, this study).

Yin (2007) proposed that in the Arunachal Himalaya, Cenozoic deformation is associated with development of a thick-skinned thrust system that has incorporated components of the Indian cratonic basement into both the MCT footwall and hangingwall sequences. A balanced cross-section constructed for the region between the Arunachal Main Boundary Thrust and the Indo-Chinese border indicates at least 500 km horizontal shortening (Yin et al., 2006), which is notably greater than that estimated elsewhere (Schelling and Arita, 1991; DeCelles et al., 2001b). The difference may be attributable to westward-decreasing convergence velocities between India and Eurasia (Patriat and Achache, 1984; Dewey et al., 1989); however, it has also been suggested that this estimate may include a component of Paleozoic shortening that is difficult to separate from Cenozoic deformation (Yin, 2007).

1.3 Purpose of this study

Our current paradigm for the role of continent-continent collision in the evolution of the Himalayan crustal lithosphere derives largely from geologic studies of the frontal ranges, with particular focus on central portions of the Himalayan Arc. The majority of studies have also focussed on the Miocene to recent Neohimalayan episode; comparatively little is known about the first 30–40 Ma of Tertiary orogenesis. Large-

scale regional geological mapping studies have shown that the first-order structure and distribution of litho-tectonic units in the HFTB appear to be broadly continuous over *ca.* 2000 km. This has lead to many models established in the central Himalaya being extrapolated along the length of the Himalayan Arc, even though their lateral continuity has not been demonstrated.

The objective of this study are to address outstanding problems in our understanding of the Indo-Asian collision zone and test the spatial continuity of existing models by examining poorly studied sections of the HFTB in an area remote from the classically studied central Himalaya. A roughly N-S transect was studied through the eastern Himalaya at *ca.* 92°E (*Figure 1.5*). This geotransect includes a cross section through the structurally highest and inferred earliest accreted units of the HFTB, which may have preserved a record of the earliest history of Himalayan orogenesis. The studied area also includes the along strike equivalents of geologic structures that feature in models developed to explain other parts of the Himalaya, and conveniently links with the well-documented Zedong window (Yin et al., 1994, 1999; Harrison et al., 2000) and ongoing work in the Arunachal Himalaya (Yin et al., 2006).

Chapter 2

Structure of the Tethyan Himalaya

2.1 Introduction

Comprehensive understanding of the geodynamics of continental collision and orogenesis requires information pertaining to the nature and distribution of lithotectonic units, their individual histories and mutual relationships, and the processes by which they arrived at their current assembly. To this end, structural geology is a valuable tool in understanding the geometry of orogenic belts; providing both a framework in which to interpret, and a means with which to correlate other aspects of study.

Over a century of research has furnished a good understanding of the first-order geology of the Himalayan Fold and Thrust Belt (HFTB) (Suess, 1875; Argand, 1924; Gansser, 1964; LeFort, 1975, 1996; Yin and Harrison, 2000). The distribution and present-day relationships between most regional lithotectonic units are generally agreed (LeFort, 1975, 1996; Yin and Harrison, 2000; Yin, 2006), although aspects of their structural evolution remain in dispute (*e.g.* Gehrels et al., 2003; Yin, 2006;

Celerier, 2007). The past three decades have, however, witnessed a strong academic focus on frontal parts of the range. These areas are dominated by structures that have largely been attributed to the Neohimalayan episode (see discussion in LeFort, 1975, 1996; Yin and Harrison, 2000; Yin, 2006). Many studies have also chosen to concentrate on central and western parts of the Himalayan Arc; relatively little is known about the evolution of the North Himalaya, or indeed the early history of Himalayan orogenesis.

2.1.1 Purpose of this chapter

The metasedimentary sequences outcropping within the Tethyan Himalaya comprise the structurally highest units of the Himalayan fold and thrust belt (HFTB) (LeFort, 1975). They are inferred to be the earliest orogen-wide units to be accreted (LeFort, 1975), and as such, are uniquely placed to retain information regarding the formative stage of Himalayan orogenesis. Moreover, they also play host to other lithological and structural features - in particular the North Himalayan Granites and North Himalayan Domes - that have been important in the development of Himalayan evolutionary models (*e.g.* Burg et al., 1984b; Chen et al., 1990; Harrison et al., 1997a, 1999a; Lee et al., 2000; Beaumont et al., 2001).

Several attempts have been made to constrain the structural history of the Tethyan Himalaya through field studies and the construction of balanced cross sections, however, a unifying structural model is lacking. Geopolitical barriers restricting access to the mountainous Himalayan boarder regions continue to present a significant obstacle to realizing a detailed regional correlation. Nevertheless, some notable patterns have emerged. In the following sections, published data from a variety of locations along the Himalayan Arc are reviewed and discussed in conjunction with new results from the eastern Himalaya. Similarities between several

key geotransects permit construction of a regional correlation scheme describing the sequence of deformations affecting the structurally highest and inferred earliest accreted units of the HFTB. Unfortunately, however, temporal constraints on several key events are limited. The structural settings of igneous bodies outcropping within the Tethyan Himalaya are reviewed in *Chapter 3*. These data constrain the timing of key regional deformation events, and provide valuable new insight into the formation of the North Himalayan Domes.

2.2 The Tethyan Himalaya

The Tethyan Himalaya occupy the area between peaks of the High Himalaya and the Indus Tsangpo Suture, along the length of the main Himalayan Arc (*Figure 1.2*). The vast majority of the outcrop in this region comprises a deformed Paleo-Proterozoic to Eocene package of predominantly low-grade metasediments collectively termed the Tethyan Himalayan Sequences (THS). These units are thought to have been deposited on the northern passive margin of the Indian continent prior to closure of the Tethys Ocean (Brookfield, 1993; Liu and Ensele, 1994; Pan et al., 2004). The THS extend for over 1500 km, from Pakistan almost to the eastern Syntaxis (Booth et al., 2004; Craw et al., 2005; Zeitler, 2006), following the trace of the Himalayan Arc (Pan et al., 2004, *Figure 1.2*). For almost all of this length, the sequence is bounded to the north by the south-dipping Great Counter Thrust (GCT) and to the south by the north-dipping South Tibetan Fault System (STFS); these structures are thought to have been active contemporaneously during the Miocene (Quidelleur et al., 1997; Yin and Harrison, 2000).

Seismic studies along a NNE-SSW profile at *ca.* 89°E have identified a prominent reflector dipping at 12.5°NNE about 6 km beneath the High Himalaya, continuing to 22 km depth, where it flattens to a dip of 2.5° NNE (Makovsky et al., 1996).

This structure is interpreted as the northward projection of the STFS, forming the present-day basal detachment which juxtaposes THS metasediments against the underlying GHC (Makovsky et al., 1996). Both the northward extent of the GHC and the northward projection of the STFS are subject to ongoing debate, however Yin et al. (1994) and other workers have suggested that during top-to-the-north directed movement in the Miocene, the STFS may have transferred slip onto GCT at depth, effectively transposing the entire THS some distance to the north.

2.3 Published geotransects

Geotransects have been conducted through the THS (or parts thereof) at a variety of locations from the western syntaxis (Zeitler and Chamberlain, 1991a,b; Zeitler et al., 1993, 2001a,b), almost as far east as Lhasa. The dynamics of the syntaxial regions are not considered in the context of this study, hence the following discussion is confined to studies along the main Himalayan Arc. The locations of six key transects and the study area are shown on *Figure 2.1*; their results are summarised below.

2.3.1 Central southern Tibet

Balanced cross sections have been constructed along N-S oriented transects at *ca.* 87° and 89°E through central southern Tibet (Ratschbacher et al., 1992, 1994, *Figure 2.1*(*e*)). These studies used 1:1,000,000 scale Chinese geological maps and field data and employ a structural model based on south-directed imbricate stacking of deep rooted thrust sheets, locally incorporating slivers of the inferred underlying GHC. Results indicate that southern parts of the THS have accommodated *ca.* 50% shortening, increasing to *ca.* 70% in the north, with an average of 67% across the complete section (Ratschbacher et al., 1992, 1994). The timing of south vergent deformation in this region is poorly constrained, however geometric arguments require that it predate north-directed slip on the GCT (Ratschbacher et al., 1994, *Figure*

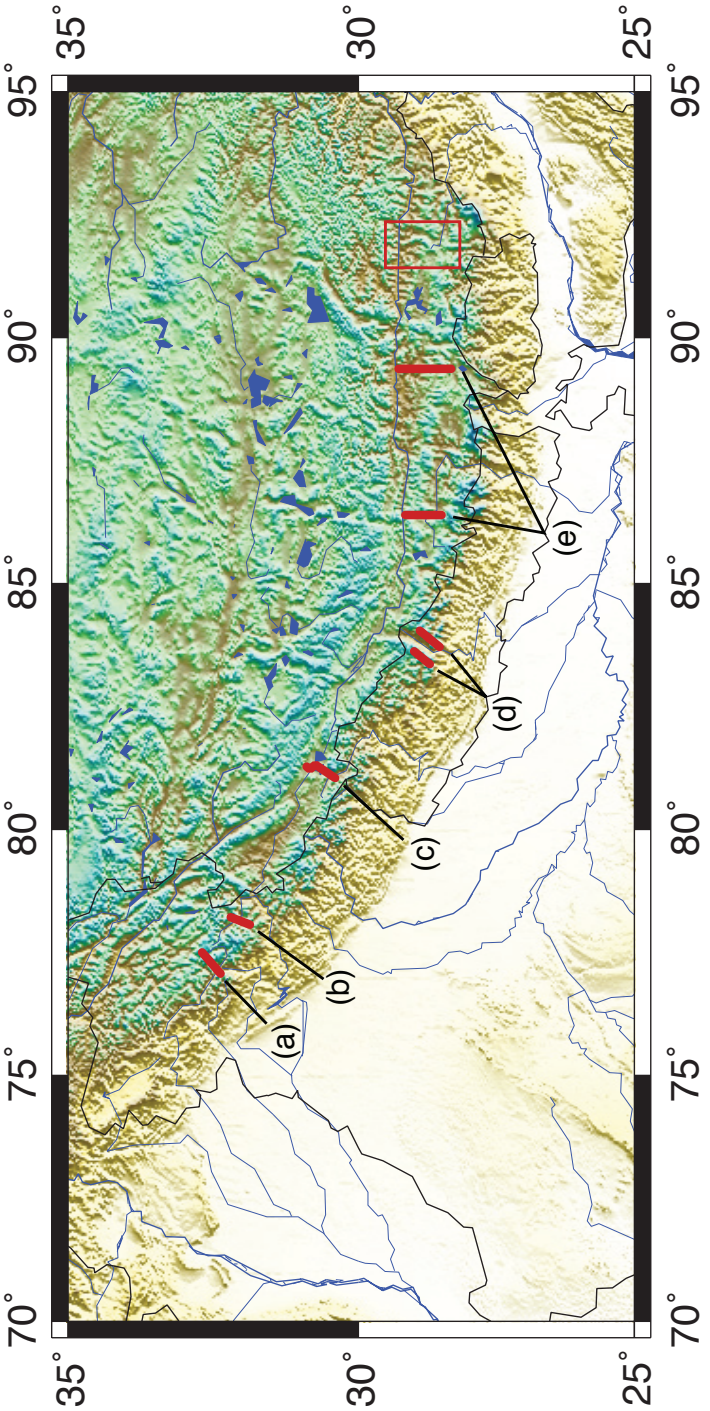

Figure 2.1: Digital elevation model (ETOPO2) of the Himalaya and southern Tibet. Red lines show the location of published cross sections constructed in the THS, (a,b) northwest India (Vannay and Steck, 1995; Wiesmayr and Grasemann, 2002), (c) southwest Tibet (Murphy and Yin, 2003), (d) northern Nepal (Godin, 2003), (e) central southern Tibet (Ratschbacher et al., 1992, 1994). The red box shows the location of the study area in the eastern Himalaya, and the map shown in Figure 2.2.

1.2). Two samples of white mica from the northern THS were dated by the K-Ar method. Three size fractions from a Triassic quartz phyllite all yielded ages within error of 49 Ma, which is tentatively suggested to be the age of major regional crustal thickening. A second sample from the northern margin of the THS yielded an age of 17.5±0.9 Ma, which is interpreted to record the initiation of backthrusting along the GCT (Ratschbacher et al., 1994). These structures were locally overprinted by E-W extension associated with formation of the Yadong-Guru rift and other NNE-SSW trending graben structures (Ratschbacher et al., 1994; Armijo et al., 1986).

2.3.2 Northwest India

Studies in the NW Indian Himalaya (Spiti valley *Figure 2.1*(*a*), and the Lahul region *Figure 2.1*(*b*)) suggest that the principal phase of Tertiary shortening in the local THS metasediments was also associated with the formation of south-vergent contractional structures. However, in southern parts of the section these structures (local D2) appear to overprint an earlier shortening event (Vannay and Steck, 1995). This event (local D1) is represented by NW-SE trending isoclinal to sub-isoclinal similar folds associated with a penetrative axial planar schistosity and NE-SW trending stretching lineation, which has been locally re-oriented by dextral strike-slip shearing (Vannay and Steck, 1995). The origin of this early deformation is unclear, but, Vannay and Steck (1995) have suggested that it may be related to an early phase of NE directed 'nappe-stacking', possibly associated with inversion of south-dipping relict normal faults during the early stages of Tertiary collision.

The second phase of deformation in the NW Indian THS (local D2) is associated with a system of SW directed thrusts and reverse faults, and NW-SE trending (SW-verging) asymmetric folds (Vannay and Steck, 1995; Wiesmayr and Grasemann, 2002). The style of deformation is characteristic of the brittle upper crustal regime

(Vannay and Steck, 1995; Wiesmayr and Grasemann, 2002), and at least some slip surfaces appear to correspond to inverted Carboniferous normal faults reactivated during Tertiary compression (Vannay and Spring, 1993). D2 folds are associated with a variably developed spaced axial planar crenulation cleavage and NE-SW oriented stretching lineation. However, several workers have noted that the style of folding, location of slip surfaces, and orientation of axial planar fabrics may be strongly influenced by competency contrasts in the surrounding strata (Vannay and Steck, 1995; Wiesmayr and Grasemann, 2002). In the Lahul region (*Figure 2.1*(*a*)), both D1 and D2 structures, and the principal mylonitic foliation in the GHC, are overprinted by regional doming and localised NE-vergent back folding associated with a SW dipping axial planar crenulation cleavage and sporadic NE-SW oriented stretching lineation (Vannay and Steck, 1995). While no late-stage folding has been identified in Spiti (*Figure 2.1*(*b*)), D2 fabrics in southern (structurally lower) parts of the section are overprinted by a weakly developed spaced cleavage that is concordant with the principal mylonitic foliation in the GHC (Wiesmayr and Grasemann, 2002).

A balanced section constructed along the upper Pin valley (Spiti, *Figure 2.1*(*b*)) indicates that this region experienced *ca.* 30% shortening during the tertiary (Wiesmayr and Grasemann, 2002). This value is notably lower than those calculated for larger transects (*e.g.* Ratschbacher et al., 1994, 1992) and the difference is attributed to the more frontal position of this section, consistent with the trend of southward-decreasing total accumulated shortening noted by (Ratschbacher et al., 1994) further to the east. Three samples of recrystallized illite separated from the axial planar cleavage domains of D2 folds yielded $^{40}Ar/^{39}Ar$ total gas ages from 47 Ma to 56 Ma (Wiesmayr and Grasemann, 2002). Given that the largest size fraction analysed was 6-11 μm and there is a positive correlation between age and grainsize, the range of ages may reflect closure, or even loss of ^{39}Ar due to recoil (McDougall

and Harrison, 1988). These data are interpreted to record the approximate timing of major south-vergent shortening in the in the NW Indian THS (Wiesmayr and Grasemann, 2002). Cross-cutting regional doming in the Lahul region is required to post-date formation of the principal mylonitic foliation in the GHC, thought to be associated with Miocene slip on the MCT (Vannay and Steck, 1995).

2.3.3 Northern Nepal

The structural framework described for southern parts of the THS outcropping in northern Nepal (*Figure 2.1*(*d*)) appears to differ somewhat from that documented elsewhere along the Himalayan Arc. In particular, the second phase of deformation in Nepal is dominated by north-vergent folds (Burchfield et al., 1992; Godin et al., 1999a,b; Godin, 2003, and refs. therein), whereas elsewhere south-vergent structures abound (Ratschbacher et al., 1994; Vannay and Steck, 1995; Wiesmayr and Grasemann, 2002, this study).

The earliest deformation preserved in northern Nepal (local D1) occurs at outcrop scale as rootless isoclinal fold hooks associated with a bedding parallel schistosity in Paleozoic strata, but has also been inferred at km-scale based on remote observations of a major refolded nappe (the Fang nappe) at *ca.* 7000 m elevation close to the peak of Annapurna I (Godin et al., 1999a; Godin, 2003). D1 structures are overprinted by macroscopic northeast-verging high amplitude tight folds (local D2), associated with a penetrative schistosity in pelitic units and a spaced cleavage in more competent layers (Godin et al., 1999a). These folds were originally interpreted to have resulted from gravitational collapse associated with normal-sense motion on the STFS (Burchfield et al., 1992, and references therein), however Godin et al. (1999b,a) have noted that D2 fabrics are in fact transposed and overprinted by (and therefore pre-date) a mylonitic foliation associated with normal-sense move-

ment on the STFS (local D3). D1-D3 structures and fabrics are overprinted, first by post-peak metamorphic south-vergent kink folds (local D4) associated with a spaced crenulation cleavage and localised minor thrusting at lower structural levels, and finally by northwest-southeast trending extensional structures (local D5) formed during opening of the Thakkhola graben (Godin, 2003). Palinspastic bed-length restoration implies that the local D2 deformation phase (the dominant shortening event) accommodated a minimum of 43% horizontal shortening and 150% vertical thickening (Godin, 2003). Based on cross cutting relationships discussed above, this deformation is required to pre-date Miocene (Hodges et al., 1992, 1996; Dezes et al., 1999) normal sense motion on the STFS.

2.3.4 Southwest Tibet

Palinspastic reconstruction of the THS in southwest Tibet (Murphy and Yin, 2003, *Figure 2.1*(*c*)) indicates that the region experienced a similar structural evolution to that documented in central southern Tibet and northwest India. Based on field data compiled from Heim and Gansser (1939), Cheng (1987) and their own studies, Murphy and Yin (2003) suggest that the region has experienced 60% horizontal shortening (176 km), corresponding to 112 km (38%) within the THS and 64 km (21%) within the ITS fault systems. Their reconstruction indicates that the earliest deformation occurred in the late Cretaceous to Paleocene, associated with south-directed obduction of the Kiogar-Jungbwa ophiolite along the Kiogar-Jungbwa thrust. This deformation was followed by formation of a complex system of south-directed thrusts, including activity on the Gangdese Thrust (GT) from 30 to 23 Ma (Harrison et al., 2000; Murphy and Yin, 2003). The timing of south-vergent deformation is poorly constrained, but must be complete prior to activity on a series of north-directed back thrusts related to the GCT between 19 Ma and 13 Ma (i.e. contemporaneous with movement on the STFS) (Quidelleur et al., 1997; Yin

et al., 1999; Harrison et al., 1999b; Murphy and Yin, 2003). Significantly, Murphy and Yin (2003)'s reconstruction implies that the locus of shortening during the early stages of collision may have been situated some distance (possibly >60 km) south of the ITS, and that a significant amount of unsubducted oceanic lithosphere could have been present south of of the ITS at that time.

2.3.5 Pre-Himalayan deformation

A number of workers have commented on the importance of structures pre-dating the initiation of continental collision in the early Tertiary, both as a source of potential confusion when compiling Himalayan shortening budgets, and as stress guides influencing the location, geometry and style of subsequent deformation (see discussion in Yin and Harrison, 2000). Unfortunately, the role of pre-Himalayan deformation has been largely neglected in the vast majority of Himalayan evolutionary models (*cf.* Gehrels et al., 2003, 2006). Workers in the Nepal Himalaya have argued that several major Himalayan lineaments may have originated as components of a Paleozoic thrust belt, associated with a major regional unconformity and widespread Cambro-Ordovician granitoid magmatism (Miller et al., 2001; Gehrels et al., 2003, 2006). In NW India, a similar Cambro-Ordovician unconformity has been observed cutting mesoscopic upright NW-SE trending folds, and nearby, an extensional fault accommodating *ca.* 70 m dip-slip motion is transgressed by Ordovician conglomerates suggesting a pre-Ordovician age of displacement (Wiesmayr and Grasemann, 2002).

Both Vannay and Steck (1995) in NW India and Godin (2003) in northern Nepal, have described early N-verging compressional structures. Vannay and Steck (1995) have suggested that in NW India, this deformation may have been controlled by stress localisation associated with reactivation of pre-Himalayan lineaments during

the early stages of Himalayan orogenesis. In general, the magnitude and distribution of pre-Himalayan deformation is poorly constrained. However, based on the available data, it appears that structures confined to Ordovician and older strata should not be automatically assigned to the Himalayan epoch, and that care should be taken when evaluating all deformation structures to consider potential reactivation of the pre-existing structural grain.

2.3.6 Summary

Shortening in the THS has been accommodated chiefly through dissection of the Indian foreland sequences into a predominantly north-dipping regional fold and thrust belt (*e.g.* Ratschbacher et al., 1994; Wiesmayr and Grasemann, 2002; Murphy and Yin, 2003; Pan et al., 2004, this study). Although some studies have detected an early North-vergent event, most workers agree that the principal phase of Tertiary shortening in the THS led to formation of predominantly south-vergent thrusts and brittle folds, associated with a variably developed spaced axial planar foliation (Ratschbacher et al., 1994; Wiesmayr and Grasemann, 2002; Murphy and Yin, 2003; Godin, 2003; Pan et al., 2004, this study). This deformation is required to pre-date Miocene north-directed movement on the STFS-GCT fault systems (based on cross cutting relationships), and sparse geochronological data suggest that it may even by as old as Eocene (Ratschbacher et al., 1994; Wiesmayr and Grasemann, 2002). Younger deformation events include local folding and E-W extension associated with formation of broadly N-S trending graben (*e.g.* Armijo et al., 1986; Burchfield et al., 1991; Wiesmayr and Grasemann, 2002). Most workers have estimated the Tertiary shortening budget of the THS to be between 30% and 68% (Ratschbacher et al., 1994; Wiesmayr and Grasemann, 2002; Murphy and Yin, 2003; Godin, 2003); although these values may be underestimated due to the lack of hanging wall cut-offs, and evidence for penetrative deformation and volume loss within many of the thrust

sheets (Murphy and Yin, 2003, this study). Access restrictions limiting the majority of studies to either northern or southern parts of the THS may explain some disparity among their various interpretations.

2.4 The eastern Tethyan Himalaya

The eastern THS (90–94°E) comprises a deformed, broadly southward-younging, Triassic to Cretaceous sequence of predominantly low-grade metasediments (Liu and Ensele, 1994; Pan et al., 2004, this study). The stratigraphy of this sequence is simplified from Pan et al. (2004). Depositional ages are based largely on sparse paleontological evidence (Liu and Ensele, 1994; Garzanti, 1999). Northern parts of the section are made up of a thick clastic-dominated sequence, comprising turbidites, fine-grained sandstones and slate (*Figure 2.2*). These units were laid down during the Triassic, in association with rifting of the Neotethys Ocean (Liu and Ensele, 1994; Pan et al., 2004, this study). The central THS is primarily composed of shallow water carbonates and siliciclastics deposited as part of the Indian passive margin sequence during the Jurassic phase of drift sedimentation, although some Cretaceous units are found outcropping in structural depressions (Liu and Ensele, 1994; Pan et al., 2004, *Figure 2.2*). Southern parts of the section are composed almost entirely of Cretaceous marine clastics and carbonate platform deposits formed shortly prior to final closure of the Neotethys Ocean (Liu and Ensele, 1994; Pan et al., 2004, *Figure 2.2*).

The contacts between the main lithotectonic units of the eastern THS are thought to have been depositional prior to Himalayan orogenesis (Liu and Ensele, 1994; Garzanti, 1999), although present day contacts have in some cases been modified by Tertiary deformation (*e.g.* Lhunze Thrust, see below). Metamorphic grade is generally lower greenschist facies in northern parts of the section, decreasing to

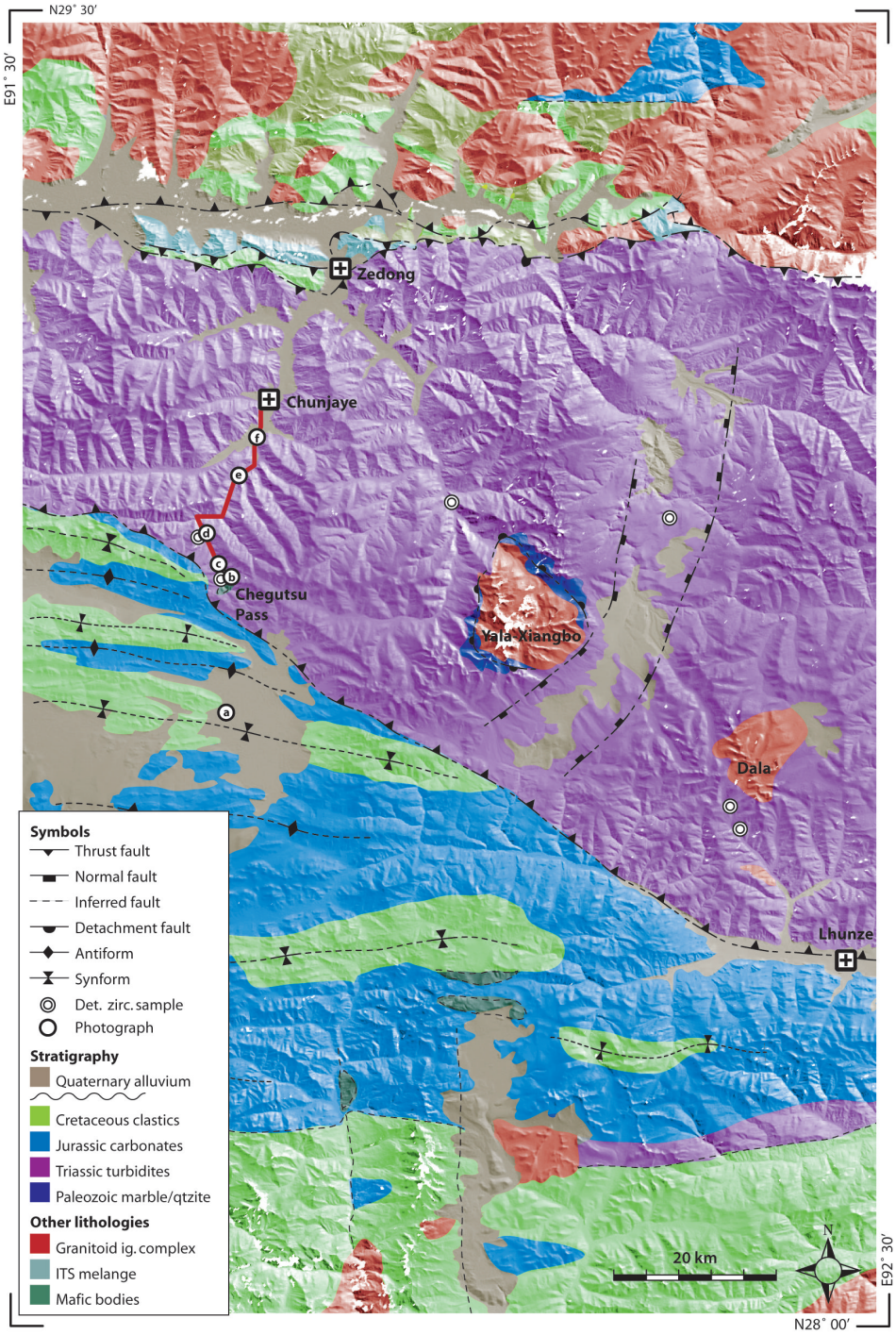

Figure 2.2: Overview regional geological map of the eastern Tethyan Himalaya showing the locations of samples, photographs and structural data discussed in the text (compiled from Pan et al., 2004; Harrison et al., 2000, this study).

sub-greenschist facies southwards. Access to this area by non-Chinese nationals is severely limited by the Chinese military authorities. However, reconnaissance studies conducted along a roughly N-S oriented transect at *ca.* 92°E indicate that the structure of the eastern THS, as will be outlined below, is similar to that documented elsewhere in southern Tibet and NW India.

2.4.1 Structure of the Cretaceous and Jurassic strata

The Cretaceous units outcropping in southern parts of the section could not be studied due to access restrictions. However, in the central THS (*e.g.* N28°43.853' E091°37.553') the Cretaceous and Jurassic sequences are deformed together into a series of macroscopic, upright, open folds (*Figure 2.2*). The regional extent and geometry of these structures is inferred from outcrop patterns (Pan et al., 2004, *Figure 2.2*) and satellite imagery (ASTER, Google Earth), correlated with field observations (*e.g. Figure 2.3(a)*). Northwards towards the Triassic strata, the axial spacing between folds decreases and their geometries become south-vergent, marking a progressive tightening of this fold generation (*Figure 2.2*). The contact between the northernmost Jurassic/Cretaceous and southernmost Triassic units could not be observed directly in the field due to access restrictions and poor exposure. However, outcrop patterns (Pan et al., 2004, *Figure 2.2*) suggest that it truncates folded Jurassic/Cretaceous strata, and hence it is interpreted to be tectonic. This structure (the Lhunze Fault) is likely comparable to the N-dipping Gyirong-Kangmar Thrust, which has been mapped *ca.* 200 km along strike to the west (Chen et al., 1990; Lee et al., 2000). Although the available data cannot exclude normal-sense displacement on a S-dipping fault plane. The timing of activity on the Lhunze Fault is required to post-date formation of the E-W trending folds.

(a) Open, E-W trending macroscopic folds of Cretaceous & Jurassic strata (W)

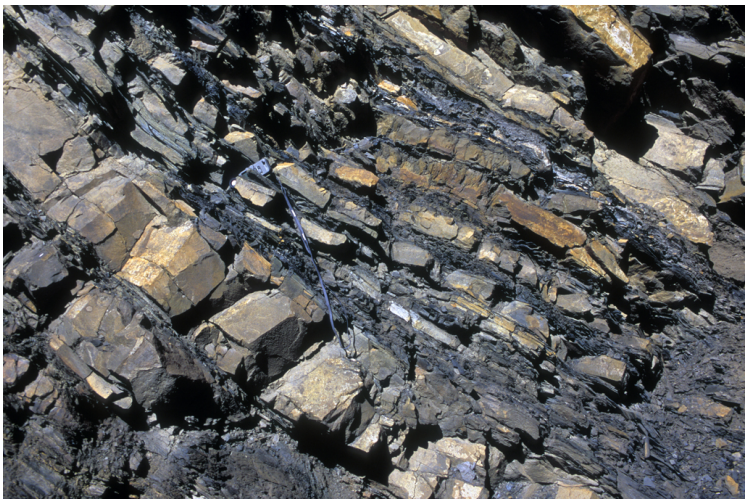

(b) Style of the Triassic turbidites (W)

Figure 2.3: Structural features of the THS metasediments in the eastern Himalaya. Image locations (a)-(f) correspond to symbols on *Figure 2.2*, view directions listed in brackets. *Continues on next page...*

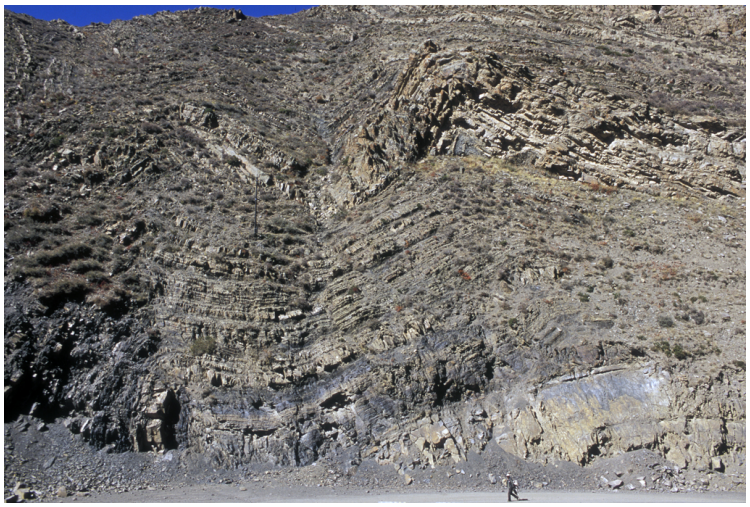

(c) S-vergent open folds of Triassic strata just N of Lhunze Fault (W)

(d) S-vergent close folds of Triassic strata, location few km to north of (a), note fold styles are notably tighter (W)

Figure 2.3: *Continued...*

(c) Chevron folds of Triassic strata few km south of Chunjaye (W)

(d) Isoclinal folds of Triassic strata close to Chunjaye (E)

Figure 2.3: *Continued...*

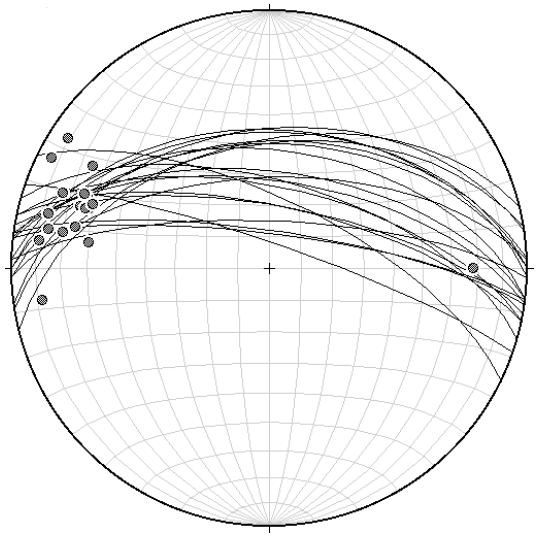

Figure 2.4: Stereonet showing axial surfaces (great circles) and hinge lines (poles) of folds in the Triassic metasediments. All data collected along transect between Chunjaye and Chegutsu pass marked in red on *Figure 2.2*

2.4.2 Structure of the Triassic strata

In the hanging wall of the Lhunze Fault close to Lhunze (N28°30.421' E092°16.332'), Triassic siliciclastic sediments are folded into mesoscopic, E-W trending, south-vergent folds. The style and orientation of these structures is very similar to that observed in the northernmost Jurassic/Cretaceous units outcropping along strike to the west; hence they are interpreted to be correlative. Detailed structural observations were collected along a short transect (*ca.* 30 km, marked as a solid red line on *Figure 2.2*) from Chegutsu Pass (N28°50.716' E091°38.480') northwards down a valley towards the village of Chunjaye (N29°01.727' E091°40.898'). The transect was chosen to characterise the structure of the Triassic metasediments because it has relatively uninterrupted roadside exposure, and lies *ca.* 30 km to the west along strike from the Yala-Xiangbo Dome (*Figure 2.2*, see below).

The Triassic strata of this area comprise deci-centimetre to meter-scale turbidite sequences, showing flute casts at the base of coarse grained massive sandstone beds, fining upwards to silt and laminated black shale (*Figure 2.3(b)*). Southern parts of the transect are dominated by sandy units, whereas to the north finer grained silt and shale abound. Close to Chegutsu Pass (N28°51.135' E091°38.329', *Figure 2.2*), the Triassic metasediments are deformed into a series of meso- to macroscopic E-W trending (shallow west plunging), south vergent folds, with axial planes dipping at *ca.* 55° to the North (*Figure 2.3(c)*). A variably developed north-dipping axial planar foliation is observed in the hinge zones, although its orientation is locally variable where the style of folding becomes disharmonic. Travelling northwards, the spacing between fold axes is reduced and the orientations of axial planes becomes less variable. This tightening of folds is associated with a more intense axial planar foliation, observed as a slaty cleavage in fine-grained units and spaced cleavage in more competent layers (*Figure 2.3(d)*). Central parts of the transect (*e.g.* N28°55.895' E091°38.809') are characterised by meso- to macroscopic E-W trending, south-vergent chevron folds, associated with a penetrative schistosity in fine-grained units and well developed spaced cleavage in more competent layers (*Figure 2.3(c)*). Northwards towards Chunjaye, the style of folding tightens further, eventually becoming isoclinal at the ten- to hundred-meter scale (*e.g.* N28°58.660' E091°39.995', *Figure 2.3(d)*). All units in this area contain a penetrative schistosity that is axial planar to isoclinal folds.

North of Chunjaye towards the Indus-Tsangpo Suture, a progressive rotation of the dominant foliation in the Triassic metasediments (which is axial planar to isoclinal folds at Chunjaye) is observed. This fabric eventually becomes south-dipping, sub-parallel to the Great Counter Thrust (locally known as the Renbu Zedong Thrust) adjacent to the suture. This relationship suggests that the axial

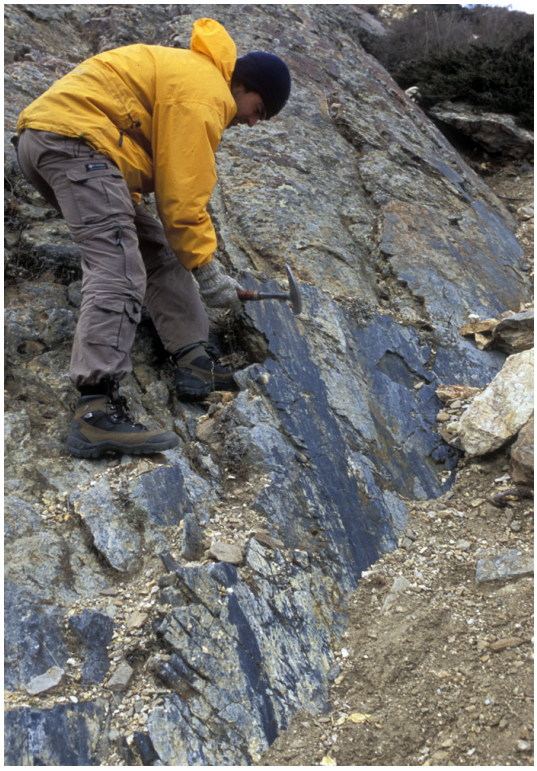

Figure 2.5: Outcrop of fault zone on southeastern edge of Yala-Xiangbo Dome (view North). This structure is interpreted as having formed in association with a major NNE-SSW trending rift cutting the eastern Tethyan Himalaya (*Figure 2.2*).

planar foliation has been re-oriented by motion on this structure. Further proof of this overprinting relationship is provided by rootless isoclinal folds preserved in low strain zones adjacent to the Renbu Zedong Thrust. This geometry is interpreted to post-date isoclinal folding, and is attributed to rotation and reactivation of existing fabrics during formation of major fault-bend fold structure associated with motion on the Renbu Zedong Thrust.

2.4.3 Recent rifting

In the central Tethyan Himalaya, the Triassic metasediments are cut by a *ca.* 12 km wide, NNE-SSW trending graben that is clearly visible on satellite imagery (*Figure*

1.3, *Figure 2.2*). The topographic expression of this structure appears to be continuous across much of the eastern Tethyan Himalaya. A small fault zone was observed outcropping at the base of the Yala-Xiangbo pass where the graben appears to cut the south-east limb of the Yala-Xiangbo dome (*Figure 2.5*). The fault surface dips steeply (*ca.* 70°) ESE, and shows a slickenslide lineation plunging in the approximate dip direction of this plane. Both the texture of the slickenslides and the orientation of fault breccia imply normal-sense displacement. This structure is interpreted to represent either the western graben-bounding fault or a smaller associated subsidiary fault. The graben itself is partially filled by flat lying, poorly consolidated sediments. Formation of this structure is interpreted to post-date motion on the Lhunze and Renbu-Zedong thrusts.

2.4.4 Summary

Collectively, the structures documented in the THS metasediments of the eastern Himalaya are interpreted as recording three regional deformation events. The first comprises N-S shortening associated with formation of a series of E-W trending, shallow W-plunging, upright or south-vergent folds (D_1). The intensity of deformation associated with these structures increases northwards, as indicated by the tightening of F_1 folds and the progressive development of an axial planar foliation. These structures are constrained to be Tertiary in age by stratigraphic arguments, and represent the majority of deformation related to Himalayan orogenesis. The second phase of deformation (D_2) was characterised by N-S shortening associated with displacement along north- and south- directed thrusts that overprint F_1 folds. The Lhunze Fault, outcropping in the central Tethyan Himalaya, is considered analogous to the north-dipping Gyirong-Kangmar Thrust, which has been mapped *ca.* 200 km along strike to the west and is thought to have accommodated *ca.* 2000 m vertical displacement during the Miocene (Quigley et al., 2006, and refs. therein).

The south-dipping Renbu Zedong Thrust, adjacent to the Indus Tsangpo Suture, accommodated a minimum of 12 km top-to-the-north displacement between 19 Ma and 15 Ma (Quidelleur et al., 1997). Structural observations conducted in this study do not constrain the relative timing of movement on the Renbu Zedong Thrust and Lhunze Fault. The third phase of deformation is represents roughly E-W extension associated with formation of a major NNE-SSW trending rift. This structure is similar to other N-S trending rifts found at various locations along the Himalayan Arc and throughout the Tibetan Plateau, and likely formed during the Pliocene (Armijo et al., 1986; Burchfield et al., 1991).

2.4.5 A note on the location of the eastern ITS

In the central Himalaya, the southern margin of Eurasia adjacent to the ITS is marked by Xigaze group sediments, which are thought to have originated as forearc deposits to the south-facing Gangdese arc prior to closure of the Neotethys (Einsele et al., 1994; Pan et al., 2004, *Figure 1.2*). In the eastern Himalaya, however, Xigaze units are absent and calc-alkaline plutonics of the Gangdese batholith have been thrust over components of the ITS (Yin et al., 1994, 1999; Harrison et al., 2000, *Figure 2.2*). Based on sparse paleontological evidence and their present day outcrop position, rocks directly south of the surface expression of the ITS have traditionally been assigned to the Triassic successions of the THS forming part of the continental margin deposits of northern India (*e.g.* Liu and Ensele, 1994; Pan et al., 2004). A few studies however, have proposed that these rocks may in fact represent either remnants of the Xigaze group or Indus-Tsangpo melange, thereby placing the true location of the ITS up to 120 km further south (Yin, 2006; Aitchison et al., 2007, and refs. therein).

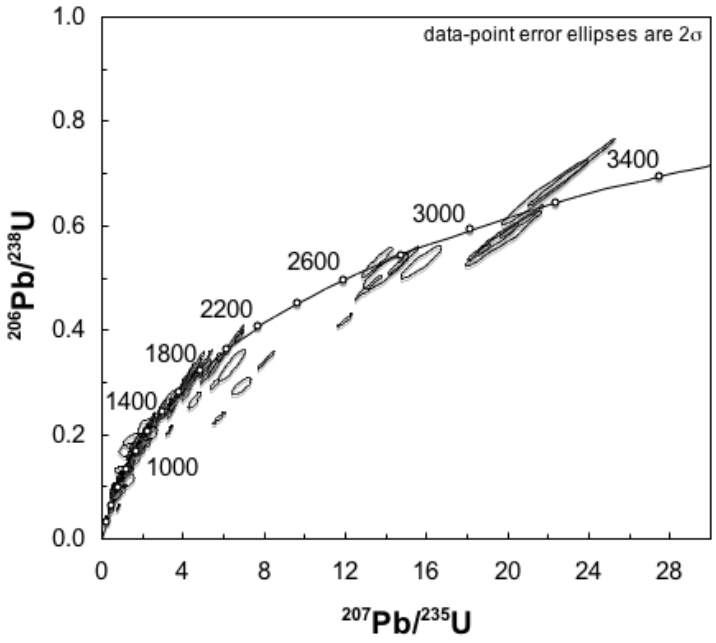

(a) Concordia plot

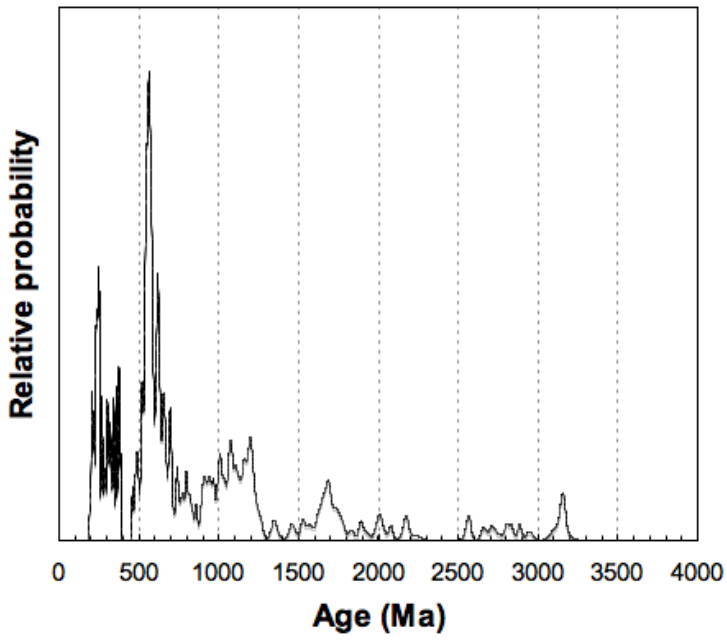

(b) Age probability plot

Figure 2.6: ^{204}Pb corrected concordia and age-probability plots for U-Pb dating of zircons from 6 samples of Triassic THS metasediments. Sample locations as shown on *Figure 2.2*.

Reconnaissance mapping in the northern THS at *ca.* 92°E has provided no confirming evidence that rocks in this area represent components of a melange. Indeed the structural continuity of the THS section (discussed above) argues strongly against this hypothesis. Although the possibility that they represent parts of the Xigaze forearc cannot be automatically discounted. Widespread calc-alkaline magmatism in the Gangdese arc and deposition of the Xigaze forearc sediments is thought to have occurred in the Cretaceous-Paleocene (Debon et al., 1986; Dürr, 1996), at which time the northern margin of India was undergoing a relatively tectonically stable phase of drift sedimentation (Liu and Ensele, 1994; Garzanti, 1999). Detrital zircon populations were separated from six samples collected from the Triassic units of Pan et al. (2004, sample locations marked on *Figure 2.2*) and analysed by ion-microprobe (according to the procedure described in *Chapter 4* to test for the presence of a Cretaceous sedimentary source. Two hundred and fifty grains were analysed, typically ranging in length from 80-300 μm, and exhibiting a broad spectrum of morphologies and cathodoluminescence zonation patterns. Calculated ages for all six samples range from *ca.* 200 Ma to >3000 Ma (*Figure 2.6*), from which we conclude that there is currently no evidence in dispute of the traditional stratigraphic paradigm.

2.5 Regional structural evolution

Studies in northwest India, central and eastern Tibet, and northern Nepal place constraints on the structure of the Tethyan Himalaya. Although no unifying model has yet been proposed, several key themes have emerged. In the following sections, a tentative correlation scheme is proposed, from which conclusions may be drawn about the structural evolution of the inferred earliest accreted units of the Himalayan fold and thrust belt.

The oldest structures found in the Tethyan Himalaya are those appearing to have pre-Himalayan formative ages by stratigraphic argument. Although the spatial association, distribution and magnitude of these deformations are not well constrained, the available data are consistent with Paleozoic and older strata now comprising components of the HFTB having experienced a common phase of pre-Ordovician deformation associated with formation of a regional unconformity and widespread Cambro-Ordovician magmatism. These structures may also have played a role in localising subsequent deformations.

The earliest potentially correlative deformations are found in the THS of northwest India and northern Nepal. They are represented by broadly E-W trending (NW-SE in the western Himalaya) isoclinal folds associated with a penetrative axial planar schistosity. In northwest India, these structures are present throughout the stratigraphic section, whereas in northern Nepal, they have so far only been documented in the Paleozoic and older strata (Godin, 2003). Although this observation could be interpreted as indicating that structures in northern Nepal have pre-Himalayan formative ages, workers in both regions have ascribed them to the early Himalayan episode, possibly associated with reactivation of the pre-existing structural grain. These structures are assigned to the first phase of regional deformation (D_1^r), which may require further subdivision as more data become available. The apparent absence of similar structures in central and eastern Tibet may be due to the lack of detailed mapping in these areas.

The dominant structures found in the THS metasediments of northwest India and central and eastern Tibet comprise a system of E-W trending, predominantly south-vergent folds and thrusts. The style of folding in all of these areas is typically open to close (although sometimes disharmonic), associated with a spaced axial

planar cleavage in competent units and sporadically developed N-S oriented stretching lineation. Most workers independently attribute these as the principal Tertiary thickening structures in their respective study areas. The similarity of structural style, orientation, fabric development and position in the overall local deformation scheme, suggest that these events are correlative, representing a regional phase of Tertiary shortening responsible for major crustal thickening throughout the THS (D_2^r).

The apparent prevalence of north-vergent folds in northern Nepal could be taken as indicating that structural evolution of this area differs from that described elsewhere. These structures were originally attributed to gravitational sliding associated with Miocene movement on the STFS (Burchfield et al., 1992). However Godin et al. (1999a) have shown that they are in fact overprinted by and therefore pre-date, a mylonitic foliation formed during normal-sense motion on this structure. The absence of detailed structural mapping around the Nepal-Tibet border has hindered correlation between these structures and those observed at the same structural position elsewhere. However Godin (2003) noted a northward progression from north-vergent to upright folds analogous to those observed in central-southern parts of the eastern THS. Moreover, a recent cross-section constructed in this region from a compilation of existing and new data, clearly shows the axial surfaces of upright folds rotated into parallelism with the STFS (Crouzet et al., 2007). The apparent northward vergence of these structures in northern Nepal is therefore attributed to local reorientation associated with motion on the STFS-MCT fault systems, and/or reactivation of the pre-existing structural grain. This interpretation is considered preferable to the alternative in which north-vergent structures represent an additional deformation episode for which there is as yet no correlative evidence elsewhere along the Himalayan Arc.

Event	Structures	Timing
Pre-H	Folds and faults in Paleozoic and older strata.	Pre-Ordovician.
D_1^r	Broadly E-W trending isoclinal folds associated with a penetrative axial planar schistosity. Found throughout the stratigraphic section in NW India, appear to be confined to Paleozoic strata in northern Nepal. May be associated with re-activation of pre-existing structural grain.	Early Tertiary, based on stratigrahic arguments and cross-cutting relationships.
D_2^r	E-W trending, predominantly S-vergent folds and thrusts. Found throughout the THS, represent dominant thickening structures in the Tethyan Himalaya. Fold styles locally disharmonic, appear to tighten northward, associated with a variably developed spaced axial planar foliation and N-S trending stretching lineation.	Pre-Miocene based on cross-cutting relationships, sparse geochronology indicate could be as old as Eocene.
D_3^r	Mylonitic foliation around STFS, renewed thrusting and development of major fault-bend fold in northern Tethyan Himalaya associated with activity on GCT. Re-orientation of pre-existing structures.	Miocene, based on timing of GCT-STFS slip.
D_4^r	Local doming and minor folding of the southern THS.	Mio-Pliocene, based on cross-cutting relationships.
D_5^r	Broadly E-W extension associated with formation of arc-normal graben.	Pliocene based on structural association and cross-cutting relationships.

Table 2.1: Summary of regional deformation sequence inferred for the THS metasediments, including temporal constraints.

Southern parts of the THS in NW-India and northern Nepal are cut by a mylonitic foliation analogous to that which is found in the underlying units of the GHC. Most workers have argued that this fabric was formed during Miocene motion on the MCT-STFS fault system, which is thought to have been active contemporaneously with reverse-sense slip on the GCT (Quidelleur et al., 1997). These events are collectively ascribed to the third phase of regional deformation (D_3^r). Other similar structures such as the Gyirong-Kangmar Thrust and Lhunze Fault outcropping within the THS are also assigned to this phase, although their exact age is not known. Late-stage spatially restricted deformations, such as minor kink folding in northern Nepal (Godin, 2003; Godin et al., 1999a) and doming in NW-India (Vannay and Steck, 1995), are likely attributable to localised effects associated with assembly of the Lesser-Himalayan duplex, out of sequence motion on the MCT and renewed shortening in the THS following cessation of normal-sense slip on the STFS. These events are assigned to D_4^r, which may not be correlative across the entire THS. The most recent regionally correlative deformation event so far documented is associated with formation of a series of NNE-SSW trending (arc-normal) rifts; these structures are assigned to D_5^r.

2.5.1 Timing of Tertiary deformation

The regional deformation sequence described above is summarised in *Table 2.1*. Published constraints on the absolute timing of these events are, however, relatively limited. The absence of regional unconformities, thickening strata or voluminous coarse-grained continental clastic sedimentation in the Cretaceous units of the THS (Liu and Ensele, 1994) suggests that the vast majority of regional deformation structures described above are Paleocene or younger and thus associated with the Himalayan phase of orogenesis. The timing of the first regional deformation event

(D_1^r) is poorly constrained, however based on the available data it is assigned an early Tertiary Age. Sparse geochronological evidence suggests that regional E-W trending folds and thrust representing the dominant thickening structures in the Tethyan Himalaya (D_2^r) may have Eocene formative ages. However cross cutting and overprinting relationships require that they pre-date Miocene movement on the GCT-SFTS fault systems (D_3^r). Localised deformations that are speculatively attributed to assembly of the Lesser Himalayan Duplex and reactivation of the MCT likely occurred during the late Miocene (D_4) (Celerier, 2007), and rifting associated with E-W extension of the Tibetan Plateau is thought to have begun in the Pliocene (D_5^r) (Armijo et al., 1986; Burchfield et al., 1991).

2.6 Conclusions

Studies in northwest India, northern Nepal, and central-southern Tibet, have revealed notable similarities in the structure of the Tethyan Himalaya along the main Himalayan Arc. Combined with new results from the eastern Himalaya, these data permit construction of a model for the sequence of regional deformations affecting the Tethyan Himalaya.

The role of pre-Himalayan deformation in the Tethyan Himalaya is poorly constrained. However, based on the available data, it appears that structures confined to Ordovician and older strata should not be automatically assigned to the Himalayan epoch, and that care should be taken when evaluating all deformation structures to consider potential reactivation of the pre-existing structural grain.

Tertiary deformation has led to dissection of the Indian passive margin into a predominantly north-dipping regional fold and thrust belt. The first deformation event (D_1^r) appears to have been associated with formation of broadly E-W trending

isoclinal structures and a penetrative axial planar schistosity. The structural style of this event may have been influenced by stress localisation associated with reactivation of the pre-existing structural grain. The second phase of deformation (D_2^r) was associated with formation of a series of E-W trending, predominantly south-vergent folds and thrusts, and a variably developed spaced axial planar foliation. These are the dominant thickening structures affecting the THS metasediments of the Tethyan Himalaya. Sparse geochronological data suggest that this event could have occurred during the Eocene, however, it is required to pre-date Miocene slip on the STFS-GCT fault system (D_3^r). Subsequent local folding and doming (D_4^r) are attributed to ongoing deformation and assembly of the frontal ranges. The youngest regional deformation so far detected is associated with rifting and development of N-S trending graben structures (D_5^r).

Although this scheme does not represent exhaustive study, it provides - to our knowledge - the first unifying model for the structural evolution of the inferred earliest accreted units of the Himalayan Fold and Thrust Belt. These results bear upon the nature of deformation implied by Himalayan evolutionary models, and provide a contextual framework in which to interpret and correlate other aspects of study.

Chapter 3

Magmatic emplacement and thermal history

3.1 Introduction

Igneous bodies in zones of active orogenesis can be both inherited (pre-orogenic), as well as formed by ongoing and new processes linked to continental and lithospheric deformation. As such, geometric relationships between these bodies and their host lithologies can in some cases be used to constrain the relative timing of key tectonic events (Hutton, 1788; Lyell, 1830). Many such bodies also contain phases that are suitable for radiometric dating, allowing absolute temporal information, and in some cases their thermal history, to be recovered (McDougall and Harrison, 1988, and refs. therin). Collectively, these data are valuable in aiding orogenic reconstruction.

In the Himalaya, igneous bodies outcrop at a variety of locations and have frequently been used to constrain Himalayan evolutionary models (LeFort, 1975, 1996; Yin and Harrison, 2000; Yin, 2006, and refs. therein). To date, however, the majority of studies have focussed on bodies outcropping along the frontal ranges, those

within the Tethyan Himalaya have received relatively little attention. Such units include the North Himalayan Granites (NHG) and North Himalayan Domes (NHD), which comprise the northernmost of two parallel granitoid belts, representing one of the most characteristic features of the Himalayan Arc (Harrison et al., 1997a, 1998a). Although several recent studies have provided new insight into the genesis of the NHG and NHD (*e.g.* Lee et al., 2000, 2004; Zhang et al., 2004a), the majority of published data are derived from a small area the central Tethyan Himalaya; relatively little is known about those outcropping further to the east.

3.1.1 Purpose of this chapter

Data presented in *Chapter 2* permit construction of a framework for the structural evolution of the Tethyan Himalaya. Unfortunately, however, its generality is limited by the lack of constraints on the timing of several key deformation events. This information can potentially be derived from igneous bodies emplaced during the Himalayan episode. Furthermore, studies of several NHD have suggested a remarkable degree of structural similarity (Lee et al., 2000, 2004; Quigley et al., 2006), leading some workers to argue that they may have experienced a common history (*e.g.* Aoya et al., 2005). These results have been used to endorse regional tectonic models with wide-ranging implications (*e.g.* Lee and Whitehouse, 2007). However, many aspects of the formation of the NHD remain poorly understood and regional continuity of structural elements has in general not been widely demonstrated.

In the following sections, the structural context of igneous lithologies outcropping within the Tethyan Himalaya are reviewed and discussed in conjunction with new data from the eastern Himalaya. Our results both significantly extend the known spectrum of Himalayan granitoid magmatism, and constrain the timing of key regional deformation events. Moreover, new data from the Yala-Xiangbo Dome

highlight shortcomings in present understanding of the formation of the NHD, suggesting that more work is required before a robust consensus can emerge.

3.2 Igneous bodies in the Tethyan Himalaya

Igneous bodies outcrop at several locations within or adjacent to the Tethyan Himalaya. In the central THS (*ca.* 60 km south of the ITS), granitoids are emplaced as dykes, sills and small plutons (the North Himalayan Granites, NHG) within the cores of North Himalayan Domes (NHD, *Figure 1.2*) (Burg and Chen, 1984; Chen et al., 1990; Harrison et al., 1997a; Yin and Harrison, 2000; Lee et al., 2000). Further south, leucogranite sheet, dyke and laccolithic bodies crop out close to the STFS, representing the structurally highest components of the High Himalayan Leucogranite (HHL, *Figure 1.2*) suite (LeFort et al., 1987; Inger and Harris, 1993; LeFort, 1996; Harrison et al., 1997a). Along to the northern margin of the THS, various mafic and other lithologies are found in association with the Indus-Tsangpo Suture (ITS, *Figure 1.2*). Several studies have also reported a variety of other smaller mafic and intermediate bodies at various locations within the deformed THS metasediments throughout the Tethyan Himalaya (Pan et al., 2004; Quigley et al., 2006, this study).

The majority of the HHL outcrop, not within the Tethyan Himalaya, but within the Greater Himalayan Crystalline sequences along the frontal ranges. These bodies are further discussed in subsequent chapters. The NHD and NHG are considered below.

3.2.1 The North Himalayan Domes and Granites

The NHD comprise a series of roughly elliptical structures, in which strongly foliated metasediments dip radially away from a core region that has been at least partially exposed through erosion (Burg et al., 1984b; Chen et al., 1990). To date, at least six

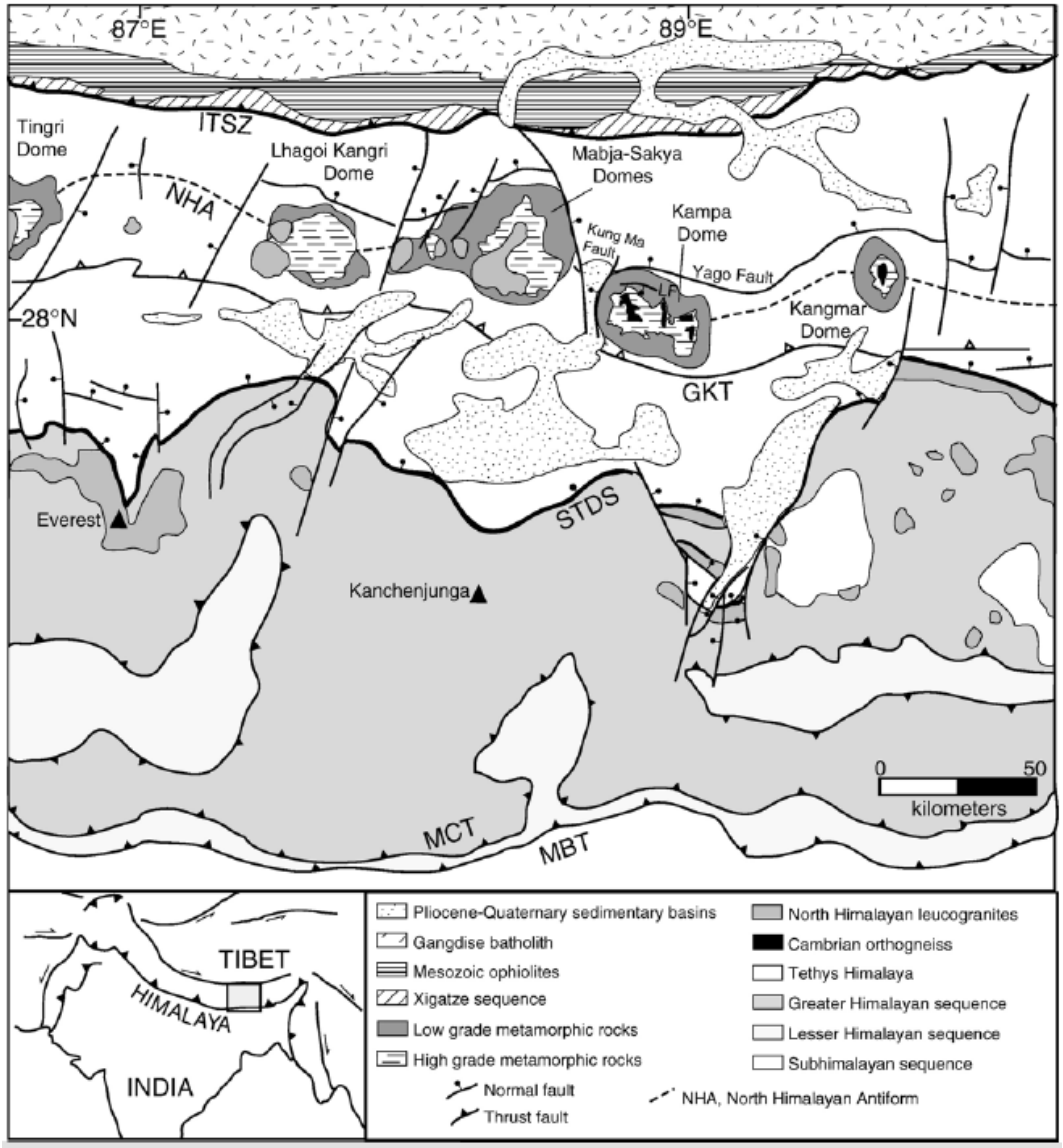

Figure 3.1: Map of the North Himalayan Domes studied to date (after Quigley et al., 2006, and refs. therein)

such structures have been identified within the central Tethyan Himalaya between *ca.* 85° and 90°E (*Figure 3.1*) (Watts and Harris, 2005; Quigley et al., 2006, and refs. therein). Although detailed studies have only been conducted in a few areas, results to date have suggested that the NHD show a remarkable degree of structural and lithological similarity (Lee et al., 2000, 2004; Zhang et al., 2004a; Quigley et al., 2006, and refs. therein).

The majority of the outcrop within the NHD is thought to expose parts of the Cambrian to Eocene THS metasediments, however the cores regions of several structures also contain granitic orthogneiss and/or migmatites (Burg et al., 1984a; Debon et al., 1986; Chen et al., 1990; Lee et al., 2000; Watts and Harris, 2005). U-Pb dating of zircons from granitic orthogneiss in the Kangmar Dome (the Kangmar Granite) yielded Cambrian ages (Schärer et al., 1986; Lee et al., 2000), which led to the suggestion these units may represent basement onto which the THS were deposited (Burg et al., 1984a; Lee et al., 2000). However, although this hypothesis has not been disproved, subsequent work has shown that deformed granites in the Malashan area (*ca.* 86°E) have Miocene formative ages (Aoya et al., 2005), indicating that not all such lithologies are necessarily correlative. Furthermore, a recent study has proposed - on the basis of their geochemistry - that orthogneisses from the Kangmar and Lhagoi-Kangri domes may be lithologically equivalent to upper parts of the GHC sequence as documented in northern Nepal (Zhang et al., 2004a). As such, shear zones associated with the contact between these units and the overlying THS metasediments are interpreted as exhumed portions of the STFS (Chen et al., 1990; Hauck et al., 1998; Lee et al., 2000, 2004; Zhang et al., 2004a). Metamorphic grade within the NHD increases with structural depth, from sub/lower greenschist facies in the surrounding THS metasediments, to upper amphibolite facies in the cores of most structures (Chen et al., 1990; Lee et al., 2000, 2004, this study). Thermo-

barometry from the Kangmar and Mabja-Sakya domes yielded temperatures and pressures of *ca.* 500°C, *ca.* 400 MPa in the chloritoid zone, and *ca.* 700°C, *ca.* 800 MPa in the core domains (Lee et al., 2000, 2004).

Studies of several NHD have proposed broadly similar structural histories. Most record an early phase of contractional deformation associated with the development of E-W trending folds and a spaced axial planar foliation (D_1^d) (Lee et al., 2000, 2004; Quigley et al., 2006, this study). These early structures - best preserved in the upper levels - are likely correlative with regional shortening in surrounding THS metasediments (Lee et al., 2000, 2004; Quigley et al., 2006, this study). Towards the core domains, D_1^d structures are overprinted by progressive development of a mylonitic foliation and broadly N-S oriented stretching lineation (*Figure 3.2*) (Chen et al., 1990; Lee et al., 2000, 2004; Quigley et al., 2006). Several workers have noted that shear-sense indicators associated with this fabric are bimodal, perhaps reflecting reactivation (Lee et al., 2000, M. Quigley *pers. comm.*, this study). This deformation (D_2^d) has been attributed to vertical thinning and horizontal stretching, possibly associated with collapse of over-thickened crust (Lee et al., 2000, 2004; Quigley et al., 2006). Formation of the domal geometries that now characterise the NHD (D_3^d) was associated with warping of D_2^d fabrics, and in some cases, strain localisation and development of relatively narrow shear zones in the flanking sequences (Burg et al., 1984a; Chen et al., 1990; Lee et al., 2000, 2004; Aoya et al., 2005; Quigley et al., 2006). The majority this deformation appears to have occurred in the high-temperature ductile regime (Lee et al., 2000, 2004), although shear zones at Kampa may have been active to greenschist facies conditions (Quigley et al., 2006). Some NHD are also cut by NNW-SSE trending steep normal faults, that probably formed during recent E-W extension (D_4^r) of the Tibetan Plateau (Lee et al., 2000, 2004; Quigley et al., 2006).

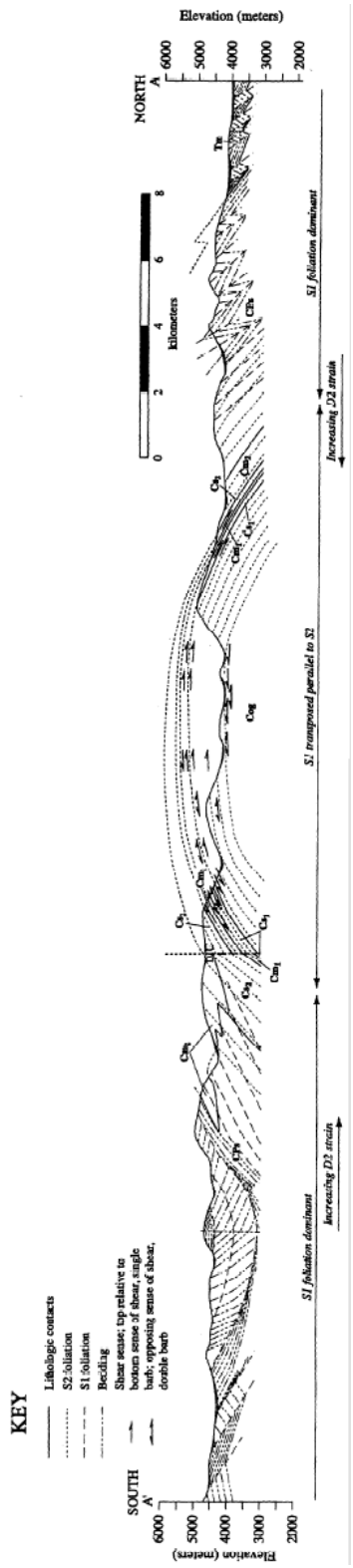

Figure 3.2: Schematic cross section through the Kangmar Dome (Lee et al., 2000).

The North Himalayan Granites outcrop as sheet/dyke complexes and small plutons within the core domains of most NHD *Figure 3.1.* The NHG *sensu stricto* are often considered to be dominated by two-mica granites (e.g. Harrison et al., 1997a). However more recent work has shown that muscovite granites and pegmatites, tourmaline-bearing assemblages and other leucocratic dyke swarms are also found (Lee et al., 2000, 2004; Zhang et al., 2004a; Quigley et al., 2006; Lee and Whitehouse, 2007, and refs. therein). Emplacement of most studied NHG is interpreted to be syn- to post-kinematic with D_2^d deformation (Chen et al., 1990; Lee et al., 2000, 2004; Aoya et al., 2005; Quigley et al., 2006; Lee and Whitehouse, 2007). The majority have yielded Miocene crystallisation ages, although at least one older Oligocene age has also been reported (Harrison et al., 1997a, 1998a; Zhang et al., 2004a, and refs. therein).

The North Himalayan Antiform

The NHD are often connected on regional geologic maps, to define a curvi-linear trend termed the North Himalayan Antiform (NHA), oriented sub-parallel to the main Himalayan Arc (*Figure 1.2*). The presence of this feature is inferred largely on the basis of a seismic section through the Kangmar Dome, which appears to show a ramp at mid-crustal depths (Hauck et al., 1998). However, while extrapolation from the Kangmar Dome along strike is not in principle unreasonable, there is, to our knowledge, no significant field evidence suggesting the presence of a regionally extensive antiformal structure in the Tethyan Himalaya. Indeed, in central parts of the Himalayan Arc, the intervening THS units between several NHDs are mapped as Cretaceous, whereas to the north and south, older strata abound (Pan et al., 2004). This observation suggests that outcrop patterns are more consistent with a regional synformal rather than an antiformal geometry in this part of the Tethyan Himalaya.

It is therefore suggested that in the absence of confirming data, the notion of a North Himalayan antiform (*senso stricto*) should be treated with caution.

3.2.2 Mafic and other bodies

The structural context of mafic bodies is not considered in detail in this study. However, other workers have suggested that many of those found outcropping in association with the ITS represent NeoTethyan oceanic material obducted during the early stages of Himalayan orogenesis (*e.g.* Yin and Harrison, 2000, and refs. therein). Reconnaissance investigations broadly support this hypothesis, although several recent studies have also identified scattered Mio-Pliocene plutons along the ITS that are identified as components of a suite of potassic to ultra-potassic rocks found throughout the Tibetan Plateau (Mo et al., 2006, and refs. therein; Ding Lin *pers. comm.*; unpublished data). To our knowledge, no systematic study of mafic bodies outcropping within the Tethyan Himalayan Sequences (THS) has so far been published in the western scientific literature. However, reconnaissance investigations conducted by this study, and those of several other workers (M. Quigley *pers. comm.*, S. Wallis *pers. comm.*), suggest that the majority of these bodies represent dykes and sills whose emplacement appears to pre-date regional deformation of the surrounding metasediments. Attempts to date several such bodies outcropping in the eastern Himalaya by U-Pb geochronology proved unsuccessful as no zircons were found.

3.3 The eastern Tethyan Himalaya

The range of igneous lithologies found in the eastern Tethyan Himalaya is similar to that observed elsewhere along strike. Mafic/ultra-mafic and intermediate bodies outcrop along the northern margin of the THS adjacent to the Indus-Tsangpo Suture (ITS) and within the Zedong Window (Yin et al., 1994, 1999; Harrison et al., 2000; Pan et al., 2004). In the central THS (*ca.* 60 km south of the ITS), the Yala-Xiangbo

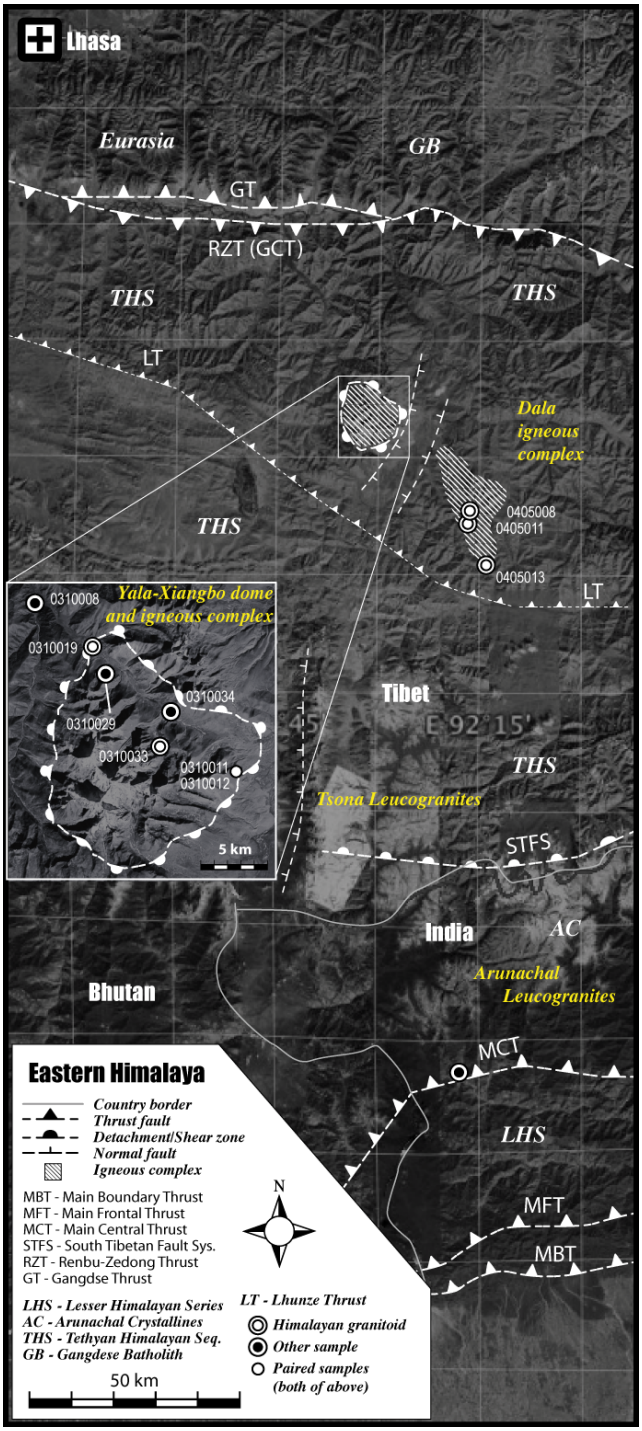

Figure 3.3: Simplified map and digital elevation model of the eastern Himalaya at *ca.* 92°E, showing the location of $^{40}Ar/^{39}Ar$ and K-Ar samples presented in this study (Compiled from Pan et al., 2004; Yin et al., 2006, Google Earth, this study).

igneous complex is emplaced into the core of the Yala-Xiangbo dome (*Figure 3.3*, *Figure 2.2*); and in the southern Tethyan Himalaya, the Tsona Leucogranites outcrop close to the STFS (*Figure 3.3*). Throughout the THS, a variety of smaller mafic and intermediate bodies are also found within the deformed metasediments. In addition to these bodies, however, a third suite of granitoids are also found. The Dala Granitoids comprise undeformed sub-elliptical plutons and dykes outcropping from *ca.* 70 km to 100 km south of the ITS (*Figure 3.3*). These bodies form an igneous complex (the Dala igneous complex) within the deformed Triassic THS strata, and represent a new mode of magmatism that has not so far been documented elsewhere along the main Himalayan Arc. Emplacement of these and the Yala-Xiangbo granitoids has important implications for our understanding of the tectonics of the Tethyan Himalaya.

3.3.1 The Dala Granitoids

The Dala Granitoids (DG) comprise a suite of plutons and dykes outcropping within the deformed upper-Triassic sub-greenschist facies metasediments of the eastern THS. Access restrictions imposed by Chinese military authorities precluded detailed mapping of individual bodies. However, a roadside contact observed in the field between a large body of DG and its country rock (N28°39.015' E092°12.301' 5012 m) can be traced on satellite imagery to define an elliptical pluton approximately 10 km in longest dimension (*Figure 2.2*). At outcrop scale, the principal regional foliation in the Triassic metasediments is axial planar to E-W trending folds and abuts directly against the Dala contact aureole. In the surrounding psammitic units, this fabric is a variably developed spaced cleavage defined by the alignment of chlorite, graphite and iron oxide minerals. In thin section, associated quartz grains show fracturing, abundant deformation lamellae and undulose-extinction patterns characteristic of a low-temperature deformation regime (*Figure 3.4(a)*). This fabric is axial planar to

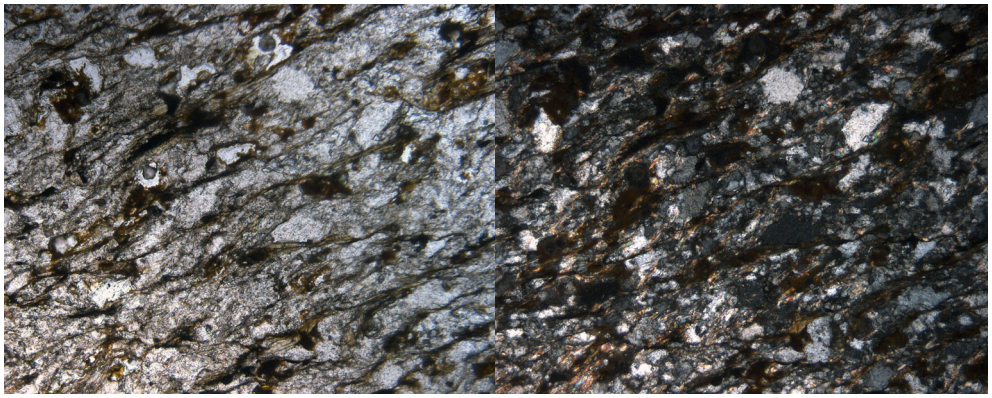

(a) Triassic psammites of the surrounding THS metasediments

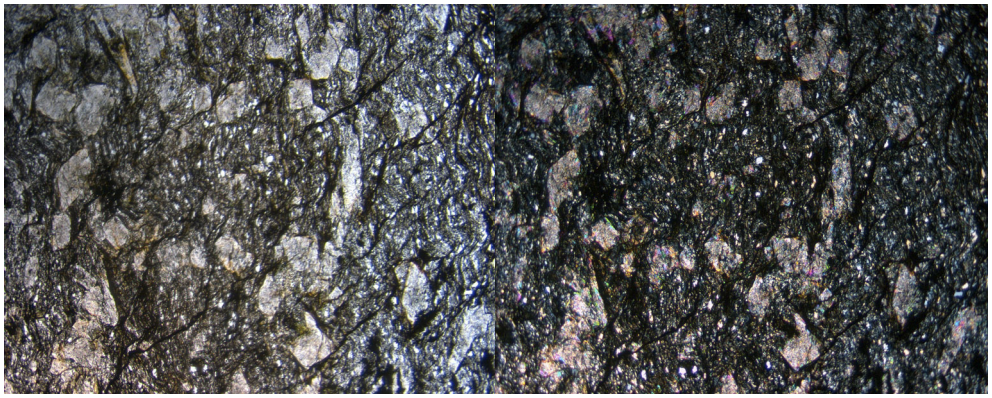

(b) Andalusite hornfels contact aureole

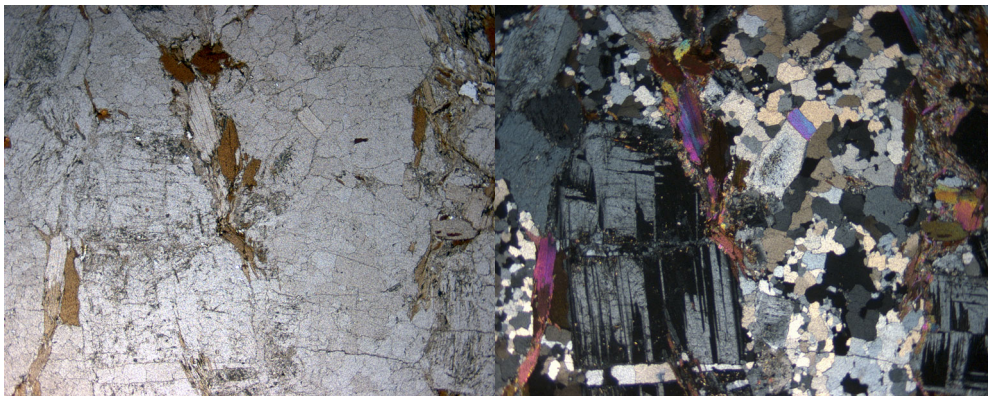

(c) Dala granitoid

Figure 3.4: Thin section photo micrographs of Dala lithologies; left col. ppl, right col. xpl.

regional south-vergent folds that are interpreted to have formed during regional D_2^r deformation as described in *Chapter 2*.

Microstructural observations indicate that foliated host phyllites in the Dala granites contact aureole have been overgrown by abundant andalusite porphyroblasts (now largely pseudomorphed by white mica) during contact metamorphism (*Figure 3.4(b)*). Relics of the original fabric are seen as graphite stringers within some porphyroblasts aligned parallel to the principal matrix foliation. In some sections, a second fabric (associated with new-grown biotite, now largely transformed to chlorite) is observed crenulating the axial planar regional foliation. This fabric was not detected in the surrounding metasediments, and its relationship to andalusite porphyroblasts growth is ambiguous. It is attributed to minor localised deformation associated with early emplacement of the granitoid bodies. The Dala granites themselves are comprised of quartz, plagioclase and K-feldspar, with lesser biotite and occasional muscovite (*Figure 3.4(c)*). Quartz grains in some samples show evidence of grainsize reduction suggesting that they have experienced minor deformation. However in such cases, uniform extinction patterns, foam textures and the absence of deformation lamellae indicate that - unlike in the surrounding metasediments - this minor granite deformation occurred at temperatures sufficient to allow near complete strain-recovery. This is interpreted as indicating that the minor deformation preserved in the Dala granites occurred during cooling. Collectively, structural observations from the Dala Granitoids and their country rock indicate that emplacement occurred after major south-vergent deformation (D_2^r) of the THS metasediments.

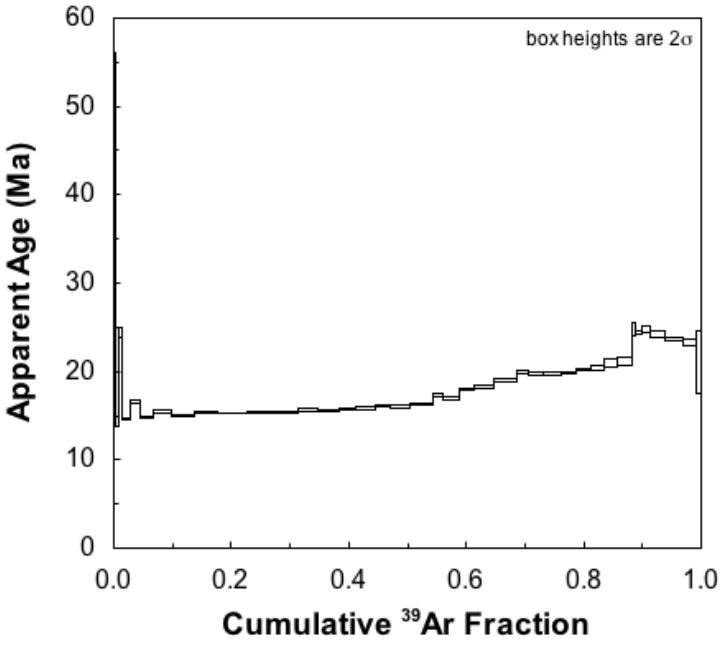

(a) Sample 0405008

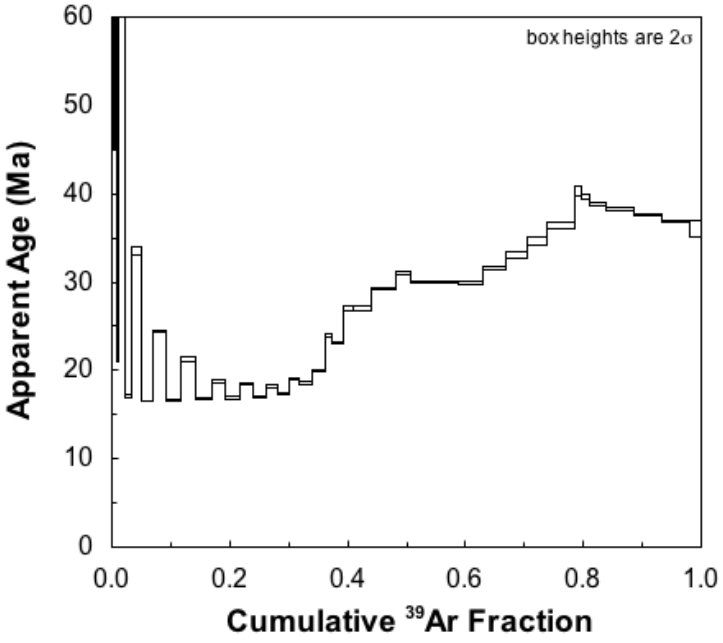

(b) Sample 0405011

Figure 3.5: K-feldspar $^{40}Ar/^{39}Ar$ apparent age spectra from the Dala granites.

Age and thermal history

U-Pb dating of zircons from Dala Granitoid samples indicate that they crystallised at 44.1±1.2 Ma, making them the earliest evidence of Eohimalayan granitoid plutonism thus far documented anywhere along the main Himalayan chain (*Chapter 4*). Biotites separated from three of the same samples (*Figure 3.3*) were analysed by the K-Ar method. Two samples from a large pluton (0405008 & 0405011) yielded ages of 31.5±0.3 Ma and 39.8±0.5 Ma respectively, and a third sample from a dyke outcropping a few kilometers north of the Lhunze thrust (0405013) yielded an age of 42.8±0.5 Ma. K-feldspar separated from the samples 0405008 and 0405011 was analysed using $^{40}\mathrm{Ar}/^{39}\mathrm{Ar}$ thermochronology. Step-heating experiments were conducted a using procedure involving isothermal duplicates, designed to allow correction for excess radiogenic argon ($^{40}Ar^{*}$) derived from decrepitation of fluid inclusions (Harrison et al., 1994). Excluding excess argon released on the first isothermal duplicate of the initial steps, both samples yielded coherent age spectra, in which age increases proportional to cumulative ^{39}Ar fraction over the majority of the gas release (*Figure 3.5*).

Data from both samples was interpreted using multiple diffusion domain (MDD) theory in order to recover the thermal histories (Lovera et al., 1989, 2002; Harrison and Zeitler, 2005; Harrison et al., 2005). Results indicate that both samples experienced rapid cooling at 15 Ma, although the apparent cooling recorded by sample 0405011 was initiated slightly earlier than sample 0405008. This apparent disparity may be attributable the presence of small amount of excess argon in the older sample. Collectively, biotite K-Ar and K-feldspar $^{40}\mathrm{Ar}/^{39}\mathrm{Ar}$ data are interpreted as indicating that the DG cooled to ambient mid-crustal temperatures ($\leqslant$300°C) by the late-Eocene to early-Oligocene, where they remained broadly isothermal until their rapid exhumation at around 15 Ma.

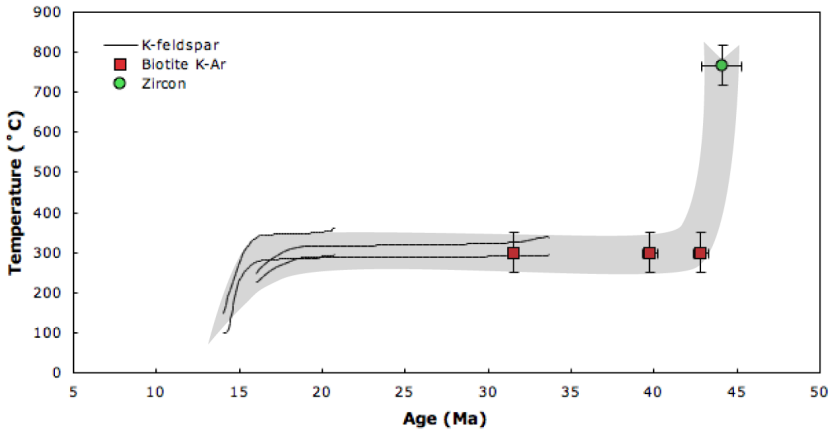

Figure 3.6: Thermal history of the Dala Granitoids. Data from zircon U-Pb dating and saturation thermometry (*Chapter 4*), biotite K-Ar and K-feldspar $^{40}Ar/^{39}Ar$ thermochronology. See text for discussion.

3.3.2 The Yala-Xiangbo Granitoids

The Yala-Xiangbo Granitoids form part of the Yala-Xiangbo igneous complex, which occupies central regions of the Yala-Xiangbo Dome. The complex is dominated by leucogranite sheets, dykes and small plutons, although in central regions, mafic sills are also found.

The Yala-Xiangbo Dome

The Yala-Xiangbo Dome outcrops in the Tethyan Himalaya at *ca.* 92°E; about 50 km south of the Indus Tsangpo Suture and 250 km SE of Lhasa (*Figure 1.2*, *Figure 3.3*). It is the easternmost in a series of zones of focussed exhumation (the North Himalayan Domes, NHD), which define a curvi-linear trend sub-parallel to the Himalayan Arc (see above). Geological mapping was conducted along a NNW-SSE oriented valley cutting the eastern limb of structure (*Figure 3.3*, *Figure 3.7*). The core regions were also explored by way of several glacial valleys, although the central peaks themselves climb to almost 7000 m elevation and were not accessed. Key

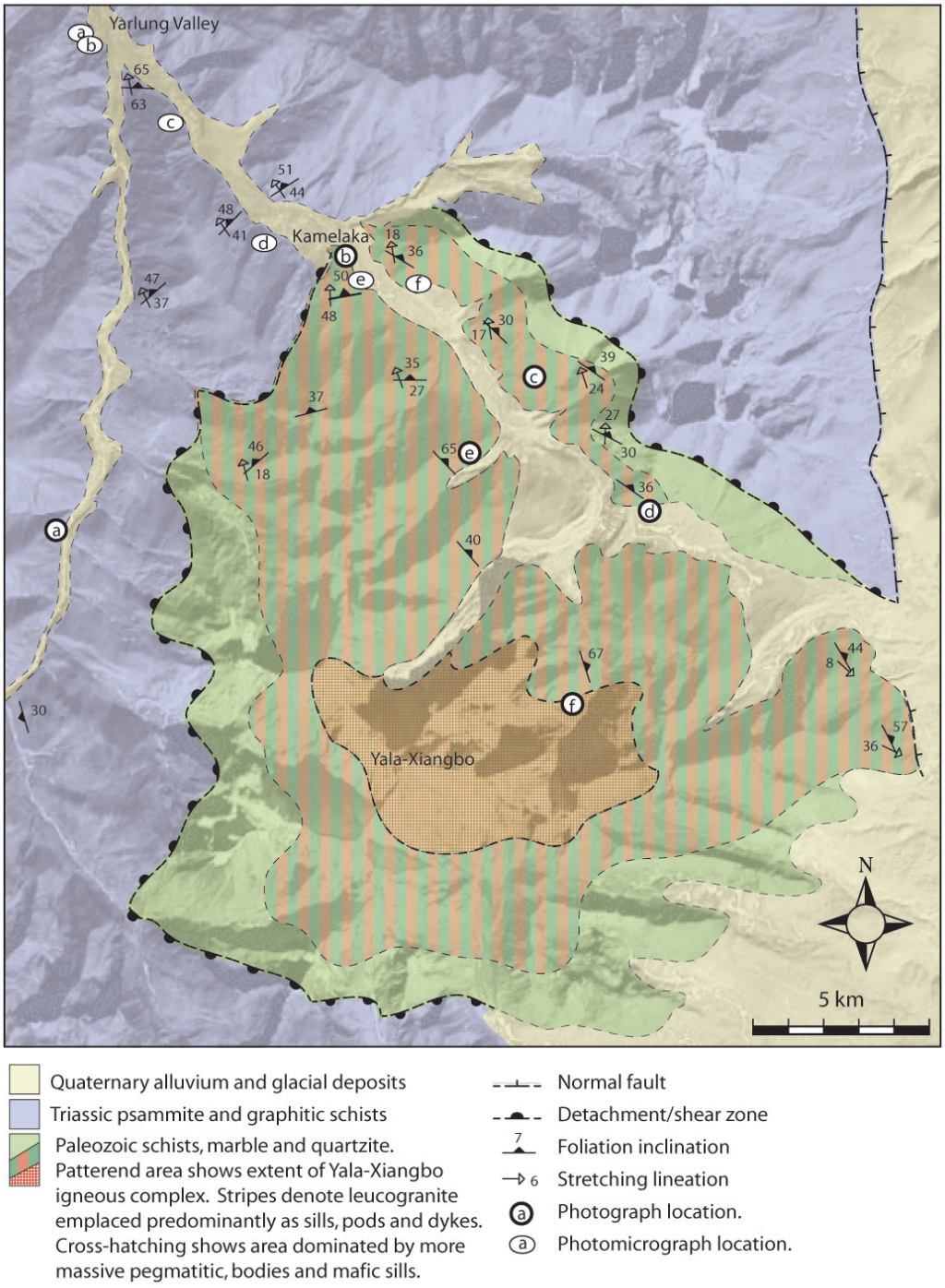

Figure 3.7: Simplified geological map of the Yala-Xiangbo Dome, compiled using a combination of field and remote sensing (ASTER, Google Earth) data.

features observed in these areas were traced regionally using reconnaissance surveys and remote sensing data (ASTER, Google Earth).

The structurally highest units of the Yala-Xiangbo Dome comprise phyllites, psammites and graphitic schists that are components of the Triassic THS metasediments described in *Chapter 2* (*Figure 3.8(a)*, *Figure 3.7*). These units are underlain by repeated sequences of pelite, quartzite and marble, which have been previously assigned a Paleozoic depositional age on the basis of sparse paleontological evidence (Brookfield, 1993; Liu and Ensele, 1994; Pan et al., 2004, *Figure 3.7*, *Figure 3.8(c)*). The core regions of the dome are dominated by paragneiss and migmatite - also thought have Paleozoic protolith ages (Pan et al., 2004). However, no outcrops of orthogneiss were found. Metamorphic grade as defined by index minerals is sub- to lower greenschist facies at the highest structural levels (comparable to that observed in the surrounding THS metasediments), increasing via a Barrovian-type sequence over *ca.* 13 km structural section to upper amphibolite facies in the core of the dome.

The large scale structure of the Yala-Xiangbo Dome appears to be broadly similar to that described from other NHD (*e.g. Figure 3.2*). At N28°57.354, E091°53.447, *ca.* 35 km south of the of Indus Tsangpo Suture along the Yarlung valley (*Figure 2.2*), lower greenschist facies phyllites and graphitic schists are cut by a penetrative slaty cleavage dipping steeply (*ca.* 80°) to the NNW. The structural and lithological characteristics of this area are similar to those observed in the Triassic metasediments *ca.* 20 km along strike to the west, and hence are interpreted as placing an approximate northern bound on the extent of local deformation(s) associated with the Yala-Xiangbo Dome. Southwards along the Yarlung valley, towards the dome core, the intensity of foliation gradually increases. At N28°56.630, E 091°53.751, decussate chlorite and garnet can be seen overgrowing the substantially recrystallised

regional foliation (*Figure 3.9(a)*, *Figure 3.9(b)*), marking significantly higher metamorphic temperatures than those observed regionally in the Tethyan Himalaya. A few kilometers beyond, where the Yarlung valley forks around the dome core (*Figure 3.7*), strongly foliated garnet-biotite bearing graphitic schists (*Figure 3.9(c)*) dip *ca.* 65° to the north and show an weakly developed *ca.* N-S trending stretching lineation. Both metamorphic grade and the intensity of deformation recorded by this fabric are significantly greater than that considered characteristic of the regional THS metasediments. However, it remains roughly axial planar to E-W trending isoclinal folds. Occasional NNE-SSW trending minor folds oriented parallel to the stretching lineation suggest that this geometry is not simply a primary feature associated with increasing foliation intensity with structural depth, although it may involve reactivation of pre-existing fabrics.

Metamorphic grade continues to increase southwards along the eastern Yarlung fork towards the village of Kamelaka (N28°53.206', E091°57.252') as marked by the appearance of staurolite (*Figure 3.9(d)*). This grade increase is accompanied by progressive development of a north dipping (*ca.* 50°) mylonitic foliation and N-S trending stretching lineation. Close to the village of Kamelaka, garnet-staurolite bearing graphitic schists are in sheared contact with kyanite-bearing pelites, quartzites and marble (the Kamelaka shear zone). The contact itself is poorly exposed, however, it appears to represent a north-dipping (*ca.* 45–50°) high-strain zone of a few tens to hundreds of meters thickness, oriented sub-parallel to the north-dipping mylonitic foliation in the adjacent units. Shear-sense indicators - principally asymmetric strain shadows on garnet porphyroblasts - are inconclusive. However, geometries suggesting top-to-the-north motion appear to dominate in the majority of outcrops. This high-strain zone can be traced regionally, defining a roughly elliptical geometry that separates the inner and outer domains of the Yala-Xiangbo Dome (*Figure 3.7*).

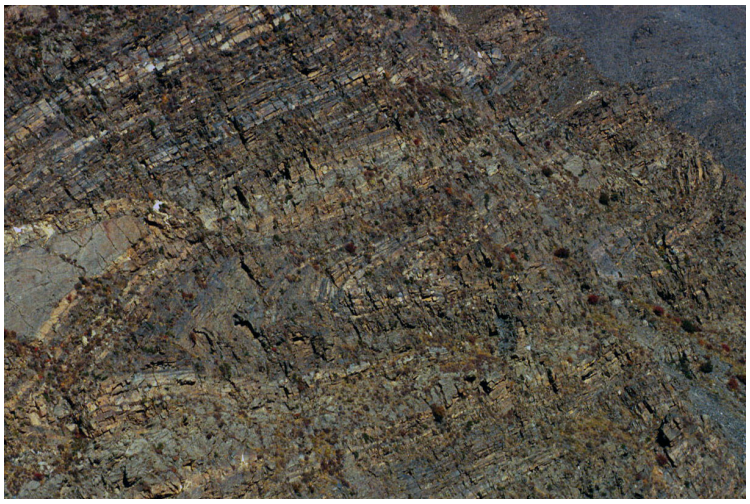

(a) Reoriented D_2^r folds in flanking Triassic metasediments. Image height *ca.* 50 m, view NW.

(b) Leucogranite pods and boudins in garnet-mica schist close to Kamelaka, view W.

Figure 3.8: Photographs of selected structural features from the Yala-Xiangbo Dome. Locations correspond to symbols on *Figure 3.7*

(c) Contact between marble-quartzite band and garnet mica schist. Image height *ca.* 50 m, view NW.

(d) Leucogranite bands emplaced sub-parallel and near perpendicular to the host foliation, neither contain penetrative fabrics. Image height *ca.* 3 m, view NE.

Figure 3.8: *Continued...*

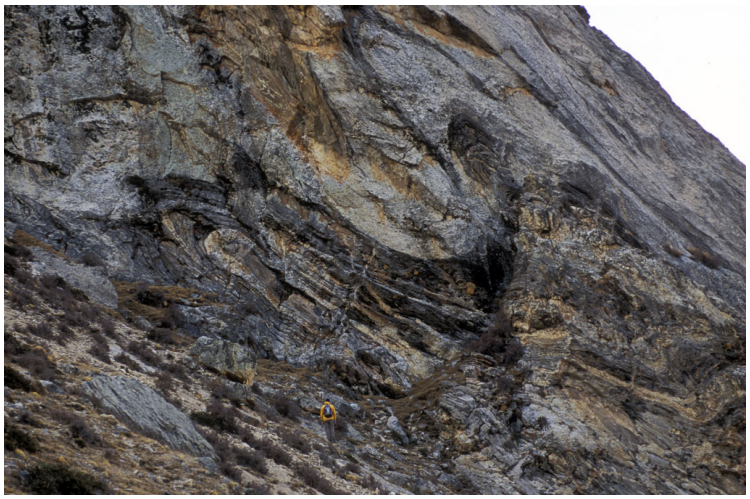

(c) Folded leucogranite sills in the margins of a pegmatitic body containing xenolith of wall rock. Note person for scale, view W.

(d) Leucogranite, pegmatite and small mafic sills in the core domain. Image height *ca.* 500 m, view N.

Figure 3.8: *Continued...*

Structurally beneath the Kamelaka shear zone (within the inner domain), alternating layers of garnet-mica schist, quartzites and marble, are cut by a penetrative schistosity and associated N-S stretching lineation having both similar orientation and style to that observed at higher structural levels. Previous studies of other NHD (*e.g.* Lee et al., 2004; Quigley et al., 2006) have not distinguished this type of compositional layering as anything other than a depositional feature. At Yala-Xiangbo, however, several traverses have indicated that quartzite/marble rich horizons can be traced defining kilometre-scale roughly E-W trending isoclinal folds draped across the dome. The axial planes of these structures are oriented roughly parallel to the plane of the dominant foliation, although the structures themselves appear to be significantly attenuated with respect to those observed at higher levels.

The innermost regions of the Yala-Xiangbo dome are relatively inaccessible and could not be surveyed in detail. However, excursions up several glacial valleys revealed abundant migmatitic paragneisses of broadly pelitic composition, although several large outcrops of quartzite and marble were also found. Examination of debris flow chutes draining high-elevation portions of the core domain revealed a variety of lithologies, including grey gneiss, leucoctratic gneiss, and garnet amphibolite. The structural context of these units could not be directly established.

The Yala-Xiangbo igneous complex

The Yala-Xiangbo igneous complex outcrops in the footwall of the Kamelaka shear zone. It is dominated by leucogranites and leuco-pegmatite, exhibiting substantial variability in terms of texture, mineralogical composition and emplacement relations. At structurally higher levels (close to the Kamelaka shear zone), most leucogranites are emplaced as sills, pods and boudins that are oriented sub-parallel to the

principal foliation in the surrounding host lithologies (*Figure 3.8(b)*). These bodies locally contain a proto-mylonitic foliation (*Figure 3.9(e)*), although the amount of sub-solidus deformation recorded by this fabric is significantly less than that in the adjacent pelites. Moreover, occasional cross-cutting granite pillars and leucocratic veins have not been extensively offset by shearing. The majority of granitoid bodies comprise muscovite-bearing assemblages (*e.g. Figure 3.9(f)*), although some two-mica, quartzo-feldspathic and tourmaline bearing units were also found.

The proportion of leucocratic material to host rock increases with structural depth towards the core domain. This trend is accompanied by a general increase in the grainsize of leucocratic bodies, many of which appear to cross-cut structures and fabrics in their host lithologies (*Figure 3.8(d)*). Indeed some even contain meter to ten-meter scale xenoliths of foliated wall-rock, although smaller veins and sills in the margins of these large bodies are clearly interleaved and locally folded with the surrounding metasediments (*Figure 3.8(c)*). No obvious compositional or textural differences were detected between these various types of bodies. Moreover, neither show evidence of extensive penetrative sub-solidus deformation. Collectively, these relationships suggest that, while leucogranite emplacement was probably late syn- to post-kinematic with respect to deformation recorded in the surrounding lithologies, the majority of crystallisation was post-kinematic.

In the core domain of the Yala-Xiangbo dome, a second type of igneous lithology was also found. These bodies comprise tens to hundreds of meter scale dark green or black irregular pods and sheets outcropping in association with pegmatite, paragneiss and migmatite in the central peaks (*Figure 3.8(d)*). Unfortunately, the largest outcrops are at high elevation and could not be studied directly. However, their forms are clearly visible in the steep sides of several glacial valleys, and their

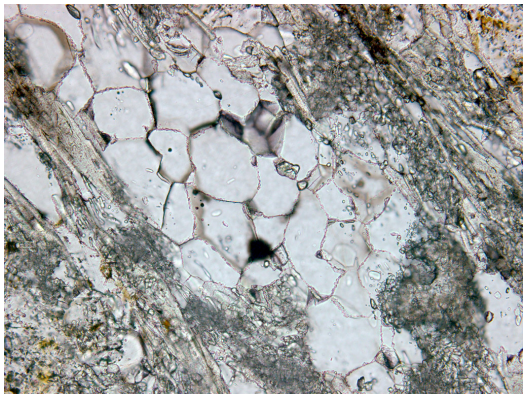

(a) Recrystallisation and foam texturing of the cover sequences.

(b) Garnet and decussate chlorite overgrow regional foliation.

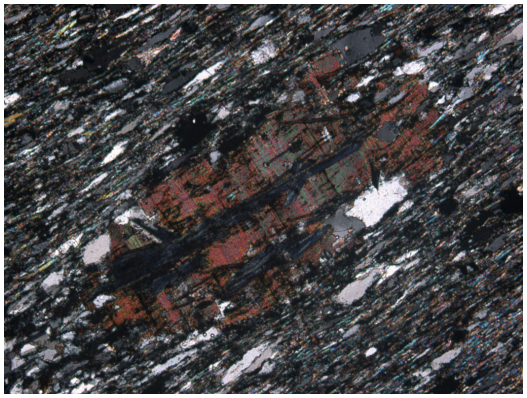

(c) Biotite overgrowing penetrative schistosity.

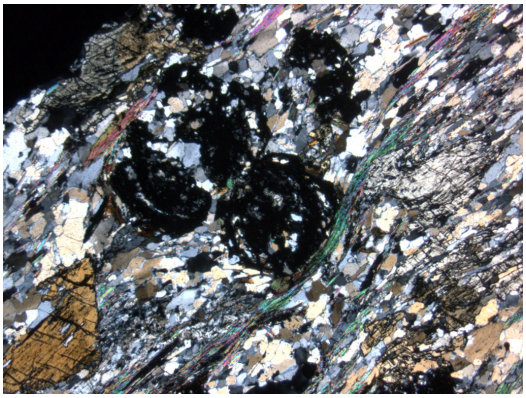

(d) Snowball garnet in staurolite-bearing pelite.

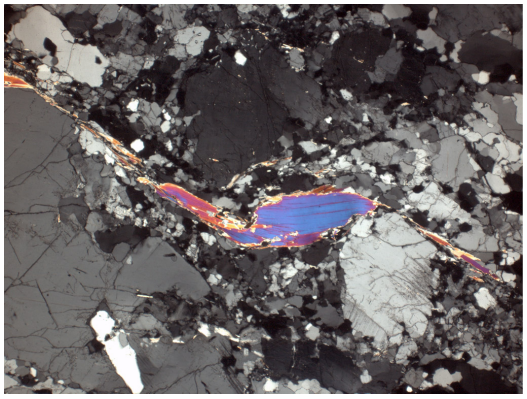

(e) Leucogranite proto-mylonite indicating top-to-north sense of shear.

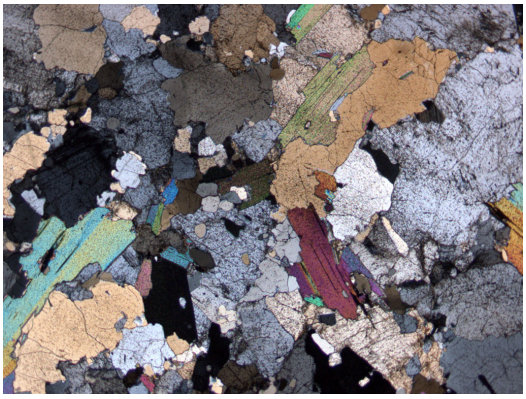

(f) Leucogranite not preserving mylonitic fabric.

Figure 3.9: Thin section photomicrographs of lithologies from the Yala-Xiangbo Dome. Locations as shown on *Figure 3.7*

compositions may be estimated by examination of rockfall debris. Based on remote observations, the long axes of most of these bodies appear to lie close to the plane of the dominant fabric in the surrounding units. However, some have shapes suggesting that they may have originally cross-cut this foliation and been modified by ongoing deformation. Examination of float debris indicates that most are composed of variably deformed garnet amphibolite, locally cut by biotite-rich veins. It is not possible to uniquely distinguish these bodies from other mafic lithologies observed at high structural levels in the surrounding THS metasediments. However, based on the available data they appear to differ in terms of size, geometry/emplacement relations, stratigraphic association and composition (being generally more mafic), and hence are assigned a separate grouping.

Age and thermal history

U-Pb dating of the zircons from the Yala-Xiangbo granitoids indicates that the majority of these bodies crystallised during the Eocene (*ca.* 42 Ma, see *Chapter 4*). Younger Miocene ages from a few granitoids on the northern edge of the complex close to the Kamelaka shear zone are interpreted as documenting a recrystallisation event that was probably associated with hydrothermal fluids (*Chapter 4*). U-Th-Pb dating of monazites from pelitic units in the footwall of the Kamelaka shear zone provides evidence that these units experienced two phases of amphibolite grade metamorphism. The first occurred during the Eocene, approximately co-incident with leucogranite magmatism, and the second during the Miocene during motion on the STFS-GCT fault system (*Chapter 4*). These events are respectively interpreted as being roughly correlative with Eohimalayan and Neohimalayan metamorphism as described elsewhere in the Himalaya (LeFort, 1996).

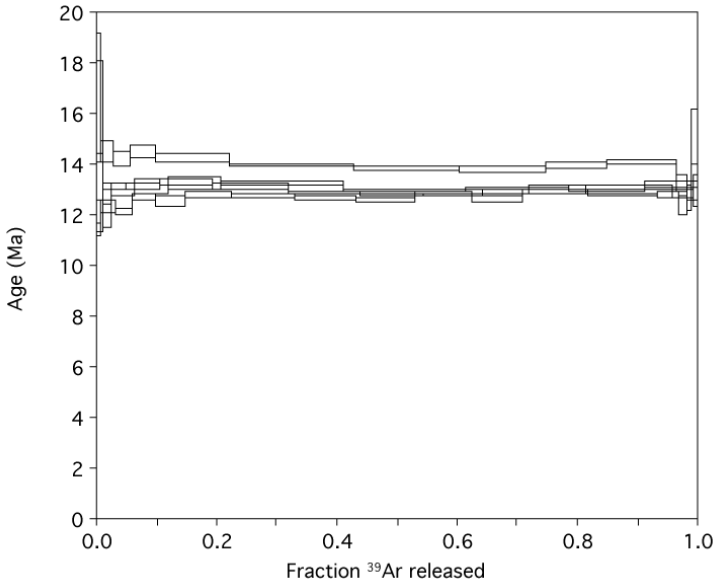

(a) Muscovite

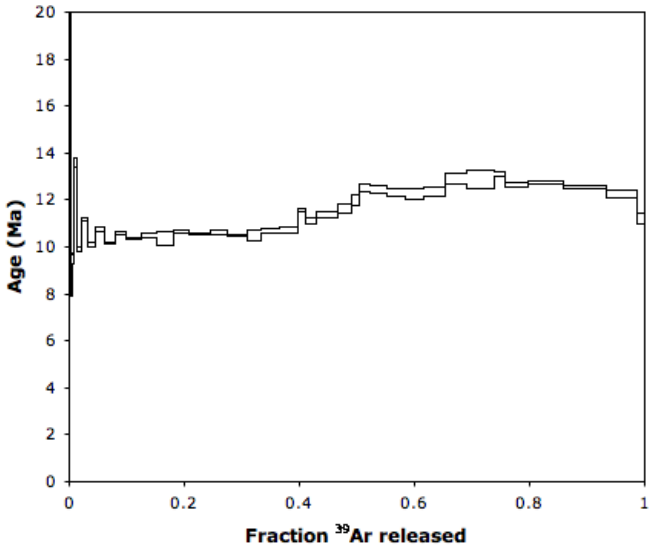

(b) K-feldspar

Figure 3.10: $^{40}Ar/^{39}Ar$ age spectra of muscovites and K-feldspar from the Yala-Xiangbo dome

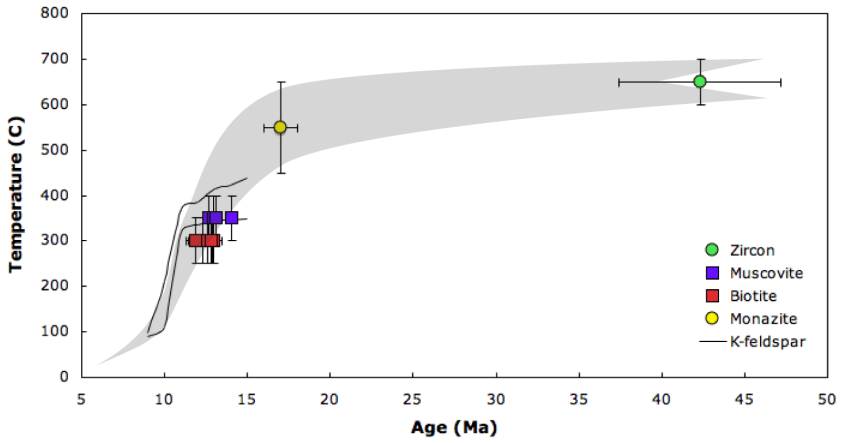

Figure 3.11: Thermal history of the Yala-Xiangbo dome. Data from zircon U-Pb dating and saturation thermometry (*Chapter 4*); monazite U-Th-Pb dating (*Chapter 4*); muscovite, biotite and K-feldspar $^{40}Ar/^{39}Ar$ thermochronology. See text for discussion.

Samples from several locations within the Yala-Xiangbo dome were selected for $^{40}Ar/^{39}Ar$ thermochronology. Muscovite and biotite was separated from granitoid and pelitic units outcropping close to the Kamelaka shear zone on both the northern and southern sides of the dome, and from two locations at deeper structural levels close to the core domain (*Figure 3.3*). K-feldspar was also separated from one granitoid sample outcropping in the foot-wall of the Kamelaka shear zone on the northern side of the dome, and biotite from one sample in the hanging wall close to the Yarlung fork (*Figure 3.3*). Step-heating experiments were conducted on the muscovite and K-feldspar samples; biotites were analysed by laser fusion (analytical procedures are described in *Appendix 7*). All muscovite and K-feldspar samples yielded flat age spectra showing little or no evidence of contamination by excess argon (*Figure 3.10*). Total fusion ages (see *Table 3.1*) from all analyses are close to 13 Ma, although the single muscovite from the southern side of the dome is slightly older (*ca.* 14 Ma). The total gas age of the single K-feldspar sample is slightly younger (*ca.* 12 Ma). Data from this sample were interpreted using multiple

Sample	Lithology	Mineral	Age (Ma)	$\pm 1\sigma$
0310008	Greenschist	Bio	12.27	0.30
0310011	Pelite	Bio	12.87	0.16
0310012	Leuc	Bio	12.97	0.21
0310012	Leuc	Msc	14.02	0.16
0310019	Leuc	Msc	12.70	0.10
0310019	Leuc	Ksp	11.77	0.15
0310029	Pelite	Bio	11.89	0.26
0310029	Pelite	Msc	12.97	0.12
0310033	Pelite	Bio	12.56	0.13
0310034	Pelite	Bio	12.84	0.19
0310034	Pelite	Msc	13.11	0.15

Table 3.1: Summary of $^{40}Ar/^{39}Ar$ results from the Yala-Xiangbo Dome. Sample locations as shown on *Figure 3.3*.

diffusion domain (MDD) theory in order to recover the thermal histories (Lovera et al., 1989). Results indicate that it experienced rapid cooling at *ca.* 12 Ma, which is consistent with the form of the mica age spectra and biotite total fusion ages. Collectively, these data are interpreted as recording rapid cooling associated with exhumation of the Yala-Xiangbo Dome and igneous complex during the mid-Miocene (*Figure 3.11*).

3.3.3 The Tsona Leucogranites

The Tsona Leucogranites outcrop as sheets, dykes and laccolithic bodies within the metasediments of the southernmost Tethyan Himalaya. Access restrictions precluded direct observation of individual bodies in the field. However, reconnaissance mapping conducted by Dr Ding Lin indicates that their emplacement relations are broadly similar to those described for the HHL of northern Nepal (e.g. Inger and Harris, 1993). They outcrop in the hanging wall of the STFS and are generally oriented sub-parallel to a north dipping mylonitic foliation (which is associated with a roughly N-S oriented stretching lineation). Although field data are limited, this foli-

ation appears to be consistent with that described elsewhere along strike, attributed to normal-sense motion on the STFS (D_3^r as defined in *Chapter 2*). Leucogranite bodies themselves do not show evidence of penetrative sub-solidus deformation, indicating that although they may have been emplaced during ongoing deformation, their crystallisation was largely post-kinematic.

3.4 Discussion

Published studies have revealed several suites of igneous lithologies outcropping within the Tethyan Himalaya. Most of these units are seemingly continuous along the length of the Himalayan Arc, and have been important in the construction of Himalayan evolutionary models (LeFort, 1996; Yin and Harrison, 2000; Yin et al., 2006, and refs. therein; this study). Although a similar range of igneous lithologies are present in the eastern Himalaya, new results highlight several key factors not so far recognised in the existing paradigm for Himalayan magmatism. These factors are important in understanding regional deformation patterns and the formation of the NHD, which collectively impact upon models for Himalayan orogenesis.

3.4.1 Timing of regional deformation

The THS metasediments are the structurally highest and earliest inferred accreted units of the Himalayan Fold and Thrust Belt. As such, they may retain valuable information regarding the early history of Himalayan orogenesis (*Chapter 2*). According to the regional deformation scheme established in *Chapter 2*, the majority of crustal thickening in the Tethyan Himalaya was associated with formation of E-W trending, predominantly S-vergent folds (D_2^r). However, the timing of this event is poorly constrained. Structural observations indicate that the Dala Granitoids were emplaced after regional D_2^r deformation, and their crystallisation is dated at 44.1±1.2 Ma (see *Chapter 4*). These data not only make them the first evidence

of Eohimalayan granitoid plutonism so far documented anywhere along the main Himalayan Arc, but also place a lower bound on the timing of regional crustal thickening of the THS metasediments at *ca.* 45 Ma. This result is supported by existing K-Ar and $^{40}Ar/^{39}Ar$ data from NW-India and central Tibet, suggesting that regional D_2^r deformation was underway by 47-56 Ma (Wiesmayr and Grasemann, 2002) and *ca.* 49 Ma (Ratschbacher et al., 1994, 1992). Furthermore, based on a standard alluminosilicate P-T diagram (*e.g.* Cesare et al., 2003), the Dala Granitoids andalusite hornfels contact aureole constrains the depth of emplacement and maximum overburden removed since that time to $\leqslant$12 km. These results are important as they imply that Eohimalayan crustal thickening was under way significantly earlier than was previously thought.

3.4.2 Structural evolution of the NHD

Several studies of the NHD have described an early contractional event (D_1^d) that appears to be correlative with the dominant thickening structures in the surrounding THS metasediments (Lee et al., 2000, 2004; Quigley et al., 2006, this study). In the Kangmar, Mabja-Sakya and Kampa domes (three of the best studied NHD), as in the Yala-Xiangbo dome, this deformation is represented by E-W trending folds associated with a spaced axial planar cleavage (Lee et al., 2000, 2004; Quigley et al., 2006, this study). These structures are interpreted as being correlative with the regional D_2^r event described in *Chapter 2.* As such, emplacement of the Dala Granitoids also constrains the timing of early contractional deformation (D_1^d) within these NHD as being pre *ca.* 45 Ma.

Most published studies of NHD have described a second phase of deformation (D_2^d) associated with the formation of high-strain ductile (mylonitic) fabrics (Lee et al., 2000, 2004; Aoya et al., 2005; Quigley et al., 2006). This deformation is

interpreted to have occurred during extension, on the basis of structural and thermobarometric arguments (Lee et al., 2000, 2004). Lee and Whitehouse (2007) have argued that in the Mabja-Sakya dome, (D_2^d) deformation was temporally associated with peak metamorphism and migmatisation of pelitic lithologies in the core domain. As such, they interpret the oldest in a series of U-Pb ages from migmatitic zircon rims as recording the onset of this deformation event at *ca.* 35 Ma. Deformed leucogranites nearby, yielding early Miocene U-Pb ages, are interpreted as recording ongoing deformation at this time, and younger undeformed bodies (*ca.* 16 Ma) as providing an upper bound on the cessation of this event (Lee et al., 2004; Lee and Whitehouse, 2007). Lee and Whitehouse (2007) further argue that their data constrain the onset of and duration of extension associated with ductile extrusion of the Tibetan middle crust. Ignoring wider problems with the channel flow/shallow anatexis model (Harrison, 2006), we question the use of the oldest in a series of migmatitic zircon rim crystallisation ages as a reliable indicator of the "onset" of a deformation event, and suggest that data presented by Lee and Whitehouse (2007) do not preclude alternative interpretations. Furthermore, several key factors do not support extrapolation of this hypothesis to the Yala-Xiangbo Dome.

Field observations discussed in the preceding sections indicate that emplacement of the Yala-Xiangbo granitoids was syn- to post-kinematic with respect to the formation of ductile mylonitic fabrics preserved in the core of this structure. U-Pb dating of several such granitoids has yielded Eocene crystallisation ages, suggesting that the approximate timing of cessation of this deformation must also have been Eocene. Of course, it is not possible to rule out the existence of un-sampled Miocene granitoids comprising a significant volumetric proportion of the Yala-Xiangbo igneous complex, and nor can we preclude protracted deformation of an Eocene crystal mush. However, these hypotheses require special pleading and therefore do not provide

best and simplest explanation of the available data. Moreover, data presented in this study do not require the formation of mylonitic fabrics in the core domain to to have occurred during extension, indeed at deeper structural levels beneath the Kamelaka shear zone, cross-cutting relationships between ductile fabrics and thickening structures (isoclinal folds) were not reliably demonstrated.

In the absence of additional data it is not possible to place further constraints on the origin of these fabrics at Yala-Xiangbo or elsewhere. However, we speculate that they may plausibly have originated in association with regional shortening, and been later re-activated in extension. Moreover, we note that these results highlight the structural complexity preserved within the NHD, and caution against over zealous future interpretations.

3.4.3 Miocene regional exhumation

A number of studies have describe Miocene exhumation along Northern parts of the THS (Quidelleur et al., 1997; Lee et al., 2004; Quigley et al., 2006; Lee and Whitehouse, 2007, and refs. therein). North-directed slip on the Great Counter Thrust causing uplift and erosion adjacent to the Indus Tsangpo Suture (Quidelleur et al., 1997), appears to have been quasi-synchronous with formation of the domal geometries used to characterise the NHD (D_3^d) (Lee et al., 2004; Quigley et al., 2006; Lee and Whitehouse, 2007)). $^{40}Ar/^{39}Ar$ thermochronology of muscovite, biotite and K-feldspar from the Yala-Xiangbo dome and the Dala granitoids indicate rapid cooling at *ca.* 15 Ma, in good agreement with the results of similar studies elsewhere (*e.g.* Lee et al., 2004; Quigley et al., 2006; Lee and Whitehouse, 2007). However, due to their age these units can provide some additional insight into the intervening period between the Eohimalayan and Neohimalayan orogenic episodes. The Dala granitoids crystallised at 44.1±1.2 Ma and cooled rapidly to mid crustal

Region	NHD	Notes	Timing
Pre-H	-	See *Chapter 2*.	Pre-Ordovician.
D_1^r	-	See *Chapter 2*.	Early Tertiary.
D_2^r	D_1^d	E-W trending folds assoc. thickening of THS metasediments; see also *Chapter 2*.	Pre-45 Ma, based on the Dala Granitoids and other sparse geochronology.
-	D_2^d	Development of mylonitic foliations in Yala-Xiangbo Dome (and perhaps other NHD), possibly associated with reactivation of pre-existing fabrics.	Eocene, based on the Yala-Xiangbo Granitoids.
D_3^r	D_2^d	Development/re-activation of Mylonitic fabrics in other NHD.	Miocene, based on timing of GCT-STFS slip.
-	D_3^d	Formation of domal geometries and exhumation of the NHD.	Miocene, based on $^{40}Ar/^{39}Ar$ thermochronology.
D_4^r	-	See *Chapter 2*.	Mio-Pliocene, based on cross-cutting relationships.
D_5^r	D_4^d	Broadly E-W extension associated with formation of arc-normal graben.	Pliocene based on structural similarity and cross-cutting relationships.

Table 3.2: Summary of the structural evolution of the Tethyan Himalaya.

temperatures, where they appear to have remained broadly isothermal until the mid Miocene (above, and *Chapter 4*). The Yala-Xiangbo granitoids, meanwhile, appear to have remained roughly isothermal at higher temperatures during the same period (above, and *Chapter 4*). Collectively, these results suggest that units now comprising the Tethyan Himalaya experienced relatively little tectonic activity during this time, in turn implying that the locus of shortening must have shifted elsewhere. This hypothesis will be further examined in *Chapter 6*.

3.5 Conclusions

Igneous bodies outcrop at a variety of structural positions within the Tethyan Himalaya. Along the northern margin of the THS, mafic lithologies are found in association with the Indus Tsangpo Suture. These units likely represent dismembered oceanic material obducted during the early stages of Himalayan orogenesis. In the central THS, the North Himalayan Granites are emplaced into the cores of North Himalayan Domes, and, further south, leucogranites are emplaced adjacent to the STFS and represent the structurally highest components of the High Himalayan Leucogranite suite. A variety of other smaller mafic and intermediate dykes and other bodies also outcrop throughout the Tethyan Himalaya. These units appear to be broadly continuous into the eastern Himalaya, however, in addition, a new mode of Himalayan magmatism has also been found. The Dala Granitoids represent the first evidence of Eohimalayan plutonism so far documented anywhere along the main Himalayan Arc. Their emplacement has important implications for the evolution of the Himalayan Fold and Thrust Belt.

Structural studies indicate that the Dala Granitoids were emplaced after D_2^r deformation accounting for the majority of crustal thickening within the THS metasediments. As such, their crystallisation ages constrain the timing of this deformation to be pre *ca.* 45 Ma. Moreover, early contractional structures present within the NHD (D_1^d) are likely correlative with this regional deformation event and therefore similarly constrained. The Dala Granitoids andalusite hornfels contact aureole also places a limit on the depth of emplacement of these bodies and the maximum overburden removed since that time of *ca.* 12 km.

The Yala-Xiangbo Dome comprises the easternmost in a series of elliptical zones of focussed exhumation (the North Himalayan Domes, NHD) in which strongly foli-

ated metasediments dip radially away from a high-grade core. Although structurally and lithologically similar to other studied NHD, Eocene crystallisation ages of the Yala-Xiangbo Granitoids constrain the age of several key features as being significantly older than regional extrapolation would imply.

Collectively, data presented in this chapter may be used to refine the regional deformation scheme described in *Chapter 2* as summarised in *Table 3.2*.

Chapter 4

Zircon U-Pb geochronology and Ti thermometry of granitoids

4.1 Introduction

Granitoids are frequently found in regions that have experienced prolonged crustal thickening. This spatial and temporal association places significant requirements on models of orogenesis. In the Himalaya, the distribution and timing of granitoid magmatism bear upon the thermal budget and locus of tectonic activity within the orogen, which in turn place constraints on evolutionary models (Debon et al., 1986; LeFort et al., 1987; Harrison et al., 1997a, 1998a; Beaumont et al., 2001, 2004; Jamieson et al., 2004).

A variety of methods are applicable to studies of granitoid formation. Arguably the most pertinent are those bearing on the processes of magma genesis and the timing of it's emplacement. To this end, the mineral zircon is particularly valuable. It is ubiquitous in granitic - and indeed virtually all crystalline - rocks in the crust, contains sufficient quantities of radioactive U and Th to be a precise geochronometer,

and hosts important isotopic tracers such as Hf and O. Furthermore, it is characterized by very low diffusivities of most elements, such that their concentrations and/or isotopic ratios generally retain attributes of the zircon's formative environment (Cherniak and Watson, 2003, and refs. therein).

Recent work has demonstrated the temperature dependency of Ti concentration in zircon coexisting with rutile (Watson and Harrison, 2005; Watson et al., 2006). This has provided a means to assess the crystallisation temperature of zircon that can be reliably attributed to a given magmatic episode, and in some cases, formative environment. Zircon Ti concentration ([Ti]) appropriate to crustal temperatures can only be measured using the highest sensitivity methods, such as Secondary Ion Mass Spectrometry (SIMS) (Watson and Harrison, 2005; Watson et al., 2006, this study). This approach holds the promise of determining formation age and temperature with spatial resolution sufficient to reveal histories of individual magmatic episodes as recorded by individual zircon grains.

4.1.1 Himalayan granitoids

The Himalayan Orogen is marked by two belts of granitoids oriented sub-parallel to the trace of the main Himalayan Arc (LeFort, 1975; LeFort et al., 1987; LeFort, 1996; Yin and Harrison, 2000). Together, they provide one of the most distinctive geological features of the Himalayan chain, and place valuable constraints on Himalayan evolutionary models (Yin and Harrison, 2000, and refs. therein).

The High Himalayan Leucogranites (HHL, *Figure 1.2*) are a series of sheet, dyke and laccolithic bodies emplaced into the upper Greater Himalayan Crystalline (GHC) and lower Tethyan Himalayan (THS) sequences along the crest of the High Himalaya (LeFort, 1975; LeFort et al., 1987). They comprise muscovite-biotite and

muscovite-tourmaline bearing assemblages, are generally thought to have been emplaced between 23 and 18 Ma and derived from melting of the underlying pelitic lithologies (LeFort, 1975; Schärer, 1984; LeFort et al., 1987; Schärer et al., 1986; Harris and Inger, 1992; Inger and Harris, 1993; Guillot et al., 1994; Harrison et al., 1995, 1997a, 1998a). Models proposed to account for the formation of the HHL include fluid present melting associated with movement on the Main Central Thrust (MCT) (LeFort et al., 1987), decompression enhanced fluid absent melting associated with movement on the MCT and South Tibetan Fault System (STFS) (Harris and Massey, 1994), shear heating associated with movement on the MCT (Harrison et al., 1997a, 1998a; England et al., 1992), and internal heating associated with radioactive decay (Nelson et al., 1996; Beaumont et al., 2001).

The North Himalayan Granites (NHG, *Figure 1.2*) are emplaced *ca.* 80 km to the north of the HHL, within the central Tethyan Himalaya. Although the petrogenesis of these bodies is poorly constrained, they are generally thought to have been emplaced between *ca.* 10 and 17 Ma, although an older age of 27 Ma has also been reported (Zhang et al., 2004a, and refs. therein). Models proposed to account for formation of the NHG include thermal blanketing by the overlying THS metasediments (Pinet and Jaupart, 1987), shear heating along a shallow décollement that is generally equated with the MCT (Harrison et al., 1997a), decompression melting during extensional collapse (Lee et al., 2004), and instability in the roof of an orogenic channel (Beaumont et al., 2001, 2004; Jamieson et al., 2004).

4.1.2 Purpose of this chapter

Over two decades of research have led to the widespread perception that Tertiary granitoid magmatism along the main Himalayan Arc is is almost entirely confined to the past *ca.* 25 Ma, intimately associated with activity on the main Himalayan

fault systems during the Neohimalayan episode (LeFort et al., 1987; England et al., 1992; Harris and Massey, 1994; Harrison et al., 1997a, 1998a). This, in turn, has impacted upon our wider understanding of Himalayan tectonics and the construction of various evolutionary models. Unfortunately, however, the data on which many models are based is spatially biased, in the case of the HHL, towards results from central Nepal, and for the NHG, by the limited number of bodies studied. The goals of this chapter are twofold. Firstly, to evaluate the spatial and temporal distribution of granitic magmatism along a N-S oriented transect through the eastern Himalaya (*Figure 4.1*). Secondly, to provide insight into the formative processes of these bodies through the application of the newly calibrated Ti-in-zircon thermometer (Watson and Harrison, 2005; Watson et al., 2006). Our results both significantly expand the spectrum of documented Himalayan granitic magmatism, and provide new insights into the petrogenesis of zircon in granitic rocks.

4.2 Sample selection

Four suites of granitoid samples were selected for analysis along a N-S oriented transect at *ca.* 92°E (*Figure 4.1*). In the Arunachal Himalaya, 3 samples were chosen from granitoids outcropping between the Main Central Thrust (MCT) and South Tibetan Fault System (STFS). These samples, the Arunachal Leucogranites (AL, *Figure 4.1*), comprise muscovite-biotite and muscovite-tourmaline bearing assemblages forming sheet/dyke or laccolithic bodies emplaced into upper parts of the Greater Himalayan Crystallines (GHC). They are considered analogous to the High Himalayan Leucogranites (HHL) as described elsewhere along the main Himalayan Arc in terms of petrography and emplacement relations (LeFort et al., 1987; Deniel et al., 1987; Inger and Harris, 1993; LeFort, 1996; Harrison et al., 1999d). A further three leucogranite samples, the Tsona leucogranites (TL), were obtained by Dr Ding Lin in the vicinity of the STFS, close to the Indo-Chinese border (*Figure*

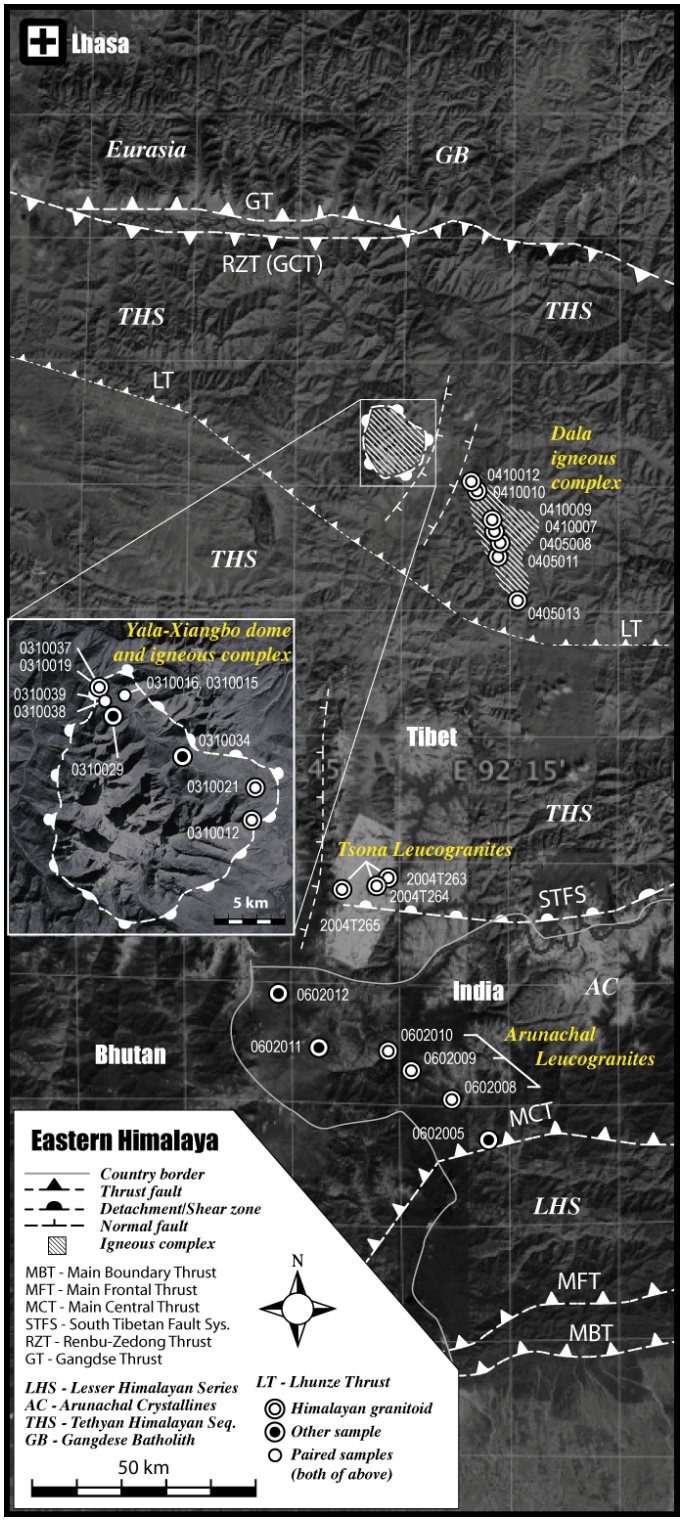

Figure 4.1: Schematic geological map of the eastern Himalaya (*ca.* 92°E) showing principal tectonic features and the locations of samples discussed in this chapter (Compiled from Yin et al., 1994; Harrison et al., 2000; Pan et al., 2004; Yin et al., 2006, this study).

4.1). The structural context of the TL could not be directly established due to access restrictions by Chinese military authorities. However, reconnaissance studies conducted during sampling indicate that their petrography and emplacement relations are similar to the AL, and hence they are also thought to be equivalent to the HHL suite, albeit structurally higher components. In the central THS, 8 samples were selected from the Dala Granitoids (DG). The DG comprise a series of dykes and undeformed elliptical plutons forming an igneous complex emplaced into the deformed sub-greenschist facies metasediments of the central THS (*Figure 4.1*). Their petrography and emplacement relations are discussed in detail in *Chapter 3*. In the northern THS, 6 samples were obtained from the Yala-Xiangbo granitoids (YX_G) outcropping as part of the Yala-Xiangbo igneous complex in the core of the Yala-Xiangbo Dome (*Chapter 3*, *Figure 4.1*). They are superficially similar to the North Himalayan Granites (NHG) in terms of emplacement style and structural position. As a further test for existing Himalayan paradigms, three samples of high grade rocks from the GHC sequences of the Arunachal Himalaya, and 6 samples from the high grade pelites outcropping in the core of the Yala-Xiangbo Dome were also selected for analysis (*Figure 4.1*). These samples were chosen to provide comparison with units thought to be important in the formation of the HHL in northern Nepal and the NHG.

4.3 U-Pb & Th-Pb geochronology

Zircons were extracted using conventional crushing, heavy liquid and magnetic separation techniques. Monazites were also separated from 5 Yala-Xiangbo Granitoid samples and 1 sample of the Yala-Xiangbo Pelites. Grains were mounted in epoxy along with reference materials (zircon FC1: 1099.0±0.5 Ma, monazite FT554: 45±1 Ma; Paces and Miller, 1993; Harrison et al., 1999d) and polished to expose mid-sections using a rotary polisher and diamond paste. Polished mounts were examined

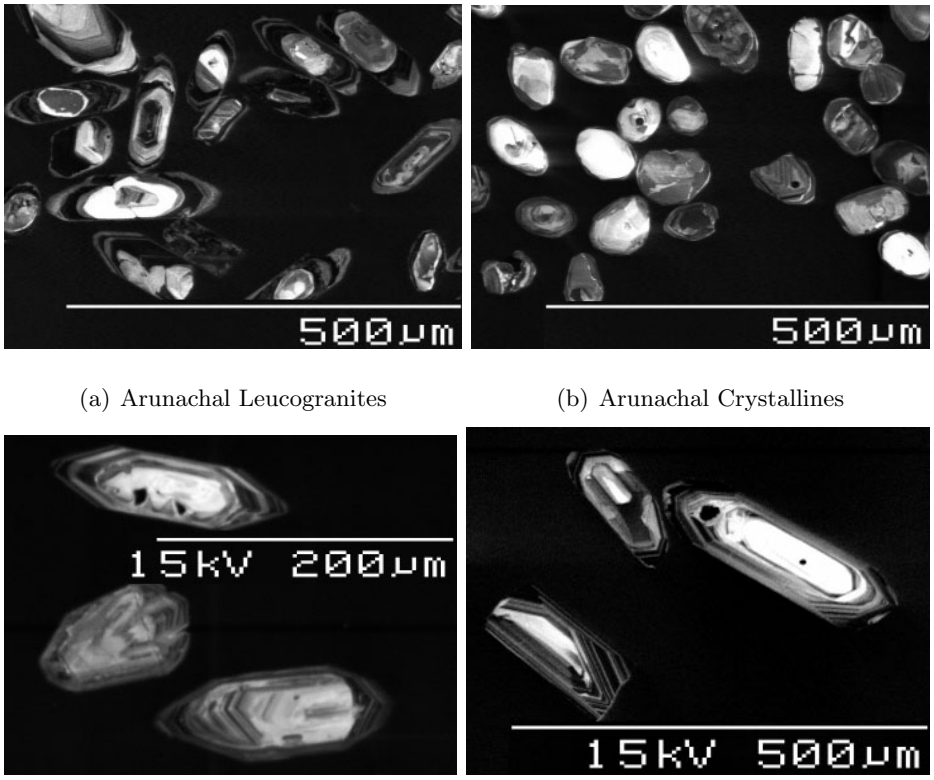

(a) Arunachal Leucogranites (b) Arunachal Crystallines

(c) Tsona Leucogranites (d) Dala Granitoids

Figure 4.2: Cathodoluminescence images of zircons from the Arunachal Leucogranites, Arunachal Crystallines, Tsona Leucogranites and Dala Granitoids. The rim domains typically yield Himalayan ages (<65 Ma), inherited cores are pre-Himalayan.

using optical and electron microscopy including cathodoluminescence spectroscopy to check for inclusions, cracks and other imperfections (which were avoided during analysis), and to assess the two-dimensional internal structure of the grains. For most samples, grains typically ranged from 100 to 500 μm in length, exhibiting subhedral to euhedral (granitoid) or rounded (detrital) morphologies.

Zircons from the Arunachal Leucogranites, Tsona Leucogranites and Dala Granitoids often show cathodoluminescence patterns that are indicative of inherited cores

overgrown by concentrically zoned rims (*Figure 4.2*). The CL characteristics of the core domains are similar to those observed in detrital grains separated from nearby lithologies. This pattern is interpreted as representing inherited restitic grains overgrown by magmatic rims during granitoid formation. *Figure 4.3(a)-(e)* illustrate the range of CL patterns observed in zircons from the Yala-Xiangbo Granitoids, these grains are notably more variable and somewhat harder to interpret. Samples from southern parts of the complex (*e.g. Figure 4.3(*a*)*) contain relatively pristine zircons, with CL patterns similar to those observed in the Dala Granitoids *ca.* 50 km to the south. Those collected further north (*e.g. Figure 4.3(b)-(e)*), however, show progressively more anomalous looking zircons. These grains are characterised by unusual CL patterns varying, from patchy textures cross cutting the concentric zonation (*Figure 4.3(b)*) to mottled, often tabular grains, which have a spongy appearance under backscatter electron imaging (*Figure 4.3(c)-(e)*). Monazites from all Yala-Xiangbo Granitoid samples are typically subhedral and do not appear especially unusual. Zircons from the Yala-Xiangbo high-grade pelite samples (*e.g. Figure 4.3(f)*) show a range of CL patterns compatible with their inferred detrital origin.

4.3.1 Analytical methods

Isotopic analyses were conducted using the SHRIMP RG ion microprobe facility at The Australian National University. Analytical procedures for zircon were similar to those described by Williams (1998), and to Harrison et al. (1995, 1999d) for monazite. Analytical conditions were 10 kV primary beam accelerating voltage, a 2-5 nA O_2^- primary beam current, and a 12-30 μm diameter spot. The secondary beam was configured using 10 kV accelerating voltage, mass resolution of 5000, and ion-counting single electron multiplier in peak hopping mode. Isotopic compositions were measured directly without correction for mass fractionation ($\leqslant$0.25% per AMU).

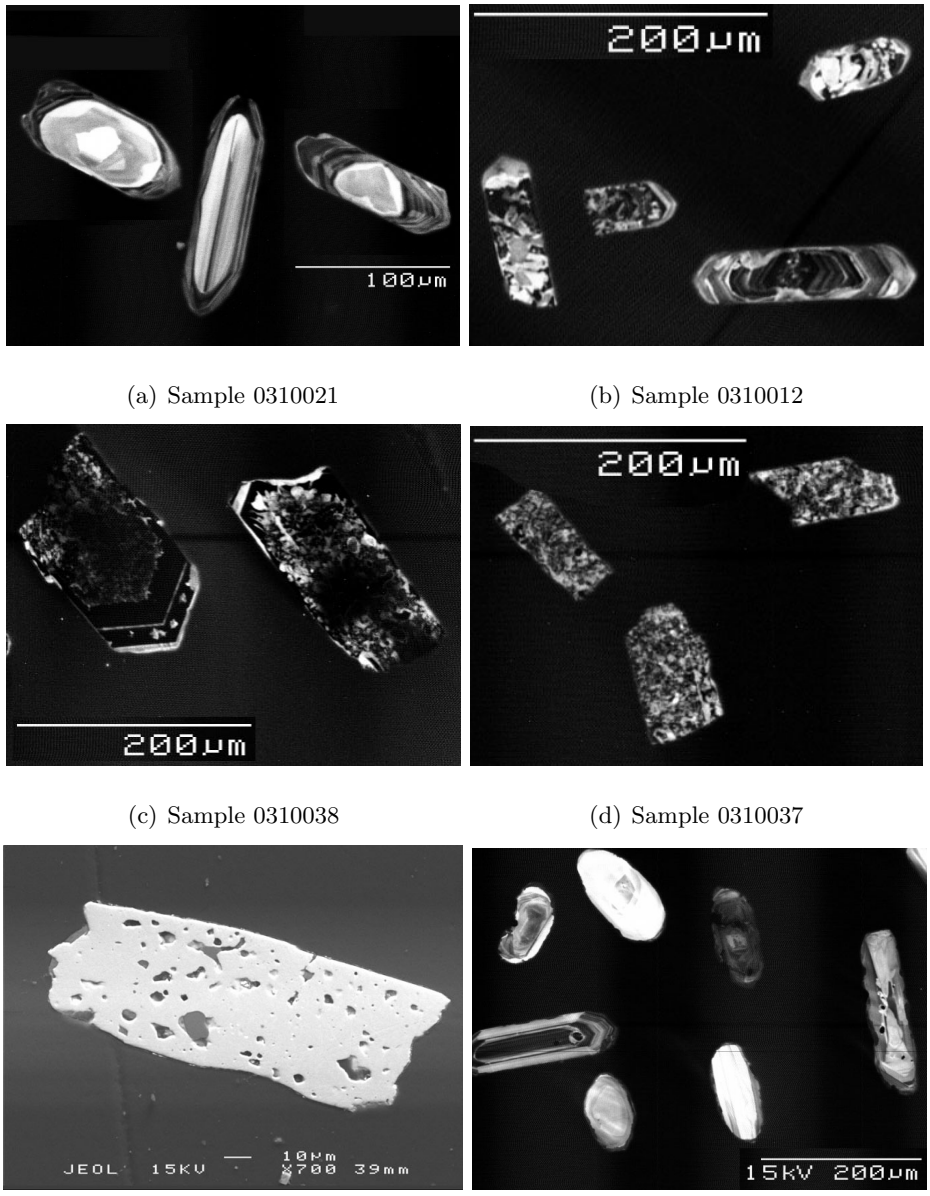

(a) Sample 0310021

(b) Sample 0310012

(c) Sample 0310038

(d) Sample 0310037

(e) Sample 0310037

(f) Yala-Xiangbo pelites

Figure 4.3: Cathodoluminescence and backscatter electron images of zircons from the Yala-Xiangbo Granitoids and Yala-Xiangbo pelites. The inclusion rich cores shown on (c) are undateable. Subfigure (e) shows electron backscatter image of "spongy" grain hosting inclusions of quartz and feldspar. See text for further discussion

Analytical results were evaluated using a procedure designed to maximise automatic detection of potentially spurious analyses, with a view to reducing potential biasing of the final results through human error induced by qualitative comparison of data points individually. Raw data were assessed by examining counting statistics and critical ratios for each isotopic species. Measurements found to deviate significantly from expected analytical precision were examined for analytical faults or complexities (*e.g.* breaching inclusions or cracks, and spurious electronic noise). Zircon data reductions were performed using the SQUID Excel macro (zircon, Ludwig, 2001) and including corrections for fractionation of Pb relative to U and Th, standardising U-Pb isotopic ratio measurements against FC1 (Paces and Miller, 1993), and absolute U+Th content measurements against SL13 (Claoue-Long et al., 1995). Monazite data reductions were performed by T. Ireland using ANU SHRIMP Group PRAWN and Lead software packages. Common lead corrections assumed the laboratory-derived common lead composition of Broken Hill galena (Cumming and Richards, 1975).

The rim domains of most granitoid zircons yielded calculated $^{206}Pb/^{238}U$ apparent ages <65 Ma. Zircon data were evaluated for concordancy in the U-Pb system by plotting the $^{206}Pb/^{238}U$ and $^{207}Pb/^{235}U$ ratios on a concordia plot, from which we conclude that the U-Pb ages from the rim domains of granitic samples are concordant (see *Figure 4.4*) and date the timing of crystallisation. Cores yield apparent ages typically ranging from 200 Ma to 3500 Ma for samples outcropping within the Tethyan Himalaya, and >450 Ma to 3500 Ma otherwise. Analyses of the core domains are also largely concordant (see *Figure 4.4*). Monazite data were evaluated by co-plotting the calculated apparent $^{206}Pb/^{238}U$ and $^{208}Pb/^{232}Th$ ages. *Figure 4.5* shows that the older group of $^{206}Pb/^{238}U$ ages are notably more scattered and

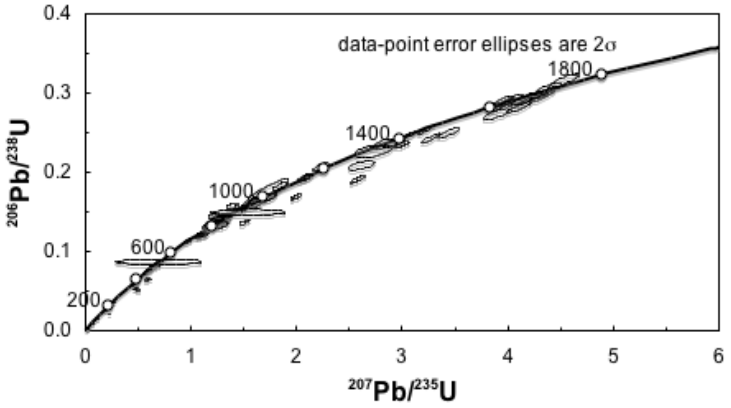

(a) Arunachal Leucogranites ^{204}Pb corrected - all analyses

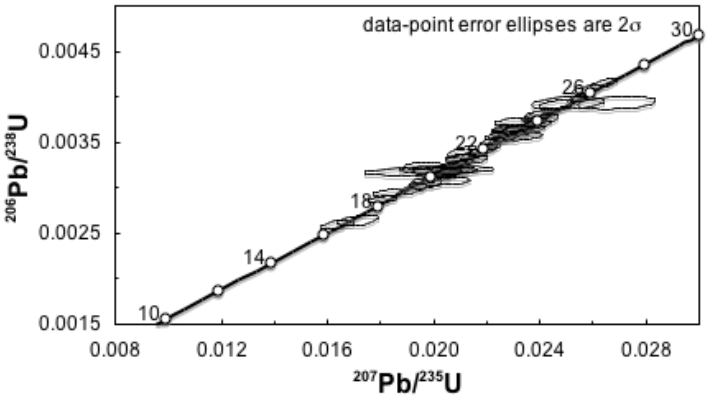

(b) Arunachal Leucogranites ^{208}Pb corrected - Himalayan analyses

Figure 4.4: Zircon U-Pb concordia plots for the Arunachal and Tsona Leucogranites, and Dala and Yala-Xiangbo Granitoids. First plot in each pair shows ^{204}Pb corrected data for all analyses, second plot shows ^{208}Pb corrected data for analyses yielding Himalayan (< 65 Ma) ages only. *Continues on the next page...*

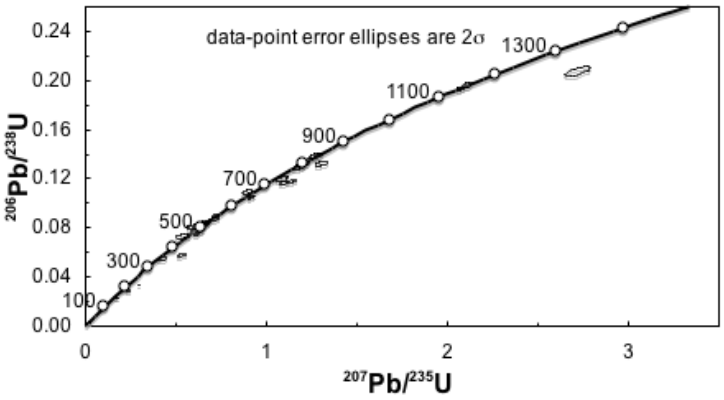

(c) Tsona Leucogranites ^{204}Pb corrected - all analyses

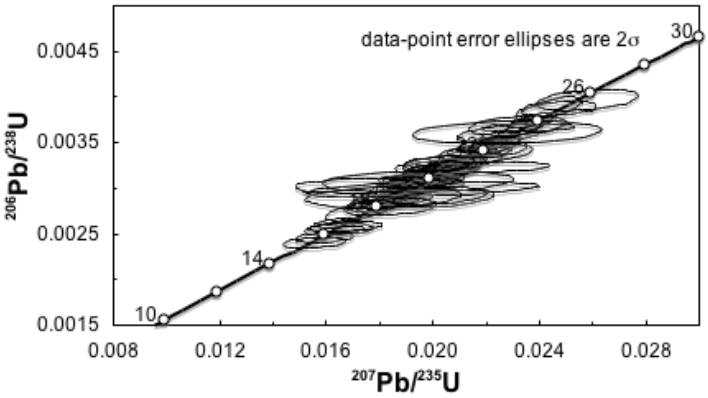

(d) Tsona Leucogranites ^{208}Pb corrected - Himalayan analyses

Figure 4.4: *continued...*

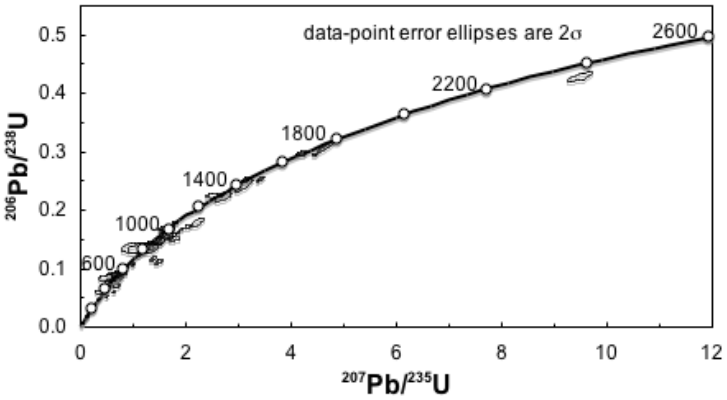

(e) Dala Granitoids ^{204}Pb corrected - all analyses

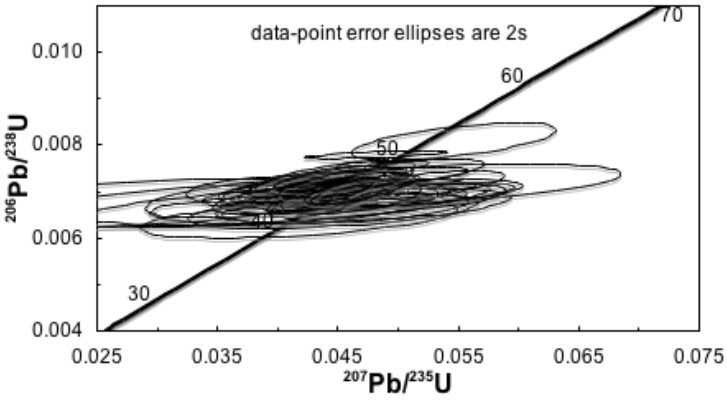

(f) Dala Granitoids ^{208}Pb corrected - Himalayan analyses

Figure 4.4: *continued...*

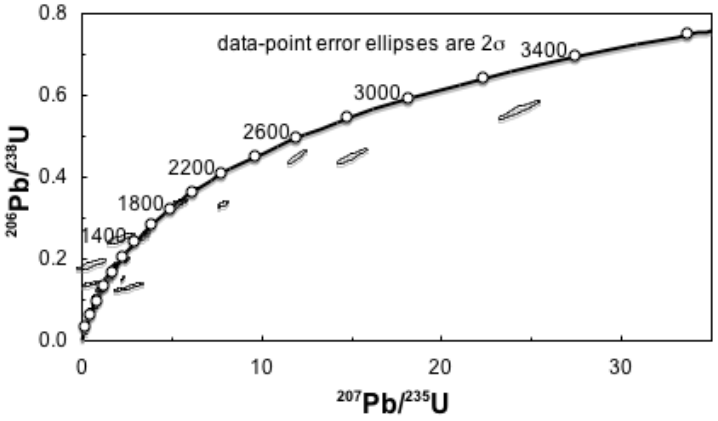

(g) Yala-Xiangbo Granitoids ^{204}Pb corrected - all analyses

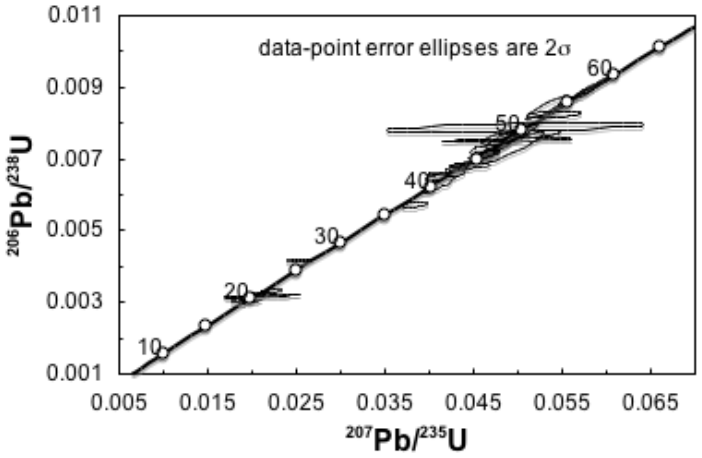

(h) Yala-Xiangbo Granitoids ^{208}Pb corrected - Himalayan analyses

Figure 4.4: *continued...*

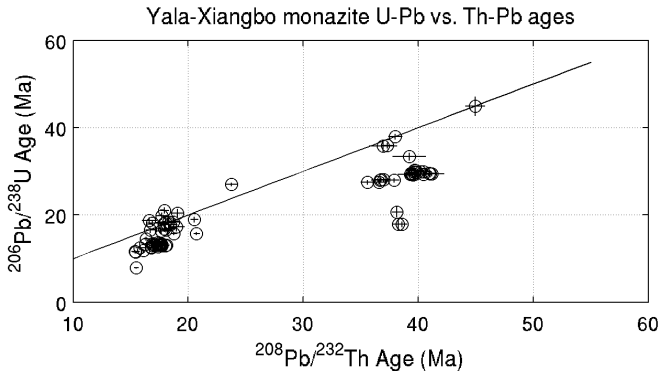

Figure 4.5: Calculated apparent ^{206}Pb/^{238}U vs. ^{208}Pb/^{232}Th ages for the Yala-Xiangbo monazites shown with the expected 1:1 correlation (solid line). Note that the older ^{206}Pb/^{238}U ages are consistently younger and more scattered than the corresponding ^{208}Pb/^{232}Th ages for the same analyses. This may reflect formation of U-rich exsolution lamellae (Harrison et al., 2002) associated with the later monazite growth event, although other spurious analytical faults cannot be entirely ruled out (B. Hacker *pers. comm.*).

younger than their ^{208}Pb/^{232}Th equivalents. This may reflect formation of U-rich exsolution lamellae (Harrison et al., 2002) associated with the younger monazite growth event, although other spurious analytical faults cannot be entirely ruled out (B. Hacker *pers. comm.*).

Final zircon U-Pb ages were calculated according to an automated procedure designed to optimize accuracy and precision while simultaneously minimising the requirement for qualitative judgements of individual datum. The best-estimate ^{206}Pb/^{238}U apparent age was calculated by taking a weighted mean of the ^{204}Pb, ^{207}Pb, and ^{208}Pb corrected values for each analysis. If the MSWD of these three ages was found to exceed a critical threshold of 2, the datum was automatically flagged for further consideration due to poor agreement between the three common Pb corrections. The final age was calculated by taking a weighted mean of the best estimate ^{206}Pb/^{238}U, and the ^{207}Pb/^{206}Pb apparent ages. However, if the

MSWD of these two numbers was found to exceed a critical threshold of 7, the datum was again flagged for further consideration (due to inconsistency between the U-Pb and Pb-Pb apparent ages). In such cases, the final age was taken as the best estimate $^{206}Pb/^{238}U$ age for samples in which the weighted mean of the $^{206}Pb/^{238}U$ and $^{207}Pb/^{206}Pb$ apparent ages was less than 800 Ma, or the $^{207}Pb/^{206}U$ apparent age otherwise. In cases where the $^{207}Pb/^{206}Pb$ apparent age was within error of zero (i.e. young samples with low radiogenic ^{207}Pb content), the $^{207}Pb/^{206}Pb$ apparent age was ignored. Post-analysis imaging of the sampling area for each datum was compared with the cathodoluminescence image to check for overlap on multiple zones potentially leading to mixed ages. Individual measurements were only rejected from the final dataset where several lines of evidence indicate that they were analytically flawed. According to this scheme, typically up to 15% of the measurements from a given analytical session were flagged for detailed consideration, with <5% rejected from the final results. Final monazite ages were taken as the calculated ^{207}Pb-corrected $^{208}Pb/^{232}Th$ age.

4.3.2 Results

Approximately 600 zircons from 26 samples and *ca.* 80 monazites from 6 samples were analysed, the results are tabulated in *Appendix .1*. The distribution of zircon ages within each sample suite is displayed (*Figure 4.6*) as a probability density function (PDF) calculated according to *Equation 4.12*. Note that using this method, each PDF is normalised to n, such that the relative peak heights are proportional only to the probability distribution within each sample. Normalisation is required to compare data sets of different size, however curves calculated from a small number of clustered data can appear misleading when compared to larger, more broadly distributed samples (because the integral of each function is unity). The reader may wish to note the relative sample sizes listed in the plot titles or legend.

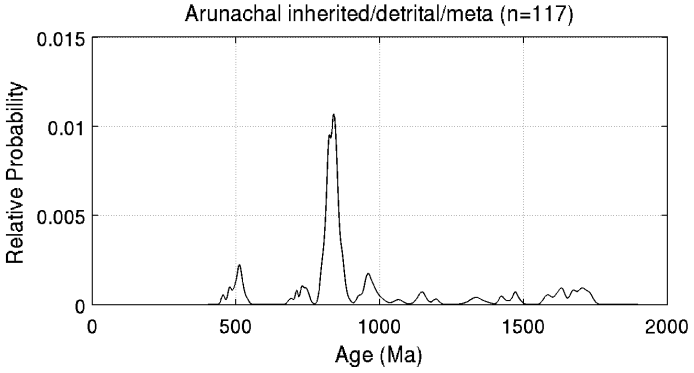

(a) Arunachal Leucogranites pre-Himalayan

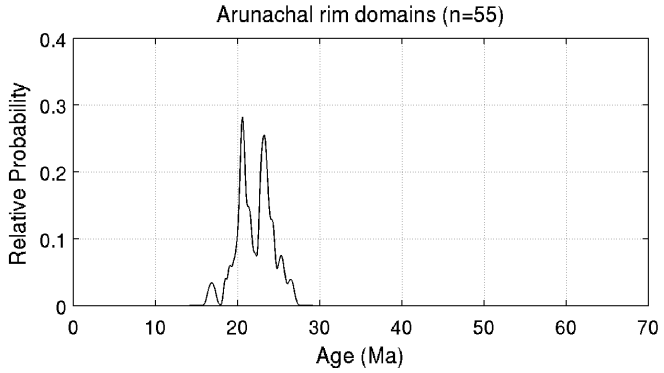

(b) Arunachal Leucogranites Himalayan

Figure 4.6: Age-probability plots for the Arunachal and Tsona Leucogranites, and the Dala and Yala-Xiangbo Granites. First plot in each pair shows shows pre-Himalayan age analyses (200–2000 Ma), which are primarily derived from the core domains. The second shows Himalayan age analyses (<70 Ma) which are primarily derived from the rim domains.

Continues on next page...

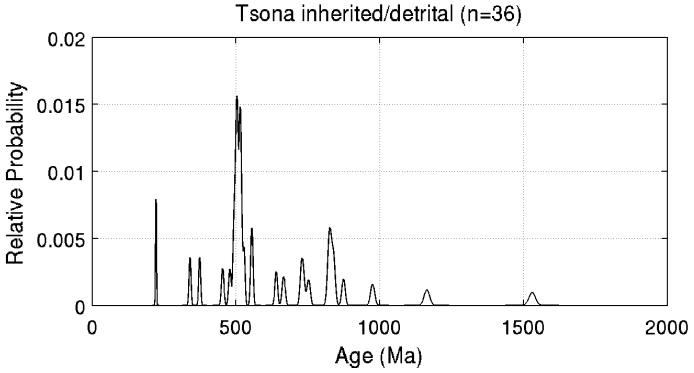

(c) Tsona Leucogranites pre-Himalayan

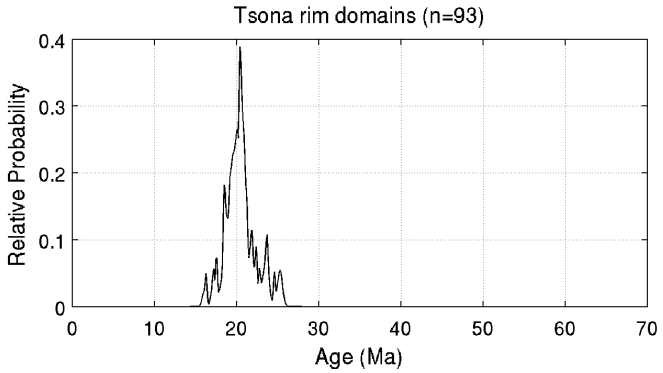

(d) Tsona Leucogranites Himalayan

Figure 4.6: *continued...*

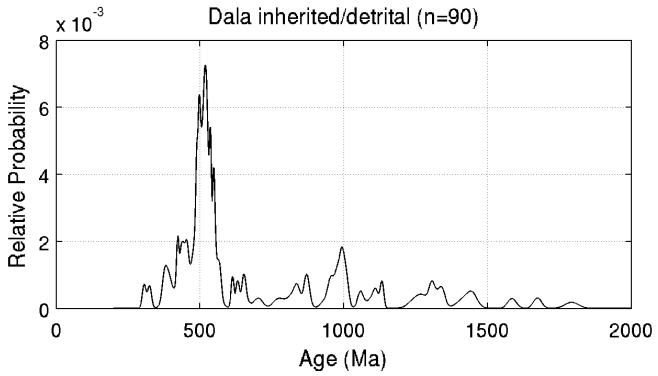

(e) Dala Granitoids pre-Himalayan

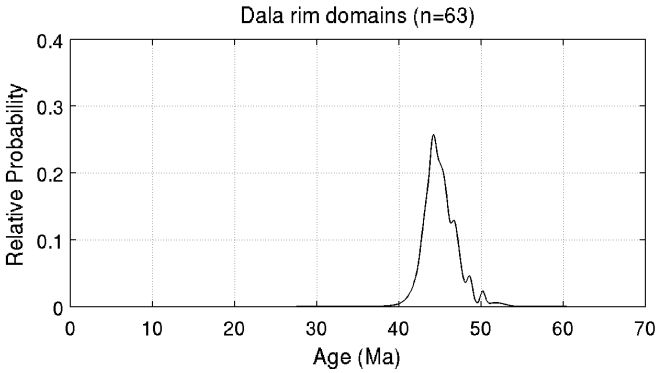

(f) Dala Granitoids Himalayan

Figure 4.6: *continued...*

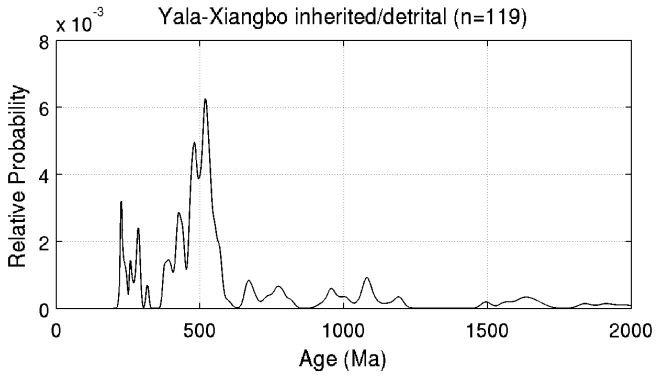

(g) Yala-Xiangbo Granitoids pre-Himalayan

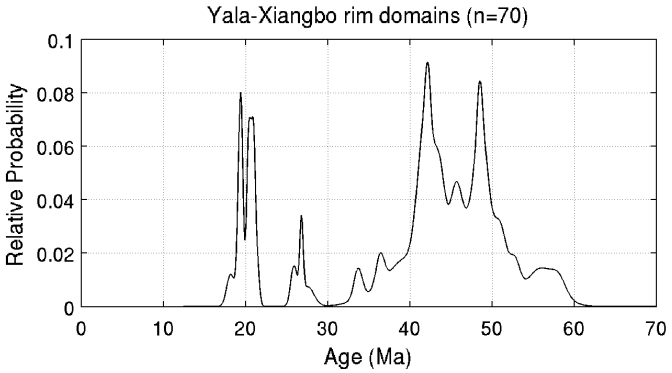

(h) Yala-Xiangbo Granitoids Himalayan

Figure 4.6: *continued...*

The first in each pair of plots in *Figure 4.6* shows the distribution of probability in a sub-set of analyses yielding ages in the range 200–2000 Ma, which are predominantly derived from the core domains. All sample suites contain a variety of age populations ranging from Phanerozoic to Precambrian and the general form of the age-distribution is broadly comparable to studies of Indian and Eurasian detrital sediments from elsewhere in the Himalaya (*e.g.* Gehrels et al., 2003; Myrow et al., 2003). Detailed analysis of individual PDFs is limited by sample size, however, it is noteworthy that while the largest peak in the Yala-Xiangbo, Dala, and Tsona PDFs is at *ca.* 500 Ma, the Arunachal suite collectively shows a more prominent *ca.* 800 Ma peak that is apparently unrepresented elsewhere. The second in each plot pair shows the probability distribution within a second sub-set (10-70 Ma) representing the younger Himalayan age populations from each sample suite (*Figure 4.6*), which are primarily derived from analyses of rim domains. In the Arunachal, Tsona and Dala suites, these data cluster into single peaks at *ca.* 20 Ma, *ca.* 21 Ma and *ca.* 45 Ma respectively. Samples from the Yala-Xiangbo granites however form a broad distribution, with the dominant peak at *ca.* 45 Ma, and smaller peaks at *ca.* 25 and *ca.* 20 Ma.

Figure 4.7 shows PDFs calculated for sub-sets of each suite, separated by individual rock sample. Samples from the Arunachal leucogranites appear to show a weakly bimodal distribution (peaks at *ca.* 21 and 23 Ma) with large tails, however it is unlikely that this modality is statistically significant given the number of grains analysed. Two samples from the Tsona leucogranites show prominent overlapping peaks at *ca.* 21 Ma, the third however, displays a broad range of ages from 16-26 Ma. Six samples of Dala granite yielded a series of overlapping age-probability peaks ranging from 42-50 Ma. Samples from the Yala-Xiangbo Granitoids appear to be divisible

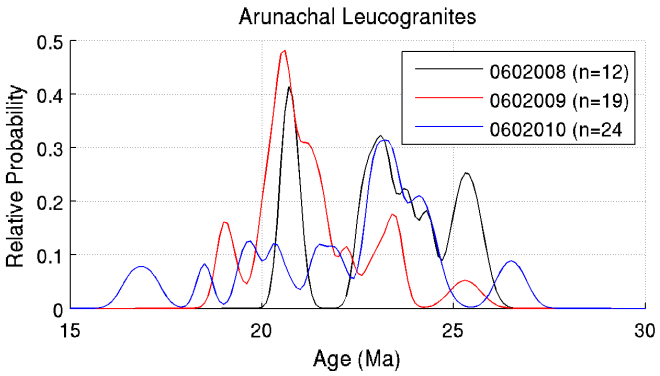

(a) Arunachal Leucogranites

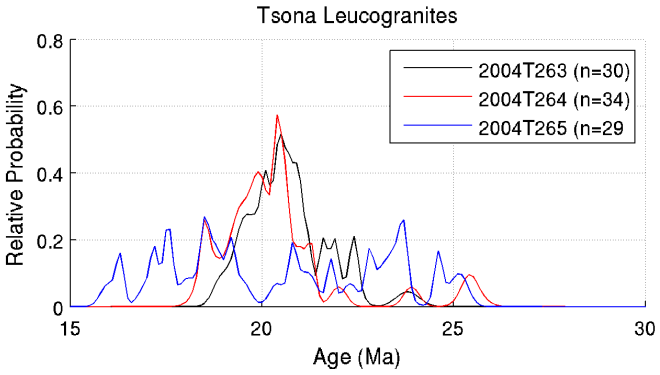

(b) Tsona Leucogranites

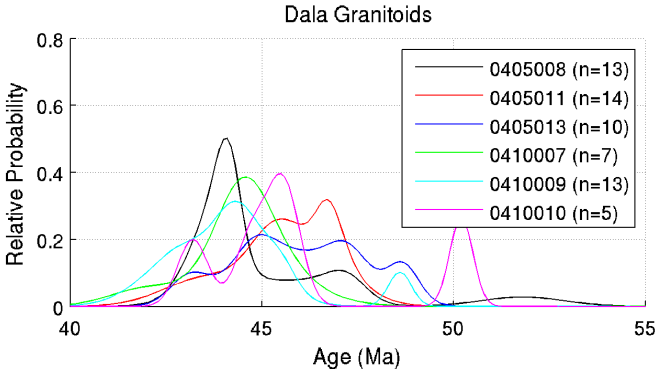

(c) Dala Granitoids

Figure 4.7: Age-probability plots by sample, for the Arunachal and Tsona Leucogranites, the Dala and Yala-Xiangbo Granitoids, the Arunachal Crystallines, and the Yala-Xiangbo pelites. Data are plotted by rock sample. *Continues on next page...*

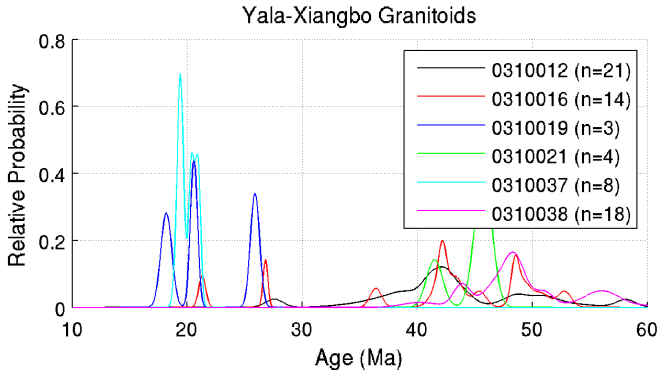

(d) Yala-Xiangbo Granitoids

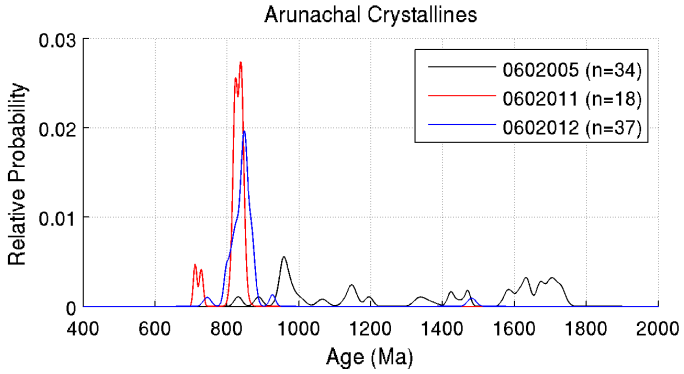

(e) Arunachal Crystallines

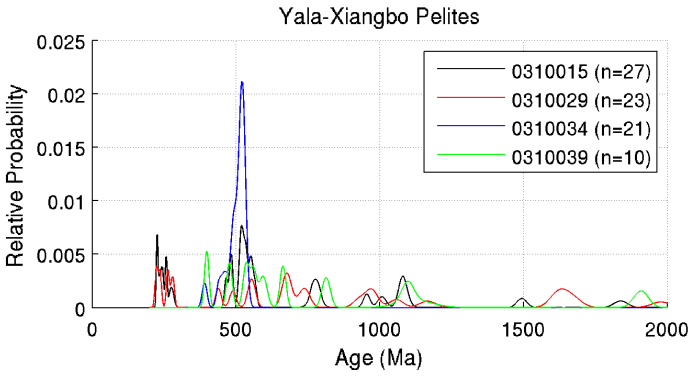

(f) Yala-Xiangbo pelites

Figure 4.7: *continued...*

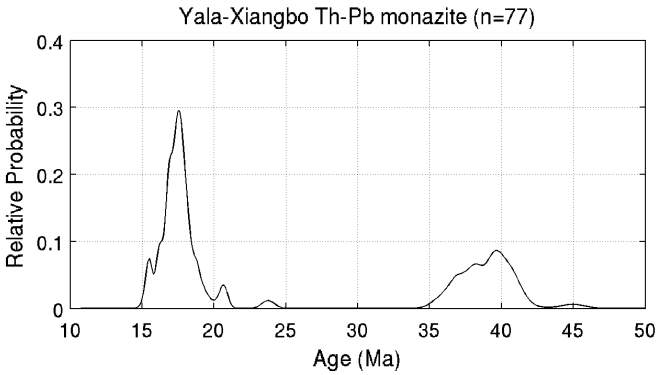

(a) Yala-Xiangbo monazites

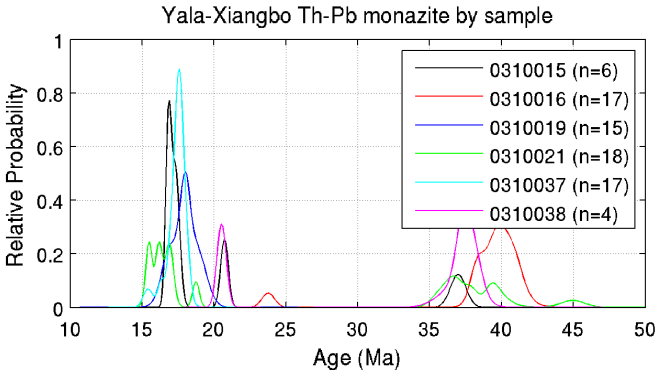

(b) Yala-Xiangbo monazites by sample

Figure 4.8: Monazite Th-Pb age probability plots for 77 analyses from 5 samples of the Yala-Xiangbo Granitoids and 1 sample of the Yala-Xiangbo pelites (0310015). Subfigure (a) shows all data together, subfigure (b) shows data separated by individual rock sample.

into two modes. Eocene ages (samples 0310012, 0310016, 0310021, 0310038) are predominantly derived from analyses of zircons or parts thereof showing relatively pristine concentric CL zonation. Miocene ages (samples 0300019, 0310037), however, are confined to grains or parts thereof showing mottled/patchy/spongy CL zonation. Samples in which both Eocene and Miocene ages were found (*e.g.* 0310016), also show transitional CL zonation patterns.

Monazites separated from the Yala-Xiangbo Granitoids and 1 sample of the Yala-Xiangbo Pelites yielded a similar bimodal distribution of Himalayan ages, with peaks respectively at *ca.* 18 and *ca.* 40 Ma (*Figure 4.8*). Samples 0310016 and 0310038 yielded predominantly Eocene ages, whereas in samples 0310019 and 0310037 all ages were Miocene. Samples 0310015 and 0310021 yielded ages from both populations.

Figure 4.7 also shows PDFs calculated from high grade metamorphic units of the Arunachal and Tethyan Himalaya, separated by individual rock sample. The age-probability spectra derived from analysis of pelitic samples from the core of the Yala-Xiangbo Dome are dominated ages in the range 200–1200 Ma. The youngest ages in samples 0310015 and 0310029 are comparable to those found in the low grade Triassic sequences of the eastern Tethyan Himalaya (*ca.* 200 Ma, *Chapter 2*), whereas those from structurally deeper samples 0310034 and 0310039 are somewhat older (*ca.* 450 Ma). A single pelitic sample from the Arunachal Crystalline sequence yielded ages in the range *ca.* 800–1800 Ma, and two granitic samples from the Arunachal Crystalline sequence (meta Ksp-granite 0602011 and Zhimithang Gneiss 0602012) have overlapping age probability peaks at *ca.* 824 Ma.

Himalayan age zircons from the Arunachal and Tsona Leucogranites and Yala-Xiangbo Granitoids all show relatively low Th/U ratios (<0.1) compared to those observed in the Dala Granitoids (0.1–0.6). All Himalayan age grains, however, are marked by high $U + Th$ contents, $\leq$40,000 ppm in the Arunachal and Tsona Leucogranites and Yala-Xiangbo granitoids, and $\leq$8000 ppm in the Dala Granitoids. Although similar zircon trace element contents have previously been reported elsewhere in the Himalaya (*e.g.* Zhang et al., 2004a), some workers have suggested that values in this range may be uncharacteristic of naturally occurring zircon (*e.g.* M.

Sample	**N**	ρ	$> \rho_c^{99}$	**Age (Ma)**	$\pm$
Arunachal	55	.51	y	20.2	2.0
Tsona	93	.59	y	18.8	1.2
Dala	61	.64	y	44.1	1.2
Yala-Xiangbo	47	.62	y	42.3	4.9

Table 4.1: Parameters used for correction of apparent age increase due to matrix effects associated with high U+Th content in some grains. ρ is Spearman's rank coefficient, ρ_c^{99} indicates whether the calculated ρ exceeds the critical value for significantly non-zero correlation at the 99% confidence interval. The quoted age is the median of the corrected data and its associated uncertainty, including uncertainty on the linear regression (see text for explanation).

Fanning *pers. comm.*). However, other 4+ cations representing continuous solid solutions with zircon, such as Hf, are present and variable at the percent level. Furthermore, studies have shown that zircons containing similar concentrations of U and Th may be synthesised experimentally (Rubatto and Hermann, 2007).

Matrix effects

A number of workers have noted so called 'matrix effects', caused by compositional differences leading to differing relative sensitivities of Pb^+/U^+ between the sample and standard (Williams and Hergt, 2000; Butera et al., 2001; Hermann et al., 2006). This is particularly noted for samples analysed by SIMS containing greater than 1500-2000 ppm total U and Th (Williams and Hergt, 2000; Butera et al., 2001; Hermann et al., 2006), leading to an apparent positive correlation between [U] or [U+Th] and age in grains that are in fact isochronous (Williams and Hergt, 2000; Butera et al., 2001; Hermann et al., 2006). The median [U] of the data shown in *Figure 4.7* is *ca.* 6000 ppm, suggesting this effect may also be relevant to samples from the eastern Himalaya.

Several methods have been proposed to aid removal of matrix effects. The simplest involves correcting analyses containing >1500-2000 ppm U via linear regression back to the average of the lower [U] data (Butera et al., 2001; Hermann et al., 2006). This method assumes that there is a linear relationship between Pb^+/U^+ ionization yields and U+Th content, which, although not proven, appears to be valid for the majority of cases (T. Ireland *pers. comm.*). A variation (using non-parametric statistics, see below) was applied to Himalayan-age data from the Arunachal and Tsona Leucogranites, and the Dala and Yala-Xiangbo Granitoids. Although those from the younger zircon growth event recorded at Yala-Xiangbo were excluded due to uncertainties in their petrogenesis (see below) and insufficient number of analyses to achieve statistical significance.

The non-parametric Spearman rank correlation coefficient (Press et al., 1992) was computed for each sub-set and compared to tabulated critical values. In cases where the critical value for significantly non-zero rank correlation was exceeded at the 99% confidence level, linear regressions were performed using both parametric (least squares) and non-parametric (robust) techniques. Analyses containing > 2000 ppm were corrected back to a horizontal trend intersecting the median of those containing ≤2000 ppm [U+Th]. In cases where no grains containing ≤2000 ppm [U+Th] were found, all analyses were corrected back to an intercept at 2000 ppm. Results were plotted in [U+Th]-age space, separated both by location (sample suite) and individual rock sample. Little advantage was gained by treating rock samples individually, hence the results shown in *Figure 4.9* and *Table 4.1* are for combined sample suites grouped by location.

The results indicate that all sample suites show significantly non-zero, positive correlation between apparent age and U+Th content at the 99% confidence inter-

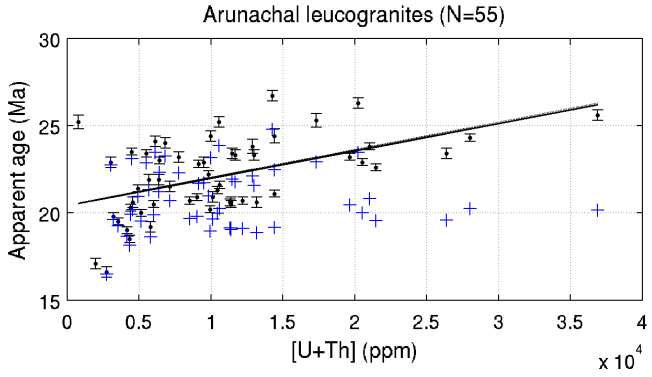

(a) Arunachal Leucogranites

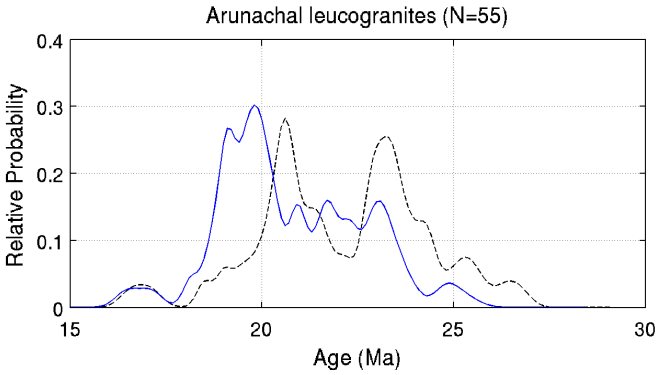

(b) Arunachal Leucogranites

Figure 4.9: Correction of matrix effects. First plot in each pair shows the variation in age with total U+Th content for each sample suite; The original data are shown in black with error bars, corrected data are shown in blue. Solid and dotted lines are respectively the robust and least-squares regressions used to calculate the correction. The second plot shows PDFs calculated for the original (black) and corrected (blue, see text for discussion) data according to *Equation 4.12*. *Continues on next page...*

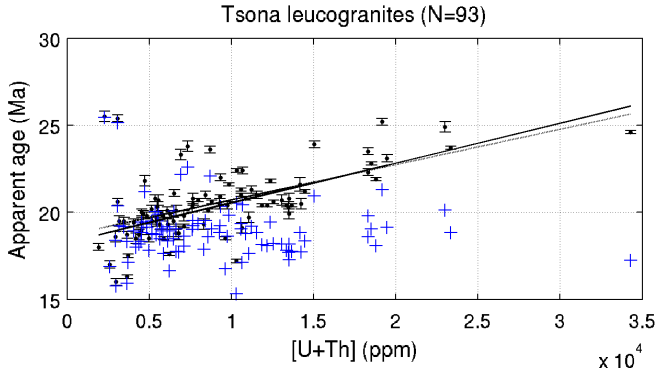

(c) Tsona Leucogranites

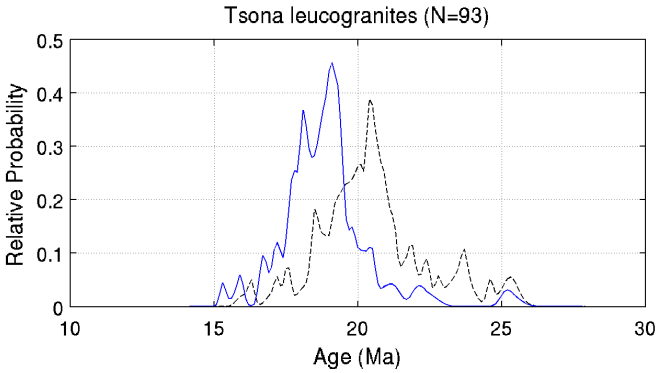

(d) Tsona Leucogranites

Figure 4.9: *Continued...*

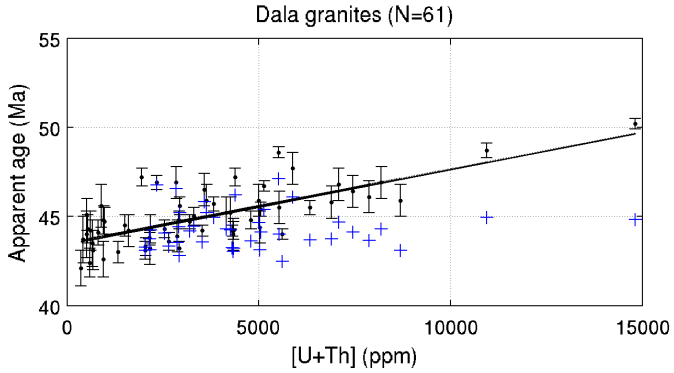

(e) Dala Granitoids

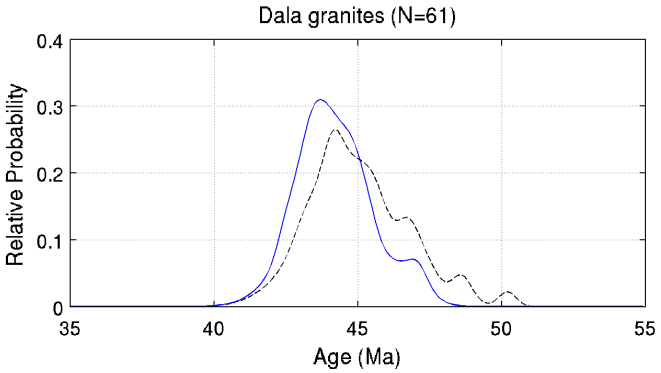

(f) Dala Granitoids

Figure 4.9: *Continued...*

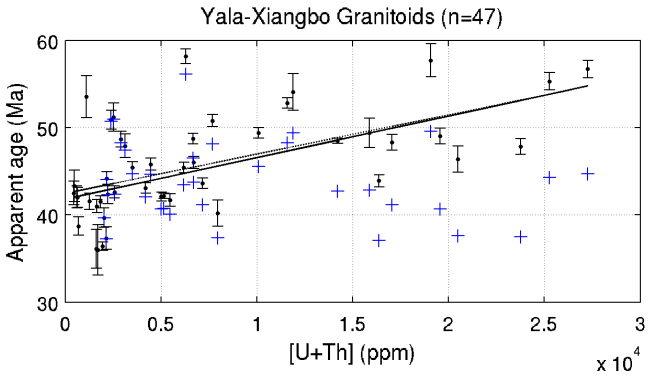

(g) Yala-Xiangbo Granitoids

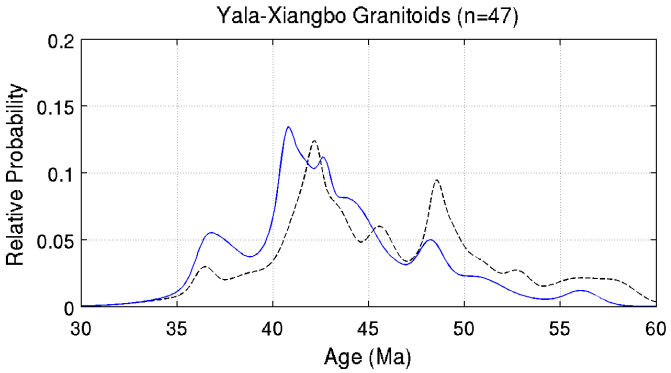

(h) Yala-Xiangbo Granitoids

Figure 4.9: *Continued...*

val (*Table 4.1*). *Figure 4.9* also shows PDFs calculated from the corrected data, which are clearly condensed and shifted to slightly younger ages compared to those generated using the original values. Note that the apparent bimodality shown by the Arunachal sample suite is removed, indicating that older peak was an artefact of the high [U+Th] grains. An assumption inherent in this technique is that the data are derived from the same population (zircon growth event). Both the Dala Granitoids and the Tsona Leucogranites are emplaced into relatively lower grade (sub-anatectic) metasediments, and therefore probably crystallised relatively quickly. The Arunachal Leucogranites and Yala-Xiangbo Granitoids, however, outcrop within units that have experienced upper amphibolite facies metamorphism, and hence a single relatively short crystallisation event cannot be automatically assumed. Unfortunately it is not possible to resolve these differences within the scope of the available data. However, it is argued that the observed correlations between apparent age and U+Th content are compelling evidence that the approach described above provides an improvement over the uncorrected data.

4.4 Zircon titanium thermometry

The Ti-in-zircon thermometer (Watson and Harrison, 2005; Watson et al., 2006; Ferry and Watson, 2007), provides an empirical framework under which the crystallization temperature of zircon may be estimated by measuring its titanium content ([Ti]). The technique was first applied to ancient zircons from Jack Hills (Western Australia), leading Watson and Harrison (2005) to propose the existence of wet, minimum melting during the Hadean Eon, a hypothesis with far ranging implications that has stimulated ongoing debate thereafter (Glikson, 2006; Nutman, 2006; Watson and Harrison, 2006).

4.4.1 Background

The governing thermodynamic relationship for the thermometer (Watson and Harrison, 2005), is given as:

$$a_{TiO_2}^{Zircon} = \gamma_{TiO_2}^{Zircon} \cdot X_{TiO_2}^{Zircon} = \exp \frac{-\Delta G^0}{RT} \tag{4.1}$$

In which a_{TiO_2} is the activity of TiO_2, γ is the activity coefficient, X is the mole fraction of TiO_2 in zircon, ΔG^0 is the standard-state free energy change, R is the gas constant and T is the absolute temperature. If γ is assumed to be constant, then the logarithm of Ti is expected to vary linearly with the inverse of T. The thermometer was calibrated from 1025° to 1450°C (1 to 2 GPa) using zircons synthesized experimentally under hydrothermal conditions, and from *ca.* 580° to 1070°C by analysis of natural zircons in which crystallisation temperature could be constrained by way of independent geothermometers (Watson and Harrison, 2005). Assuming $a_{TiO_2} = 1$, the resultant temperature dependence of [Ti] in zircon is given by *Equation 4.2*.

$$\log(Ti_{ppm}^{Zircon}) = 6.01 \pm 0.03 - \frac{5080 \pm 30}{T(K)} \tag{4.2}$$

This relationship has subsequently been revised to include the effect of sub-unity a_{SiO_2} (Ferry and Watson, 2007) yielding:

$$\log(Ti_{ppm}^{Zircon}) = 5.711 - \frac{4800}{T(K)} - \log(a_{SiO_2}) + \log(a_{TiO_2}) \tag{4.3}$$

In the rutile and quartz saturated case ($a_{TiO_2}, a_{SiO_2} \approx 1$), *Equation 4.3* provides a direct estimate of the crystallisation temperature of zircon. Whereas in the absence of either buffering phase, the respective activities may be determined by some other means and the final temperatures corrected accordingly (Watson and Harrison, 2005; Watson et al., 2006; Ferry and Watson, 2007). While this constraint appears to place limitations on the applicability of the thermometer to rutile/quartz undersaturated systems, it is argued that the vast majority of igneous and metamorphic rocks in

existence today are expected to have a_{TiO_2} and $a_{SiO_2} \geqslant 0.5$ (Watson and Harrison, 2005; Ferry and Watson, 2007). Therefore, even where the these values cannot be directly established (*e.g.* Hadean detrital zircons), temperatures are unlikely to be incorrect by more than *ca.* 60°C where both a_{TiO_2} and a_{SiO_2} are unknown, or underestimated by more than *ca.* 40°C where only a_{TiO_2} is unconstrained (Watson and Harrison, 2005; Ferry and Watson, 2007). Furthermore, Ferry and Watson (2007) have shown that in igneous systems of granitic/granodioritic composition, sub-unity a_{TiO_2} and a_{SiO_2} are expected to be mutually compensatory such that the correct temperature will be recorded.

4.4.2 Analytical methods

Several analytical techniques are potentially useful in measuring the titanium content of zircon. EPMA analyses may be performed relatively quickly and at low cost, but acceptable analytical precision is only possible in grains containing greater than *ca.* 40 ppm titanium (Watson et al., 2006, C. McFarlane *pers. comm.*). Unfortunately, this is significantly above the expected range for most naturally occurring samples. LA-ICPMS measurements are relatively quick and effective, however limitations on sensitivity, spot size, sample destruction and analytical drift (C. Allen *pers. comm.*) make this approach unfavourable for detailed studies in which several kinds of data may be required from each grain.

Watson et al. (2006) have described the SIMS-based approach used to measure the [Ti] of natural zircons constraining the lower temperature portion of the thermometer calibration curve. These workers measured ^{49}Ti and ^{30}Si on a Cameca 3f, calibrated against experimental run products (Run 57 and Run 95). Initial attempts were made to replicate this approach using the SHRIMP RG facility at The Australian National University and the same experimental standard material (kindly

provided by E.B. Watson). However, similar problems were encountered to those described by Watson et al. (2006), in which the small grainsize of Run 59 zircons ($\leqslant$ 30 μm) contained within Ti-rich glass lead to significant analytical dispersion. Run 57 zircons, although larger, were also found to be zoned (by factor of 2) and contain rutile inclusions, hence requiring detailed electron-imaging and cross-correlation of analysis spots with EPMA measurements. Given these analytical obstacles and limited availability of such experimental run products, it was concluded that development of an analytical protocol allowing [Ti] measurements to be calibrated against synthetic glass or a natural U-Pb zircon standard would be preferable. The procedures adopted by this study are described in detail in the following sections, with a view to providing an informative reference for future research.

The isotope $^{49}Ti^{+}$ was measured against $^{44}SiO^{+}$ using the SHRIMP II multicollector (S2MC). SiO^{+} was measured with a Faraday cup and $^{49}Ti^{+}$ using an electron multiplier. The primary (O_2^{-}) beam current of was 4-5 nA, with spot sizes ranging from 12-25 μm. Tests showed that SiO^{+} background counts were consistently in the order of 0.1% of the total SiO^{+} counts on zircon, and were subsequently measured and pre-set at the start of each analytical session. $^{49}Ti^{+}$ backgrounds, measured at various intervals during each analytical session, were consistently in the order of 2-4 counts per second and maybe pre-set or subtracted during data reduction. Surface contamination and contamination at grain boundaries was found to be variable and locally significant, indicating that pre-analysis rastering is important. Other potential sources of excess titanium include cracks and inclusions of Ti-rich minerals (*e.g.* rutile and titanite).

Results based on four, 10 second counting periods per analysis and the above analytical configuration, demonstrate that the $SiO^{+}/^{49}Ti^{+}$ ratio can be measured

Standard	n	Ti (ppm)	2σ (ppm)
SL13	9	6.32	0.33
Temora	7	9.01	0.56
FC1	9	21.6	1.6

Table 4.2: Titanium contents of natural zircon U-Pb standards measured by LA-ICPMS. Ti contents are in ppm, uncertainties are 2σ, n is the number of analyses.

consistently down to at least 3 ppm titanium in a range of natural zircons and standard silicate glasses. Analytical precision based on counting statistics for the $SiO^+/^{49}Ti^+$ ratio in NIST glasses (610, 612 and 615) over the course of an analytical session (24 hrs.) was routinely in the order of 0.2% (*ca.* 0.1% in 610). Internal precision based on the standard error the same ratio measured in SL13 over the course of an analytical session can be <0.5%, but is almost always < 1%. Tests show that little advantage can be gained by increasing either the number or length of the counting periods except at very low [Ti], as the greatest source of uncertainty in final [Ti] and temperature estimates (discussed below) is derived from variability in the natural zircon standards.

Standardization

Six standards were considered for use as SIMS [Ti] reference material; three silicate glasses and three natural zircons. NIST SRM glasses 610, 612 and 615 conveniently bracket the expected range of natural zircon [Ti], they also have the advantage of being widely available and are commonly used in a variety of other analytical procedures. Natural zircon U-Pb reference materials SL13, Temora and FC1 (Paces and Miller, 1993; Claoue-Long et al., 1995; Black et al., 2003) were chosen for compatibility with existing SIMS geochronological procedure.

In the context of this study, it is important to consider the accuracy of the [Ti] assigned to NIST SRM, in particular 612, which is used as a reference material for both for SIMS and LA-ICPMS measurements, but has been suggested to be heterogeneous with respect to some elements (Eggins and Shelley, 2002). The original value quoted in the NIST SRM 612 certificate has been widely revised, but is commonly taken as 50 ppm after Pearce et al. (1997). However, several workers have commented that this value maybe as much as 20% too high (S. Eggins, A. Kallio *pers. comm.*). This study adopts a nominal value of 41±1 ppm obtained by cross-calibration with USGS glasses and XRF for NIST 612 (S. Eggins *pers. comm.*), 434±14 ppm for NIST 610 (Pearce et al., 1997), and 3.4±0.3 ppm for NIST 615 (Horn et al., 1997). The reader is cautioned to consider all relevant standard values adopted when inter-comparing results from other studies. The [Ti] of natural zircon standards was investigated by LA-ICPMS, and the results are summarised in *Table 4.2*. Results indicate that the zircon SL13 is relatively homogeneous, containing 6.32±0.33 (2σ) ppm Ti, while igneous zircons Temora and FC1 show greater dispersion. These data are consistent with the reproducibility of the $SiO/^{49}Ti$ ratio in SL13 (discussed above), and indicate that while SL13 may be used routinely as a SIMS reference material based on a nominal value for [Ti]. Standardization against Temora and FC1 will in most cases require cross-calibration of individual standard spots against a secondary technique such as LA-ICPMS.

Calibration and data reduction:

The reciprocal $SiO/^{49}Ti$ ratio in both zircons and NIST glasses was found to vary linearly over the expected range of most natural zircon [Ti] (1-40 ppm) and appears to be continuous over at least three orders of magnitude. This relationship suggests that the absolute [Ti] of unknown zircons may be easily calibrated against a known reference material in Ti - $(SiO/^{49}Ti)^{-1}$ (ppm) space. Two calibration methods were

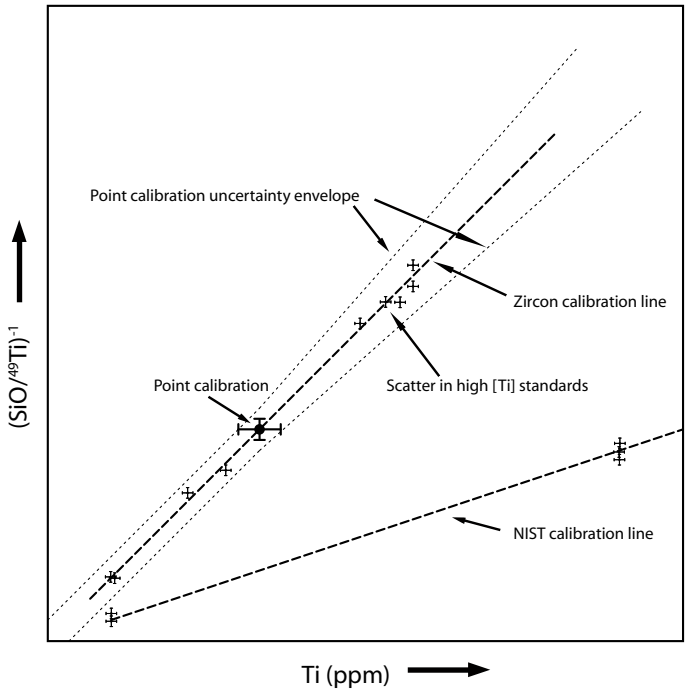

Figure 4.10: Schematic SIMS titanium calibration methods. Note simple point calibration and uncertainty envelope (dotted lines), minimum uncertainty is that of the calibration point, at higher [Ti] the envelope is scaled according to distance from the origin. Alternative cross calibration (dashed lines) allowing standardization against NIST glass by measuring multiple NIST and zircon standards.

tested, the simplest uses multiple measurements of a single standard and zero intercept to constrain a calibration line. This approach allows for efficient analyses and relatively straightforward data reduction, however the uncertainty envelope is somewhat complex and the absolute form of the calibration curve must be inferred. It is best suited to cases in which the expected [Ti] of the unknowns is comparable (within a factor of 2-3) to that of a well constrained reference material (*e.g.* SL13). An alternative approach involves measuring multiple reference materials to populate a cross calibration between natural zircon and NIST glass. Cross calibration is required to correct for the differing ion yields resulting from differences in the silicate glass and zircon structure. This approach is expected to produce greater accuracy and precision over a range of [Ti] and is generally considered more robust, however in practice, precision may be limited by inhomogeneity in natural (particularly igneous) zircon standards, requiring cross-referencing of individual standard spots with a secondary technique (*e.g.* LA-ICPMS or EPMA).

Natural zircon standard SL13 was chosen as a reference material for single-point calibration, analysed once for every 3-5 unknowns per analytical session. Natural zircon standard FC1 was also analysed after each SL13 and used as a secondary reference material to monitor machine drift and reproducibility of the data reduction procedure. Raw data, primarily comprising total counts per scan and secondary beam monitor readings for each species, were evaluated by calculating basic counting statistics for each analysis. In rare cases where results were found to deviate significantly from expected analytical precision (typically $\leqslant$2 analyses per session), these data were examined for evidence of analytical faults or contamination (*e.g.* by breaching a Ti-rich crack or inclusion). Background subtractions were performed in counts-per-second in accordance with the analytical setup discussed above.

The SiO/^{49}Ti ratio for each analysis was calculated by taking the median of the ratios for n scans, and the standard error from counting statistics was calculated for this value. Standard measurements were evaluated for internal consistency, and where significant drift was detected during the course of an analytical session, a correction was applied by performing a robust regression to the standard measurements and correcting all analyses with respect to a horizontal line intercepting at the median SiO/^{49}Ti ratio of SL13. Typically this correction makes only a fractional difference to the final temperature estimates, but can significantly improve the calculated measurement uncertainties (discussed below) by reducing the uncertainty on the calibration point(s). In the single-standard case, the position of the final calibration point is taken as the absolute [Ti] of the standard and the reciprocal of the median SiO/^{49}Ti ratio, used to constrain a calibration line with zero intercept. The [Ti] of the unknowns is calculated according to *Equation 4.4*, in which C_u and C_s are the [Ti] in the unknown and the standard, and R_u and $\overline{R}_s$ are respectively the measured SiO/^{49}Ti ratio in the unknown and the median of the measured SiO/^{49}Ti ratios in the standard. Final temperature estimates were calculated according to *Equation 4.2* (after Watson and Harrison, 2005; Watson et al., 2006).

$$[Ti]_{unk} = \left(\frac{SiO}{^{49}Ti}\right)^{-1}_{unk} \times \frac{[Ti]_{std}}{\left(\frac{\overline{SiO}}{^{49}Ti}\right)^{-1}_{std}} \quad \text{or simplified...} \quad C_u = R_u^{-1} \cdot C_s \cdot \overline{R}_s \qquad (4.4)$$

Measurement uncertainties on the [Ti] and temperature estimates using a point and zero intercept calibration were calculated by propagating the uncertainty derived from counting statistics, calibration uncertainty, uncertainty on the absolute [Ti] of the standard, and uncertainty on the thermometer calibration. The final uncertainty is presented in both *absolute* and *relative* terms, in which the relative uncertainty is derived exclusively from the relative analytical uncertainty on the SIMS [Ti] measurements, and the absolute uncertainty contains all of the above

components. Under normal analytical conditions the principal components of uncertainty are expected to be independent, indicating that an analytical expression for the uncertainty on the unknown [Ti] can be derived by multiplying the partial derivatives with respect to each term in *Equation 4.4* by the uncertainty on each term, and summing the results in quadrature. This expression is given as *Equation 4.5*, in which δX represents the absolute uncertainty on the term X, and $\frac{\partial C_u}{\partial X}$ is the partial derivative with respect to that term, keeping all other terms constant. The relative uncertainty in the unknown [Ti] requires only the first and second square-bracketed terms, which are respectively the uncertainty derived from counting statistics and calibration uncertainty. The absolute uncertainty also requires the third square-bracketed term, which is the component derived from uncertainty on the absolute [Ti] of the standard. Note that δR_u is taken as twice the standard error based on counting statistics, $\delta\overline{R}_s$ is taken as the 2σ uncertainty at the calibration point for all $C_u \leqslant C_s$, and is scaled accordingly otherwise. δC_s is taken as the two sigma uncertainty derived from some other analytical procedure.

$$\delta C_u = \sqrt{\left[\delta R_u \cdot \left(\frac{\partial C_u}{\partial R_u}\bigg|_{\overline{R}_s, C_s}\right)\right]^2 + \left[\delta\overline{R}_s \cdot \left(\frac{\partial C_u}{\partial \overline{R}_s}\bigg|_{R_u, C_s}\right)\right]^2 + \left[\delta C_s \cdot \left(\frac{\partial C_u}{\partial C_s}\bigg|_{R_u, \overline{R}_s}\right)\right]^2} \tag{4.5}$$

where

$$\frac{\partial C_u}{\partial R_u} = -R_u^{-2} \cdot C_s \cdot \overline{R}_s \quad \text{and} \quad \frac{\partial C_u}{\partial \overline{R}_s} = R_u^{-1} \cdot C_s \quad \text{and} \quad \frac{\partial C_u}{\partial C_s} = R_u^{-1} \cdot \overline{R}_s$$

$$\delta R_u = 2\sigma_{R_u} \quad \text{and} \quad \delta\overline{R}_s = \begin{cases} 2\sigma_{\overline{R}_s} \cdot R_s^{-1} \cdot R_u & : \quad C_u \leqslant C_s \\ 2\sigma_{\overline{R}_s} \cdot R_s^{-1} \cdot C_s^{-1} \cdot C_u \cdot R_u & : \quad C_u > C_s \end{cases} \quad \text{and} \quad \delta C_s = N$$

Cross-calibration against NIST glass was obtained by measuring three NIST glasses (610, 612 and 615) and three zircon reference materials multiple times during a single analytical session, cross-calibrating the absolute [Ti] of zircon standard

spots against independent measurements using LA-ICPMS. Raw data, internal consistency and machine drift were evaluated and corrected using a similar procedure to that described for the single-standard case. Linear regressions were performed to both standard sets using the routine *xyefit* (Press et al., 1992) and the resultant equations combined, such that the expected reciprocal $SiO/^{49}Ti$ ratio in zircon can be expressed as a function of that measured in NIST glass according to *Equation 4.6*, in which R_g is the measured $SiO/^{49}Ti$ in NIST glass, and a_z, b_z and a_g, b_g are respectively the intercept and slope terms for the zircon and glass standard sets. Note that the goodness-of-fit parameters for both regressions are typically >0.999. However, the absolute values of the a and b parameters are likely to be machine specific.

$$R_s^{-1} = a_z + \frac{b_z \cdot R_g^{-1} - b_z \cdot a_g}{b_g} \quad \text{where} \tag{4.6}$$

$$a_z = -6.63 \times 10^{-6} \pm 1.35 \times 10^{-5} \quad \text{and} \quad b_z = 2.37 \times 10^{-5} \pm 1.65 \times 10^{-6}$$

$$a_g = -5.97 \times 10^{-6} \pm 1.15 \times 10^{-6} \quad \text{and} \quad b_g = 9.97 \times 10^{-6} \pm 1.01 \times 10^{-7} \tag{4.7}$$

Accordingly, unknown zircons can be analysed against at least two NIST glasses, and the unknown [Ti] calculated relative to a linear regression to the cross-calibrated standard measurements (*Equation 4.8*).

$$C_u = \frac{R_u^{-1} - a_s}{b_s} \tag{4.8}$$

Uncertainty in the calculated [Ti] using a linear cross-calibration with NIST glass may be expressed in a similar way to that described above for a point and zero-intercept calibration. Uncertainty in the cross-calibration is calculated by multiplying the uncertainty on each term in *Equation 4.6* by the partial derivative with

respect to each term and summing the results in quadrature (*Equation 4.9*).

$$\delta R_s^{-1} = \sqrt{\begin{array}{l}\left[\delta a_z \cdot \left(\left.\frac{\partial R_s^{-1}}{\partial a_z}\right|_{b_z,R_g,a_g,b_g}\right)\right]^2 + \left[\delta b_z \cdot \left(\left.\frac{\partial R_s^{-1}}{\partial b_z}\right|_{a_z,R_g,a_g,b_g}\right)\right]^2 \\ + \left[\delta R_g \cdot \left(\left.\frac{\partial R_s^{-1}}{\partial R_g}\right|_{a_z,b_z,a_g,b_g}\right)\right]^2 + \left[\delta a_g \cdot \left(\left.\frac{\partial R_s^{-1}}{\partial a_g}\right|_{a_z,b_z,R_g,b_g}\right)\right]^2 \\ + \left[\delta b_g \cdot \left(\left.\frac{\partial R_s^{-1}}{\partial b_g}\right|_{a_z,b_z,R_g,a_g}\right)\right]^2\end{array}} \tag{4.9}$$

where

$$\frac{\partial R_s^{-1}}{\partial a_z} = 1 \quad \text{and} \quad \frac{\partial R_s^{-1}}{\partial b_z} = \frac{R_g^{-1} - a_g}{b_g} \quad \text{and} \quad \frac{\partial R_s^{-1}}{\partial R_g} = \frac{-b_z \cdot R_g^{-2}}{b_g}$$

$$\frac{\partial R_s^{-1}}{\partial a_g} = \frac{-b_z}{b_g} \quad \text{and} \quad \frac{\partial R_s^{-1}}{\partial b_g} = -b_g^{-2} \cdot \left(b_z \cdot R_g^{-1} - b_z \cdot a_g\right) \quad \text{and} \quad \delta R_g = 2\sigma_{R_g}$$

The cross-calibration uncertainty is propagated by including uncertainties calculated according to *Equation 4.9* as input parameters to the linear regression (also using *xyefit*) required to solve *Equation 4.8*. Accordingly, the final uncertainty on the calculated [Ti] is given by *Equation 4.10*. Note that under this scheme, correct incorporation of uncertainties on the absolute [Ti] of the reference materials is dependent on including the correct uncertainties on both axes for each linear regression. As such, fitting routines supplied with many popular spreadsheet packages are unsuitable. Furthermore, correct propagation of the cross-calibration uncertainty into the session calibration requires that the proper uncertainty on each standard analysis be calculated according to *Equation 4.9* prior to calculation of the session slope and intercept parameters required to solve *Equation 4.8*. Accordingly, the final absolute [Ti] uncertainty (*Equation 4.10*) will include components derived from uncertainty on the absolute $SiO/^{49}Ti$ ratio for each analysis, uncertainty on the absolute [Ti] of the reference materials, and uncertainty on the cross-calibration between zircon and

NIST, and the final session calibration. In cases where only the relative uncertainty is required, the routine *xyfit* (Press et al., 1992) may be substituted for *xyefit* and the uncertainties on the absolute [Ti] of the reference materials ignored.

$$\delta C_u = \sqrt{\left[\delta R_u \cdot \left(\frac{\partial C_u}{\partial R_u}\bigg|_{a_s,b_s}\right)\right]^2 + \left[\delta a_s \cdot \left(\frac{\partial C_u}{\partial a_s}\bigg|_{R_u,b_s}\right)\right]^2 \left[\delta b_s \cdot \left(\frac{\partial C_u}{\partial b_s}\bigg|_{a_s,R_u}\right)\right]^2} \tag{4.10}$$

where

$$\frac{\partial C_u}{\partial R_u} = \frac{-R_u^{-2}}{b_s} \quad \text{and} \quad \frac{\partial C_u}{\partial a_s} = \frac{-1}{b_s} \quad \text{and} \quad \frac{\partial C_u}{\partial b_s} = -b_s^{-2} \cdot \left(R_u^{-1} - a_s\right) \quad \text{and} \quad \delta R_u = 2\sigma_{R_u}$$

An analytical expression for the uncertainty in the temperature calibration (*Equation 4.2*) can be derived using a similar method to that described for *Equation 4.5*. This expression is given as *Equation 4.11*. The relative temperature uncertainty requires only the third square-bracketed term, which is the uncertainty on the [Ti] propagated from *Equation 4.5* or *Equation 4.10*. The absolute temperature uncertainties also require the first and second square-bracketed term, which express the uncertainty in the thermometer calibration as given by Watson and Harrison (2005). Note that all the uncertainty terms are calculated at two sigma, such that the final relative and absolute uncertainties on the [Ti] and temperature estimates are also two sigma.

$$\delta T = \sqrt{\left[\delta a \cdot \left(\frac{\partial T}{\partial a}\bigg|_{b,Ti}\right)\right]^2 + \left[\delta b \cdot \left(\frac{\partial T}{\partial b}\bigg|_{a,Ti}\right)\right]^2 + \left[\delta Ti \cdot \left(\frac{\partial T}{\partial Ti}\bigg|_{a,b}\right)\right]^2} \tag{4.11}$$

where

$$\frac{\partial T}{\partial a} = \frac{-b}{(a - \log Ti)^2} \quad \text{and} \quad \frac{\partial T}{\partial b} = \frac{1}{a - \log Ti} \quad \text{and} \quad \frac{\partial T}{\partial Ti} = \frac{b}{Ti \cdot (a - \log Ti)^2}$$

According to the scheme outlined above, the form of the uncertainty envelope as shown in *Figure 4.11* is both non-linear, and unique to each analytical session.

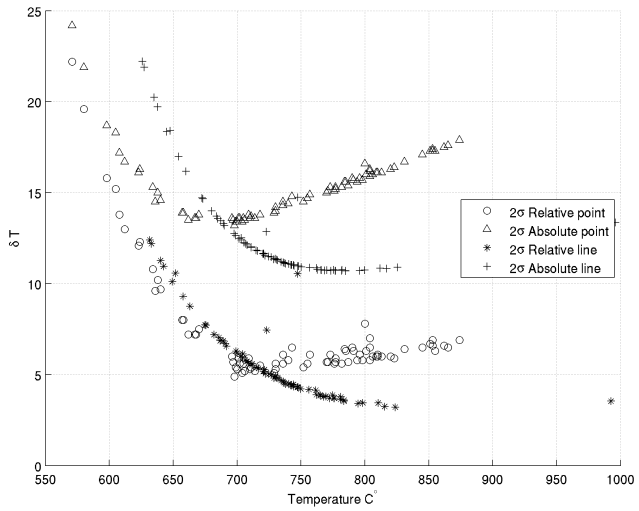

(a) Form of the uncertainty envelopes

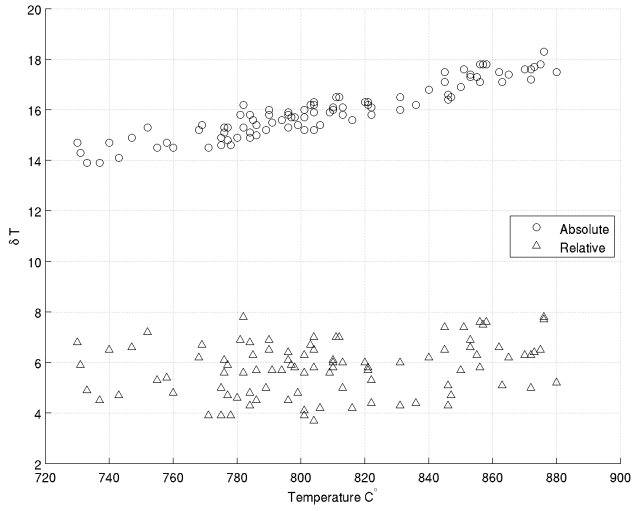

(b) Reproducibility of the calculated uncertainty

Figure 4.11: (a) Form of the relative and absolute temperature uncertainty envelopes using point and zero intercept, and line cross calibrations. (b) Reproducibility of the calculated uncertainty on analysis of FC1 over multiple analytical sessions using a point and zero intercept calibration. Note the minimum relative (spot-to-spot) uncertainty on all data is in the order of ±5°C.

The sensitivity of the S2MC is such that over the range for which the thermometer has been calibrated, analytical uncertainty derived from counting statistics has little effect on the overall shape of the uncertainty envelope except at very low [Ti]. The thermometer calibration uncertainty (Watson and Harrison, 2005), while contributing significantly to the overall uncertainty in T, is systematic and will be the same across multiple analytical sessions. The largest source of uncertainty controlling the overall shape of the uncertainty envelope for both the point and line calibration methods is uncertainty in the [Ti] calibration, derived both from uncertainty in the absolute [Ti] and variability of the measured $SiO/^{49}Ti$ ratio in the reference material(s). For the point and zero intercept calibration method, tests have shown that SL13 is relatively homogeneous with respect to Ti, and can be measured with reproducibility comparable to analytical precision ($<0.5\%$ 1σ) over the course of an analytical session. Reproducibility of the $SiO/^{49}Ti$ ratio however can be strongly affected by poor surface conductivity and contamination, and best results are obtained by ensuring the standard is well prepared and allowing adequate rastering time at the start of each analysis. The largest source of of uncertainty using the line cross-calibration method is derived from variability in the absolute [Ti] and measured $SiO/^{49}Ti$ in the natural zircon reference materials at higher [Ti]. Significantly improved precision may be achieved through further development of natural zircon reference materials at higher [Ti], with homogeneity comparable to that observed in SL13.

A potential work-around catering for scatter in reference materials at higher [Ti] involves artificially perturbing the inferred standard [Ti] within the expected range, based on measured dispersion in the $(SiO/^{49}Ti)^{-1}$ ratio. This approach has the potential to improve calibration precision without the requirement for individual standard spot [Ti] measurements, however robust implementation requires extensive

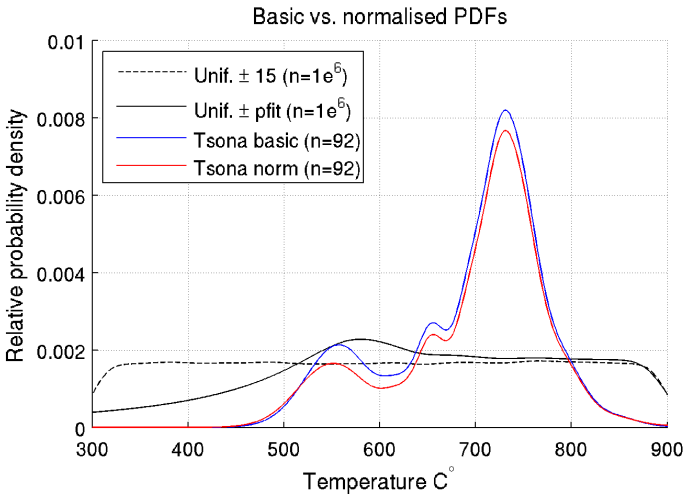

Figure 4.12: Plot showing the effect of non-linearity in the uncertainty envelope on the form of the Probability Density Functions (PDF) calculated according to *Equation 4.12*. Dashed black line shows PDF calculated from very large uniform random distribution with uniform measurement uncertainty (15°C). Solid black line shows PDF calculated from the same distribution to which a non-linear uncertainty envelope of the form shown in *Figure 4.11* has been applied. Blue and red solid lines are respectively the PDF calculated using data from the Tsona Leucogranites, and the same PDF normalised to that shown by the solid black line, such that the effects of non-linearity in the uncertainty envelope are removed.

analytical testing and rigorous data processing to ensure that the absolute accuracy of the measurements are not compromised. For the purposes of this study, the [Ti] of the majority of unknown zircons falls within a factor of 2-3 of SL13, therefore a simple single point and zero intercept calibration was chosen for most analyses.

A note on data presentation:

Following the example of Watson and Harrison (2005), the convention adopted for the presentation of zircon thermometry data has been to display crystallization temperature estimates as a histogram (*e.g.* Watson et al., 2006; Watson and Harrison, 2006; Valley et al., 2006). Unfortunately, however, this approach limits the resolu-

tion of the data to the width of the bins and ignores the measurement uncertainties. Improved data presentation is sought by calculating a probability density function (PDF), similar to that which is commonly used for detrital zircon age-probability spectra.

$$f_p = \sum_{i=1}^{n} \frac{1}{\sigma_i \sqrt{2\pi}} \exp\left\{ \frac{-(p - A_i)^2}{2\sigma_i^2} \right\} \cdot n^{-1} \tag{4.12}$$

In this study, the form of PDF curves is calculated according to *Equation 4.12* (modified from Sambridge and Compston, 1994), in which A and σ are vectors, respectively of observations and their associated measurement uncertainties, and f is the probability density at the position p (typically evaluated over the range of the data) based on those measurements. A potential caveat to this technique is that given the form of the measurement uncertainty envelope is non-linear with an intermediary minima, the PDF for an infinite uniform distribution subject to the same uncertainty envelop is also expected to be non-linear. This feature may potentially lead to bias in certain visual representations of the data. Tests have shown that under normal analytical conditions, the form of the absolute uncertainty envelope calculated using a point and zero-intercept calibration may be adequately approximated by a 4^{th} order polynomial curve-fitting routine. Accordingly, the PDF calculated from our data may be normalised to that calculated from a very large uniform distribution to which the same uncertainty envelop has been applied by way of a polynomial approximation, thereby removing the effect of the non-linearity in the uncertainty envelope. A comparison between regular and normalised PDFs calculated for 92 data from the Tsona granites (*Figure 4.12*) shows that while the temperature probability below 650°C in the regular PDF is marginally over estimated, the effect is not sufficient to change the overall appearance of the curve. Therefore, for the remainder of this study temperature probability curves are presented without normalisation, and the reader is simply cautioned that where a large number of data fall below 650°C, the relative probability in this region may be slightly over-estimated.

4.4.3 Results

Approximately 400 analyses of [Ti] from 18 samples yielded a broad spectrum of apparent crystallisation temperatures ranging from *ca.* 500-900°C, the results are tabulated in *Appendix .1.* Analysis spot locations were chosen to correlate with the results of U-Pb dating, with particular emphasis on grains yielding Himalayan crystallisation ages. Temperature probability density functions (PDF) calculated according to *Equation 4.12* indicate that the peak probability for data from all four sample suites falls between 700° and 750°C (*Figure 4.13(a)*), which may be a reasonable average value for crustal rocks. However, PDFs calculated only from the Himalayan zircon populations (<65 Ma, *Figure 4.13(b)*) display notably different characteristics among the four sample suites. The Arunachal and Tsona Leucogranites show offset peaks at *ca.* 660°C and 730°C respectively, although the Arunachal peak has a small shoulder on the high-temperature side that coincides with the primary peak in the Tsona samples. Both suites also show lower temperatures trailing off to below 600°C. Separated by individual rock sample, the position of the dominant temperature peak in the Arunachal Leucogranites (*Figure 4.13(c)*) increases from *ca.* 640°C to *ca.* 700°C proportional to increasing structural height (*Figure 4.1*) for samples 0602008, 0602009 and 0602010, although all three curves show smaller peak shoulders at *ca.* 750°C. Sample 2004T263 of the Tsona Leucogranites shows a single dominant peak centred at *ca.* 750°C, whereas sample 2004T264 shows smaller peaks at *ca.* 750°C and *ca.* 550°C respectively (*Figure 4.13(d)*). Sample 2004T265 shows a broad distribution ranging from *ca.* 800 to 550°C. The Dala Granitoids show a strongly asymmetrical distribution that is skewed to higher temperatures, rising rapidly from 900° to a peak at *ca.* 800°C, before declining gradually to below 600°C (*Figure 4.13(b)*). All Himalayan zircons analysed from the Yala-Xiangbo Granitoids yielded relatively low crystallisation temperature estimates forming a broad peak centred at *ca.* 550°C (*Figure 4.13(b)*). These data were, however, derived exclu-

sively from analyses of grains from sample 0310038, which show a transitional CL pattern (*Figure 4.3*). The width of the YX_G peak is significantly enhanced by the large uncertainties on analyses of these low [Ti] grains.

The apparent temperature probability distribution calculated from a combined subset (> 65 Ma) representing the pre-Himalayan populations from all sample suites (*Figure 4.13(e)*) yields a broad peak centred close to 700°C. This distribution reflects integrated sampling of a range of inherited and detrital sources spanning >2 Ga, and arguably represents a proxy for the approximate Ti-temperature distribution that would be expected from average continental crust. *Figure 4.13(f)* also shows individual PDFs calculated for three samples of the Arunachal Crystalline sequence and the combined PDF for 6 samples of high-grade pelites outcropping in the core of the Yala-Xiangbo Dome. The probability distributions for the Yala-Xiangbo pelites, Arunachal GHC (0602005) and Zhimithang Gneiss (0602012) are broadly comparable to that derived from inherited grains in the magmatic samples. However, the distribution shown by sample 0602011 (Arunachal meta Ksp-granite) forms a notably tighter peak centred at 710°C.

4.5 Discussion

Ion microprobe U-Pb dating of zircons from granitoid and crystalline samples collected at variety of structural positions within the eastern Himalaya, yielded a broad spectrum of ages ranging from Phanerozoic to Precambrian. The distribution of ages from detrital and inherited grains broadly supports the lateral continuity of major lithotectonic units along the length of the Himalayan Arc, as inferred from regional mapping studies (Gansser, 1964; LeFort, 1975, 1996; Yin and Harrison, 2000; Yin, 2006). However, several important differences were also observed that may impact upon existing and new evolutionary models when applied to the eastern Himalaya.

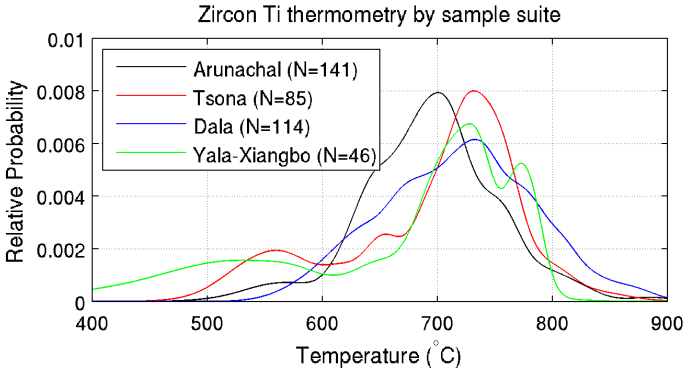

(a) All analyses

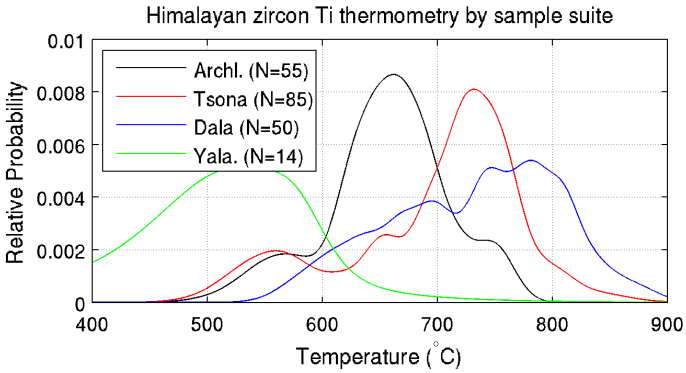

(b) Himalayan granitoid zircons

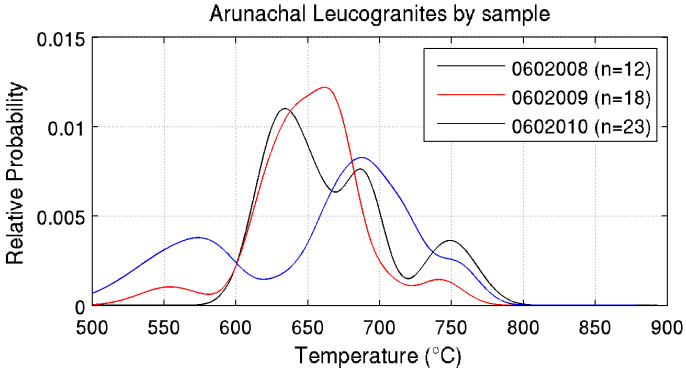

(c) Arunachal Leucogranites

Figure 4.13: Temperature probability plots for all sample suites. Analyses defined as Himalayan comprise those for which the corresponding U-Pb age <65 Ma was measured. Pre-Himalayan analyses comprise those for which the corresponding U-Pb age is >65 Ma. Data are plotted by individual rock sample, excluding subfigure (e). *Continues on next page...*

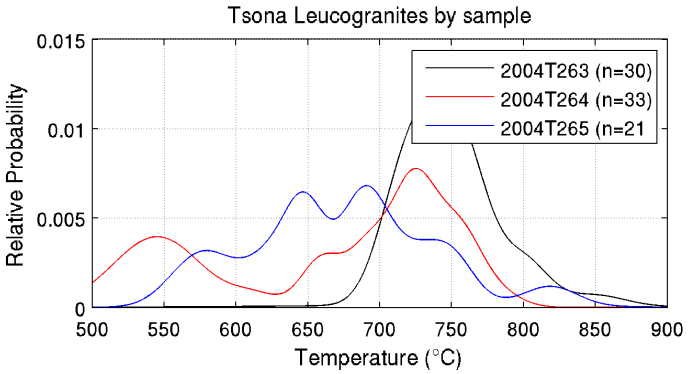

(d) Tsona Leucogranites

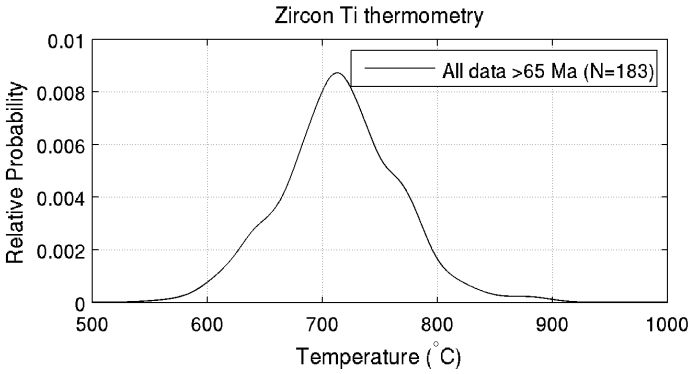

(e) All pre-Himalayan data

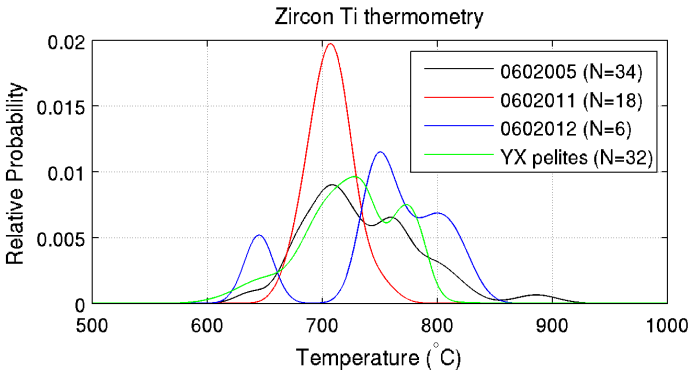

(f) Yala-Xiangbo pelites

Figure 4.13: *Continued...*

4.5.1 Himalayan granitoids

Zircons from the Arunachal and Tsona Leucogranites (AL, TL) and Dala and Yala-Xiangbo Granitoids (DG, YX_G) all yielded age populations <65 Ma, which are primarily derived from analyses of the rim domains. These populations are interpreted to date crystallisation, indicating that all four suites are attributable to granitic magmatism associated with the Himalayan episode. The AL yielded a single Himalayan population, with ages ranging from *ca.* 16-24 Ma. The TL also yielded a single, but slightly narrower spread ranging from *ca.* 16-21 Ma. The best estimate for the timing of crystallisation of these bodies is taken as the median and standard error of these data, indicating that both crystallised within error of 19 Ma (20.2±2.0 Ma for the AL, and 18.8±1.2 Ma for the TL). The DG yielded a single Himalayan population with ages ranging from *ca.* 43-49 Ma. The best estimate for the timing of crystallisation of these bodies is also taken as the median and standard error of these data, 44.1±1.2 Ma. The YX_G yielded a more complex distribution. The majority of the data comprise a broad Eocene peak, centred at *ca.* 42 Ma. However, grains showing anomalous CL patterns (see above) yielded Oligo-Miocene ages, closer to *ca.* 20 Ma. A similar modality is also observed in Th-Pb monazite data, with peaks at *ca.* 18 and *ca.* 40 Ma respectively. The implications of these results are further discussed below.

The TL and DG are emplaced into rocks that have not experienced upper-amphibolite grade metamorphism (*Chapter 3*), hence their crystallisation ages are inferred to approximate the timing of their emplacement. The AL however, outcrop within the Arunachal Crystalline sequences, whose along-strike equivalents are thought to have experienced upper amphibolite grade metamorphism during the Neohimalayan episode (LeFort, 1996). Therefore, the timing of emplacement of

these bodies cannot be automatically equated with their crystallisation age, although geochemical data presented in *Chapter 5* argue that this represents the most likely hypothesis. Similarly, the Yala-Xiangbo Granitoids outcrop within pelitic sequences that are known to have experienced amphibolite grade metamorphism at temperatures in excess of 600°C (*Chapter 3*, unpublished data). Moreover, migmatites are present in the core of the structure (*Chapter 3*), indicating that these bodies could reflect proximal melting of the surrounding metasediments associated with high-grade metamorphism.

The bimodal distribution of monazite ages observed in the Yala-Xiangbo pelitic sequences (sample 0310015) is interpreted to reflect two phases of Himalayan amphibolite grade metamorphism in the Tethyan Himalaya (respectively mid-Eocene and early-Miocene), broadly co-incident with the Eohimalayan and Neohimalayan metamorphic episodes that have been widely documented elsewhere in the Himalaya (*e.g.* LeFort, 1996). In the Yala-Xiangbo Granitoids, the earlier event is associated with crystallisation of monazite, and zircons showing concentric or oscillatory CL zoning patterns that are characteristic of growth in a magmatic environment. These grains are interpreted as providing the best constraint on the magmatic age of these bodies. Younger Miocene ages from anomalous zircons are interpreted to reflect recrystallisation, possibly in the presence of a fluid phase (accounting for their spongy, porous texture), associated with Neohimalayan metamorphism. This interpretation is consistent with the absence of Eocene monazites in samples yielding only Miocene zircon ages, as monazite is generally more soluble than zircon in aqueous fluids (Ayers and Watson, 1991). It is also in good agreement with the work of Batt et al. (1999), who attributed similar looking zircons from pegmatites in the Southern Alps of New Zealand to fluid mitigated recrystallisation. Therefore, although limited Miocene magmatism in the Yala-Xiangbo igneous complex cannot

be excluded, the most robust estimate for the crystallisation age of the majority of the Yala-Xiangbo Granitoids taken as the median and standard error of the larger Eocene peak, 42.3±4.9 Ma.

The spread of Himalayan magmatic ages recorded by both the AL and the YX_G is greater than that which would be expected for simple emplacement and cooling of a moderate sized body at shallow crustal levels. A component of this spread may be attributable to amalgamation of samples from adjacent bodies and spurious noise in the age analyses, however, the width of these peaks likely also reflects protracted zircon growth of these near-minimum-melt magmas in an actively deforming syn-metamorphic terrane. The width of the DG peak may also be marginally amplified through amalgamation samples from adjacent bodies with slightly varying emplacement ages, although some older grains are likely attributable to ongoing crystallisation during magma ascent and/or mid-crustal residence.

The timing of emplacement of the Arunachal and Tsona Leucogranites is consistent with the range of ages documented from the central Himalayan HHL (Schärer, 1984; Schärer et al., 1986; Deniel et al., 1987; Copeland et al., 1990; Edwards and Harrison, 1997), broadly supporting the extrapolation of current paradigms for Miocene peraluminous magmatism in the frontal Himalaya to lateral portions of the Himalayan Arc. Relatively few comparative data exist from the North Himalayan Granites. Although most bodies fall in the range 10 to 17 Ma, an older age of 27 Ma has been determined (Zhang et al., 2004b,a). Data from the Yala-Xiangbo Granitoids further extend this range to *ca.* 42 Ma, indicating that peraluminous magmatism in the North Himalaya began barely 20 Ma after the initiation of collision, and continued sporadically for at least half the history of Himalayan orogenesis.

Emplacement of the Dala Granitoids at *ca.* 44 Ma also falls significantly outside the scope of current paradigms for intra-Himalayan granitic magmatism. These bodies provide, to our knowledge, the first evidence of Eohimalayan granitoid plutonism so far documented anywhere along the main Himalayan arc, and place valuable constraint on the on the timing of deformation of the structurally highest and inferred earliest accreted units of the Himalayan Fold and Thrust Belt (*Chapter 3*). The correlation between emplacement of the DG and formation of the Yala-Xiangbo Granitoids, strongly suggests that both are associated with a regional tectonothermal event common at least to the eastern THS, and potentially to the Tethyan Himalaya as a whole.

4.5.2 Other lithologies

The distribution of zircon U-Pb ages derived from the two structurally higher pelitic samples outcropping within the Yala-Xiangbo Dome (0310015, 0310029, *Figure 4.1*) is similar to that observed in the surrounding low-grade Triassic metasediments of the Tethyan Himalayan Sequences (*Chapter 2*). Whereas the youngest ages from those at deeper structural levels (0310034, 0310039; *Figure 4.1*) are Ordovician. Although not an exhaustive study, this result appears to support the preservation of Paleozoic sequences in the core of this structure, as has been inferred from paleontological evidence (*Chapter 3*). The form of the age-probability spectra are, however, somewhat dissimilar both to that which is considered characteristic of the GHC sequences elsewhere in the Himalaya (*e.g.* Gehrels et al., 2003) and to samples of the Arunachal Crystalline sequence (discussed below). These results suggest that the high-grade units in the core of the dome represent structurally deeper equivalents of the surrounding Triassic THS metasediments subject to Eohimalayan and Neohimalayan amphibolite grade metamorphism.

The distribution of ages in the three Arunachal Crystalline samples appears to differ from that considered characteristic of units outcropping at similar structural positions elsewhere in the Himalaya. Pelitic sample 0602005 from the base of the Arunachal Crystalline sequence yielded ages that, although plausibly comparable to pre-Ordovician strata of central Nepal (*e.g.* Gehrels et al., 2003), do not appear characteristic of the GHC sequences elsewhere in the Himalaya, in terms of both range and distribution of ages. Moreover, granitic samples 0602011 and 0602012 both yielded ages close to 800 Ma (*Figure 4.6*). Although *ca.* 800 Ma granitoids have been documented in the MCT hanging wall elsewhere along the Himalayan Arc (*e.g.* 823±5 Ma Chor Granite; Singh, 2003), these bodies are not generally considered characteristic of the GHC proper (LeFort, 1996; Yin and Harrison, 2000; Myrow et al., 2003; Gehrels et al., 2003). Yin (2007) have argued - on the basis of similar data - that parts of the Arunachal Crystalline sequences are correlative with Indian basement lithologies as exposed in the Shillong Plateau. Their interpretation implies that crustal shortening in the Arunachal Himalaya was dominated by thick-skinned deformation (*cf.* DeCelles et al., 2001a,b). The results of this study broadly support their conclusions.

4.5.3 Titanium thermometry

Titanium thermometry of Himalayan-age zircons from the Arunachal and Tsona Leucogranites (AL, TL) yielded offset overlapping apparent temperature peaks centred at *ca.* 660° and *ca.* 730°C respectively. The Dala Granitoids (DG) however, show a broader distribution that is significantly skewed to higher temperatures, rising rapidly from *ca.* 900°C to a peak at *ca.* 800°C, and then decreasing gradually to below 600°C. Apparent temperatures from the Yala-Xiangbo Granitoids (YX_G) comprise a broad peak centred below 600°C.

Equating apparent temperature estimates with true values requires constraints to be placed on the a_{SiO_2} and a_{TiO_2} during crystallisation. In rocks of average granodioritic or granitic composition (*e.g.* the Dala Granites), sub-unity a_{TiO_2} is expected to be broadly compensated by sub-unity a_{SiO_2}(Ferry and Watson, 2007). Thin-section optical petrography (transmitted and reflected) and examination of mineral separates indicate that ilmenite is the principal Ti-bearing phase in the Dala Granitoids, whereas all other granitic samples contain rutile. Ilmenite implies $a_{TiO_2} \approx 0.5$ whereas a_{SiO_2} for the Dala Granitoids is probably closer to 0.9 or unity (J. Hermann *pers. comm.*), hence the calculated apparent temperatures for these samples may still marginally underestimate the true values (by up to *ca.* 40°C). The presence of rutile in the remaining samples implies $a_{TiO_2} \approx 1$, such that the apparent temperatures are expected to approach their true values. This interpretation assumes that zircon co-crystallised with rutile/ilmenite throughout the magmatic episode, and neglects any kinetic effects associated with zircon-rutile/ilmenite equilibrium. The reader is also cautioned that these buffering assemblages pertain only to the most recent magmatic episode. The a_{TiO_2} and a_{SiO_2} of inherited and detrital grains are unconstrained, and hence an additional uncertainty of up to *ca.* 60°C must be applied to these data.

It is generally agreed that the High Himalayan Leucogranites (HHL) formed through crustal anatexis in association with Neohimalayan metamorphism (LeFort et al., 1987; Harris and Inger, 1992; Inger and Harris, 1993; Harris and Massey, 1994; Harrison et al., 1997a, 1998a). Extending these interpretations to the eastern Himalaya, the temperature distribution shown by the Tsona Leucogranites is consistent with muscovite dehydration melting (*Chapter 5*) of pelitic lithologies, as has been proposed for other HHL in northern Nepal (*e.g.* Harris and Inger, 1992; Inger and Harris, 1993). The 660°C peak shown by the Arunachal Leucogranites,

however, is arguably better explained by "wet" melting, marking a significant deviation from existing paradigms (*Chapter 5*). Moreover, the respective positions of the dominant temperature peaks in samples 0602008 to 0602010 define an increasing trend proportional to increasing structural height, suggesting that the lowest temperatures of granite formation occurred at the base of the sequence (This point will be elaborated in *Chapter 5*). The higher temperature peak shoulders found in all AL samples could be interpreted to reflect a bimodal magma source. Several workers have suggested that the North Himalayan Granites may be attributable to mica dehydration melting (Harrison et al., 1997a, 1998a; Zhang et al., 2004a). Although the temperature distribution given by the Yala-Xiangbo Granitoids is arguably not robust (due to analysis of grains from a sample showing transitional/anomalous CL patterns), the available data are inconsistent with such processes, potentially providing further challenge to existing models. These arguments are further discussed in *Chapter 5*.

The form of the temperature distribution shown by the DG initially appears counter intuitive. Indeed some workers have remarked hypothetically on the types of distributions that would be expected from different lithologies (*e.g.* Valley et al., 2006). However, simple calculations have shown that the form of this distribution is in fact predicted by fractional crystallisation associated with monotonic cooling of a moderate sized pluton of broadly granitic composition (Harrison et al., 2007). The broad range of temperatures, however, may be attributable to secondary processes such as magma mixing, which are further discussed in *Chapter 5*.

4.5.4 Zircon petrogenesis

The opportunity to measure both age and crystallisation temperature at high resolution within individual zircon grains (see analytical method) has exciting implica-

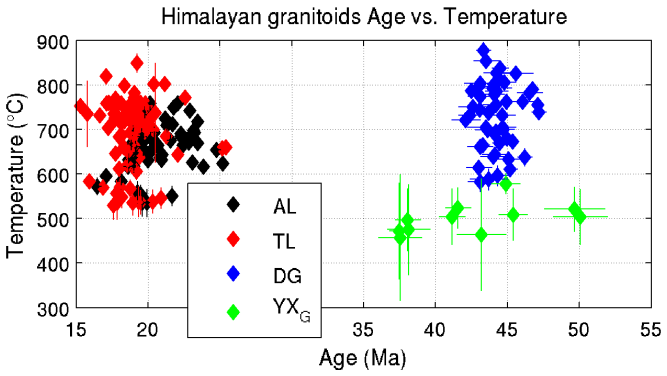

(a) Himalayan granitoids

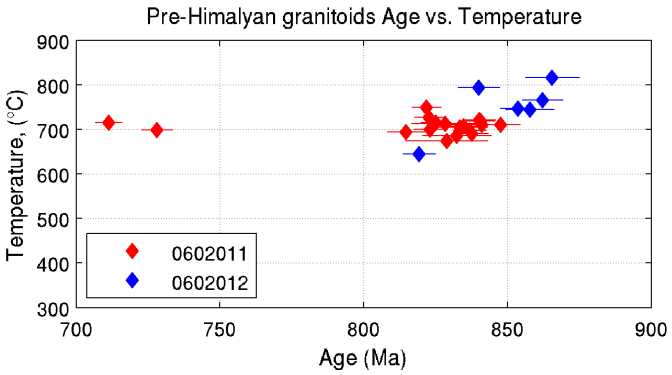

(b) Pre-Himalayan granitic rocks

Figure 4.14: Crystallisation age vs. crystallisation temperature for the Arunachal and Tsona Leucogranites (AL, TL), Dala Granitoids and Yala-Xiangbo granites (DG, YX_G). The two granitic samples from the Arunachal Crystalline sequence (0602011 and 0602012) are also shown. Note that strong correlations between age and temperature are not observed in any sample suite.

tions for understanding zircon petrogenesis in many environments. Strictly speaking, SIMS is a destructive technique and hence identical aliquots of material cannot be analysed in two separate analytical sessions. However, given that the volume of material removed by each analysis is extremely small (typically in the order of a few hundred cubic microns) and care was taken to avoid transitions between growth zones, careful correlation between the results of Ti-thermometry and conventional U-Pb ion microprobe dating is considered justifiable at the current resolution of both techniques.

Figure 4.14 shows crystallisation temperatures plotted against age for Himalayan analyses (<65 Ma) from the Arunachal and Tsona leucogranites, Dala and Yala-Xiangbo granitoids, and granitic samples from the Arunachal Crystalline sequence (Zhimithang Gneiss and meta Ksp-granite). Although the older AL grains appear to have crystallised at marginally higher temperatures, strong correlations between age and temperature are not observed in any sample suite.

Ti crystallisation temperature estimates from Himalayan (< 65 Ma) zircons were also compared to measurements of U+Th trace element content derived from U-Pb analyses (*Figure 4.15*). Neither the Tsona Leucogranites or the Dala Granitoids show a significant correlation between [U] and crystallisation temperature. The Arunachal Leucogranites, however, show a positive correlation that is statistically significant at the 5% level (based on a Spearman's rank correlation coefficient; Press et al., 1992, *Figure 4.15(a)*). All three sample suites also show significantly non-zero positive correlations between [Th] and temperature (*Figure 4.15(c)*, *Figure 4.15(d)*), and Th/U ratio and temperature (*Figure 4.15(e)*, *Figure 4.15(f)*) at the 5% and 1% levels respectively. Unfortunately, correlations between [U], [Th] or [U+Th] and age cannot be accurately assessed due to matrix effects associated with SIMS analysis

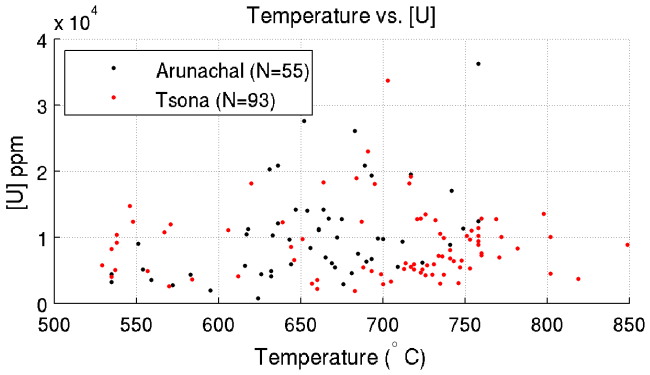

(a) Arunachal and Tsona Leucogranites

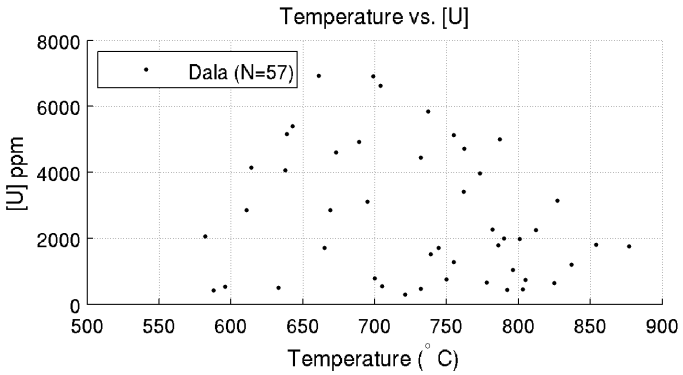

(b) Dala Granitoids

Figure 4.15: Graphs showing U+Th trace element content plotted against crystallisation temperature and age for the Arunachal, Tsona and Dala sample suites. Note that correlations between [Th] and temperature are much stronger than those involving [U].

Continues on next page...

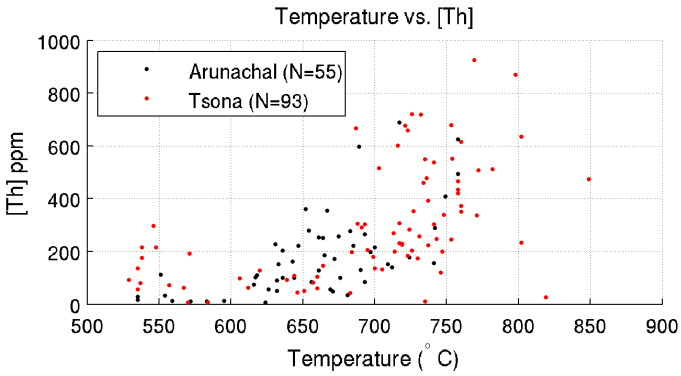

(c) Arunachal and Tsona Leucogranites

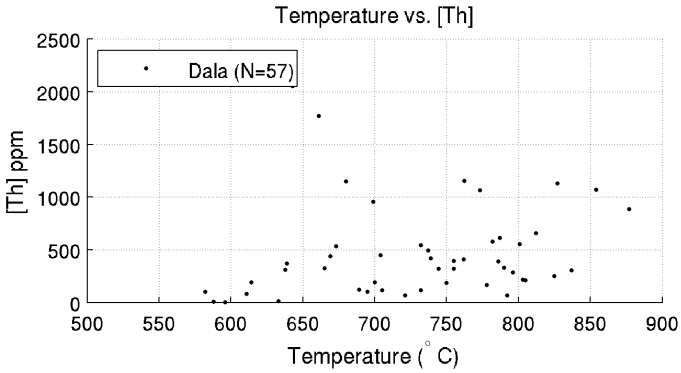

(d) Dala Granitoids

Figure 4.15: *Continued...*

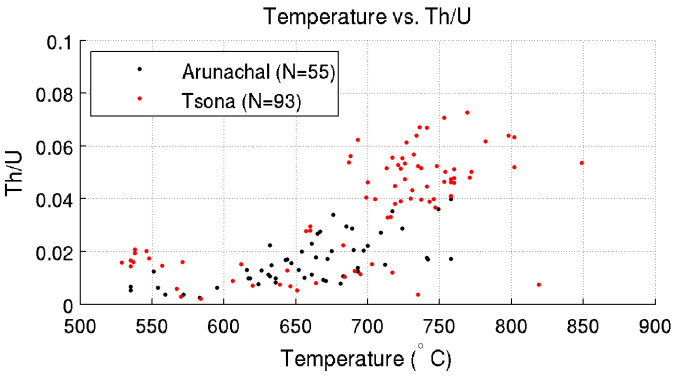

(e) Arunachal and Tsona Leucogranites

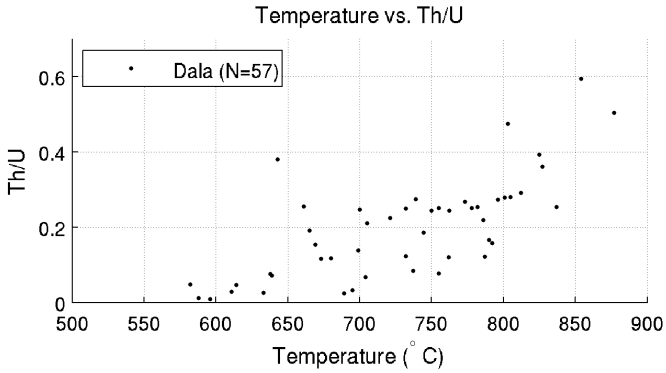

(f) Dala Granitoids

Figure 4.15: *Continued...*

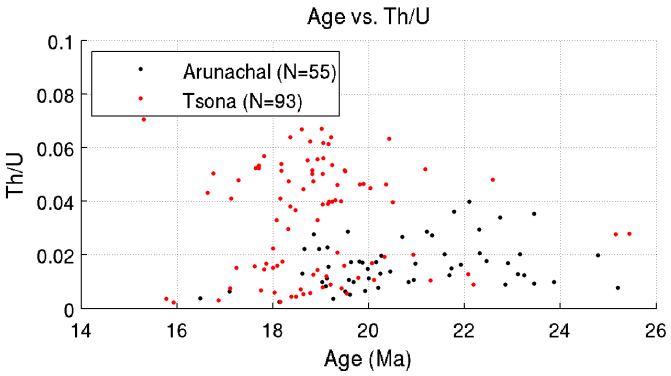

(g) Arunachal and Tsona Leucogranites

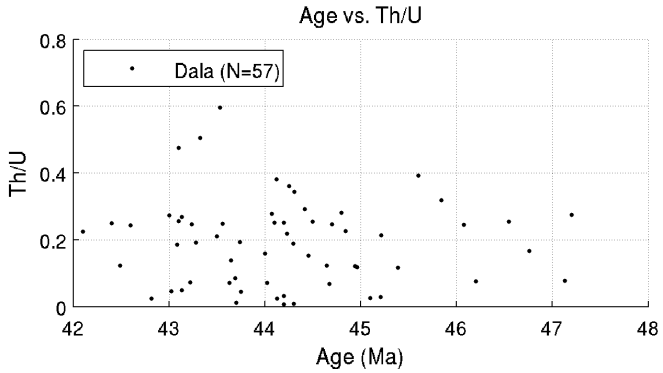

(h) Dala Granitoids

Figure 4.15: *Continued...*

(see discussion above). The Th/U ratio, however, may be marginally more reliable given that these two elements are geochemically similar and therefore any matrix effects are likely to be removed through normalisation. While the Tsona and Dala suites do not show any obvious correlation between Th/U ratio and crystallisation age, the Arunachal suite show a weak correlation (*Figure 4.15(g)*, *Figure 4.15(h)*) that is statistically significant at the 5% level. These trends provide valuable insight into the trace element systematics during zircon crystallisation. However, given that the relationships between temperature and time (age) are unclear, thorough interpretation requires more detailed constraints on the relative position of each datum in the overall zircon growth scheme. Such insight is gained by examining data collected along transects through individual zircon grains.

Most grains record a general core-to-rim decrease in temperature, age, U+Th content and Th/U ratio. However, the observed temperature and trace element trends are not necessarily either monotonic or smooth. Moreover, they appear to be directly correlative with style of CL zonation. The greatest uniformity in temperature and trace element systematics was observed in samples displaying near uniform appearance under both optical and electron imaging. *Figure 4.16* shows the results of three analyses at increasing radial distances on a representative grain from meta Ksp-granite 0602011 of the Arunachal Crystalline sequence. Excluding the bright metamorphic overgrowth, this grain appears virtually homogeneous under both optical and electron imaging. The U-Pb ages from all three analyses are mutually within error, as are the Th/U ratios. However, the grain records slightly decreasing temperature and U,Th content along its radius (progressive growth).

Oscillatory zoned zircons also showing a general core-to-rim decrease in crystallisation temperature and U+Th content, however they typically display large inter-

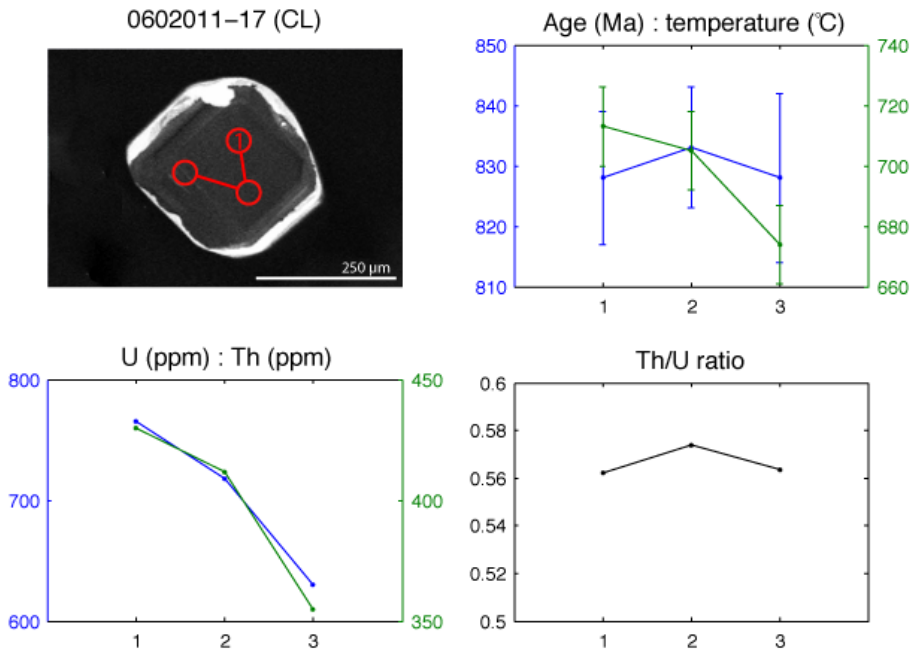

Figure 4.16: Core-to-rim ion microprobe transect showing trends in age, crystallisation temperature and trace element systematics for grain 0602011-17 from a meta Ksp-granite of the Arunachal Crystalline sequence. Note that analysis spots 1 to 3 are located at increasing radial distances from the core of the grain. Excluding the bright metamorphic overgrowth (which was avoided), all grains from this sample exhibit near identical characteristics under both optical and electron imaging. The three apparent ages are mutually within error, and the Th/U ratio is relatively constant. However, there is a notable core-to-rim decrease in both crystallisation temperature and U+Th content.

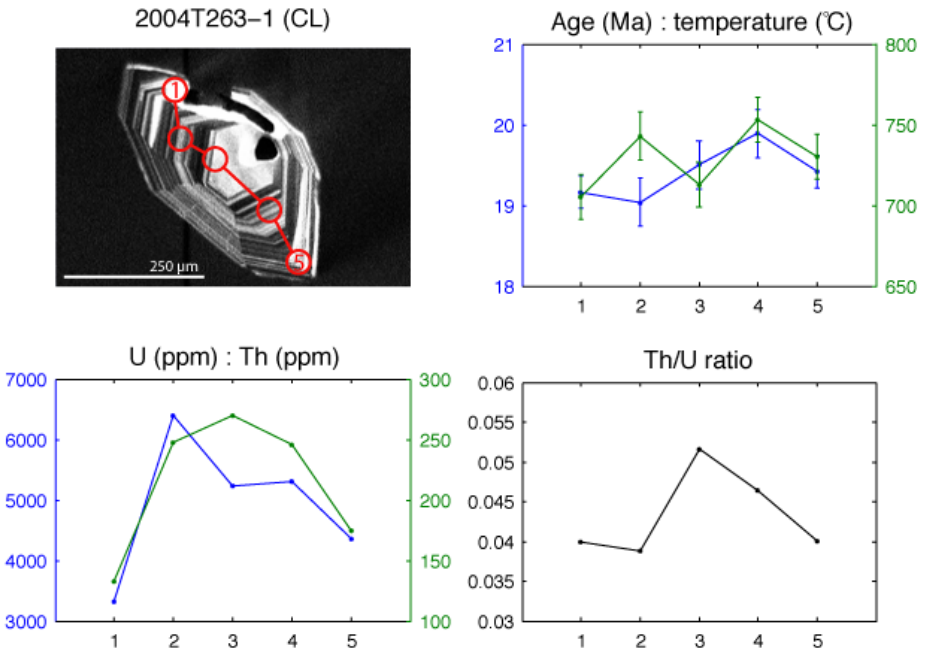

Figure 4.17: Core-to-rim ion microprobe transect showing trends in age, crystallisation temperature and trace element systematics for grain 2004T263-1 from the Tsona Leucogranites. This grain shows a general core-to-rim decrease in age, temperature and trace element systematics. However it also shows characteristics common to other concentrically zoned grains. Analysis spots 1 to 5 are each located on different CL zones. The data show significant excursions in terms of temperature and trace element characteristics between different CL zones.

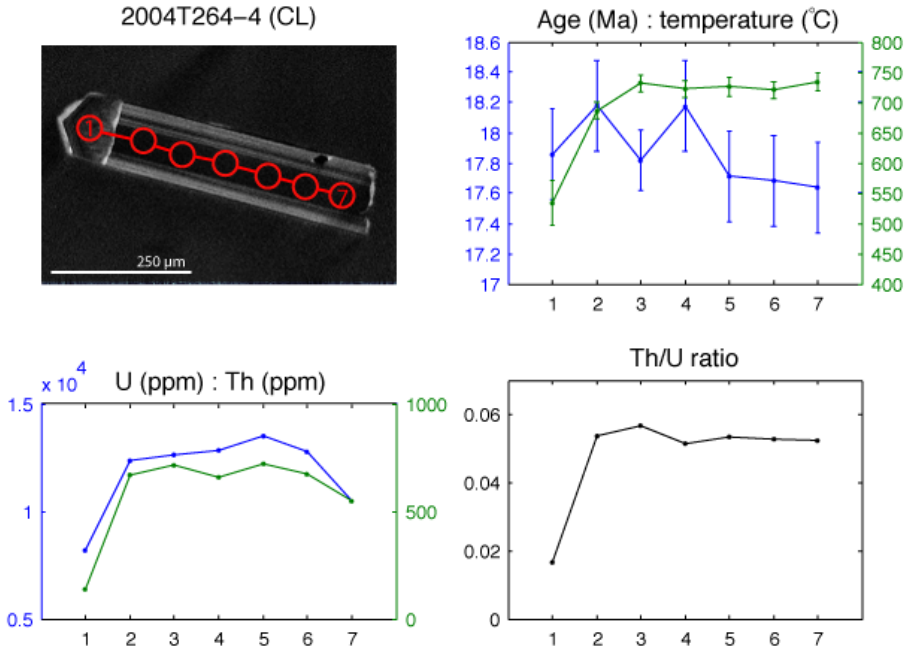

Figure 4.18: Core-to-rim ion microprobe transect showing trends in age, crystallisation temperature and trace element systematics for grain 2004T264-4 from the Tsona Leucogranites. Analysis spots 2 to 7 are located on the same CL zone and show comparable crystallisation temperatures and trace element systematics (note that age fluctuations are likely attributable to matrix effects associated with high U+Th content, see above). Analysis spot 1 is located on the grain tip, which shows notably different CL characteristics. This datum yielded lower a lower temperature, lower U+Th content and lower Th/U ratio.

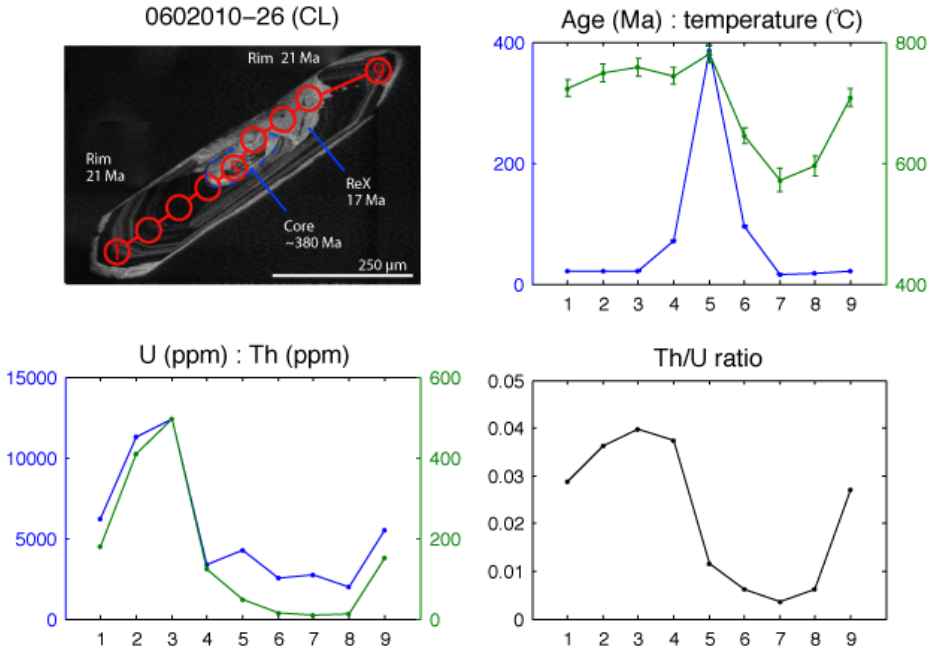

Figure 4.19: Core-to-rim ion microprobe transect showing trends in age, crystallisation temperature and trace element systematics for grain 0602010-26 from the Arunachal Leucogranites. This grain shows an inherited core overgrown by concentrically zoned magmatic rim. Part of the grain however, is characterised by a lighter grey anomalous area that clearly cross-cuts the concentric zonation. The concentrically zoned rim domain consistently shows ages the close to 21 Ma, and crystallisation temperatures of about 750°C, both decreasing slightly towards the outer margin of the grain. Th+U content and Th/U ratio are also relatively higher in the rim domains, decreasing with decreasing age and T. The age of the core domain is significantly older, consistent with its inferred origin via restitic inheritance. Analysis spots 6 to 8, however, which are located on the anomalous zone, yielded younger ages (*ca.* 17 Ma), lower temperatures, lower Th+U contents and lower Th/U ratios.

mediary excursions between CL zones, that in some cases exceed values recorded at the core. *Figure 4.17* shows one such grain from the Tsona Leucogranites. Analysis spots 1 to 5 comprise a lengthwise transect through grain 2004T263-1, respectively sampling across different CL zones. Unfortunately, the S2MC spatial resolution used for [Ti] measurements is not sufficient to sample CL zones individually, however it is clear that while analysis spots 1 and 5 close to the grain tips show generally lower temperatures, younger ages and lower Th+U contents and Th/U ratio than those near the grain core (3 and 4), there is significant variability across the CL zones. This pattern is interpreted to reflect thermal and/or compositional instability in the zircon's growth environment, possibly associated with convection and magma recharge.

Grains showing longitudinal CL zonation typically yield consistently reproducible crystallisation temperatures and U-Th systematics along the length of individual zones. *Figure 4.18* shows a series of 7 analyses from a longitudinally zoned zircon from the Tsona Leucogranites. Although the calculated U-Pb ages fluctuate within error (likely due to problems analysing high [U+Th] grains discussed above), crystallisation temperatures and trace element systematics between analyses 2 to 7 are remarkably consistent. Analysis 1 however, is located on what appears to be a sub-grain cross-cutting earlier CL zonation. This analysis yielded a notably lower temperature, lower U, Th contents and Th/U ratio. It is best interpreted in conjunction with another example grain from the Arunachal Leucogranites discussed below.

The grain shown in *Figure 4.19* conveniently provides relative spatial and textural context to many characteristics that were observed independently elsewhere. Optical and electron imaging show an inherited core overgrown by concentrically zoned rim, however some parts also display anomalous patchy CL patterns that

clearly cross-cut the concentric zonation. Nine analysis spots were chosen to provide a tip-to-tip lengthwise transect through all three CL domains. The core domain yielded an apparent age of *ca.* 400 Ma, confirming its inferred restitic origin. Analyses of the concentrically zoned rim domains consistently yielded ages close to 21 Ma, decreasing slightly towards the tips. Temperature estimates also decrease slightly towards the tips in this zone, as do U, Th contents and Th/U ratios, consistent with trends observed elsewhere. The areas of anomalous, patchy CL zonation, however, yielded notably younger ages (*ca.* 17 Ma), lower temperatures, and lower U, Th contents and Th/U ratios. Crystallisation temperatures from this zone fall below the "wet" granite solidus (*e.g.* Huang and Wyllie, 1986), which, combined with the style of CL zonation and younger ages, strongly suggests that these areas have been modified by secondary processes. They are interpreted to reflect late-stage recrystallisation, possibly associated with late- or post-magmatic fluids. Data derived from these areas comprise the low-temperature shoulders on both the Arunachal and Tsona Leucogranite temperature probability peaks. It is also noted that grains from sample 2004T265 - which yielded exceptionally broad age and temperature distributions - contain significantly more areas of patchy anomalous CL zonation than the other two Tsona Leucogranite samples, further supporting the assertion that secondary processes can alter the apparent ages and Ti-temperatures of magmatic zircons.

Collectively, the observed trends in age, crystallisation temperature, and trace element systematics can be interpreted in terms of changes in the zircon's growth environment. The absence of strong correlations between age and crystallisation temperature could reflect disequilibrium thermal conditions across the magma body (possibly associated with limited convection and magma recharge), however given the difficulties analysing high U+Th content grains, spurious noise in the age anal-

yses may present an equally viable explanation. Nevertheless, the observation that age and temperature generally decrease parallel to the growth vector inferred from CL zonation within individual zircon grains, provides strong evidence that the trends shown in *Figure 4.15* may be interpreted at the very least in terms of the zircon's formative environment, and likely in terms of the evolving magma body.

In granitoids, U and Th are primarily hosted in the accessory minerals zircon and monazite (Bea, 1996). The U and Th contents of these phases are determined by their respective melt-crystal partition coefficients and the availability of each element in the surrounding liquid during crystallisation. The latter, in turn, is a function of the initial melt concentration and the relative crystallisation rates of U and Th bearing and non-bearing phases, which respectively deplete and enrich the residual liquid in these elements. Zircon and monazite partition coefficients for U and Th are relatively high, and recent work has shown that, in the case of zircon at least, they also vary inversely with temperature (Rubatto and Hermann, 2007, and refs. therein). The apparent lack of strong correlations between zircon U content and temperature in most samples is therefore likely attributable to the local interplay of fractional crystallisation and temperature-dependant partitioning in the zircon's growth environment.

The partition coefficient for Th in monazite is significantly higher than that for zircon (Rubatto and Hermann, 2003), hence co-crystallisation with monazite will effectively starve both the melt and zircon of Th. The Arunachal and Tsona Leucogranites and Dala Granitoids contain zircon and monazite. Therefore, the observed correlations between zircon Th content and Th/U ratio with crystallisation temperature may be attributed to the decreasing availability of Th associated with ongoing co-crystallisation of monazite. Indeed further supporting evidence to this

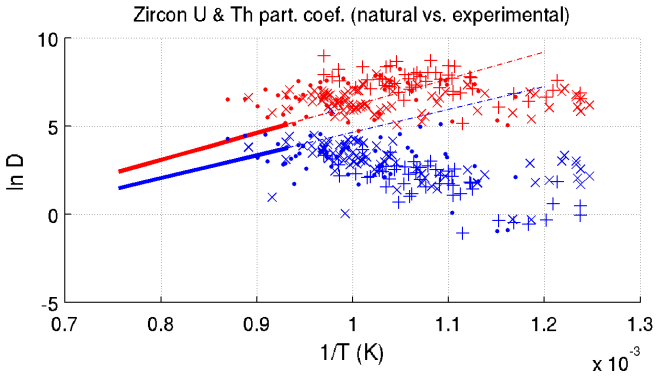

Figure 4.20: Partition coefficients for U and Th in zircon. Solid lines (red - U, blue - Th) represent robust fit to experimental data (Rubatto and Hermann, 2007), extrapolated to lower temperatures (dashed lines). Symbols show partition coefficients for individual analyses approximated using the U content derived from U-Pb dating and bulk rock U content from trace element geochemistry (*Chapter 5*) plotted against crystallisation temperature. Arunachal Leucogranites (+), Tsona Leucogranites (×) and Dala Granitoids (•).

notion is provided by apparent correlations between zircon Th/U ratio and age, both in the bulk data and within individual grains.

A first-order test to this hypothesis may be obtained by approximating the partition coefficients for each analysis using the local zircon U content derived from U-Pb dating and bulk rock U content from trace element geochemistry (*Chapter 5*). Although this approach is inherently inaccurate due to uncertainties in the melt U content at the time of crystallisation (see above), it can nevertheless provide broad comparison to experimentally derived results. Moreover, given that the zircon U contents in these samples are typically 1 to 4 orders of magnitude higher than those in the bulk rock, uncertainties in the melt concentration are unlikely to significantly effect the end result. *Figure 4.20* shows partition coefficients calculated for zircons from the Arunachal and Tsona Leucogranites and Dala Granites, plotted against temperature. The accompanying solid lines are robust regressions to experimentally

derived data (Rubatto and Hermann, 2007), which have been extrapolated to lower temperatures (dashed lines). Note that the majority of the results for U (red) are consistent with the experimental prediction. The smaller group of low temperature data which plot away from the experimental trend are primarily derived from zones of anomalous CL zonation, which have likely been modified by secondary processes (see above). Calculated Th (blue) partition coefficients match the experimental data reasonably well at high temperature, however they deviate down temperature, supporting the hypothesis that the Th contents of zircons are progressively influenced by secondary processes such as co-crystallisation with monazite.

Attempts were made to refine estimates both for the timing of crystallisation of individual samples and subsequent recrystallisation events, by way of the petrographic observations and trace element data described above. Although discernible age populations were found in some samples, exceptions were also observed (*e.g.* areas of apparent recrystallisation yielding ages comparable to the inferred magmatic population). It is not impossible that the lack of coherency in the age data reflects a geologic scenario in which the relative timing of individual magmatic and post-magmatic episodes is within the average uncertainty on individual datum. However, in cases where the relative timing of textural formation could be established within individual grains, age differences of up to *ca.* 4 Ma were locally observed (see above). Hence, it is considered more likely that the lack of coherency between similar textural zones across multiple grains, reflects analytical noise associated with matrix effects that could not be entirely removed by the first order correction described above. It is therefore concluded that differences in the relative timing of these events cannot be reliably distinguished at the resolution of the available data, although a gap of several Ma between magmatic and post magmatic episodes is plausible for most samples of the Arunachal and Tsona Leucogranites.

4.6 Conclusions

Geochronological studies of granitoids outcropping along a N-S oriented transect through the eastern Himalaya indicate that the spectrum of granitic magmatism in this region is notably more diverse than that which has been documented in other parts of the main Himalayan Arc. In the frontal Himalaya, the Arunachal and Tsona Leucogranites - emplaced respectively within the crystalline sequences of the Arunachal Himalaya in the hanging wall of the Main Central Thrust, and close to the South Tibetan Fault System - both crystallised within error of 19 Ma, in good agreement with similar studies of High Himalayan Leucogranites in Bhutan, Nepal, and northwest India. In the North Himalaya, peraluminous granitoids (the Yala-Xiangbo Granitoids) form an igneous complex within the core of the Yala-Xiangbo Dome. The emplacement style and structural position of these bodies is comparable to that documented in North Himalayan Granites along strike to the west. However, their crystallisation age (*ca.* 42 Ma) is notably older, marking a significant challenge to existing tectonic paradigms. Furthermore, in the central North Himalaya, the Dala Granitoids comprise a series of undeformed dykes and plutons forming an igneous complex emplaced into the deformed sub-greenschist facies Triassic metasediments of the Tethyan Himalaya. These bodies provide, to our knowledge, the first evidence of Eohimalayan plutonism so far documented anywhere along the main Himalayan arc. Their emplacement places valuable constraint on the timing of deformation in the structurally highest and inferred earliest accreted units of the Himalayan Fold and Thrust Belt, and impacts upon a variety of Himalayan evolutionary models.

Thermometric studies - using the newly calibrated Ti-in-zircon thermometer - constrain the formative processes of these bodies. The temperature distribution measured from the Tsona Leucogranites is consistent with muscovite dehydration melting, as has been proposed for other HHL outcropping in northern Nepal. The

Suite	**Loc.**	**Age notes**	**Temperature notes**
Yala-Xiangbo Granitoids	N. THS	Cryst. at 42.3±4.9 Ma, recryst. of northernmost samples at *ca.* 20 Ma. Significantly older than other studied NHG.	Data from 1 sample form T^{Zr}_{Ti} peak below 600°C, likely reflecting recrystallisation.
Dala Granitoids	M. THS	Emplacement and crystallisation at 44.1±1.2 Ma. First evidence of Eohimalayan plutonism along main Himalayan Arc.	Asymmetrical broad T^{Zr}_{Ti} distribution (*ca.* 550–900°C) which may reflect mixing of bimodal magma source.
Tsona Leucogranites	S. THS	Emplacement and crystallisation at 18.8±1.2 Ma, similar to other HHL.	T^{Zr}_{Ti} data form peak centered at *ca.* 730°C, which is consistent with muscovite-dehydration melting.
Arunachal Leucogranites	GHC	Cryst. at 20.2±2.0 Ma, similar to other HHL.	T^{Zr}_{Ti} data form peak centered at *ca.* 660°C; individual samples show increasing temperatures proportional to increasing structural height. Could reflect "wet" melting.

Table 4.3: Summary of the crystallisation ages and zircon Ti-temperatures (T^{Zr}_{Ti}) from granitoids in the eastern Himalaya (*ca.* 92°E).

Arunachal Leucogranites and Yala-Xiangbo Granitoids, however, yielded zircon crystallisation temperature estimates that are more consistent with "wet" melting, marking further deviation from existing models for peraluminous magmatism along the Himalayan Arc. This interpretation - marking a significant deviation from current paradigms for peraluminous magmatism along the main Himalayan Arc - is further discussed in *Chapter 5*.

The combination of zircon Ti-thermometry with conventional ion-microprobe U-Pb dating provides a new approach to studying aspects of zircon petrogenesis. Results demonstrate how zircon trace element contents are influenced by co-crystallisation with monazite. Further investigations, in conjunction with CL imagery, show the way in which these data may be interpreted in terms of changes in the zircon's formative environment at the scale of individual zircon grains.

Chapter 5

Geochemical and isotopic composition of granitoids

5.1 Introduction

In the Himalaya, the distribution and timing of granitoid magmatism bears on the thermal budget and locus of tectonic activity within the orogen (LeFort et al., 1987; LeFort, 1996; Harrison et al., 1997a; Yin and Harrison, 2000). Thus granitoid geochemistry can provide insight into the sources and distribution of protolith materials and, in some cases, the structural architecture of the orogen (Deniel et al., 1987; Inger and Harris, 1993, this study). These data in turn, place important constraints on Himalayan evolutionary models (LeFort, 1996; Harrison et al., 1998a; Yin and Harrison, 2000; Beaumont et al., 2001).

5.1.1 Himalayan granitoids

The Himalayan orogen is characterised by two belts of granitoids, oriented parallel to the trace of the main Himalayan arc (LeFort, 1975; LeFort et al., 1987; LeFort, 1996; Yin and Harrison, 2000, *Figure 1.2*). The High Himalayan Leucogranites

(HHL) comprise a series of sheet, dyke and laccolithic bodies generally emplaced close to the South Tibetan Fault System (STFS), which forms a boundary between the Greater Himalayan Crystalline (GHC) and Tethyan Himalayan (THS) sequences, along the crest of the High Himalaya (*Figure 1.2*; LeFort, 1975; LeFort et al., 1987; Burchfield et al., 1992). The North Himalayan Granites (NHG) are emplaced *ca.* 80 km to the north, in the central Tethyan Himalaya (*Figure 1.2*). They are frequently found outcropping in association with zones of focussed exhumation (North Himalayan domes, NHD; *Chapter 3*) that have often been connected on regional geological maps to define a curvi-linear structural culmination termed the North Himalayan Antiform (NHA) (Hauck et al., 1998).

Studies of the HHL suggest that these bodies were emplaced between 23 and 18 Ma (Schärer, 1984; Schärer et al., 1986; Hodges et al., 1996; Searle et al., 1997; Harrison et al., 1997a, 1998a), and are generally thought to have been derived from melting of the underlying GHC lithologies (LeFort et al., 1987; Inger and Harris, 1993). Models proposed to account for the formation of the HHL include fluid-present melting of the GHC sequence associated with movement on the Main Central Thrust (MCT) (LeFort et al., 1987), fluid-absent decompression melting associated with associated with movement on the MCT and STFS (Harris and Massey, 1994; Davidson et al., 1997), shear heating associated with movement on the MCT (Harrison et al., 1997a, 1998a; England et al., 1992), and internal heating by decay of heat-producing radioactive elements (Nelson et al., 1996; Beaumont et al., 2001).

The petrogenesis of the NHG is less well constrained than that of the HHL. Emplacement ages have traditionally been thought to range from *ca.* 10 to 17 Ma (Harrison et al., 1997a), although an older age of 27 Ma was recently determined (Zhang et al., 2004b, and refs. therein). Furthermore, new data from the eastern

Himalaya indicate that North Himalayan peraluminous magmatism in this region extends back as far as the mid-Eocene (*ca.* 42 Ma, *Chapter 4*). Various models have been proposed to account for formation of the NHG, including thermal blanketing by the overlying THS metasediments (Pinet and Jaupart, 1987), decompression melting during extensional collapse (Lee et al., 2004), instability in the roof of an orogenic channel (Beaumont et al., 2001, 2004; Zhang et al., 2004a), and shear heating along a shallow décollement that is generally equated with the MCT (Harrison et al., 1997a, 1998a). However, as yet no consensus has emerged.

5.1.2 Purpose of this chapter

Over twenty years of research have yielded a variety of models for the formation of Himalayan granitoids. While most workers agree that the HHL of central Nepal are derived from partial melting of the GHC sequences associated with movement on the major Himalayan fault systems (LeFort et al., 1987; Inger and Harris, 1993; Harris and Massey, 1994; Davidson et al., 1997; Harrison et al., 1997a, 1998a; England et al., 1992), these models have not been widely tested in lateral portions of the Himalayan Arc. A variety of models have been proposed to explain formation of the NHG (Pinet and Jaupart, 1987; Harrison et al., 1997a, 1998a; Beaumont et al., 2001, 2004; Zhang et al., 2004a), however, no consensus has yet been reached. New data from the eastern Himalaya have shown that the temporal distribution of granitic magmatism in this region extends significantly beyond that which has been considered characteristic elsewhere (*Chapter 4*). Furthermore, the first application of the newly calibrated Ti-in-zircon thermometer (Watson and Harrison, 2005; Watson et al., 2006) has suggested that the formative processes of several east Himalayan granitoids may differ substantially from those which would be expected based on most existing models. The purpose of this chapter is to consider the petrogenesis of east Himalayan granitoids in the context of existing paradigms for Himalayan

granitic magmatism. The results impact upon the lateral continuity of established models, and underscore hitherto unrecognised diversity of Himalayan granitoid bodies.

5.2 Sample selection

Four suites of granitoid samples were chosen for bulk geochemical and isotopic (Rb-Sr & Sm-Nd) analysis, outcropping along a N-S oriented transect through the eastern Himalaya (*ca.* 92°E, *Figure 5.1*). In the Arunachal Himalaya, 3 samples were selected from granitoids outcropping between the Main Central Thrust (MCT) and South Tibetan Fault System (STFS). These samples, the Arunachal leucogranites (AL, *Figure 5.1*), are Miocene (*Chapter 4*) and are considered equivalent to the High Himalayan Leucogranites (HHL) of northern Nepal (LeFort et al., 1987; Inger and Harris, 1993; Harrison et al., 1997a) in terms of petrography and emplacement relations. They comprise biotite-muscovite and tourmaline-muscovite bearing assemblages and form sheet/dyke or laccolithic bodies emplaced into upper parts of the Greater Himalayan Crystallins (GHC) and the lower Tethyan Himalayan Sequences (THS). A further three samples of leucogranite, the Tsona leucogranites (TL, *Figure 5.1*), were obtained by Dr Ding Lin in the vicinity of the STFS, close to the Indo-Chinese border. The structural context of the TL could not be directly established due to access restrictions by the Chinese military authorities. However they are of comparable age to the AL (*Chapter 4*), and reconnaissance studies conducted by Dr Ding Lin indicate that their field relations are similar to the AL. They are also thought to be comparable to the HHL, albeit structurally higher components.

In the central THS, 8 samples were selected from the Dala Granitoids (DG). The DG comprise a series of sheets, dykes and undeformed elliptical plutons forming an

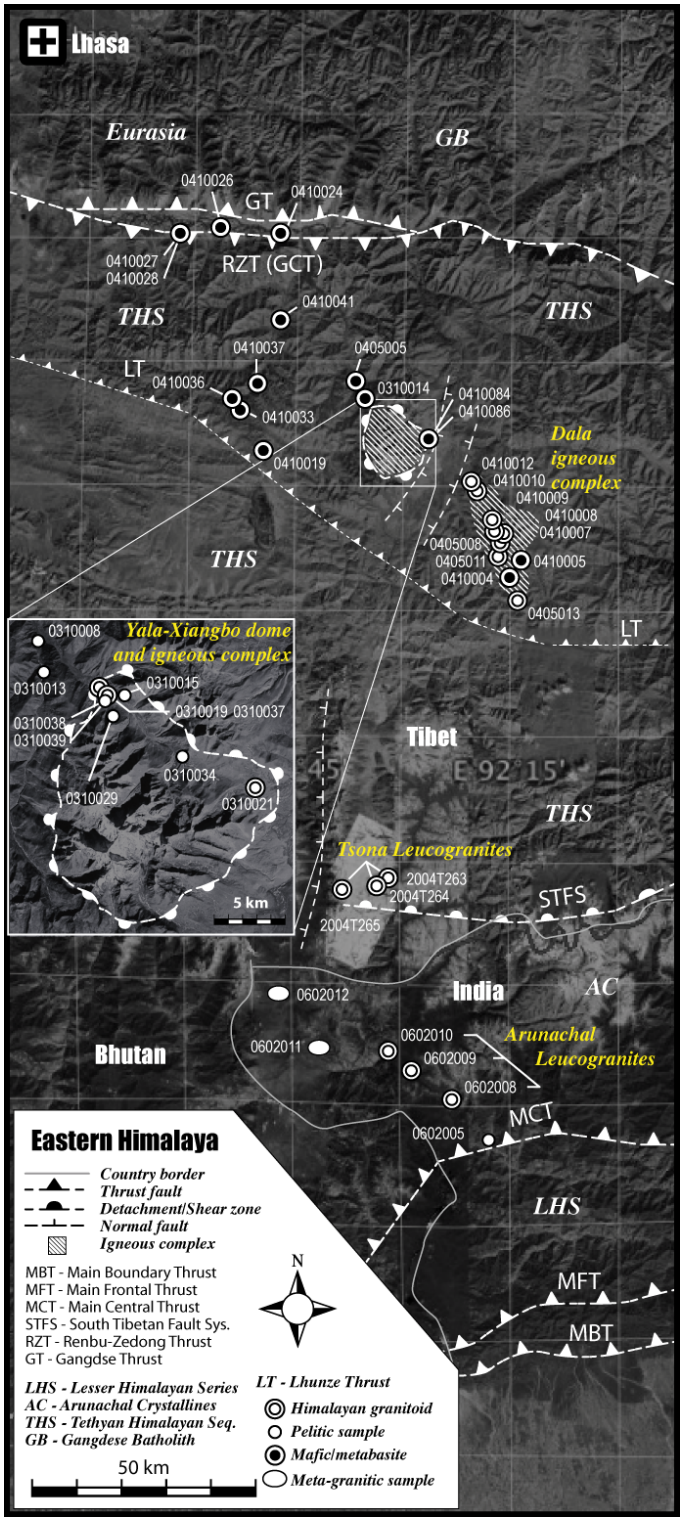

Figure 5.1: Schematic geological map of the eastern Himalaya (*ca.* 92°E) showing principal tectonic features and the locations of samples discussed in this chapter (Compiled from Yin et al., 1994; Harrison et al., 2000; Pan et al., 2004; Yin et al., 2006, this study).

igneous complex within the deformed sub-greenschist facies metasediments of the central THS (*Figure 5.1*). These granitoids are Eocene and represent a new mode of Himalayan magmatism (*Chapter 3*, *Chapter 4*). In the northern THS, 4 samples were obtained from the Yala-Xiangbo granitoids (YX_G) outcropping in the core of the Yala-Xiangbo Dome (YX_D). The majority of these bodies crystallised during the Eocene, although some experienced a Miocene recrystallisation event associated with Neohimalayan metamorphism (*Chapter 4*). They are considered analogous to the NHG in terms of emplacement style and structural position (*Chapter 3*).

A selection of other lithologies from the same transect were also chosen for comparative reference. Three samples of high grade rocks from the crystalline sequences outcropping between the MCT and STFS in the Arunachal Himalaya (the Arunachal Crystallins, AC) were selected (*Figure 5.1*). Sample 0602005 was collected from lower parts of the Arunachal Crystalline sequence in the hanging wall of the Arunachal MCT (as defined by Yin and Harrison, 2000). This sample is petrographically similar, and yielded a detrital zircon age-probability spectrum that is comparable to that derived from the GHC sequences elsewhere in the Himalaya (see *Chapter 4*). Sample 0602011 is a *ca.* 824 Ma (*Chapter 4*) meta-granite outcropping in central portions of the Arunachal GHC. Sample 0602012 was collected from the Zhimithang orthogneiss (also *ca.* 824 Ma), which is considered to represent the structurally highest components of the AC/GHC sequence in the Arunachal Himalaya (Yin et al., 2006). At least two of these samples (0602005 & 0602012) provide suitable comparison with lithologies thought to be relevant in the petrogenesis of the HHL elsewhere in the Himalaya. A further 6 samples from the high-grade pelites (YX_P) outcropping in the core of the Yala-Xiangbo Dome (*Chapter 3*) were also selected (*Figure 5.1*). These samples yield Paleozoic and older detrital zircon ages (*Chapter 4*), and provide potential comparison with high grade units thought to be important in the

Suite	Sample	Lithology	Analyses	Age/notes
Arunachal	0602008	Leucogranite	MTI	Crystallisation at 20.2±2.0 Ma
Leucogranites	0602009	Leucogranite	MTI	Crystallisation at 20.2±2.0 Ma
	0602010	Leucogranite	MTI	Crystallisation at 20.2±2.0 Ma
Tsona	2004T263	Leucogranite	MTI	Emplacement and cryst. at 18.8±1.2 Ma
Leucogranites	2004T264	Leucogranite	MTI	Emplacement and cryst. at 18.8±1.2 Ma
	2004T265	Leucogranite	MTI	Emplacement and cryst. at 18.8±1.2 Ma
	0310019	Leucogranite	MTI	Recryst. *ca.* 20 Ma, inferred Eocene cryst.
Yala-Xiangbo	0310021	Leucogranite	MTI	Crystallisation 42.3±4.9 Ma
Granitoids	0310037	Leucogranite	MTI	Recryst. *ca.* 20 Ma, inferred Eocene cryst.
	0310038	Leucogranite	MTI	Crystallisation 42.3±4.9 Ma
	0405008	Granodiorite	MTI	Emplacement and cryst. 44.1±1.2 Ma
	0405011	Granodiorite	MTI	Emplacement and cryst. 44.1±1.2 Ma
	0405013	Granodiorite	MTI	Emplacement and cryst. 44.1±1.2 Ma
	0410007	Qtz-monzodiorite	MTI	Emplacement and cryst. 44.1±1.2 Ma
Dala Granitoids	0410008	Granodiorite	MTI	Emplacement and cryst. *ca.* 44 Ma (unpub.)
	0410009	Granodiorite	MTI	Emplacement and cryst. 44.1±1.2 Ma
	0410010	Granodiorite	MTI	Emplacement and cryst. 44.1±1.2 Ma
	0410012	Granodiorite	MTI	Emplacement and cryst. 44.1±1.2 Ma
Arunachal	0602005	Pelite	MTI	Dominantly Proterozoic detrital ages
Crystallines	0602011	Meta Ksp-granite	MTI	Protolith *ca.* 824 Ma
	0602012	Orthogneiss	MTI	Protolith *ca.* 824 Ma
	0310008	Pelite	MTI	Inferred Triassic depositional age
	0310013	Pelite	MTI	Inferred Triassic depositional age
	0310015	Pelite	MTI	Triassic and older detrital ages
Yala-Xiangbo pelites	0310029	Pelite	MTI	Triassic and older detrital ages
	0310034	Pelite	MTI	Dominantly Ordovician detrital ages
	0310039	Pelite	MTI	Ordovician and older detrital ages
	0410004	Mafic	MT	Age unknown
	0410019	Mafic	MT	Age unknown
	0410024	Mafic	MT	Age unknown
	0410026	Mafic	MT	Age unknown
	0410027	Mafic	MT	Age unknown
	0410028	Mafic	MT	Age unknown
	0410033	Mafic	MT	Age unknown
Tethyan mafics	0410036	Mafic	MT	Age unknown
	0410037	Mafic	MT	Age unknown
	0410041	Mafic	MT	Age unknown
	0405005	Metabasite	MT	Age unknown
	0410005	Metabasite	MT	Age unknown
	0410084	Metabasite	MT	Age unknown
	0410086	Metabasite	MT	Age unknown
	0310014	Metabasite	MTI	Age unknown

Table 5.1: Details of sample suites analysed for bulk geochemical and isotopic composition. Age data derived from zircon U-Pb geochronology (*Chapter 4*), sample locations as shown in *Figure 5.1*. The ages of the Tethyan mafic bodies are unknown as U-Pb dating proved unsuccessful (no zircons were found). Analyses conducted: major element XRF (M), trace element LA-ICPMS (T), TIMS Rb-Sr & Sm-Nd isotopes (I).

petrogenesis of the NHG. Fifteen samples of mafic bodies (TM) outcropping around the Indus Tsangpo Suture (ITS) and throughout the Tethyan Himalaya were also chosen for analysis (*Figure 5.1*). Although attempts to date several of these rocks using ion-microprobe U-Pb dating proved unsuccessful (no zircons were found), these samples were chosen to test whether they may bear any genetic relationship to the Himalayan granitoids based, on their bulk geochemistry.

5.3 Analytical methods

Samples sizes were chosen based on grainsize to provide a representative analysis of not less than 1 million grains (typically around 2 kg of material). Efforts were made to obtain the freshest possible material from each location, and samples were cleaned and abraded individually to remove any surface dirt and obvious weathering or alteration products. Samples were crushed using a mechanical jaw crusher, which was cleaned at regular intervals using solvents and compressed air. Crushed sample chips were "coned and quartered", and the remainder processed to powder in a tungsten carbide grinding mill. The mill was also cleaned using solvents and quartz sand at the beginning and end of each run and between samples. Samples were packaged individually in sterile plastic containers. Care was taken at all stages of sample preparation to avoid contamination, and any potentially suspect material was discarded.

5.3.1 Bulk geochemical analyses

Bulk geochemical analyses were accomplished in two stages. Major element analyses were conducted by Dr Ulrike Troitzsch using XRF at the Department of Earth and Marine Sciences (The Australian National University). Major elements Na, Mg, Al, Si, P, S, K, Ca, Ti, Mn, Fe, F and Cl were assessed by XRF on a Phillips (PANalytical) PW2400 X-ray fluorescence spectrometer. Lithium borate discs were prepared

by fusion of 0.27 g of dried sample powder and 1.72 g of "12-22" eutectic lithium metaborate-lithium tetraborate. The major elements were calibrated against 28 international standard rock powders.

Trace element analyses were conducted by LA-ICPMS using fused disks prepared by Dr Ulrike Troitzsch from the same powder batches. Approximately 35 elements were assessed, using an Agilent 7500S quadrupole ICP-MS attached to a 193 nm wavelength Lambda Physik LPX 120I ArF excimer laser, through an effective small volume ablation cell and smoothing device. Unknowns and reference materials were ablated using an 80 μm laser spot and laser fluence of approximately 8 J/cm^2. Each element was counted sequentially in a time-resolved, peak hopping mode, for a period of approximately 0.01 seconds. Gas backgrounds were collected for the first 20 seconds, followed by 40 seconds of ablation. Spectra were inspected and the background and laser-on intervals chosen visually. A few seconds of data at the beginning of the ablation period were discarded to allow for signal stabilisation and ablation of surface contaminants.

Data reduction and limit-of-detection calculations were based on the method of Longerich et al. (1996). Data were processed on a mass-sweep by mass-sweep basis (a time basis that approximates depth), standardising against NIST SRM 612, assuming the elemental concentrations of Pearce et al. (1997) with updates. An internal standard element (Si, Al or Ca) was chosen from XRF analysis and all data reduced as ratios relative to this standard value (rather than cps/ppm being derived directly from the standard). This approach improves accuracy, in part through the removal of matrix effects. The three potential standardising elements (Si, Al & Ca) were tested independently for each analytical session, the final choice being made with a view to maximising analytical accuracy and precision (below). Average

background subtractions were performed for each mass sweep, and inter-element fractionation factors calculated based on the known ratios in the reference material. Bracketing standards were ablated for every 10 unknowns (*ca.* 20 mins) to account for machine drift, and the fractionation factors interpolated between these values. Analytical precision and accuracy were monitored by multiple ablations of BCR-2G, a non-fluxed glass of the USGS standard Columbia River Basalt. Calculated concentrations in BCR were found to reproduce published values (Norman et al., 1998) to within 10% (in virtually all cases), and in most cases to within 5%.

5.3.2 Rb-Sr & Sm-Nd isotopic analyses

Isotopic analyses were performed by Dr Marc Norman at the Research School of Earth Sciences (The Australian National University). Rb-Sr and Sm-Nd isotope data were obtained using routine methods for cation exchange chromatography to purify the elements of interest, and thermal ionisation mass spectrometry for measurement of isotope ratios. Methods followed those outlined by Gingele and De Deckker (2005) with the exception that samples were digested in high-pressure Teflon digestion vessels after spiking with enriched isotopes for concentration determinations by isotope dilution. [^{87}Rb] measurements for the YX_G and DG sample suites were not obtained via TIMS analysis. These values were calculated using the $^{87}Sr/^{86}Sr$, and the bulk Rb & Sr concentrations from trace element (LA-ICPMS) analysis using a procedure designed by Charlotte Allen. The method was tested using data from the AL & TL (for which TIMS $^{87}Rb/^{86}Sr$ ratios were obtained), and found to reproduce the TIMS-derived values within uncertainty.

5.4 Results

A total of 41 samples were analysed for bulk-rock geochemistry, and 28 for Rb-Sr and Sm-Nd isotopic composition. Results are tabulated in *Appendix .1*. For

comparative purposes, some data have been plotted with published values from the Gangdese Batholith (GB) (Debon et al., 1986; Harrison et al., 2000). The GB granitoids comprise a suite med- to high-K calc-alkaline bodies (55-75% SiO_2), and are considered representative of the dominant style of granitic magmatism along the southern margin of Eurasia prior to collision (Debon et al., 1986; Harrison et al., 2000).

5.4.1 Major elements

Most granitoid samples fall in a relatively restricted range of SiO_2 (70-75%), and can be classified based on CIPW normative compositions (after Streckeisen and Le Maitre, 1979). Samples of the DG form a tight cluster within the granodiorite field on a QAP diagram (*Figure 5.3(a)*), although one, slightly more mafic outlier falls within the quartz-monzodiorite field. The AL, TL & YX_G are more compositionally heterogeneous than the DG, scattering between the granodiorite, monzo-granite and quartz-monzonite fields. Whereas the two granitic AC samples (0602011 & 0602012) plot respectively close to the TL in the monzo-granite field (Zhimithang gneiss) and distinct from all other sample suites in the alkali-feldspar granite field (meta-granite). All suites show relatively high alkali contents, however only the GB, DG & TM sample suites show appreciable correlation between major element content and silica (*Figure 5.2(a)*, *Table 5.2*).

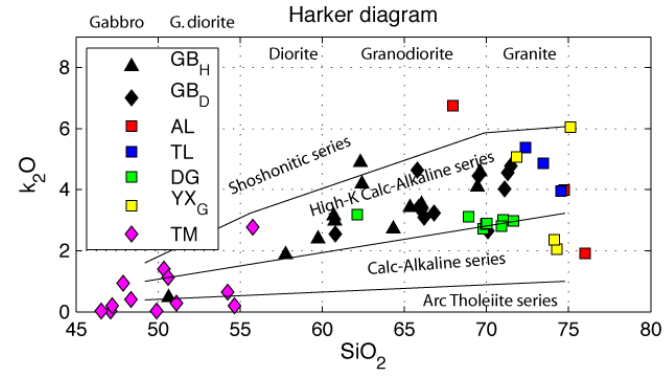

(a) K_2O-SiO_2 Harker diagram

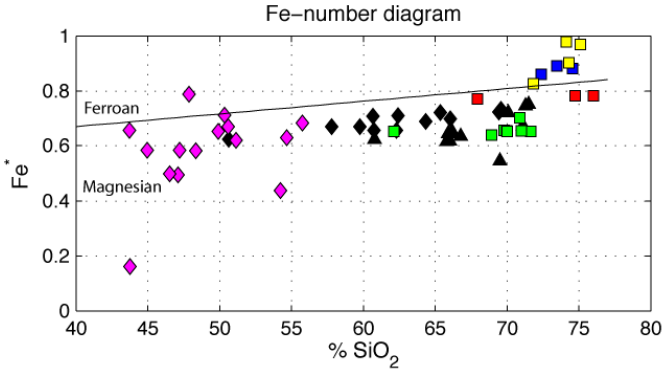

(b) Fe-number diagram

Figure 5.2: Classification diagrams illustrating the major element composition of the Gangdese Batholith granitoids Gangdese Batholith (GB Debon et al., 1986; Harrison et al., 2000), Yala-Xiangbo Granitoids (YX_G), Dala Granitoids (DG), and Tethyan mafic bodies (TM). Key for all figures as shown on subfigure (a). K_2O-SiO_2 Harker diagram (after Peccerillo and Taylor, 1976); modified Fe-number diagram ($Fe^* = FeO^{total}/(FeO^{total} + MgO)$) (Frost et al., 2001); Modified Alkali-Lime Index diagram ($MALI = Na_2O + K_2O - CaO$) (Frost et al., 2001); Alumina Saturation Index diagram (Shand, 1943).

Continues on next page...

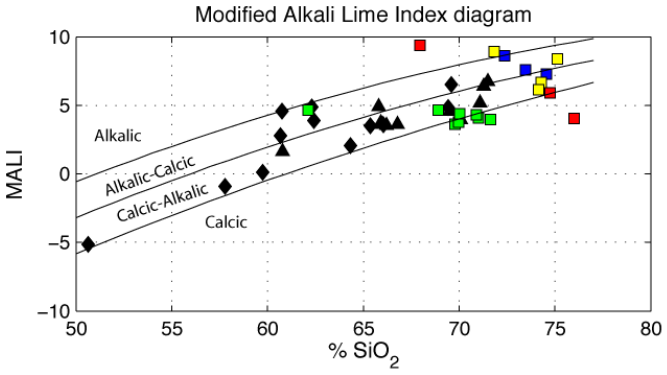

(c) Modified Alkali-Lime Index

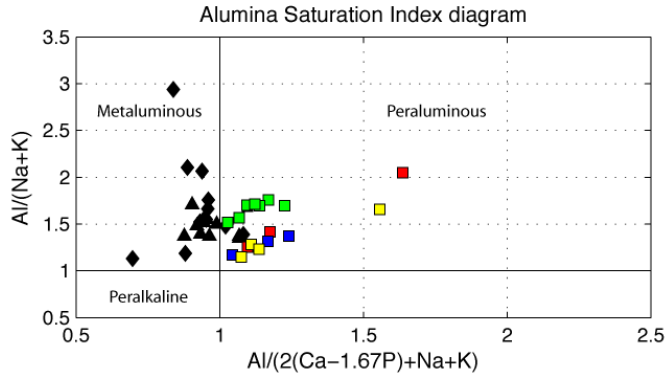

(d) Alumina Saturation Index

Figure 5.2: *Continued...*

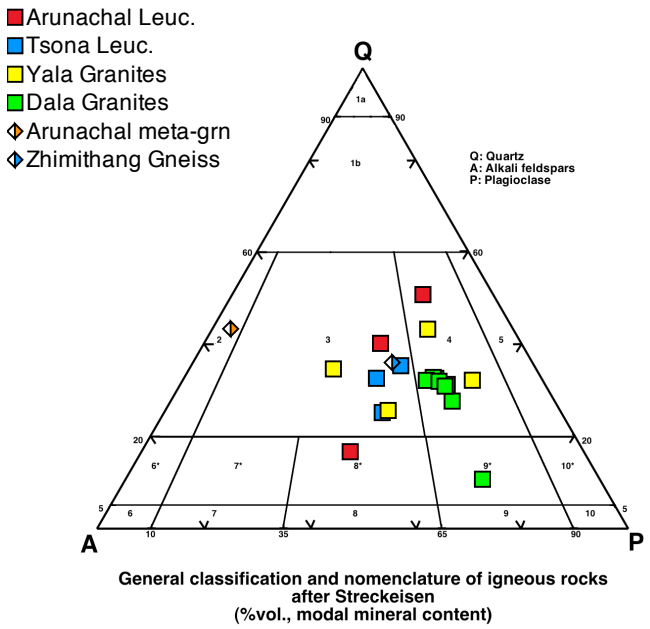

(a) QAP diagram

Figure 5.3: Ternary plots showing the major phase/element composition of the various samples and sample suites (see *Table 5.1*); modal compositions are CIPW normative. (a) QAP (quartz alkali-feldspar plagioclase) classification diagram (after Streckeisen and Le Maitre, 1979); (b) Na_2O-K_2O-CaO diagram, arrow indicates differentiation trend from (Atherton et al., 1979); (c) AFM diagram, boundary between the calc-alkaline and tholeiitic fields from Irvine and Baragar (1971); (d) Ternary phase diagram in the system Quartz-Albite-Orthoclase$\pm H_2O\pm$Anorthite.

Continues on next page...

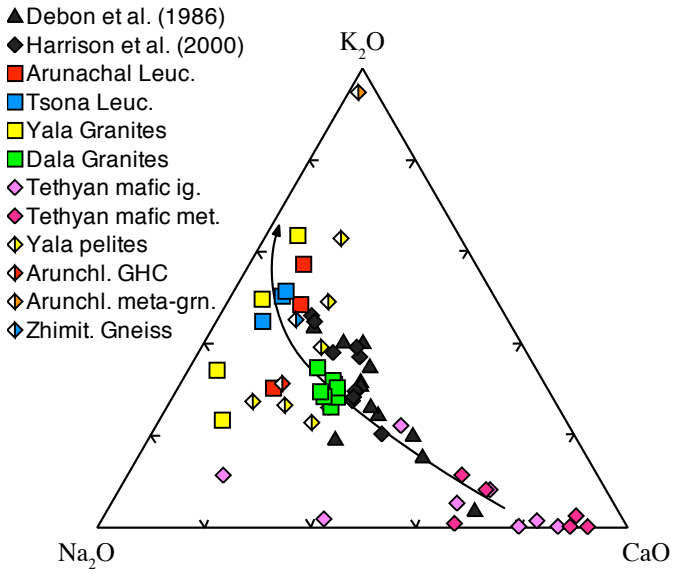

(b) Na_2O-K_2O-CaO diagram

Figure 5.3: *Continued...*

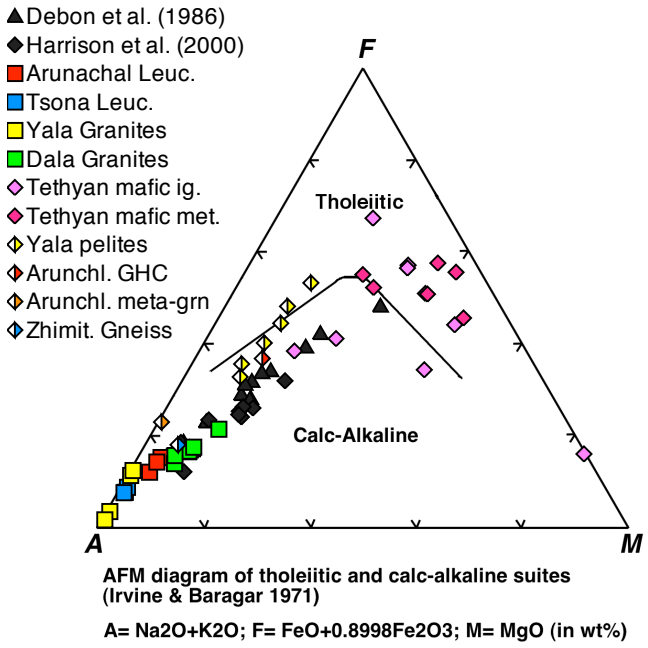

(c) AFM diagram

Figure 5.3: *Continued...*

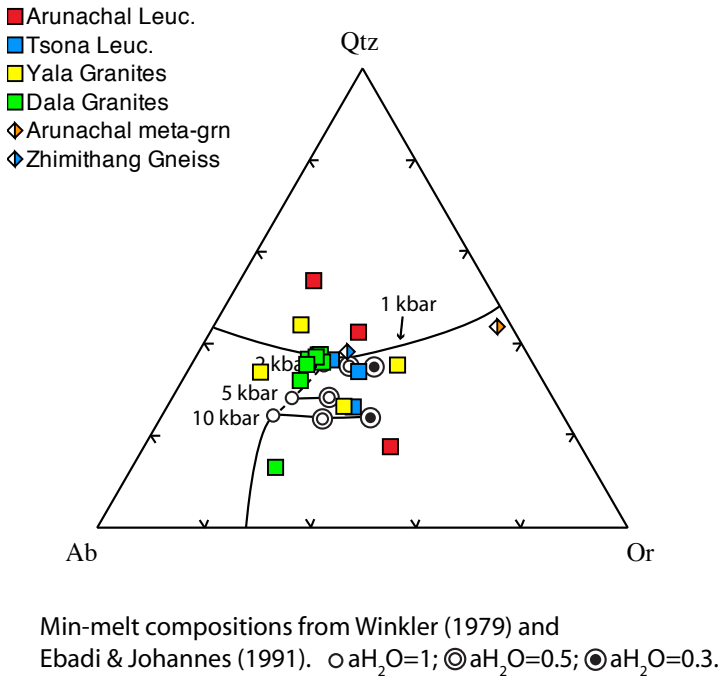

(d) Phase diagram

Figure 5.3: *Continued...*

Suite	**SiO_2**	**K_2O + Na_2O**	**K_2O / Na_2O**	**CaO (Wt. %)**	**Fe***	**MALI**	**ASI**
AL	75–77	5.1–10.5	0.6–1.8	1.1–1.2	0.77–0.78	4.0–9.4	0.8–2.1
TL	72–75	8.0–9.6	1.0–1.3	0.7-1.0	0.86–0.89	7.3–8.6	0.9–1.3
YX_G	72–75	6.5–9.5	0.4–2.1	0.4–1.0	0.83–0.99	6.1–8.9	0.7–2.2
DG	62–72	6.6–8.4	0.6–0.8	2.1–3.7	0.65–0.70	3.6–4.6	1.2–1.3
TM	45–56	1.3–6.7	<0.1–0.7	0.6–13.4	0.16–0.79	-	-
YX_P	66–74	3.9–5.8	0.5–2.8	0.9–1.7	0.76–0.8	2.1–4.8	1.4–2.2
0602005	87	2.42	0.63	0.57	0.77	9.4	0.84
0602011	77	8.58	29.6	0.14	0.98	8.4	0.47
0602012	74	7.44	1.14	1.28	0.75	6.2	1.1

Table 5.2: Range of major element composition of various suites/samples. Fe*, MALI & ASI parameters after Frost et al. (2001). Acronyms as for *Table 5.1.*

Figure 5.2(b)–Figure 5.2(d) show the major element composition of the various sample suites plotted in terms of the three principal granitoid classification parameters of Frost et al. (2001), Fe* (modified Fe-number), MALI (modified alkali-lime index) and ASI (alumina saturation index). This classification scheme was chosen in preference because it places greater emphasis on distinguishing the processes of granite formation, with only minimal reference or assumption regarding the nature of the associated tectonic environment. Fe* (modified Fe-number) is defined as $Fe^* = FeO^{total}/(FeO^{total} + MgO)$, and conveys information about the differentiation history of the magma. The Modified Alkali Lime Index (MALI, $Na_2O + K_2O - CaO$) expresses the compositions and abundances of the feldspars in the rock, which is related to the sources of the magma. The Alumina Saturation Index (ASI) depends primarily on the micas and accessory minerals, and provides information about the sources and conditions of melting (Frost et al., 2001).

Figure 5.2(b) shows Fe* plotted against wt. % SiO_2. The TM, GB & DG suites are comparable in terms of Fe*, plotting almost entirely within the magnesian field, distinguishable only by their silica contents. Their magnesian character likely reflects the role of aqueous fluids during differentiation, which lead to early crystallisation of ilmenite, thereby preventing Fe enrichment (Osborn, 1959). The AL, TL & YX_G samples scatter at high SiO_2 around the magnesian-ferroan boundary, although the TL & YX_G appear to be marginally more ferroan than the AL, all three sample suites plot within the peraluminous leucogranite field of Frost et al. (2001). *Figure 5.2(c)* shows MALI plotted against wt. % SiO_2. All sample suites plot along a trend that is largely contained between the extreme alkalic and calcic end members, although the AL show somewhat greater dispersion in terms of MALI. The majority of the data are relatively aluminous (*Figure 5.2(d)*). Samples of the GB, however, are largely confined to the metaluminous field, whereas data from all the remaining

granitoids fall within the peraluminous field. The AL, TL, YX_G & YX_P define a roughly linear, positively correlated trend. The DG also show comparable linearity, although their trend is slightly offset to higher $Al/(Na + K)$.

The DG, AL, TL, YX_G, & GB collectively plot along a calc-alkaline trend in an AFM diagram (*Figure 5.3(c)*). Although two samples of the TM are consistent with this trend, the majority are confined to scatter within the tholeiitic field. The DG, GB & TM are mutually consistent with a differentiation trend on a K_2O-Na_2O-CaO diagram (*Figure 5.3(b)*). Whereas while the AL, TL & YX_G overlap the same differentiation trend at high total Na+K content (low CaO), they show significantly greater dispersion in terms of relative alkali abundance. All but one samples of the DG are consistent with pressure-dependent minimum melt compositions at high water activities in the ternary Qtz-Ab-Or system (*Figure 5.3(d)*). The AL, TL & YX_G however do not cluster around minimum melt compositions, instead defining a spread reflecting greater variability in terms of major phase abundance.

The major element compositions of high-grade units YX_P & AC (shown for comparative reference on *Figure 5.2*) are broadly comparable to those of the AL, TL & YX_G. Sample, however, 0602011 (Arunachal 800 Ma meta-granite) is relatively ferroan and potassic and compositionally distinct with respect to the majority of the data.

5.4.2 Rare Earth Elements

Figure 5.4 shows rare earth element patterns for all samples, normalised to the average abundance in C1 Chondrite (McDonough and Sun, 1995). Results are plotted with published data from the GB (Harrison et al., 2000) for comparative reference. Samples from the GB show consistent LREE enrichment ($La_N = 150 - 250$)

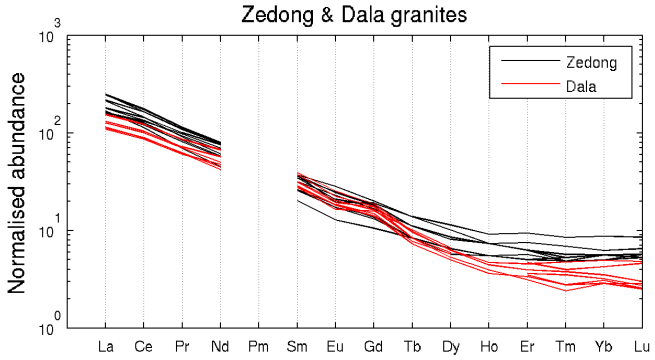

(a) Dala Granitoids

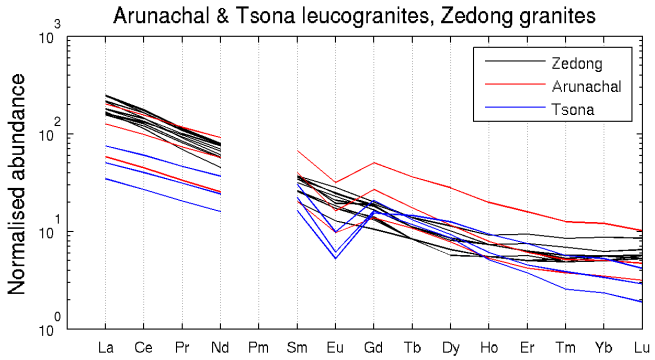

(b) Arunachal and Tsona Leucogranites

Figure 5.4: Chondrite normalised REE diagrams for the Arunachal and Tsona Leucogranites, Dala and Yala-Xiangbo Granitoids, Tethyan mafic, Arunachal Crystalline, and Gangdese Batholith (Harrison et al., 2000) sample suites. Discrimination diagram shows the expected fields for samples respectively containing cumulus feldspar or feldspar in the residue (after melting), and xenocrystic garnet or garnet in the residue, based on their Eu anomalies and HREE trends. *Continues on next page...*

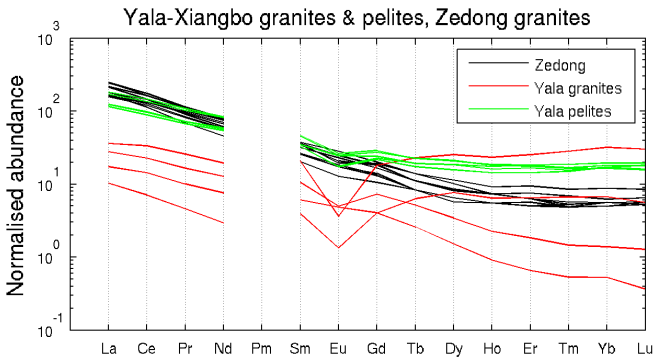

(c) Yala-Xiangbo Granitoids and pelites

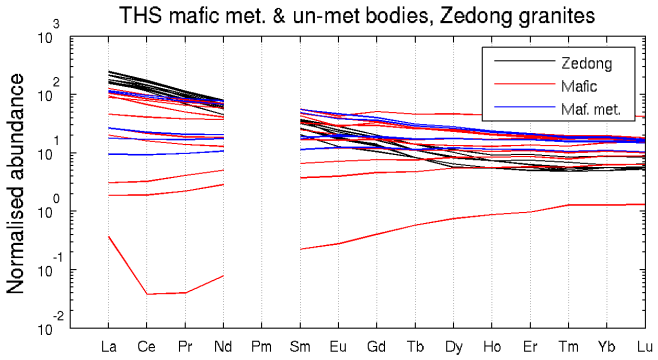

(d) THS mafic bodies

Figure 5.4: *Continued...*

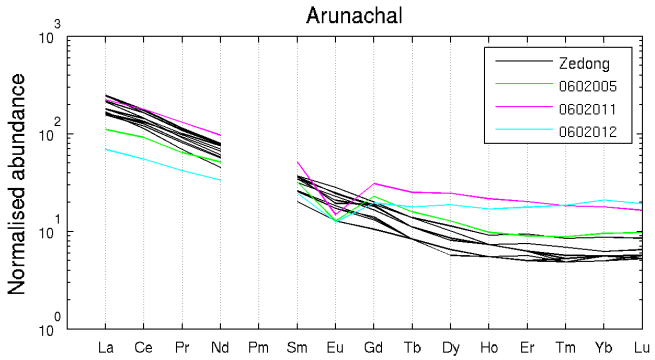

(e) Arunachal Crystallins

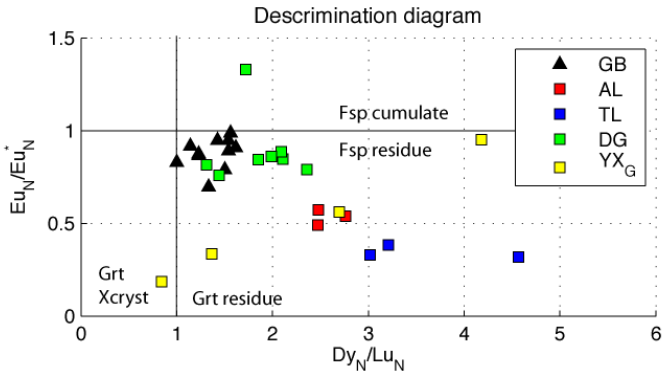

(f) Discrimination diagram

Figure 5.4: *Continued...*

and negatively sloping trends ($(La/Yb)_N = 18.5 - 44.6$, $(La/Sm)_N = 4.4 - 8.3$), with no discernible Eu anomaly. HREE are typically flat or slightly decreasing ($Yb_N = 5.3 - 8.7$, $(Gd/Yb)_N = 1.9 - 3.3$). The DG (*Figure 5.4(a)*) show REE patterns that are almost indistinguishable from those of the GB in terms of both trend and concentration. The only notable difference being slightly lower HREE enrichment ($Yb_N = 2.9 - 4.9$).

The AL & TL (*Figure 5.4(b)*) show significantly more variability in terms of REE composition than either the DG or the GB. They have uniformly decreasing trends (AL $(La/Yb)_N = 16.7 - 24.9$, TL $(La/Yb)_N = 6.6 - 22.2$) and negative Eu anomalies. In general, the REE compositions of the AL & TL are comparable to those described from other HHL (*e.g.* Inger and Harris, 1993). The YX_G (*Figure 5.4(c)*) appear to show two classes of REE trend, both are depleted in LREE with respect to other granitoid samples ($La_N = 10.3 - 35.9$). The first is similar to that of the TL, although comparatively depleted in HREE ($Yb_N = 0.5 - 1.5$) and showing smaller Eu anomalies. The second shows large Eu anomalies and comparatively enriched HREE trends ($Yb_N = 6.7 - 31.8$).

The YX_P (*Figure 5.4(c)*) are comparable or slightly depleted with respect to the GB in terms of LREE content ($La_N = 115 - 180$). Their trends, however, are generally flatter and notably more HREE enriched ($(La/Yb)_N = 6.8 - 11.1$, $Yb_N = 16.4 - 19.4$). Similar REE patterns have been observed in flanking schists from North Himalayan Domes *ca.* 450 kilometres to the west (Zhang et al., 2004a). The TM (*Figure 5.4(d)*) show a range of REE patterns varying from horizontal to slight positive or slight negative slopes ($(La/Yb)_N = 0.3 - 6.3$). Excluding a single anomalous trend which plots partially below Chondrite (altered ultra mafic), they generally show depleted LREE ($La_N = 1 - 125$) and enriched HREE ($Yb_N = 1 - 45$)

with respect to the GB. Crystalline samples from the Arunachal Himalaya (*Figure 5.4(e)*) yielded REE patterns that are comparable to those of the AL, although marginally more HREE enriched ($Yb_N = 9 - 20$). A REE discrimination diagram (*Figure 5.4(f)*) indicates that - excluding one sample each of the DG and YX_G which may respectively contain cumulus feldspar and xenocrystic garnet - the majority of the data plot within the garnet–feldspar residue field, consistent with expected trends for incorporation of crustal material (Spear, 1995).

5.4.3 Trace elements

Granitoids from all sample suites show trace element patterns characterised by incompatible element (LILE) enrichment relative to High Field Strength (HFSE) and Rare Earth (REE) elements (*Figure 5.5*). Trace element compositions are shown normalised to average concentrations in primitive mantle (McDonough and Sun, 1995), and plotted with published data from the GB (Harrison et al., 2000). All samples show limited Nb–Ta fractionation, which almost certainly results from minor Ta contamination during sample preparation using a tungsten carbide mill. The GB granitoids (Harrison et al., 2000) are characterised by tightly bunching trends, showing LILE and LREE enrichment, positive Pb and negative Ba, Nb, Ta, P, Sm, & Ti anomalies. Th/U ratios range from 0.9 to 2.2 ($Th_N = 170 - 450$, $U_N = 150 - 450$). Samples of the DG (*Figure 5.5(a)*) show trace element patterns that are almost indistinguishable from those of the GB on a log plot. The AL, TL & YX_G (*Figure 5.5(b)*, *Figure 5.5(c)*), however, collectively show significantly more inter-sample heterogeneity than either the DG or the GB. Although their trace element patterns are of similar general form to the GB & DG, they are distinguishable by relatively depleted in Ba, Sr, Zr, Ti & LREE with respect to the DG & GB trends. They are generally more comparable to those of the HHL and NHG (*Figure 5.5(e)*, *Figure 5.5(f)*).

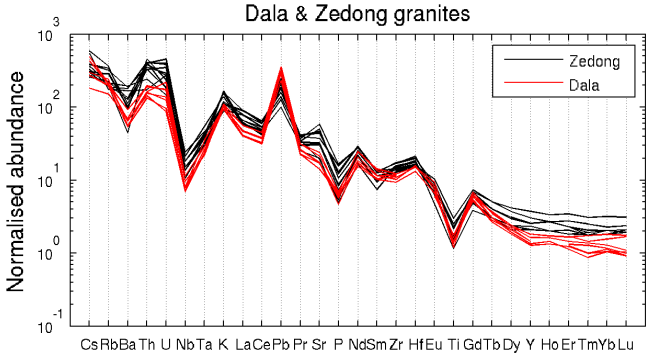

(a) Dala Granitoids

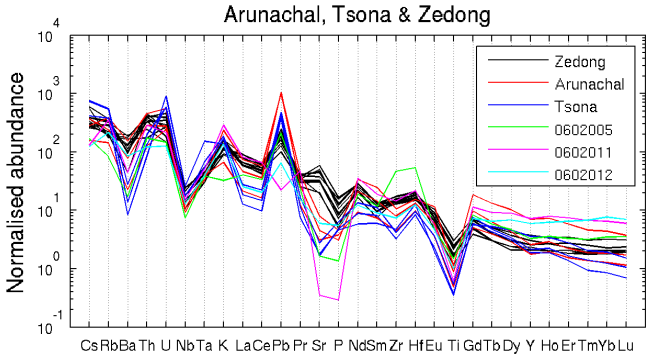

(b) Arunachal and Tsona Leucogranites

Figure 5.5: Pyrolite (Primitive Mantle) normalised spyder diagrams for all sample suites shown with published data from the Gangdese Batholith (Harrison et al., 2000). High Himalayan Leucogranites, Greater Himalayan crystallins, North Himalayan Granites, and North Himalayan Crystallins (Inger and Harris, 1993; Zhang et al., 2004a) are also shown for comparative reference. *Continues on next page...*

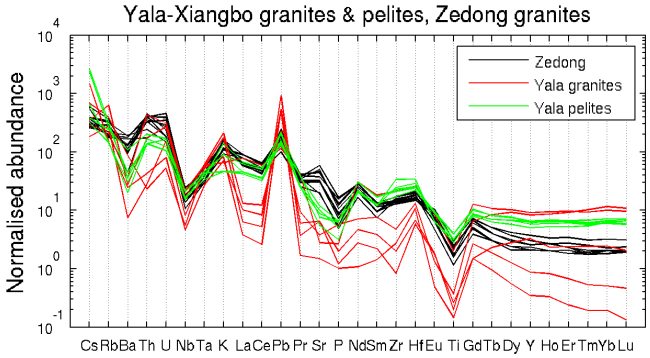

(c) Yala-Xiangbo Granitoids and pelites

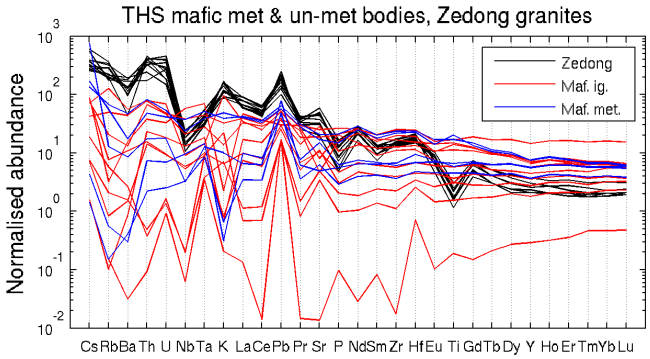

(d) THS mafic bodies

Figure 5.5: *Continued...*

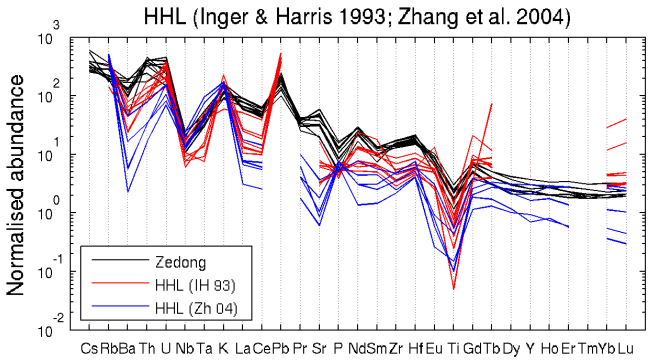

(e) High Himalayan Leucogranites

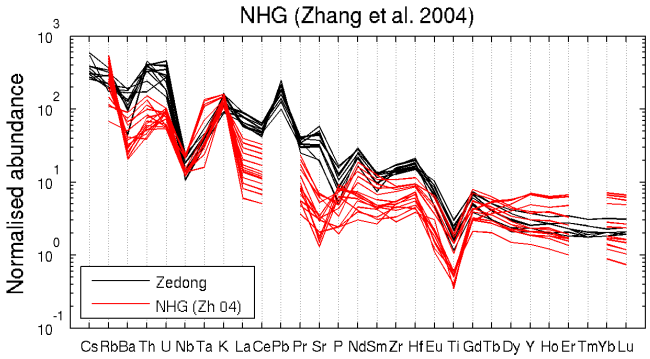

(f) North Himalayan Granites

Figure 5.5: *Continued...*

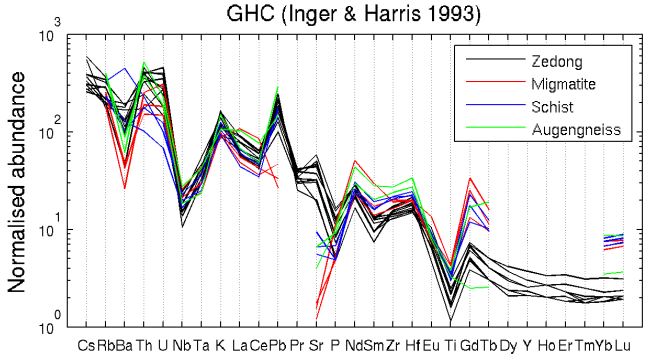

(g) Greater Himalayan Crystallins

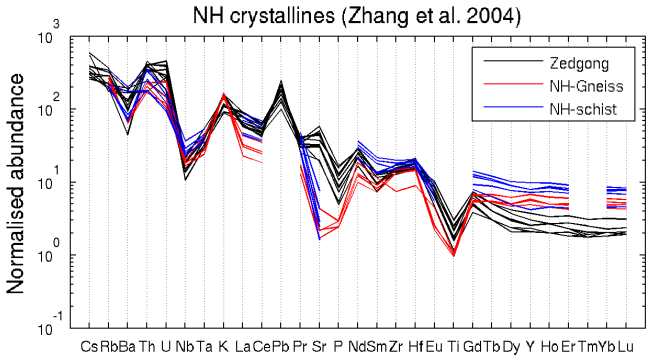

(h) North Himalayan Crystallins

Figure 5.5: *Continued...*

Crystalline samples from the Arunachal Himalaya (AC) show comparable patterns to the AL, with the exception of a few elements. Sample 0602005 is notably K-depleted, and enriched in Zr & Hf, sample 0602011 shows distinctive strongly negative Sr & P anomalies, and sample 0602012 shows smaller Ba & Pb excursions and flatter HREE patterns than most other Arunachal samples. These samples are generally comparable to published data from the GHC (*Figure 5.5(g)*). The YX_P trace element patterns are similar to those of other North Himalayan Crystallins (NHC gneiss and schist, *Figure 5.5(h)*), but also do not differ greatly from those of the GHC. TM trace element patterns (*Figure 5.5(d)*) are highly variable, but generally show positive Pb anomalies (likely associated with secondary alteration) and relatively flat REE trends. Metamorphosed samples of the TM suite are not distinguishable from their igneous counterparts in terms of trace element composition.

5.4.4 Rb-Sr & Sm-Nd isotopic analyses

The results of Rb-Sr & Sm-Nd isotopic analyses (summarised in *Table 5.3*) show a relatively restricted range of measured $^{143}Nd/^{144}Nd$ (0.51178-0.51293) relative to $^{87}Sr/^{86}Sr$ (0.70803-0.87676). Initial isotopic ratios for the AL & TL show relatively consistent negative ϵ_{Nd} (-13 to -15) and somewhat variable ϵ_{Sr} (750 to 1700). The YX_G show slightly higher ϵ_{Nd} (- 8 to -13) and generally more primitive ϵ_{Sr} (150 to 350), excluding one sample (0310021) for which the calculated ϵ_{Sr} is *ca.* 1500. The DG show a relatively restricted range of both ϵ_{Nd} (-10 to -13) and ϵ_{Sr} (115 to 170). High grade lithologies from the Arunachal Himalaya show a similar range of ϵ_{Nd} to the AL & TL (-12 to -16), but notably greater range of ϵ_{Sr} (670 to >2500). Whereas pelitic units from the core of the Yala-Xiangbo dome (YX_P) typically show ϵ_{Nd} in the range -6 to -8, although one sample (0310034) yielded a significantly more negative value of *ca.* -13. The calculated ϵ_{Sr} from the YX_P are also relatively primitive

Suite	Sample	$\epsilon_{Nd}^{T_0}$	$\epsilon_{Sr}^{T_0}$	T_1 (Ma)	$\epsilon_{Nd}^{T_1}$	$\epsilon_{Sr}^{T_1}$
DG	0405008	-12.60	199.21	44	-12.18	190.49
DG	0405011	-13.13	200.17	44	-12.71	191.42
DG	0405013	-10.81	188.40	44	-10.40	175.97
DG	0410007	-13.40	191.61	44	-12.96	185.79
DG	0410008	-13.86	199.86	44	-13.45	192.03
DG	0410009	-13.86	199.05	44	-13.38	190.75
DG	0410010	-13.38	186.84	44	-12.92	182.12
DG	0410012	-11.41	170.00	44	-11.02	165.43
AL	0602008	-14.90	1706.94	20	-14.75	1690.01
AL	0602009	-15.37	1352.69	20	-15.21	1334.59
AL	0602010	-15.28	1413.30	20	-15.16	1396.09
TL	T263	-13.35	851.78	20	-13.26	777.36
TL	T264	-13.10	882.94	20	-13.06	743.93
TL	T265	-14.16	1104.54	20	-14.14	1026.50
YX_G	0310019	-11.28	156.58	20	-11.15	143.14
YX_G	0310021	-8.12	1476.98	20	-8.16	1378.38
YX_G	0310037	-10.28	157.57	20	-10.18	121.41
YX_G	0310038	-12.86	350.42	20	-12.93	243.58
AC	0602005	-16.75	2445.10	20	-16.56	2425.15
AC	0602011	-15.27	14266.08	20	-15.04	13897.72
AC	0602012	-12.30	681.66	20	-12.18	668.99
YX_P	0310008	-6.89	191.78	20	-6.65	173.80
YX_P	0310013	-8.64	206.74	20	-8.43	197.47
YX_P	0310015	-6.83	168.46	20	-6.64	160.01
YX_P	0310029	-7.08	153.48	20	-6.87	140.27
YX_P	0310034	-12.93	2000.34	20	-12.73	1953.01
YX_P	0310039	-9.73	198.85	20	-9.50	170.25
TM	0310014	5.68	50.09	20	5.72	50.40

Table 5.3: Summary of the Sr-Nd isotopic composition of samples from the Dala Granitoids (DG), Arunachal Leucogranites (AL), Tsona Leucogranites (TL), Yala-Xiangbo Granitoids (YX_G), Arunachal Crystallines (AC), Yala Xiangbo Pelites (YX_P), and one sample of the Tethyan Mafics (TM).

(150 to 350), although the same anomalous sample yielded a more evolved value (*ca.* 2000). Comparisons between these data and published values for other regional lithotectonic units are discussed in the following sections.

Bulk Rb/Sr ratios in the AL are in the order of 1.5, comparable with two samples of the AC (0602005, 0602012). Bulk Rb/Sr ratios in the TL however, are significantly higher (6-12). Ratios in the YX_G and YX_P are in the range 1-9 and 0.7-4 respectively. Rb/Sr ratios in the DG are consistently around (0.2-0.5).

5.5 Discussion

The major element characteristics of granitoids from the eastern Himalaya broadly distinguish them into two groups. Samples of the Dala Granitoids (DG) and Gangdese Batholith (GB) are predominantly magnesian and show variation in major element composition with SiO_2. They are largely contained between the end-member calcic and alkalic trends, and are typically metaluminous to weakly peraluminous. These samples are consistent with a generalised differentiation trend, and plot at pressure-dependent eutectic compositions. The Arunachal and Tsona Leucogranites (AL, TL) and Yala-Xiangbo Granitoids (YX_G) comprise a second group that are notably more variable in terms of major element characteristics. They do not show appreciable correlation between major element composition and SiO_2, have variable alkali contents and are moderately to strongly peraluminous. They plot within the peraluminous leucogranite field (in terms of Fe^* and MALI) of Frost et al. (2001), and typically show non-eutectic phase compositions. The distinction between these two groups is attributed to fundamental differences in their petrogenesis.

The major element characteristics of the DG and GB are consistent with their formation through magma differentiation along a liquid line of descent, towards the

water-saturated granite eutectic. The absence of a pronounced Eu anomaly, however, suggests that they are arguably better attributed to mixing between mafic and crustally derived material, as has previously been proposed for the GB granites (Debon et al., 1986; Mo et al., 2006). They are geochemically 'well behaved', and are considered representative of melt compositions. In the case of the GB, such characteristics have been cited as evidence in support of their inferred origin as components of an Andean-type complex along the southern margin of Eurasia (Debon et al., 1986; Harrison et al., 2000; Yin and Harrison, 2000).

The characteristics of the AL, TL and YX_G do not indicate that they were derived predominantly through magma differentiation. These samples are better attributed to crustal anatexis associated with amphibolite grade metamorphism of pelitic rocks, as has been widely proposed for other HHL and NHG (LeFort et al., 1987; Deniel et al., 1987; Inger and Harris, 1993; Harrison et al., 1997a; Zhang et al., 2004a). Compositional variability shown by the TL is likely reconcilable with local variations in pressure and fluid availability during melting. These samples are considered representative of melt compositions. Similar factors likely also played a role in formation of the AL and YX_G, however extreme end member compositions are potentially indicative of secondary processes. Extensive fractional crystallisation is generally not favoured for the HHL on the basis of structural, mechanical and petrographic arguments (see discussion in Inger and Harris, 1993), hence incorporation of cumulus phases is unlikely. Incomplete magma-crystal separation and limited entrainment of restitic phases arguably represent more plausible processes. However, in the case of the AL, extensive incorporation of either restitic/cumulus feldspar or xenocrystic garnet, is effectively ruled out by the moderate to strongly negative Eu anomalies and decreasing HREE patterns shown by all samples. It is more likely that the observed inter-sample heterogeneity results from local variations in source

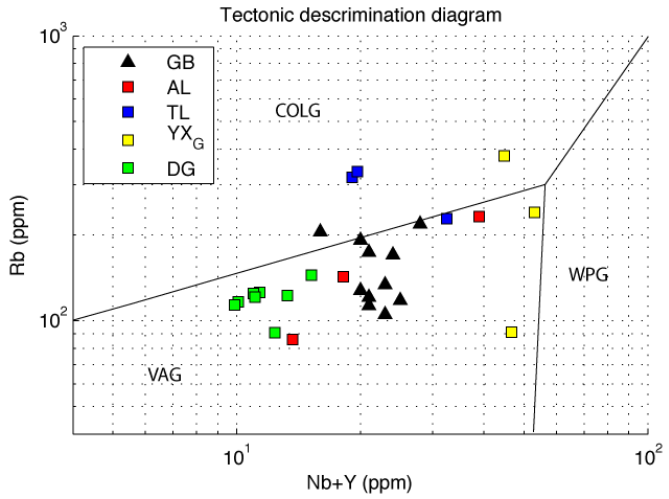

Figure 5.6: Tectonic discrimination diagram (Nb+Y vs. Rb) showing samples of the Arunachal & Tsona Leucogranites (AL, TL), Yala-Xiangbo & Dala Granitoids (YX_G, DG) and the Gangdese Batholith (GB Harrison et al., 2000). COLG - syn-collisional granites; WPG - within plate granites; VAG - volcanic arc granites (after Pearce et al., 1984). Note that data from the Dala Granitoids cluster within the VAG field.

rock composition, process and degree of melting, as has been proposed for other HHL (*e.g.* Inger and Harris, 1993). Similar arguments apply to the YX_G, however in this case, limited incorporation of extraneous material cannot be entirely ruled out.

5.5.1 Petrogenesis of the Dala granites

The DG plot with samples of the GB in the volcanic-arc granite field of a trace element discrimination diagram (*Figure 5.6*). They are consistent with water-saturated eutectic compositions between 1 and 3 kbar, which is in good agreement with field relations indicating their emplacement at shallow crustal levels (*Chapter 3*). Ion microprobe U-Pb dating indicates that the DG crystallised at 44.1±1.2 Ma (*Chapter 4*), concomitant with magmatism in the GB (Debon et al., 1986; Harrison et al., 2000; Dong et al., 2005; Mo et al., 2005). Mutual consistency of the DG and GB

major and trace element characteristics strongly suggest that their petrogeneses are linked. If correct, the DG therefore provide the first documented evidence of Himalayan syn-orogenic Gangdese-type magmatism south of the ITS; anywhere along the Main Himalayan Arc.

The geochemical characteristics of the GB have been interpreted to reflect mixing of mafic magmas with a component of sialic material (Debon et al., 1986; Mo et al., 2006). These mafic magmas are generally agreed to have formed in association with north-dipping oblique subduction of Neotethyan oceanic crust (Debon et al., 1986; Mo et al., 2006). Whereas the sialic component likely reflects relatively young crustal material, possibly derived from the accretionary wedge (Debon et al., 1986; Mo et al., 2006). The bulk geochemical characteristics of the DG are consistent with similar processes, and their ϵ_{Sr} isotopic compositions support a relatively primitive mantle source. However, the DG also show comparatively negative ϵ_{Nd}, which appears to require a component of more evolved crustal material.

Potential source materials for the DG may be assessed through construction of isotopic mixing models between various mafic and crustal end members. Although isotopic data were not collected from mafic samples outcropping within the Tethyan Himalaya, the majority of these bodies do not show palpable geochemical similarity to either the DG or GB, and they hence are considered more likely to pre-date Himalayan orogenesis. *Figure 5.7* shows mixing grids constructed between the inferred isotopic range of the eastern GB (Mo et al., 2006), and the median isotopic composition of various crustal end members, time corrected to 44 Ma. *Figure 5.7(a)* plot shows the plausible compositional range produced by simple mixing between material isotopically analogous to the GB and, high-grade pelitic lithologies outcropping in the core of the Yala-Xiangbo Dome (YX_P). Samples of the DG show notably

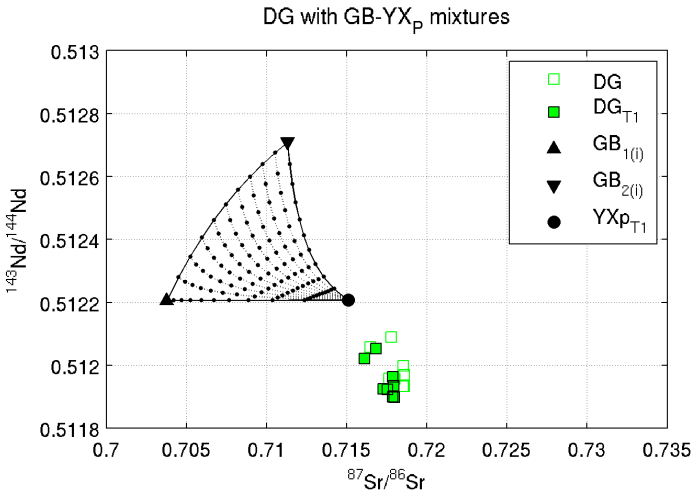

(a) Gangdese Batholith with Yala-Xiangbo pelites

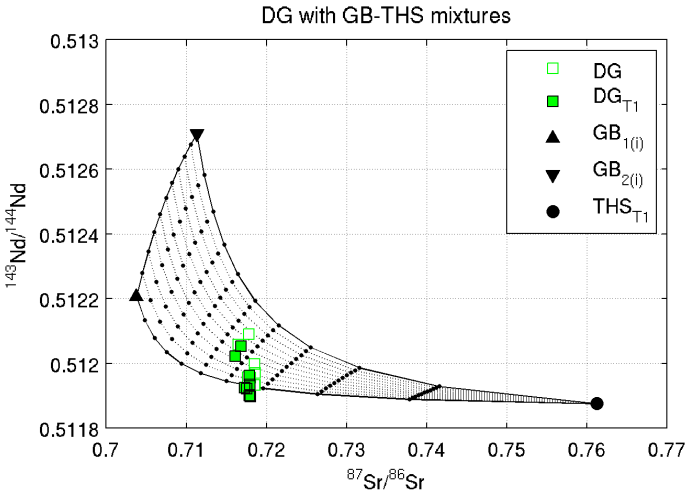

(b) Gangdese Batholith with THS metasediments

Figure 5.7: Isotopic composition of the Dala Granitoids (DG) plotted with mixing models constructed between the Gangdese Batholith (GB), Tethyan metasediments (THS), Greater Himalayan Crystallins (GHC) and Inner Lesser Himalaya (ILH). $GB_{1,2}$ are end members from a suite of analyses of samples from the GB, representing the range of documented isotopic compositions (Mo et al., 2006). Sialic end members (YX_P, GB, THS, ILH) are taken as the median of published values Richards et al. (2005, this study). Subscript *T1* denotes time corrected values to 44 Ma; subscript i denotes initial values for rocks of similar age to the DG (*ca.* 40 to 50 Ma). *Continues on next page...*

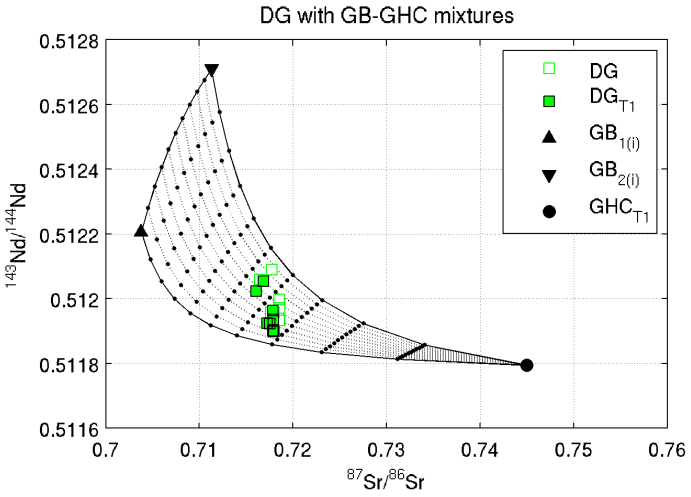

(c) Gangdese Batholith with Greater Himalayan Crystallins

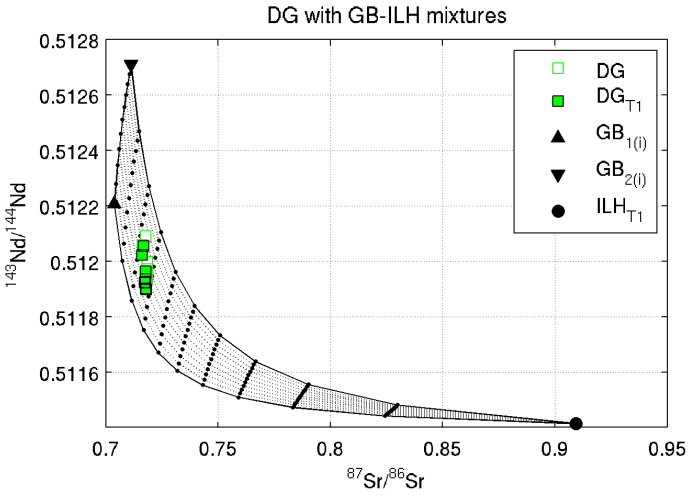

(d) Gangdese Batholith with Inner Lesser Himalaya

Figure 5.7: *Continued...*

less evolved $^{143}Nd/^{144}Nd$ and more evolved $^{87}Sr/^{86}Sr$ compositions, indicating that these end members cannot explain the observed DG isotopic range. It is conceivable, however, that the YX_P are not representative of the low-grade metasediments into which the DG are emplaced. Hence, *Figure 5.7(b)* shows a similar mixing grid constructed between the GB and published data from the THS metasediments outcropping elsewhere in the Himalaya (Richards et al., 2005). Although these data provide improvement over the YX_P, they also fail to encompass the complete range of DG isotopic compositions.

Figure 5.7(c) and *Figure 5.7(d)* show mixing grids constructed respectively between the GB and the GHC, and the GB and the ILH. Samples of the DG plot comfortably within the range of isotopic compositions expected for mixing between GB-type mafic magmas and either of the GHC or ILH crustal end members. The GHC sequences are widely cited as the basement to the Tethyan Himalaya, whereas the Lesser Himalayan series comprise more frontal parts of the range (LeFort, 1996; Yin and Harrison, 2000; Yin, 2006, and refs. therein). Moreover, studies elsewhere in the Himalaya have shown that while Eohimalayan (high pressure) metamorphism of the GHC sequences may have occurred as early as 45 Ma, post-collisional metamorphism of the Lesser Himalaya is largely confined to the Neohimalayan episode, associated with Miocene movement on the MCT (LeFort, 1996). The GHC sequences are therefore preferred as a potential source for the DG sialic component, comprising sub-equal mixtures with juvenile material similar to that which gave rise to granites of the GB. Although, given that at least parts of the THS sequences are isotopically indistinguishable from the GHC (Ahmed et al., 2000; Myrow et al., 2003; Richards et al., 2005), some contribution from these units cannot be ruled out.

The presence of Eocene Gangdese-type magmatism in the central Tethyan Himalaya has important implications for the structural architecture of the Himalayan Fold and Thrust Belt, and indeed for Himalayan evolutionary models generally. The timing of emplacement of these bodies is well correlated both with formation of the Yala-Xiangbo Granitoids *Chapter 4*, and a major phase of mantle-derived magmatism in the GB some 120 km to the north (Debon et al., 1986; Harrison et al., 2000; Dong et al., 2005; Mo et al., 2005, 2006). Moreover, these data effectively require a source of mantle-derived mafic material beneath the North Himalaya at *ca.* 44 Ma. The broader implications of these results are mentioned briefly in the preceding chapters, and will be discussed in detail in *Chapter 6*.

5.5.2 Petrogenesis of the Arunachal and Tsona Leucogranites and Yala-Xiangbo Granitoids

The geochemical characteristics of the AL, TL, $YX_{G,P}$ and AC broadly support inferred correlations with established lithotectonic units, as discussed in the preceding sections. Based on their geochemistry, several workers have proposed that the HHL of northern Nepal and the NHG of southern Tibet are derived from melting of the underlying pelitic lithologies during Neohimalayan metamorphism (LeFort et al., 1987; Harris and Inger, 1992; Inger and Harris, 1993; Guillot and Lefort, 1995; Harrison et al., 1997a; Yin and Harrison, 2000; Zhang et al., 2004a, and refs. therein). The tenability of these hypothesis in the eastern Himalaya may be similarly assessed by examining the elemental and isotopic composition of the AL, TL and YX_G.

The geochemical characteristics of the AL, TL and YX_G strongly support their inferred origin as anatectic melts. They show incompatible element enrichment, high ASI and relative HFSE depletions, which collectively, are considered characteristic of intracrustally derived granitoids (Harris et al., 1986). Their evolved isotopic

composition (relative to Miocene emplacement ages) also strongly support a crustal origin. The compositional range shown by these bodies likely reflects differences in source rock composition (Nabelek et al., 1992; Inger and Harris, 1993), as well as degree of melting and water pressure (Patino Douce and Beard, 1996; Patino Douce and Harris, 1998).

Source materials

The AL, TL and YX_G show a range of Rb-Sr and Sm-Nd isotopic compositions, which may be used to correlate them with potential source regions. The GHC sequences of the central and western Himalaya typically plot along an Rb-Sr isochron of *ca.* 480 Ma, show ϵ_{Nd} of *ca.* -15, and ϵ_{Sr} in the order of 500 to 2000 (Deniel et al., 1987; Ahmed et al., 2000; Myrow et al., 2003; Richards et al., 2005, *Figure 5.8*). Similarly, the HHL typically plot along a *ca.* 20 Ma Rb-Sr isochron, intersecting the GHC field close to initial values (Deniel et al., 1987; Inger and Harris, 1993; Miller et al., 2001; Stern et al., 1989; Ahmed et al., 2000; Zhang et al., 2004a, *Figure 5.8*). Measured ϵ_{Nd} for the HHL are typically in the range -10 to -15, and ϵ_{Sr} are comparable to the GHC. A recent study of lithologies from the North Himalaya (Zhang et al., 2004a) suggests that Cambrian orthogneisses outcropping in the cores of several North Himalayan Domes, are isotopically indistinguishable from the structurally highest components of the GHC sequence (*Figure 5.9*). These workers also noted that several NHG show comparable isotopic compositions to the HHL, and therefore argued that the GHC sequence extends beneath the North Himalaya, such that both granitoid belts are derived from the same source material. However, studies elsewhere in the Himalaya have found that at least part of the THS metasedimentary sequence, which comprise the vast majority of the outcrop in the North Himalaya, is also isotopically indistinguishable from the GHC (Ahmed et al., 2000; Myrow et al., 2003; Richards et al., 2005). Hence, by their own argument, Zhang

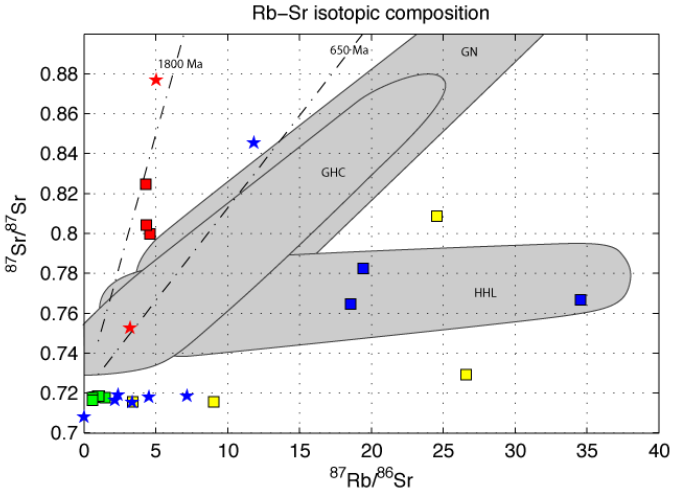

(a) Rb-Sr this study

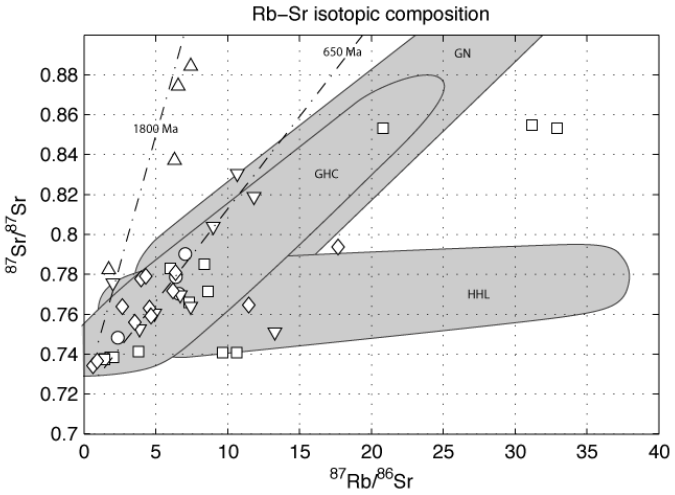

(b) Rb-Sr published

Figure 5.8: Rb-Sr isotope diagrams: (a) The Arunachal and Tsona Leucogranites (AL,TL), Yala-Xiangbo and Dala Granitoids (YX_G, DG), Arunachal crystallins (AC) and Yala-Xiangbo pelites (YX_P). (b) Published data from the North Himalayan Granites (NH_G) and North Himalayan metasediments (NH_P), (Zhang et al., 2004a), Inner Lesser Himalaya (LH_I), Outer Lesser Himalaya (LH_O), and Tethyan Himalayan metasediments (THS) (Richards et al., 2005). Labelled fields are the High Himalayan Leucogranites (HHL), Greater Himalayan Crystallins (GHC), and North Himalayan Gneiss and GHC orthogneiss (GN) (after compilation in Zhang et al., 2004a).

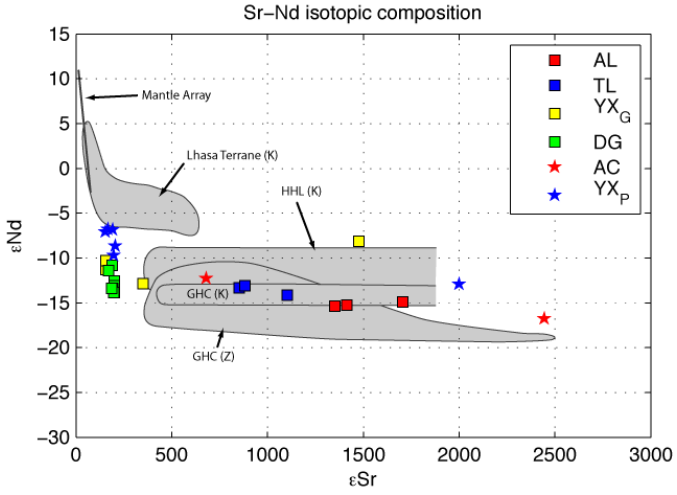

(a) ϵ_{Nd}–ϵ_{Sr} this study

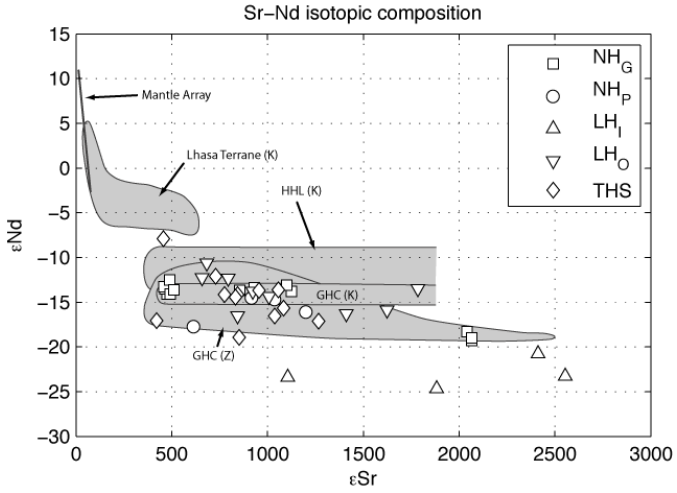

(b) ϵ_{Nd}–ϵ_{Sr} published

Figure 5.9: ϵ_{Nd}–ϵ_{Sr} isotope diagrams: (a) The Arunachal and Tsona Leucogranites (AL,TL), Yala-Xiangbo and Dala Granitoids (YX$_G$, DG), Arunachal crystallins (AC) and Yala-Xiangbo pelites (YX$_P$). (b) Published data from the North Himalayan Granites (NH$_G$) and North Himalayan metasediments (NH$_P$), (Zhang et al., 2004a), Inner Lesser Himalaya (LH$_I$), Outer Lesser Himalaya (LH$_O$), and Tethyan Himalayan metasediments (THS) (Richards et al., 2005). Labelled fields show the inferred range of isotopic compositions of the GHC, HHL and Lhasa Terrane, *K* denotes fields after Kapp et al. (2005), *Z* denotes fields after Zhang et al. (2004a).

et al. (2004a) cannot rule out the THS as a potential source for the NHG on the basis of isotopic data alone.

The TL are characterised by $^{87}Rb/^{86}Sr$ and $^{87}Sr/^{86}Sr$ ratios that are consistent with a 20 Ma Rb-Sr isochron, and fall within the documented isotopic range of other HHL on an ϵ_{Sr}–ϵ_{Nd} plot (*Figure 5.9*). Their isotopic compositions are therefore reconcilable with a source material that is isotopically analogous to both the micaschists of the central Himalayan GHC sequence (Inger and Harris, 1993) and components of the Tethyan Himalaya. However, given their structural position close to the STFS and geochemical similarity to other HHL, a GHC source is preferred.

The AL show generally lower $^{87}Rb/^{86}Sr$ and higher (more evolved) $^{87}Sr/^{86}Sr$ ratios than the TL, and fall outside the documented range of other HHL (*Figure 5.9*). Together with the AC, they appear to define an Rb-Sr isochron notably older than that which is considered characteristic of the GHC. The Rb-Sr isotopic composition of these samples are in fact more consistent with estimates from the Lesser Himalaya (*e.g.* Ahmed et al., 2000; Myrow et al., 2003; Richards et al., 2005). Excluding sample 0602011 (meta-granite, which may not be representative of a significant component of the Arunachal GHC sequence), the AC sample with the highest $^{87}Sr/^{86}Sr$ is 0602005, which was collected just above the Arunachal MCT (*Figure 5.1*). Sample 0602012 (Zhimithang gneiss, top of the AC sequence) plots at lower $^{87}Sr/^{86}Sr$ and $^{87}Rb/^{86}Sr$ within the established GHC field (*Figure 5.9*). It is therefore argued that in the Arunachal Himalaya, the hanging wall of the Arunachal MCT may include material derived from what is commonly referred to as the Lesser Himalayan sequences, and that melting of this material contributed to the formation of leucogranites of similar bulk composition to the central Himalayan HHL. Although confirming analyses are required, this conclusion provides notable

challenge to existing Himalayan paradigms. Given that the expected behaviour of thrust faults is to cut up and down section (Suppe et al., 1992), it is not surprising that some material transfer between the foot- and hanging-walls of the MCT should occur (*e.g.* Bollinger et al., 2004). A potential caveat to this hypothesis is that the both the presence of <1.8 Ga detrital zircons in these rocks (see *Chapter 2*) and their ϵ_{Nd} isotopic composition (*Figure 5.9*) potentially precludes them as components of the Inner Lesser Himalaya (Ahmed et al., 2000; Richards et al., 2005). However, since the isotope-stratigraphy of the Himalaya sequences remains somewhat contentious (Myrow et al., 2003) and recent structural studies have highlighted important differences between the Arunachal Lesser Himalaya and that described elsewhere, detailed work is required before firm conclusions may be drawn.

Samples from the Yala-Xiangbo Dome are isotopically heterogeneous. The 10 data collected cover an isotopic range that intersects with that documented from many other units outcropping within the Himalayan Fold an Thrust Belt (*Figure 5.9*). Two samples of the YX_G are isotopically comparable to the YX_P with $^{87}Sr/^{86}Sr$ of *ca.* 0.716, and ϵ_{Nd} of *ca.* -10. However, the remaining two samples show higher $^{87}Rb/^{86}Sr$ ratios and $^{87}Sr/^{86}Sr$ closer to the HHL. One anomalous sample of the YX_P has a significantly more evolved $^{87}Sr/^{86}Sr$ ratio closer to the Cambrian Orthogneiss field of Zhang et al. (2004a). Unfortunately, the isotopic range of the THS (particularly in the eastern Himalaya) is poorly constrained, however based on the available data, the YX_G are considered to be consistent with proximal melting of the surrounding metasediments, although a GHC source cannot be ruled out.

Melting processes

The elemental and isotopic characteristics of the AL, TL and YX_G are consistent with partial melting of pelitic lithologies during Himalayan metamorphism. How-

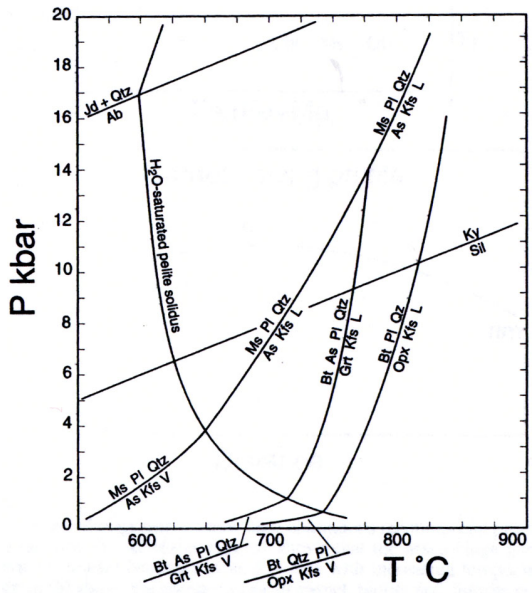

Figure 5.10: P-T diagram showing the principal melting reactions relevant to partial melting of pelites under amphibolite conditions (Spear, 1995, and references therein).

ever, the precise processes of granite genesis have important implications for Himalayan evolutionary models (*e.g.* LeFort et al., 1987; Inger and Harris, 1993; Harrison et al., 1997a, 1998a; Beaumont et al., 2001), as well as for our understanding of the feedbacks between deformation, melting and crustal rheology (*e.g.* Hollister and Crawford, 1986). The principal melting reactions relevant to pelites metamorphosed under amphibolite facies conditions are shown in *Figure 5.10*. Under fluid-present conditions and at pressures of 5–10 kbar, vapour-present melting begins at around 620–630°C (Spear, 1995, and references therein). At similar pressures and fluid-absent conditions, incongruent muscovite breakdown in "average" pelites can be initiated at 680–730°C (Spear, 1995, and references therein), although some workers have argued that this range be slightly higher (720–760°C) (Peto, 1976; Zhang et al., 2004a, and refs. therein). Incongruent fluid-absent biotite melting begins at 760–830°C (Le Breton and Thompson, 1988; Koester et al., 2002), subject to pressure, bulk composition and oxygen fugacity.

Several methods are potentially useful in distinguishing between the various processes of anatectic granite formation. These methods can be broadly categorised as either *thermometric* or *compositional*. Thermometric techniques (*e.g.* Harrison and Watson, 1983; Watson and Harrison, 1983; Rapp and Watson, 1986; Montel, 1993; Watson and Harrison, 2005; Watson et al., 2006) are primarily used to infer reactive process by constraining the temperatures of melt formation. Whereas compositional approaches (*e.g.* Harris and Inger, 1992; Harris et al., 1995; Ayres and Harris, 1997) focus on elemental systematics that are unique to one or more melting reaction. Both have previously been applied to Himalayan granitoids, and have arguably contributed to a significant component of current understanding of Himalayan orogenesis.

In granitic systems, the trace elements Rb, Sr and Ba reside predominantly in the major phases (micas and feldspars). Several studies have used partition coefficients for these elements to derive the equilibrium Rb-Sr-Ba systematics during anatexis (*e.g.* Harris and Inger, 1992; Inger and Harris, 1993). In the case of fluid-present melting, these workers argue that the restite will be depleted in feldspar, and hence, the corresponding liquid characterised by low Rb/Sr and high Sr/Ba ratios (Harris and Inger, 1992). In contrast, muscovite vapour-absent melting is suggested to result in increased proportions of feldspar in the restite, such that the corresponding liquid be characterised by high Rb/Sr and low Sr/Ba ratios (Harris and Inger, 1992). Incongruent fluid-absent melting of both muscovite and biotite (such that the melt equilibrates with a mica-free restite) is expected to lead to even stronger Rb enrichment (Harris and Inger, 1992). In reality, however, this distinction is dependent on source composition and only likely to be detectable at high melt fractions (Harris and Inger, 1992). At lower melt fractions, muscovite LILE partitioning must also

be considered (cf. Harris and Inger, 1992; Inger and Harris, 1993). Nevertheless, these attributes have been used to infer that the HHL of northern Nepal, and the NHG of southern Tibet, both formed by incongruent breakdown of muscovite under vapour-absent conditions (Harris and Inger, 1992; Inger and Harris, 1993; Zhang et al., 2004a).

Figure 5.11 shows LILE covariance diagrams for the AL, TL, YX_G, HHL, GHC and AC, plotted with calculated vectors for the three types of melting reaction described above. Note that the HHL define a trend that is parallel to the calculated vector for muscovite fluid-absent melting, which has been cited as key evidence in support of their origin through vapour absent melting of the underlying GHC micaschists (Harris and Inger, 1992; Inger and Harris, 1993; Zhang et al., 2004a). The TL plot amongst other HHL and also appear to be consistent with vapour-absent melting. Conversely, while also clustering amongst other HHL, the AL show lower Rb/Sr ratios and appear to be more consistent with vapour-present melting (*Figure 5.11*). The YX_G plot amongst other HHL but show significantly more inter-sample heterogeneity, and do not appear to define a clear trend. Unfortunately, the limited number of samples analysed (3 respectively of the AL and TL, and 4 of the YX_G) precludes reliable interpretation of the data in this way.

A recent study (Zhang et al., 2004a) used similar methods to argue that a variety of NHG from central-southern Tibet were also formed by vapour-absent muscovite melting. However, these workers also calculated zircon (T_{Zr}) and monazite (T_{Mz}) saturation melting temperatures (after Watson and Harrison, 1983; Harrison and Watson, 1983; Rapp and Watson, 1986; Montel, 1993) for their rocks. Even though many of these values fall below 720°C, they nonetheless universally attribute their samples to vapour-absent melting on the basis of trace element arguments (Zhang

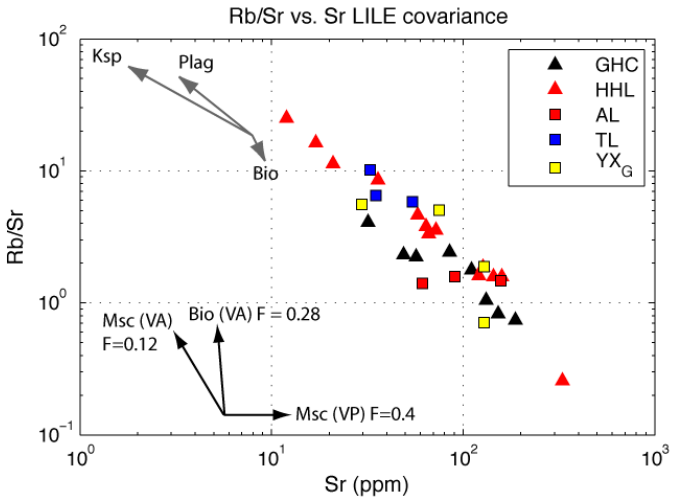

(a) Rb/Sr vs. Sr

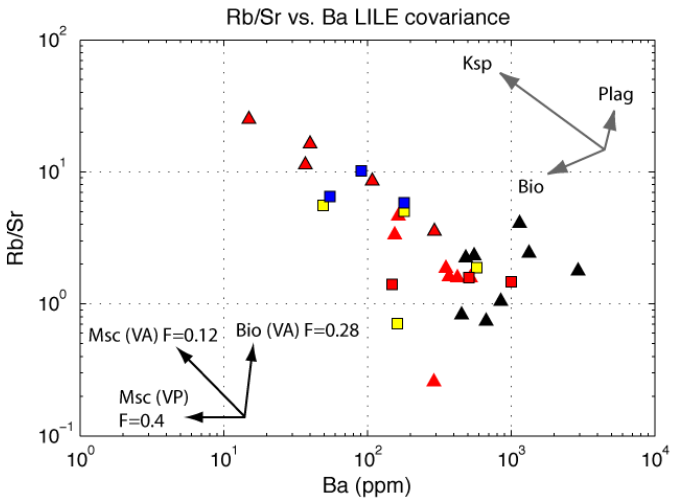

(b) Rb/Sr vs. Ba

Figure 5.11: LILE covariance diagrams showing the Arunachal Leucogranites (AL), Tsona Leucogranites (TL) and Yala granites (YX_G), plotted with published High Himalayan Leucogranites (HHL) and Micaschists (GHC) of the Greater Himalayan Crystalline sequence (Inger and Harris, 1993; Zhang et al., 2004a). Black vectors show partial melting reactions, grey vectors show 10% crystallisation of phases (after Inger and Harris, 1993).

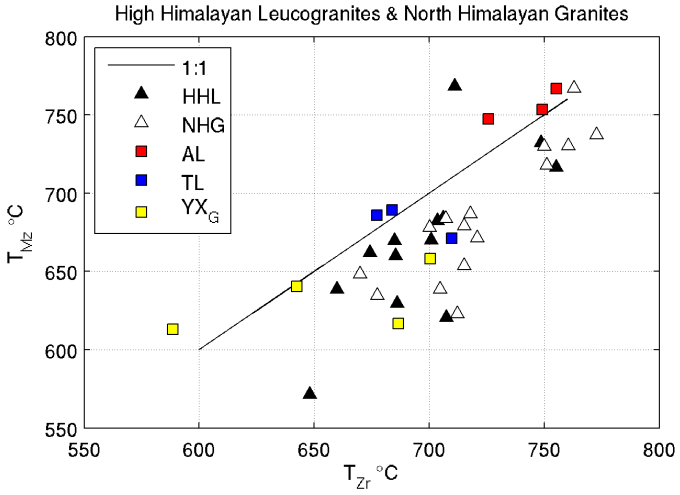

(a)

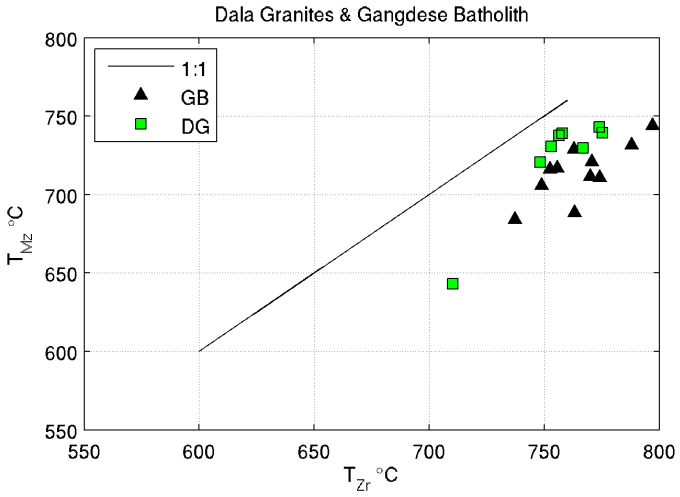

(b)

Figure 5.12: Zircon and monazite saturation melting temperatures (Watson and Harrison, 1983; Harrison and Watson, 1983; Rapp and Watson, 1986; Montel, 1993) calculated for the Arunachal and Tsona Leucogranites (AL, TL), Yala-Xiangbo Granitoids (YX_G) and Dala Granitoids (DG). Also shown are similar temperature estimates calculated using published data from the High Himalayan Leucogranites (HHL Inger and Harris, 1993; Zhang et al., 2004a), North Himalayan Granites (NHG Zhang et al., 2004a), and Gangdese Batholith (GB Harrison et al., 2000). All T_{Mz} are calculated assuming a [H_2O] of 8%.

et al., 2004a). *Figure 5.12* shows zircon and monazite saturation melting temperatures for the AL, TL and YX_G, plotted with those calculated using published data from the HHL and NHG (Inger and Harris, 1993; Zhang et al., 2004a). The data appear to define two populations, roughly separated by the muscovite vapour-absent melting reaction at 5-10 kbar (*Figure 5.10*). The TL and YX_G fall amongst the larger, lower temperature population, whereas the AL plot with a smaller group at *ca.* 730° to 780°C. This apparent inconsistency highlights some important caveats of both techniques.

Trend analysis automatically assumes that all data are derived from a single population subject to the same formative processes. While the consistency of HHL crystallisation ages along the length of the Himalayan arc suggest that the causes of melting are most likely related (Harrison et al., 1997a), there is no evidence that these bodies are mutually equilibrated. Hence, local variations in temperature, process, and degree of melting are plausible, if not expected. Moreover, in the case of trace element models, the partition coefficients used in several key studies (*e.g.* Harris and Inger, 1992; Inger and Harris, 1993) are now outdated (*e.g.* Henderson, 1982; Nash and Crecraft, 1985), and in some instances (plagioclase for example), now known also to vary with both temperature and bulk composition (Bindeman et al., 1998, J. Hermann *pers. comm.*). Indeed according to Harris and Inger (1992), no partitioning data were even available for micas at the time of publication, which could have a significant effect on C_L/C_O type calculations if these minerals are not completely extracted from the source. Furthermore, these calculations depend on accurate characterisation of the source material. While the micaschists of central Nepal represent a geochemically viable source for many studied HHL, they themselves have not actually experienced melting, and hence down-dip continuity must be assumed. It is also noted that geochemical distinctions between vapour-present

and vapour-absent melting (principally the Rb/Sr ratio) are subject to the degree of melting (F) and muscovite content of the source (Harris and Inger, 1992, Fig. 2), and hence become obscured at low values of one or both parameters (note the calculated vapour present trend shown on *Figure 5.11* assumes $F = 0.41$). Also, although significant fractional crystallisation is not widely favoured for the HHL (*e.g.* Inger and Harris, 1993), 10-20% crystallisation of K-feldspar, or K-feldspar and plagioclase could account for the entirety of the observed covariance trends (*Figure 5.11*).

Saturation melting temperatures must also be interpreted with caution. In samples without inherited zircon/monazite, the degree of saturation with respect to these phases is unconstrained, and hence temperature estimates must be regarded only as minimum values (Watson and Harrison, 1983; Harrison and Watson, 1983; Rapp and Watson, 1986; Montel, 1993). Likewise, where abundant inherited phases are present, the Zr and REE content of the melt will be overestimated by bulk-rock analysis and therefore the calculated temperatures provide only an upper bound. It is also possible (although hard to envisage for regional crustal melting) that melts which have been rapidly removed from their source region may also not have fully equilibrated with their source material, thereby rendering the governing thermodynamic relationships on which both thermometers are based, insufficient to explain the melt composition (Clemens and GTR, 1998, and refs. therein). In the case of crustal melts, T_{Mz} arguably provides a more reliable estimate of the melt-temperature than T_{Zr}, since monazite is less likely to be inherited in significant quantities (Harrison et al., 2002). However, the monazite thermometer is more susceptible to additional uncertainty in the H_2O content of the melt. The T_{Mz} given by Zhang et al. (2004a, their Table 1), for example, are only reproducible assuming a nominal water content ($[H_2O]$) of *ca.* 3%, which may well be too low (*e.g.* Holtz et al., 2001), consequently implying that their quoted temperatures are too high.

All temperatures shown on *Figure 5.12* were calculated assuming an [H_2O] of 8%, although any value in the range of 5 to 11% is probably reasonable (*e.g.* Holtz et al., 2001). The calculated T_{Zr} is unaffected by H_2O (Harrison and Watson, 1983).

The obvious implication of *Figure 5.12* is that a significant proportion of Himalayan granitoids are in fact consistent with vapour present melting. Moreover, all studied HHL and NHG contain inherited zircon (T.M. Harrison *pers. comm.*, this study) and most contain inherited monazite (Harrison et al., 1995), indicating that the calculated saturation temperatures are not likely to be underestimated. Minor deviations between the calculated T_{Mz} and T_{Zr} are attributed to differences in the relative proportions of the inherited phases. Nevertheless, given the aforementioned caveats it remains uncertain whether these values can really be regarded as precise estimates of the temperature of melt formation.

Recent calibration of the Ti-in-zircon thermometer (Watson and Harrison, 2005; Watson et al., 2006) has delivered a potential new dimension to this problem. This method provides an empirical basis under which the crystallisation temperature of zircon may be estimated by measuring its titanium content (Watson and Harrison, 2005; Watson et al., 2006, *Chapter 4*). Apparent temperature estimates are precisely equated with absolute values where a_{TiO_2} and a_{SiO_2} are also known, otherwise an additional uncertainty of *ca.* 60–70°C (for temperatures of around 700°C) applies (Watson and Harrison, 2005; Watson et al., 2006; Ferry and Watson, 2007). Recent advances in ion-microprobe analytical procedures (*Chapter 4*) have allowed zircon Ti-contents to be measured with high accuracy and precision, at resolutions sufficient to individually correlate the resultant apparent temperatures (T_{Ti}) with conventional ion-microprobe U-Pb dating (*Chapter 4*). This is particularly valuable in the context of zircon-saturated anatectic melts, as it provides a means with which

to access the crystallisation temperature of neoformed zircon which can be reliably be attributed to a particular magmatic episode. The [Ti] of zircons from all sample suites was measured by ion-microprobe, and the results are discussed in detail in *Chapter 4*. The Arunachal and Tsona Leucogranites, and the Yala-Xiangbo Granitoids are all silica-rich and contain rutile. As such, the a_{TiO_2} and a_{SiO_2} during crystallisation of these anatectic samples is inferred to approximate unity, and the calculated apparent temperatures approach their true values (see *Chapter 4* for further discussion).

Magmatic zircons from the YX_G define a broad T_{Ti} distribution centred well below the muscovite fluid-absent melting reaction; these data have been interpreted to reflect fluid-mitigated recrystallisation (*Chapter 4*). Field relations indicating abundant tourmaline and pegmatite (*Chapter 4*) together with geochemical data discussed above, collectively support fluid-present melting for these rocks. The AL and TL, however, define offset T_{Ti} peaks, respectively centred at *ca.* 660°C, and *ca.* 730°C (*Figure 4.13*). This observation is surprising in that it indicates the temperature peaks derived from Ti-thermometry are reversed with respect to those estimated using bulk-rock saturation methods (*Figure 5.12*). Several factors may potentially account for this discrepancy. Considering first whether the apparent T_{Ti} peak off set is robust, the dependence of the Ti-thermometer on a_{TiO_2}, is such that in anatectic melts the apparent T_{Ti} is more likely to under- rather than over-estimate the true value, although this is not considered likely for these samples. Interestingly however, the AL were found to contain significantly more inherited zircon than the TL, based on combined electron-imaging and ion-microprobe dating (*Chapter 4*). This suggests that the apparent offset between the AL and TL T_{Zr} is not robust, but instead due to high bulk [Zr]. The AL are estimated to contain roughly one third neoformed zircon, whereas the TL contain at least two thirds. Hence, multiplying

the Zr contents of each suite respectively by the appropriate scalar, the corrected T_{Zr} for both the AL and TL are recalculated to be within error of each other (in the range 650° to 680°C), although the AL T_{Zr} could even be lower than the TL if the proportion of inherited zircon has been underestimated. Moreover, Harrison et al. (2007) have shown that in plutonic rocks cooling from high temperature, T_{Zr} will underestimate the temperature at which zircon begins to crystallise. This may explain the offset between the TL T_{Zr} and T_{Ti} peak, further indicating that for most HHL and NHG, the bulk T_{Zr} (uncorrected) is unlikely to accurately record the temperature of melt formation.

Harrison and Watson (1983) showed that for water contents applicable to most granitic melts, zircon dissolution is fast with respect to the time scales of melt formation. Therefore, it is reasonable to assume that the AL and TL magmas were incapable of dissolving any more Zr when at their peak temperatures. Because the solubility of Zr in granitic melts varies exponentially with temperature (Watson and Harrison, 1983), Zr-saturated magmas are expected to crystallise zircon rapidly once temperature begins to decrease. This suggests that in the case of zircon-saturated anatectic melts subject to monotonic cooling, the largest T_{Ti} peak can be expected to lie at the upper end of the temperature spectrum, and will accurately record the temperature of melt formation. Although the crystallisation sequence may potentially affect the form of this distribution down temperature, this effect is only likely to be significant towards the latter stages of crystallisation, by which time [Zr] content of the magma (and hence its capacity to crystallise zircon) will be reduced. The TL are characterised by a temperature distribution showing a single peak at the upper end of the temperature spectrum (*ca.* 730°C), and single U-Pb age peak that is also slightly skewed to older ages (*Chapter 5*), both of which are adequately explained by the aforementioned scenario. The TL are therefore interpreted to be

consistent with magma formation dominated by vapour-absent muscovite melting, followed by emplacement and relatively rapid crystallisation close to the STFS.

The AL are characterised by a broader age distribution (skewed to younger ages, and temperature spectrum showing a dominant peak at *ca.* 660°C, with a small shoulder on the high temperature side (*ca.* 730°C) (*Chapter 4*). The position of this large peak is consistent with AL magma formation dominated by fluid-present melting reactions, although the higher temperature peak-shoulder may reflect some incorporation of higher-temperature material similar to that which gave rise to the TL. The Rb-Sr isotopic composition of the Arunachal Leucogranites suggests that their source included material derived from what is commonly termed the Lesser Himalayan sequences. The presence of this material within the Arunachal Crystalline sequence is attributed to footwall accretion associated with movement of the MCT, as proposed by at least one evolutionary model (Bollinger et al., 2004, 2006). Hence, melting of this material conveniently explains the presence of leucogranite outcropping at the base (and indeed throughout) the Arunachal Crystalline sequence (cf. Nepal Yin et al., 2006; Yin, 2007, this study). The high temperature shoulder on the AL T_{Ti} peak is interpreted to reflect incorporation of higher temperature material derived from vapour-absent melting within the Arunachal GHC sequences proper. This interpretation is further supported by the observed progressively higher position of the dominant temperature T_{Ti} peak proportional to increasing structural height (i.e. wettest at the bottom, *Chapter 4*), as would be expected in the context of an inverted temperature gradient. Indeed it could be argued that these data provide a snapshot of that inverted gradient - having time, temperature and geometric constraint - whereas many other lines of evidence merely record the metamorphic field gradient.

Fluid present melting of the GHC sequences was previously advocated in explaining the formation of the Miocene HHL (LeFort et al., 1987), however, this model has not been widely favoured by workers in the central Himalaya (Harris and Inger, 1992; Inger and Harris, 1993; Harrison et al., 1997a, 1998a), although such processes may be applicable to certain bodies outcropping in NW India (Prince et al., 2001). Several influential papers based in this region (*e.g.* Harris and Inger, 1992; Inger and Harris, 1993; Harrison et al., 1997a, 1998a) have contributed to the widespread perception that the HHL were formed by fluid-absent melting, almost without exception. This interpretation may be correct for the greater volumetric proportion of the HHL studied to date. However, it is argued that several key methods employed in arriving at these conclusions are insensitive to local variations in the processes of melt formation. Indeed this interpretation may account for samples exhibiting low Rb/Sr and/or saturation melting temperatures in existing published datasets (*Figure 5.11*, *Figure 5.12*).

Unlike the GHC, the exposed Lesser Himalayan sequences have not experienced widespread Eohimalayan metamorphism (LeFort, 1996; Yin and Harrison, 2000; Celerier, 2007), and hence contain abundant hydrous phases. Fluid present melting is therefore predicted by isotopic arguments suggesting that the lower parts of the Arunachal Crystalline sequence comprise material derived from the Lesser Himalaya. Some workers have also questioned the viability of fluid-present melting generally in the context of the Neohimalayan paradigm, citing problems with fluid supply, permeability, and liquid/melt migration (*e.g.* Ingebritsen and Manning, 2002). Numerical models of have demonstrated - almost without exception - that during Miocene slip, isotherms around the MCT rapidly became sigmoidal (Harrison et al., 1998a; Beaumont et al., 2001; Bollinger et al., 2004, unpublished model results). Although early studies struggled to produce sufficient heat to allow anatexis to occur in association

with slip along a fault angled close to the current dip of the MCT (England et al., 1992), more recent work has shown that this problem is removed when slip occurs on a shallow dipping ramp, or ramp-flat geometry (Harrison et al., 1998a, unpublished model results).

The majority of de-watering takes place during greenschist and lower amphibolite facies metamorphism, but H_2O-producing continuous reactions can be expected in most lithologies right up to the onset of partial melting (Spear, 1995). Hence, in the vast majority of scenarios where isotherms in crustal rocks close to the "wet" solidus are inverted, the lower temperature portion of the sigmoid has the potential to release fluid into the hotter overlying material and initiate melting. Several of the same models have also suggested that the ratio of under- to over-thrusting during MCT motion may have been as high as 3:1 (Bollinger et al., 2004, 2006, unpublished model results), which both provides optimal conditions for development of a persistent inverted geotherm, and implies that the supply of fertile material to the melt zone likely greatly outweighed the rate at which the material accumulating melt was removed. This effect may also have been further enhanced by velocity gradients across the shear zone, such that rocks closest to the central plane of zero velocity took the longest to be exhumed (or buried). Furthermore, since the proportion of melt generated is primarily limited by the availability of fluid, any such fluid migrating *e.g.* by dilatancy pumping (Brown, 1994; McCaig et al., 2000) would be expected to produce locally relatively high melt fractions (potentially sufficient to allow melt migration) upon entering the upper plate.

Although many aspects of Himalayan granitoid formation remain poorly understood, data presented in this study support local "wet" melting, both in the formation of Eocene granitoids outcropping within the North Himalaya, and Miocene

granitoids in the lower crystalline sequences of the Arunachal Himalaya. Hence, in spite of previous criticism, it is argued that fluid-present melting remains a plausible, if not likely hypothesis to explain the forming of some granitoids during Himalayan orogenesis.

5.6 Conclusions

Geochemical and isotopic studies indicate that post-collisional magmatism in the east Himalayan can be broadly categorised into two modes. The first comprises a series of dykes, sills, and small plutons outcropping in the central Tethyan Himalaya. These bodies (the Dala Granitoids, DG) represent mantle-derived magmas, formed in association with concomitant magmatism in the Gangdese Batholith (GB), which assimilated approximately 50% crustal material from the GHC sequences during ascent and emplacement at shallow crustal levels. Bodies assigned to this group appear to be confined to the Eohimalayan, and represent a new mode of magmatism not so far documented elsewhere in the Himalaya. Their emplacement provides significant challenge to existing paradigms for post-collisional granitic magmatism along the Himalayan Arc, and places valuable new constraints on the early history of orogenesis.

The second group comprises anatectic granites similar to the High Himalayan Leucogranites (HHL) and North Himalayan Granites (NHG) documented elsewhere along the Himalayan arc. Three suites were analysed. The Arunachal Leucogranites (AL) and Tsona Leucogranites (TL) are Miocene in age, and outcrop respectively within the Arunachal Greater Himalayan Crystalline (GHC) sequence and around the South Tibetan Fault System. They are considered analogous to the HHL. The Yala-Xiangbo Granitoids (YX_G) outcrop in the central Tethyan Himalaya, forming an igneous complex in the core of the Yala-Xiangbo Dome. These bodies are

broadly comparable to the NHG in terms of structural position and emplacement style, however they are notably older, being at least partially concomitant with the DG. Geochemical, isotopic and thermometric data are consistent with formation of the TL by vapour absent melting of the underlying GHC sequences, as has been widely proposed for other HHL. The AL however, although also derived from partial melting of crustal material, appear to record vapour-present melting, which marks significant deviation from existing paradigms for Neohimalayan granitic magmatism. Moreover, their source region likely includes material derived from what is commonly termed the Lesser Himalayan sequences. This conclusion is also at odds with studies of HHL elsewhere. The Eohimalayan YX_G are best attributed to proximal vapour-present melting of the surrounding THS metasediments.

Vapour-present melting of Himalayan sequences, originally proposed by early workers, has not been widely favoured by more recent studies of either the HHL or NHG. Although this conclusion may be correct for the greater volumetric proportion of Miocene peraluminous granitoids in the Himalaya, it is argued that key methods employed by these workers may be both insensitive to local variations in formative processes, and in some cases, capable of producing erroneous results. Vapour-present melting, represents a plausible, if not likely scenario to explain at least some granitoid formation during Neohimalayan MCT slip. Therefore, it is suggested that more detailed studies of individual bodies are required, including application of the newly calibrated Ti-in-zircon thermometer, which represents the most reliable method to access the formative temperatures of zircon-saturated near minimum-melt magmas.

Collectively, these data show that the spectrum of Himalayan peraluminous magmatism along the main Himalayan Arc is much more diverse than was previously thought. Results provide significant challenge to existing paradigms for Himalayan

granitic magmatism, and indicate that several evolutionary models may be in need of revision. Our data further suggest that the tectonics of the eastern Himalaya should be critically evaluated without undue preference towards conclusions drawn elsewhere.

Chapter 6

Tectonics of the eastern Himalaya

6.1 Introduction

Over a century of research has sought to understand formation of the Himalaya, one part of the world's largest active orogenic belt (Suess, 1875; Argand, 1924; Heim and Gansser, 1939; Gansser, 1964; LeFort, 1975, 1996; Yin and Harrison, 2000; Yin, 2006). These studies have given rise to a multitude of evolutionary models, some of which hold far-ranging implications for theories of orogenesis and indeed continental deformation generally (*e.g.* LeFort, 1975, 1996; Harrison et al., 1999b; Yin and Harrison, 2000; Beaumont et al., 2001, and refs. therein). Although significant achievements have been made, many aspects remain poorly understood and widespread consensus has not yet emerged.

Arguably, two significant barriers to the realisation of unifying models, have been over-reliance on regional extrapolations based on inferred correlations along the length of the main Himalayan Arc and a poor understanding of the orogen's

early history. Data presented in this study impact upon both of these factors.

6.1.1 Purpose of this chapter

The purpose of this chapter is to summarise and evaluate the results discussed in those preceding, with a view to establishing a framework for the tectonic evolution of the eastern Himalaya. The results document deformation and a magmatic emplacement episodes that are much older than those previously recognised elsewhere along the main Himalayan Arc, and place new constraint on the early history of Himalayan orogenesis. These data challenge existing paradigms in ways that vary from minor (*e.g.* the dehydration melting hypothesis for the HHL) to substantial (*e.g.* dynamics of the Indian lithosphere, the channel flow hypothesis).

6.2 Summary geological evolution

The Himalaya extend for over 2000 km from Pakistan to Burma (*Figure 1.1*, *Figure 1.2*), forming one part of the Alpine-Himalayan chain; the topographic expression of the world's largest active orogenic belt. The vast majority of the outcrop within the Himalaya appears to be made up of units deposited as part of the Indian passive margin sequences from the Paleozoic to early Tertiary (*e.g.* LeFort, 1975; Liu and Ensele, 1994; LeFort, 1996; Garzanti, 1999; Yin and Harrison, 2000; Myrow et al., 2003, and refs. therin). In the east, this interpretation is supported by recently proposed correlations between lithologies of the Arunachal Himalaya and those outcropping in the Shillong Plateau (Yin, 2007). These data provide further evidence that the Himalayan Fold and Thrust Belt (HFTB) comprises units that are predominantly of Indian affinity rather than accreted from an exotic terrane (*cf.* DeCelles et al., 2000).

The role of pre-Himalayan deformation within the HFTB, in general, poorly constrained. However, several studies have indicated that at least parts of the Himalayan sequence experienced an early Paleozoic tectonothermal event associated with widespread Cambro-Ordovician magmatism, regional uplift and the development of unconformities (*e.g.* Miller et al., 2001; Wiesmayr and Grasemann, 2002; Gehrels et al., 2003). Structures formed during this period may have played a role in localising subsequent Himalayan deformation (Vannay and Steck, 1995; Yin and Harrison, 2000; Wiesmayr and Grasemann, 2002; Gehrels et al., 2003; Yin, 2007).

The absolute timing of the initiation of collision between India and Eurasia is the subject of ongoing debate (LeFort, 1996; Yin and Harrison, 2000; Yin, 2006; Aitchison et al., 2007). Some workers suggest that collision began in the latest Cretaceous (Yin and Harrison, 2000, and refs. therein) or by *ca.* 51 Ma (Zhu et al., 2005). An alternative view, however, is that India was still too far removed from Eurasia at those times and that early Himalayan orogenesis may have begun whilst these two cratonic regions were still separated by a significant expanse of oceanic and/or transitional crust (Aitchison et al., 2007, and refs. therein). Geochemical arguments discussed below require a source of mafic material comparable to that which gave rise to the Eurasian Gangdese Batholith beneath the Tethyan Himalaya during the Eocene, suggesting that the Indian foreland must have been relatively close to a Eurasian arc at this time (*Chapter 5*). However, these data do not rule out the presence of a back arc basin, or multiple subduction zones.

The dominant process controlling the first order morphology of the HFTB since the latest Cretaceous, has been the accommodation of >500 km of N-S convergence between India and Eurasia (Johnson, 2002). This deformation has led to dissection of the Indian foreland sequences into a series of shear bounded, predominantly N-

dipping, tectono-metamorphic slices that comprise the HFTB today (LeFort, 1996; Yin and Harrison, 2000, *Figure 1.2*). Himalayan orogenesis has traditionally been separated into two episodes, distinguished by the timing of peak metamorphism and deformation in the Greater Himalayan Crystalline (GHC) sequences of central Nepal and NW India (LeFort, 1996). The results of this study broadly support this distinction.

6.2.1 The Eohimalayan

The Eohimalayan episode, as preserved along the frontal ranges of the High Himalaya, has traditionally been equated with early crustal thickening and high-pressure metamorphism, but is otherwise relatively poorly known (LeFort, 1996; Yin and Harrison, 2000). This paucity of data from the first *ca.* 35 Ma of Himalayan orogenesis has been a significant obstacle in establishing regional correlations and evolutionary models. The Tethyan Himalayan Sequences (THS) are the structurally highest and inferred earliest accreted unit of the Himalayan Fold and Thrust Belt (*Figure 1.2*). As such, they are uniquely placed to retain information pertaining to the this time period.

The earliest Himalayan deformation so far documented in the THS is represented in NW India and northern Nepal by a series of predominantly N-vergent folds and nappes that likely formed during the earliest Tertiary (*Chapter 2*; *Chapter 3* and refs. therein). These structures have not been directly identified further to the east, although this may be due to the lack of detailed studies in these areas (*Chapter 2*). The second phase of deformation is associated with development of a system of predominantly south-vergent folds and thrusts (*Chapter 2* and refs. therein). This deformation is present along the length of the main Himalayan Arc, and represents the dominant thickening event affecting the Tethyan Himalaya (*Chapter 2* and

refs. therein). Correlations with structures in the flanking sequences of the North Himalayan Domes (NHD) indicate that it is similarly represented at deeper levels within the stratigraphic section (*Chapter 3*). The age of this event is constrained to be greater than 44.1±1.2 Ma by undeformed granitoid plutons (the Dala Granitoids, *Figure 2.2*) and other geochronological evidence (*Chapter 3*, *Chapter 4*).

In the eastern Himalaya, Eohimalayan crustal thickening was temporally associated with arc-magmatism in the Gangdese Batholith (*Figure 1.2*, *Figure 2.2*), and both amphibolite grade metamorphism and granitic magmatism within the Tethyan Himalaya. The peraluminous Yala-Xiangbo Granitoids - outcropping in the core of the Yala-Xiangbo Dome (*Figure 2.2*) - crystallised at 42.3±4.9 Ma (*Chapter 4*), although there is no evidence that they experienced substantial cooling until the Miocene (*Chapter 3*). These units likely formed through partial melting during high grade metamorphism of structurally deeper parts of the Tethyan metasedimentary sequence (*Chapter 3*; *Chapter 4*; *Chapter 5*). The Dala Granitoids were emplaced into the deformed sub-greenschist facies Triassic metasediments (*Figure 2.2*) at 44.1±1.2 Ma, where they cooled rapidly to ambient mid-crustal temperatures (*Chapter 3*; *Chapter 4*). Their geochemistry reflects mixing between Gangdese-type arc magmas and a crustal component derived from units similar to the GHC sequences of the frontal Himalaya (*Chapter 4*; *Chapter 5*; *Figure 1.2*). The Gangdese granitoids themselves have traditionally been cited as components of a north-dipping subduction complex active along the southern margin of Eurasia during the Cretaceous (Yin and Harrison, 2000, and refs. therein). However, although Cretaceous bodies undoubtedly exist (Debon et al., 1986; Harrison et al., 2000), no systematic study has yet been conducted. Recent work suggests that in the eastern Himalaya, the majority of bodies may in fact have Eocene (50–40 Ma) crystallisation ages (Mo et al., 2007).

6.2.2 The Neohimalayan

The Neohimalayan episode has been relatively well documented in the frontal Himalaya. It is characterised by high-temperature metamorphism and deformation associated with Miocene slip on the MCT-MBT-STFS fault systems (LeFort, 1996; Yin and Harrison, 2000, *Figure 1.2*). In the southern Tethyan Himalaya, this deformation also led to development of a mylonitic fabric and reorientation of pre-existing structures during normal-sense motion on the STFS (*Chapter 2*). Furthermore, activity on the STFS was at least partially contemporaneous with reverse-sense motion on the Great Counter Thrust (GCT) system, which has been interpreted by some workers as part evidence indicating that these structures link at depth, effectively translating the entire THS some distance to the north (Yin et al., 1994; Quidelleur et al., 1997; Yin and Harrison, 2000; Yin, 2006, *Figure 1.2*). The latter stages of activity on these fault systems appears to have been temporally associated with crustal thinning and rapid exhumation at several North Himalayan Domes (NHD, *Chapter 3* and refs. therein). Indeed shear zones separating the inner and outer domains of several of these structures have been cited as exhumed portions of the STFS, preferentially uplifted by internal duplex development along the Main Himalayan Decollement (*Chapter 3* and refs. therein).

Relatively few data exist pertaining to the timing of movement on major fault systems in frontal parts of the eastern Himalaya. However, recently conducted geo- and thermochronology from the Arunachal Himalaya suggest that the Arunachal MCT was probably active into the late Miocene (Yin, 2007). The timing of motion on the Arunachal STFS is inferred also to be Miocene by along-strike correlation. The eastern GCT (locally known as the Renbu Zedong Thrust, RZT) experienced a main phase of slip at *ca.* 19–15 Ma (Quidelleur et al., 1997).

Neohimalayan deformation and metamorphism have traditionally been associated with granitic magmatism along the frontal ranges and in the central THS. The High Himalayan Leucogranites (HHL, *Figure 1.2*) were emplaced along the peaks of the High Himalaya between *ca.* 23–19 Ma (Harrison et al., 1998a; Yin and Harrison, 2000, and refs. therein), and are widely believed to have formed by muscovite dehydration of the underlying pelitic lithologies (*Chapter 5* and refs. therein). The North Himalayan Granites (NHG, outcropping within the Tethyan Himalaya, *Figure 3.1*) are generally thought to be slightly younger (*ca.* 19–10 Ma) and hotter, although their exact origins remain in dispute (*Chapter 5* and refs. therein). It is noted, however, that whereas the HHL form a belt of granitoids stretching along the length of the main Himalayan Arc (*Figure 1.2*), virtually all NHG studied to date are confined to smaller area between *ca.* 85° and 92°E (*Figure 3.1*, *Figure 2.2*).

In the eastern Himalaya, the Tsona Leucogranites - emplaced into southern parts of the THS close to the STFS (*Figure 4.1*)- were formed by muscovite dehydration melting of pelitic lithologies and crystallised at 18.8±1.2 Ma (*Chapter 4*; *Chapter 5*). They are broadly analogous to the HHL of northern Nepal (*Chapter 5*). The Arunachal Leucogranites - emplaced into the Arunachal Crystalline sequences in the hanging wall of the Arunachal MCT (*Figure 4.1*) - crystallised at 20.2±2.0 Ma (*Chapter 4*). However, these bodies appear to be at least partially derived from "wet" melting of material isotopically similar to the Lesser Himalayan Sequences outcropping elsewhere along the main Himalayan Arc (*Chapter 5*, *Figure 1.2*). Furthermore, samples collected at the base of the Arunachal Crystalline sequence in the immediate hanging wall of the Arunachal MCT (*Figure 5.1*) also have isotopic characteristics similar to those of the LHS metasediments (*Chapter 5*). These data are interpreted as indicating that in the Arunachal Himalaya, the hanging wall of the MCT includes material accreted from the foot wall Lesser Himalayan Sequences.

This material has experienced partial melting, giving rise to leucogranites of similar (although not identical) geochemical composition to the HHL of northern Nepal (*Chapter 5*).

The NHG outcrop in the central Tethyan Himalaya (*Figure 3.1*, *Figure 2.2*), and are most commonly found in association with North Himalayan Domes (NHD). The majority of bodies studied to date have Miocene crystallisation ages, within a few million years of the inferred timing of exhumation of their host structure based on thermochronology. In the eastern Himalaya, however, although rapid exhumation of the Yala-Xiangbo Dome (*Figure 2.2*) occurred during the Miocene - synchronous with other similar structures along strike - the Yala-Xiangbo Granitoids (*Figure 2.2*) have Eocene crystallisation ages that are significantly older than all other NHG studied to date.

The most recent large-scale structures affecting the eastern THS and indeed the Tethyan Himalaya generally, comprise a series of roughly NNE-SSW trending (arc-normal) rifts (*Figure 1.2*). These structures are present at quasi-regular intervals along the length of the main Himalayan Arc, likely formed in association with E-W extension of the Tibetan Plateau during the Pliocene (*Chapter 2*).

6.3 Discussion

Data compiled from this and other studies indicate that many aspects of the geological evolution of the eastern Himalaya (*ca.* 92°E) are similar to those described elsewhere along the main Himalayan Arc. However, several key differences emphasise along-strike heterogeneity that, to date, has not been widely recognised elsewhere. These and other factors may be used to infer aspects of the paleo-geometry of the Himalayan Fold and Thrust Belt (HFTB) that, in turn, place significant new

requirements on Himalayan evolutionary models.

6.3.1 Eohimalayan assembly of the HFTB

Current concepts of the assembly of the Himalayan Fold and Thrust Belt (HFTB) derive largely from our understanding of the Neohimalayan orogenic episode (LeFort, 1996; Yin and Harrison, 2000). Information pertaining to the nature and indeed timing of Eohimalayan deformation have so far been largely unavailable. However, the results of this and other studies provide valuable new insight into the early history of Himalayan orogenesis.

Preceding chapters introduced a regional correlation scheme describing the structural evolution of Tethyan Himalaya - the inferred earliest accreted unit of the Himalayan Fold and Thrust Belt (*Chapter 2*, *Chapter 3*). According to this scheme, Eohimalayan crustal thickening began in the early Tertiary, and was effectively complete by *ca.* 45 Ma. This age is notably older than has previously been thought. Furthermore, data from the Yala-Xiangbo Dome and Yala-Xiangbo Granitoids (*Figure 1.5*) imply that the Eohimalayan episode was at least locally associated with high-temperature metamorphism sufficient to generate peraluminous leucogranite through partial melting of pelitic lithologies. These results show that components of the Indian foreland sequences experienced significant shortening and heating during the first *ca.* 20 Ma of Himalayan orogenesis. The T-t histories of both the Dala and Yala-Xiangbo granitoids indicate that these units remained broadly isothermal from the late Eocene or early Oligocene, until their rapid exhumation in the mid Miocene. This could be interpreted to indicate that the Tethyan Himalaya experienced relatively little tectonic activity during this time period, which implies that the locus of shorting likely shifted elsewhere.

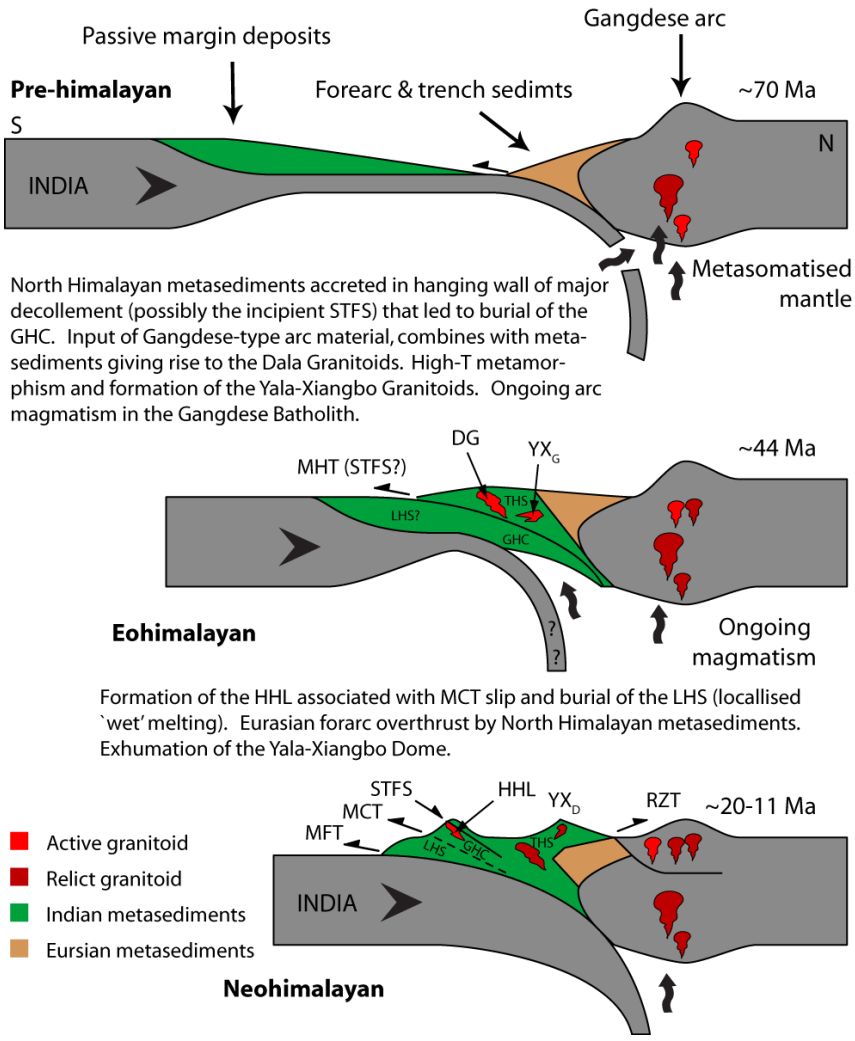

Figure 6.1: Schematic cartoon showing key features of the Eohimalayan and Neohimalayan episodes of the tectonic evolution of the eastern Himalaya. Green: Indian passive margin deposits dissected to form the principal lithotectonic units of the Himalayan Fold and Thrust Belt today (Greater Himalayan Crystallines, Lesser Himalayan Sequences and Tethyan Himalayan Sequences). Tan: Eurasian forearc deposits (Xigaze Group) south of the Eurasian arc. Also shown are the Main Himalayan Thrust (MHT), Main Frontal Thrust (MFT), Main Central Thrust (MCT), South Tibetan Fault System (STFS), Renbu Zedong Thrust (RZT), Dala Granitoids (DG), Yala-Xiangbo Granitoids (YX_G), Yala-Xiangbo Dome (YX_D), and the High Himalayan Leucogranites (HHL).

The Dala Granitoids (*Figure 1.5*) represent the first evidence of Eohimalayan granitoid plutonism so far documented anywhere along the main Himalayan Arc. As such, they are unique and not easily accommodated by existing paradigms. Their geochemistry indicates that they are derived from mixing between arc magmas, similar to those which gave rise to the Eurasian granitoids of the Gangdese Batholith, and a component of crustal material isotopically analogous to the Greater Himalayan Crystalline (GHC) sequences of the central Himalaya (*Figure 1.2*). These data are most easily explained by placing the Indian THS metasediments in the hanging wall of a thrust which led to burial of the GHC (*Figure 6.1*). Several studies have previously suggested that the paleo-STFS may have originated in compression (LeFort, 1996; Yin and Harrison, 2000, and refs. therein). Although the results of this study cannot provide unambiguous proof, the available data support this interpretation. Furthermore, the requirement for arc magma derived from the Eurasian mantle to enter the paleo-Tethyan Himalaya is most compatible with the THS metasediments being in the hanging wall of the main Himalayan decollement by *ca.* 45 Ma, and appears to precludes significant underthrusting of Indian lithosphere at that time (*Figure 6.1*).

6.3.2 Neohimalayan deformation and magmatism

According to the current paradigm (*e.g.* LeFort, 1996; Yin and Harrison, 2000, and refs. therein), magmatism and deformation were intimately associated during the Neohimalayan episode. The High Himalayan Leucogranites (HHL, *Figure 1.2*) are thought to have formed through muscovite dehydration melting associated with shear heating along a shallow-dipping decollement that is generally equated with the Main Central Thrust (MCT) (Harrison et al., 1997a, 1998a; England et al., 1992, *Figure 1.2*). The North Himalayan Granites (NHG, *Figure 3.1*, *Figure 2.2*) have been variously attributed, but may reflect biotite, or muscovite and biotite incongruent

melting occurring on deeper portions of this structure (Harrison et al., 1997a, 1998a).

The similarity of HHL crystallisation ages and the timing of MCT slip, along the length of the main Himalayan Arc, support the MCT as the dominant structure controlling the formation of the HHL (*e.g.* Harrison et al., 1997a, 1998a). Data presented in this study argue for extrapolation of this hypothesis into the Arunachal Himalaya. However, the melting processes inferred for some of the Arunachal Leucogranites differ from those considered characteristic of the HHL elsewhere. The majority of the Neohimalayan leucogranites may have been formed by fluid absent processes. However, it is argued that pockets of fluid present melting may be present along the main Himalayan Arc, and that their recognition has been hampered by the choice of interpretive technique - which depends on treating samples in groups rather than individually. Such difficulties are best addressed by way of the newly calibrated Ti-in-zircon thermometer combined with conventional ion-microprobe U-Pb dating techniques (*Chapter 4*, *Chapter 5*).

The origins of the NHG remain in dispute. However, previous studies have indicated that granitic magmatism was spatially and temporally associated with rapid exhumation of several NHD. This has led some workers to discuss the possibility that the two are in some way genetically linked (Lee et al., 2000; Beaumont et al., 2001, 2004; Zhang et al., 2004a; Lee et al., 2004). The results of this study show that while the Miocene exhumation age of the Yala-Xiangbo Dome (*Figure 2.2*) is remarkably similar to that of virtually all other NHD studied to date, the Eocene crystallisation age of the Yala-Xiangbo Granitoids is notably older. These data support a structural control in the formation of the NHD that is independent of the NHG.

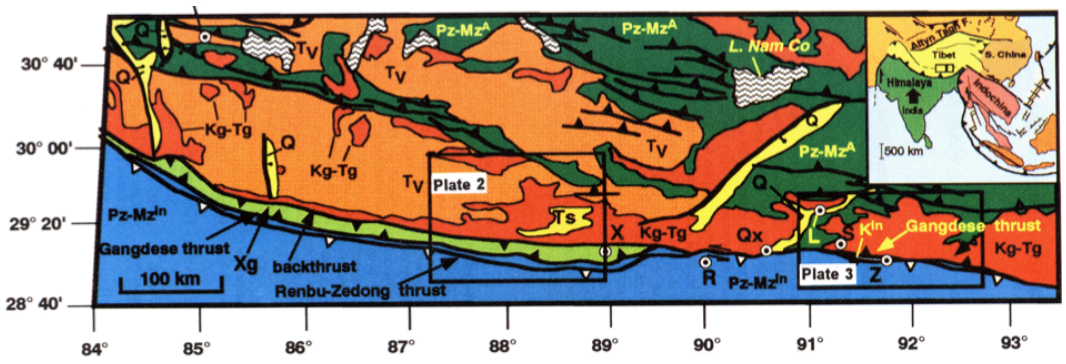

Figure 6.2: Simplified map showing outcrop patterns close to the Indus Tsangpo Suture in the central and eastern Himalaya (Yin et al., 1994). In the central Himalaya, northernmost parts of the THS (blue) are separated from components of the Eurasian Gangdese Batholith (red/orange) by the Xigaze (light green), thought to represent remnants of the forearc to Eurasia (dark green) prior to collision. In the eastern Himalaya, however, the Xigaze units are absent - possibly underthrust beneath the northern margin of the THS during Miocene motion on the RZT/GCT.

In the eastern Himalaya, the most plausible control on Miocene exhumation of the Yala-Xiangbo Dome is Miocene N-directed slip on the RZT (*Figure 1.5*, *Figure 3.1*, *Figure 6.2*). Furthermore, motion on this structure appears to have been temporally associated with fluid-mitigated recrystallisation of samples from northern parts of the Yala-Xiangbo Dome. Arguably one of the most important sources of metamorphic fluids in zones of active orogenesis is de-watering associated with pro-grade metamorphism during burial of fertile terranes (*e.g.* Spear, 1995). Regional mapping has shown that in the central Himalaya, the northernmost units of the THS are separated from southern parts of the Gangdese Batholith by an intervening metasedimentary unit termed the Xigaze Group (*Figure 6.2*). This unit comprises flysch deposits thought to represent the fore-arc to Eurasia prior to collision. In the eastern Himalaya, however, the Xigaze is absent and the THS abut directly against suture zone melange and/or components of the Gangdese Batholith (*Figure*

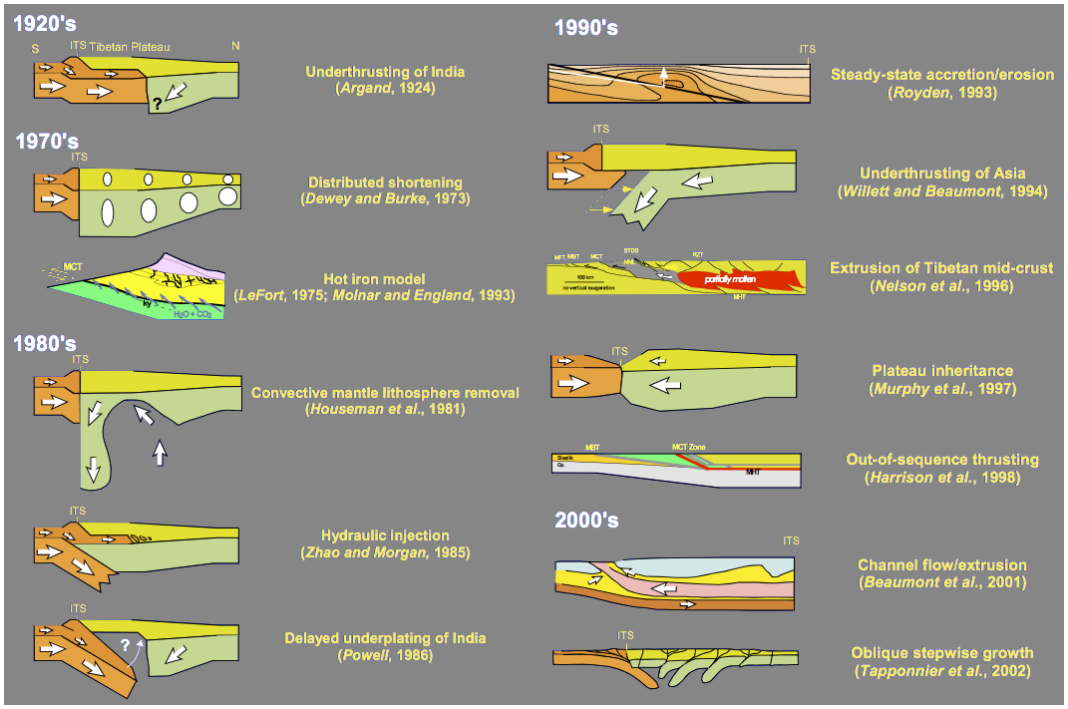

Figure 6.3: Summary of selected Himalayan evolutionary models from the past eight decades (T.M. Harrison *pers. comm.*). Note that all are based on roughly N-S oriented cross sections, aimed primarily at describing the dynamics of the more recent Neohimalayan episode.

6.2). A potential explanation for this difference is that the Xigaze terrane has been underthrust beneath the northern margin of the THS during Miocene motion on the Renbu Zedong Thrust (*Figure 6.1*). If correct, it is plausible that these units would have undergone de-watering, facilitating Miocene partial recrystallisation of lithologies along the northern margin of the of the Yala-Xiangbo Dome.

6.3.3 Tectonic models

Perhaps the most striking conclusion of this study is that the record of granitic magmatism and high-temperature metamorphism in the eastern Tethyan Himalaya extends significantly further into the geologic past than has so far been documented

elsewhere. The oldest granitoid plutons found in this region have Eocene crystallisation ages, whereas those further west are Oligocene, or more commonly Miocene (*Chapter 1*, *Chapter 4* and refs. therein). Although it is not impossible that older bodies have simply been overlooked in other parts of the main Himalayan Arc, decades of research do not favour this interpretation. Rather, it appears likely that these and other factors bear witness to fundamental differences between the eastern Himalaya and other parts of the orogen. This scenario is not easily accommodated by existing evolutionary models (*e.g.* Argand, 1924; Dewey and Burke, 1973; Houseman et al., 1981; Zhao and Morgan, 1985, 1987; Powell, 1986; Willett and Beaumont, 1994; Nelson et al., 1996).

Virtually all Himalayan evolutionary models published to date have focussed on roughly N-S oriented two dimensional cross-sections between the Indian foreland and the North Himalaya or Tibetan Plateau (*Figure 6.3*). The majority of these studies also rely, to a greater or lesser extent, on data projected from out-of-section. As such, they ignore along-strike heterogeneity and are therefore unsuitable to describe many of the results discussed above. Moreover, the vast majority invoke processes of granitoid formation that cannot account for the entire spectrum of bodies outcropping in the eastern Himalaya. Several studies have argued that the Miocene HHL - emplaced after *ca.* 40 million years of convergence - are not easily explained by internal heating associated with radioactive decay alone (*e.g.* Harrison et al., 1997a, 1998a). Therefore, it seems unlikely that older Eocene peraluminous bodies such as the Yala-Xiangbo Granitoids could be attributable to such processes, especially if they are spatially confined to the eastern Himalaya. Furthermore, the geochemical composition of the Dala Granitoids requires a source of arc-type material beneath the eastern Himalaya at this time. This is hard to reconcile with many existing evolutionary models, in particular those invoking significant underthrusting of Indian

lithosphere. As such, it is suggested that the tectonics of the eastern Himalaya may be in need of significant critical re-evaluation without undue bias towards models proposed elsewhere.

Various of studies have sought to constrain the large scale structure of the Indo-Asia collision zone through the use of seismology and tomography, often with highly variable results (*e.g.* Zhao and Xie, 1993; McNamara et al., 1997; O'Brien, 2001; Zeitler et al., 2001b; Koulakov et al., 2002; Replumaz et al., 2004). Most have focused on roughly N-S oriented sections chosen to image the geometry of the down-going Indian lithosphere and/or the first-order morphology of the HFTB. At least one popular study appears to show Indian lithosphere subducting steeply and overriding itself (*Figure 6.4*), without significantly underthrusting beneath Eurasia (consistent with the paleo-geometry inferred from the Dala Granitoids) (Replumaz et al., 2004). Recent work, however, has identified several other features that may provide insight into the origins of some unusual characteristics of the eastern Himalaya.

Tomography has revealed a slow seismic velocity anomaly beneath the eastern Himalaya (*Figure 6.6*). This zone is characterised by velocity perturbations similar to those which have been observed beneath the Deccan Traps and eastern Australia (i.e. those thought to reflect locally elevated mantle temperatures) (Kennett and Widiyantoro, 1999; Simons et al., 1999, S. Richards *pers. comm.*). Interestingly, however, this anomaly is positioned at the northern termination of the Ninety East Ridge, which extends from the central Indian Ocean (90°E) into the Bay of Bengal, roughly following the 90^{th} longitude parallel (*Figure 6.5*). Tectonic reconstructions suggest that the Ninety East Ridge originated as an oceanic transform at *ca.* 200 Ma, when Argo rifted off Australia, and continued to develop as India and Australia separated at *ca.* 120 Ma (S. Richards *pers. comm.*, joint paper in prep).

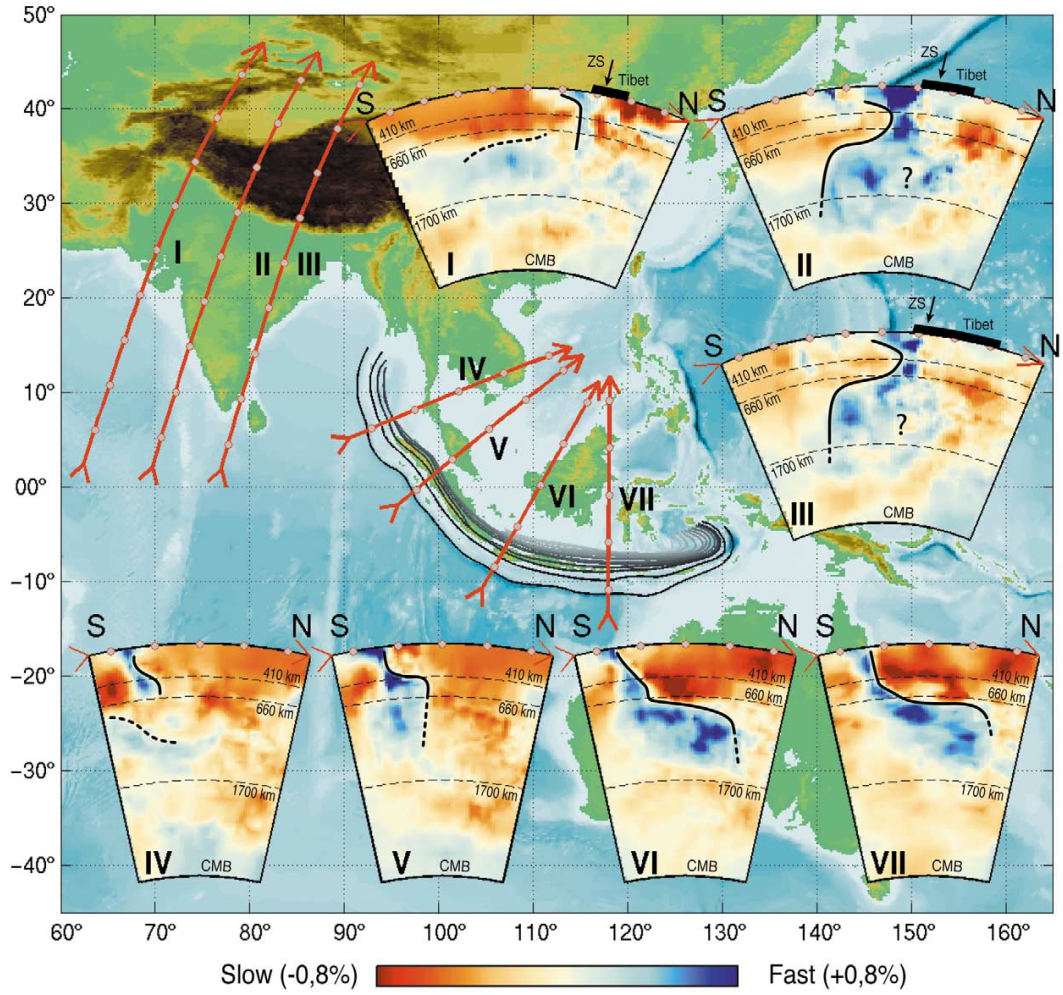

Figure 6.4: Map and tomographic sections from plate boundaries in SE Asia (Replumaz et al., 2004). Note that sections II and III (closest to the study area) show an zone of elevated seismic velocities (blue) that is interpreted as relatively col Indian lithosphere overriding itself due to ongoing convergence.

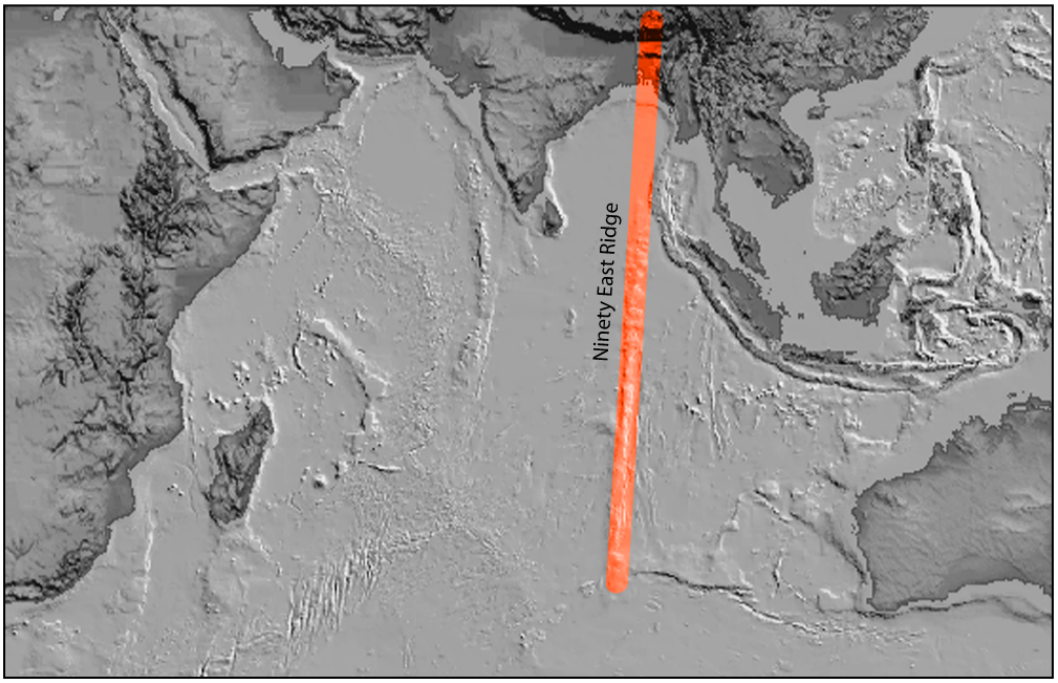

Figure 6.5: Digital elevation model (DEM) showing the showing the topographic expression of the Ninety East Ridge extending from the Indian Ocean to the Bay of Bengal. Within the Bay of Bengal the ridge is largely obscured by sedimentary deposits associated with the Bengal Fan, although it remains visible by tomography (*Figure 6.7*).

It is characterised by a linear slow seismic velocity anomaly similar to that seen beneath the eastern Himalaya, and has been the locus of ongoing magmatic activity (S. Richards *pers. comm.*, joint paper in prep). These and other lines of evidence (such as "cross-over" ages) do not support a simple hot spot trend (S. Richards *pers. comm.*, joint paper in prep). The features of the Ninety East Ridge suggest that it represents a major weakness/shear zone within the lithosphere, and potentially even a convective cell boundary in the asthenosphere (S. Richards *pers. comm.*, joint paper in prep). This interpretation holds important implications for the tectonics of the eastern Himalaya.

The results of this study provide evidence that, during the Eocene, Gangdese-type arc magmas were emplaced into low-grade portions of the tectonically thickened eastern THS metasediments, synchronous with amphibolite grade metamorphism and partial melting of the deeper structural levels. As such, these data require both a means for Eurasian arc magmas to enter the India-derived units of the proto HFTB, and a heat source for Eohimalayan metamorphism; neither of which are easily explained by the existing gamut of models. It is clear that the eastern Gangdese Batholith was undergoing a major phase of arc-granitoid formation at this time (Mo et al., 2007). One possible hypothesis is that continued northward migration of the Indian continent led to rollback of the already steeply subducting Indian slab, thereby allowing similar granitoids to be emplaced further south within the Tethyan Himalaya. However, this scenario alone cannot easily explain why Eohimalayan granitic magmatism was apparently confined to eastern portions of the proto Himalayan Arc.

Preliminary tectonic reconstructions appear to show a marked change in the movement of India at approximately 42 Ma (G. Lister *pers. comm.*). This change is

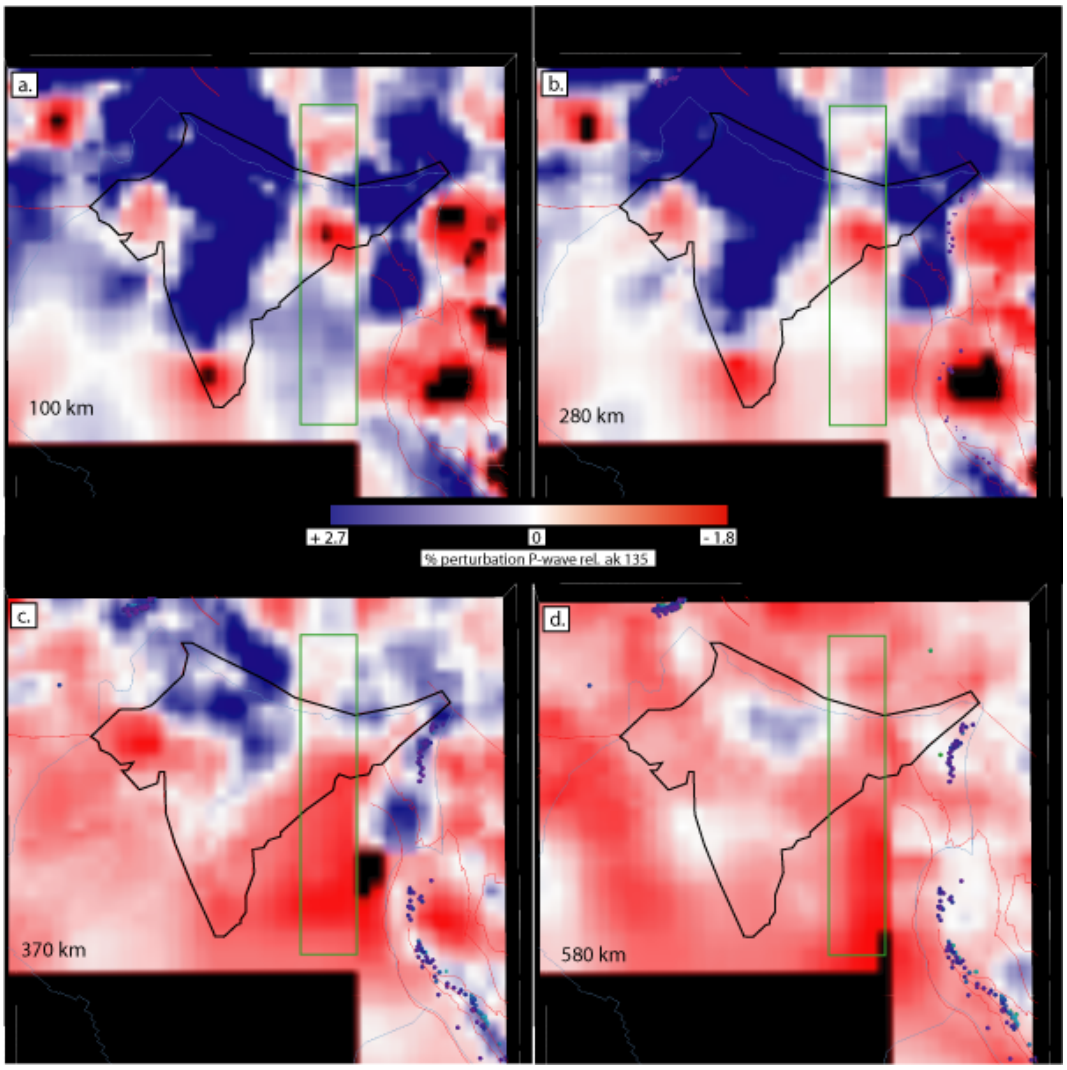

Figure 6.6: Horizontal contoured sections through P-wave tomographic data. Blue indicates fast and red indicates slow wave speed perturbations from the ak135 model of Kennett et al. (1998). A slower than average anomaly in the wavespeed exists (green boxed section) near the landward projection of the 90E bathometric volcanic ridge. The anomaly is evident to depths of of over 600 kilometres suggesting that this represents a significant mantle anomaly, potentially caused by locally elevated lithospheric and asthenospheric mantle temperatures (figure courtesy of S. Richards).

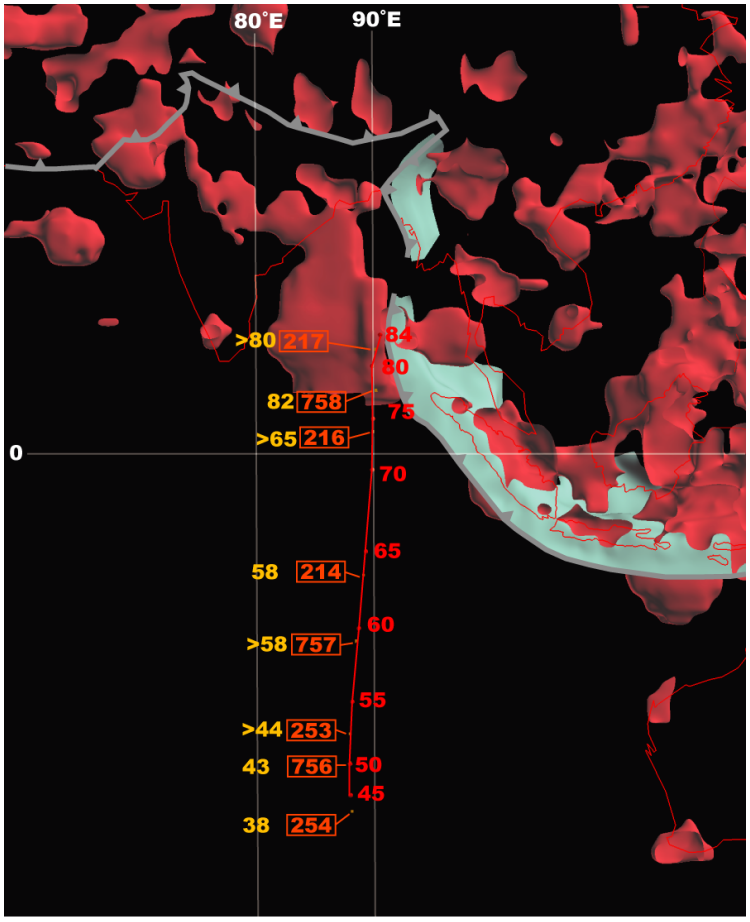

Figure 6.7: 3D map of the slow velocity structure of the mantle below India and SE Asia and its relationship to the Ninety East Ridge. The 3D geometry of the E-dipping subducted Indo-Australian plate below Sumatra is also shown in blue. The regions in red represent areas of the mantle where velocities are equal to or greater than -0.1 relative to the velocity model ak135 of Kennett et al. (1995). The dominant region of slower velocities are bounded on the eastern side by the Ninety East Ridge. Here the fast wavespeed anomaly extends to a depth of 700 kilometres. Although the anomaly extends to the west of the Ninety East Ridge, it also shallows in that direction reaching depths of 400-500 kilometres at around 84 degrees East suggesting that the anomaly is greatest below the Ninetyeast Ridge. The position of the Ninetyeast Ridge is highlighted ODP holes (Orange) together with corresponding age data for each sample (Yellow) taken from Grevemeyer and Flueh (2000). The interpreted age of positions along the ridge are shown in red (figure courtesy of S. Richards).

thought to be linked to the splitting of Kerguelen as the spreading centres between Australia and Antarctica joined with the those south of India (S. Richards and G. Lister *pers. comm.*). However, it is also remarkably similar in age to that of the Yala-Xiangbo and Dala Granitoids. If the Ninety East Ridge does represent a persistent lithospheric discontinuity extending into the present day eastern Himalaya, it may very well have played a role in Tertiary orogenesis. It is suggested that transmitted stresses associated with Eocene tectonic adjustments may have reactivated the Ninety East discontinuity, facilitating granitic magmatism that was spatially confined to the eastern Himalaya. This interpretation supports previous assertions that the formative processes some granitoids in the eastern Himalaya differ fundamentally from those so far described elsewhere (*e.g.* LeFort et al., 1987; Harris and Inger, 1992; Inger and Harris, 1993; Inger, 1994; Harrison et al., 1997a, and refs. therein). Moreover, it provides a convenient explanation for many other unusual characteristics of this region.

The presence of high temperature (*Chapter 4*) material in or beneath the eastern Himalaya provides a potential heat source for Eohimalayan high temperature metamorphism. It is suggested that elevated geothermal gradients associated with the Ninety East discontinuity localised heat transfer into the paleo east Himalayan crust, in some areas to the point of partial melting (the Yala-Xiangbo Granitoids). This interpretation is consistent with the presence of mafic sills at the deepest structural levels within the Yala-Xiangbo Dome (*Chapter 3*), although the age of these bodies is as yet unconstrained. It also suggests that further evidence of Eohimalayan thermal events (and their subsequent effects) might also be present in this region. One can speculate that additional heat input in the vicinity of the Ninety East discontinuity could have played a role in the genesis of the NHD, which effectively bracket this feature (*ca.* 85–92°E). Collectively, these results highlight the importance of

further investigating the role of pre-existing crust and lithosphere heterogeneity in determining the evolution of the Indo-Asia collision zone.

6.4 Conclusions

The eastern Himalaya comprise a roughly E-W trending regional fold and thrust belt, in which components of the Indian foreland sequences have been dissected into a series of shear-bounded tectono-metamorphic slices separated by predominantly N-dipping regional movement zones. To a first order, the distribution of lithologies and their mutual relationships are comparable to those which have been documented elsewhere along the main Himalayan Arc. However, several key differences highlight along-strike heterogeneity that has not so far been widely recognised. These factors impact upon our understanding of the formative stages of Himalayan orogenesis, and the viability of some evolutionary models.

Structural studies in the Tethyan Himalaya indicate that the principal phase of crustal thickening in the inferred earliest accreted units of the Himalayan Fold and Thrust Belt (HFTB), occurred during the Eohimalayan episode of orogenesis. This deformation begun in the Paleocene or early Eocene and was essentially complete by *ca.* 45 Ma, at which time the Tethyan Himalayan Sequences (THS) were most likely positioned in the hanging wall of a major decollement that led to the burial of the Greater Himalayan Crystallines (GHC). This structure may be equated with the incipient STFS.

In the eastern Himalaya, the Eohimalayan episode of orogenesis was associated with high temperature metamorphism of structurally deeper parts of the THS, sufficient to induce local partial melting and the generation of Eohimalayan peraluminous leucogranites. This event was contemporaneous with a major phase of granitic

magmatism in the eastern Gangdese Batholith. Moreover, it saw emplacement of Eocene granitoid plutons, partially derived from similar arc-magmas, within the Tethyan Himalaya. These data indicate that the record of both granitic magmatism and high temperature metamorphism in the eastern Himalaya extends significantly further into the geologic past, and invokes processes quite unlike those which have so far been documented elsewhere. In the eastern Himalaya, the intervening period between the Eohimalayan and Neohimalayan episodes appears to have been associated with relative tectonic quiescence, suggesting that the locus of shortening may have shifted elsewhere.

The record of Neohimalayan orogenesis preserved in the eastern Himalaya is broadly similar to other parts of the main Himalayan arc. Data from the Arunachal Himalaya and southern Tibet support the MCT as a dominant structural control on the formation of the HHL (e.g. Harrison et al., 1997a, 1998a). However, application of the newly calibrated Ti-in-zircon thermometer combined with conventional U-Pb dating indicates that in the Arunachal Himalaya, pockets of fluid-present melting were also present (*cf.* exclusively fluid absent as preferred by many previous workers). These bodies likely formed by partial melting of material incorporated into the Arunachal Crystalline sequences through footwall accretion from the Lesser Himalaya. The origins of the North Himalayan Granitoids (NHG) remain in dispute. However, our data do not support models invoking a genetic link between these and the North Himalayan Domes (NHD). Rather, it appears that key features of some NHD and NHG may been established during the Eohimalayan.

The majority of evolutionary models published so far have been based primarily on data derived from the Neohimalayan episode, and focus on arc-normal transects that average characteristics along strike (*e.g. Figure 6.3* and refs. therein). As such,

they are unsuitable to explain several key conclusions of this study (*e.g. Chapter 4*, *Chapter 5*). Recent tomographic data have revealed a slow seismic velocity anomaly beneath the eastern Himalaya, which continues southwards into the Indian Ocean. This feature is co-incident with the Ninety East Ridge, and is interpreted as a major lithospheric weakness or shear zone. We suggest that the Ninety East discontinuity has played a role in localising Eohimalayan magmatic activity in the eastern Himalaya, as well as providing a heat source for Eocene high-temperature metamorphism and partial melting of Tethyan crustal lithologies. Furthermore, key elements established during this time period may have influenced the dynamics of the subsequent Neohimalayan orogenesis. Collectively, the results of this study highlight the importance of gaining a better appreciation of the Eohimalayan episode in order to fully understand the dynamics of the Indo-Asia collision.

Chapter 7

Conclusions

The Himalaya stretch for over 2000 km, from Pakistan to Burma, forming one part of the Alpine-Himalayan chain, the world's largest active orogenic belt. Previous work has furnished a good understanding of the first order morphology and distribution of lithologies within this region, however, many aspects of the assembly of the Himalayan Fold and Thrust Belt (HFTB) remain poorly understood. The vast majority of studies to date have focussed on the Neohimalayan (Miocene to recent) episode, as preserved in central and western portions of the Main Himalayan Arc. Relatively little is known about earlier Eohimalayan (late Cretaceous to Oligocene) events throughout the Himalaya, or indeed the Neohimalayan history that is preserved further to the east. Collectively, these and other factors have favoured the development of evolutionary models that are strongly weighted towards the last third of the orogen's history, and for the most part, ignore heterogeneity along strike. The formative stages of the Indo-Asia collision remain largely unknown, as are their effects on the orogen's subsequent development.

The Himalayan Fold and Thrust Belt is characterised by a series of roughly E-W trending, internally deformed, tectonometamorphic slices, separated by predomi-

nantly N-dipping regional movement zones. The vast majority of these units are components of the Indian foreland sequences that were dissected during the Tertiary episode of Himalayan orogenesis. However, some structures attributable to pre-Himalayan deformation have been found (particularly in Paleozoic strata). The origins and regional extent of these features are at present poorly constrained, but it has been suggested that they were at last locally reactivated and may have acted as stress guides during Himalayan orogenesis.

The structurally highest units of the HFTB are the Tethyan Himalayan Sequences (THS). These units are inferred to be earliest accreted, and as such, have the potential to retain information regarding the formative stages of Himalayan orogenesis. A compilation of data from this and other studies have permitted construction of the first unifying correlation scheme describing the structural evolution of the Tethyan Himalaya. According to this scheme, thickening of the THS metasediments began in the early Tertiary, and was effectively complete by 44.1±1.2 Ma - the crystallisation age of the undeformed Dala Granitoids. This age is notably older, and implies that Eohimalayan crustal thickening was under way significantly earlier than might previously have been thought.

The Dala Granitoids represent the first evidence of major Eohimalayan granitoid plutonism so far documented anywhere along the main Himalayan Arc. Their emplacement imposes constraints on the paleo-geometry of the HFTB. The geochemistry of the Dala Granitoids indicates that they were derived from mixing between arc-magmas similar to those giving rise to a contemporaneous episode of granitoid formation within the eastern Gangdese Batholith, and a component of crustal material probably derived from the Greater Himalayan Crystallines (GHC). These data are most easily reconciled by placing the THS in the hanging wall of a major decolle-

ment that led to burial of the GHC (this structure may be equated with the incipient STFS). This interpretation also appears to preclude significant underthrusting of Indian continental lithosphere until after the mid-Eocene.

The Eohimalayan episode is thought to have been associated with high pressure metamorphism during the early stages of Himalayan orogenesis. However, new data indicate that these events were also co-incident with apparently localized high-temperature metamorphism within the eastern Tethyan Himalaya, sufficient to induce partial melting of THS metasediments (Yala-Xiangbo Dome and Eocene Yala-Xiangbo Granitoids 42.3±4.9 Ma). These data mark a significant deviation from existing paradigms, and further require a heat source for Eohimalayan metamorphism. In the eastern Tethyan Himalaya, the intervening period between the Eohimalayan and Neohimalayan orogenic episodes appears to have been associated with a relative tectonic quiescence, suggesting that the locus of shortening likely shifted elsewhere.

Both Eohimalayan granitic magmatism in the Tethyan Himalaya and Gangdese Batholith, and high temperature metamorphism of the THS metasediments appear to be spatially confined to the eastern Himalaya. This scenario is not easily accommodated by existing evolutionary models, which have largely neglected heterogeneity along the length of the main Himalayan Arc. Recent tomographic data have revealed a slow seismic velocity anomaly beneath this region, extending southwards into the Bay of Bengal, co-incident with the Ninety East Ridge. Various lines of evidence suggest that this feature represents a major lithospheric discontinuity that has been the locus of sporadic magmatic activity since at least Jurassic times. It is suggested that this feature may have played a pivotal role in localising magmatism and heat flow into the paleo eastern HFTB. If correct, this interpretation highlights

the importance of pre-existing lithosphere-scale features in shaping the early history of Himalayan orogenesis.

The Neohimalayan orogenic episode has traditionally been characterised by high temperature metamorphism and peraluminous magmatism associated with Miocene motion on the major Himalayan Fault systems (in particular the Main Central and Main Boundary Thrusts, and the South Tibetan Fault System). The results of this and other studies broadly support extrapolation of these paradigms into the eastern Himalaya. However, aspects of Neohimalayan magmatism in this region appear to differ from those described elsewhere. The Tsona Leucogranites crystallised at 18.8±1.2 Ma, and were formed by muscovite dehydration melting of pelitic lithologies similar to other High Himalayan Leucogranites (HHL). The Arunachal Leucogranites, although also comparable to the HHL in age (20.2±2.0 Ma), partially reflect fluid-present melting of material accreted to the base of the GHC from the Lesser Himalaya. It is argued that such pockets of "wet" melting may be present elsewhere along the main Himalayan Arc, potentially overlooked by the use of techniques that preclude the interpretation of samples individually. Such problems are best solved by way of the newly calibrated Ti-in-zircon thermometer, combined with conventional ion microprobe dating techniques.

The origins of the North Himalayan Granites (NHG) remain in dispute. However, data presented in this study support a structural control on the formation of the North Himalayan Domes that is independent of magmatic activity. Furthermore, it is noted that although the NHG are commonly referred to as a 'belt' of granitoids, virtually all bodies studied to date are confined to an area bracketing the Ninety East discontinuity. This observation raises the possibility that the influence of lithospheric heterogeneities may be traceable into the Neohimalayan.

Bibliography

Ahmed, T., Harris, N., Bickle, M., Chapman, H., Bunbury, J., and Prince, C. (2000). Isotopic constraints on the structural relationships between the Lesser Himalayan Series and the High Himalayan Crystalline Series, Garhwal Himalaya. *Geological Society of America Bulletin*, 112:467–477.

Aitchison, J., Ali, J., and Davis, A. (2007). When and where did India and Asia collide? In press: JGR.

Aoya, M., Wallis, S. R., Terada, K., Lee, J., Kawakami, T., Wang, Y., and Heizler, M. (2005). North-south extension in the Tibetan crust triggered by granite emplacement. *Geology*, 33(11):853–856.

Argand, E. (1924). La tectonique de l'Asie. In *International Geological Congress Report Session 13/1*.

Armijo, R., Tapponnier, P., Mercier, J., and Han, T. (1986). Quaternaty extension in southern Tibet: Field observations and tectonic implications. *Journal of Geophysical Research*, 91:13,803–13,872.

Atherton, M., McCourt, W., Sanderson, L., and Taylor, W. (1979). The geochemical character of the segmented Peruvian Coastal Batholith and associated volcanics. In Atherton, M. and Tarney, J., editors, *Origin of granite batholiths: geochemical evidence*, pages 45–64. Shiva Publishing, Nantwich, UK.

Ayers, J. and Watson, E. (1991). Solubility of apatite, monazite, zircon and rutile in supercritical aqueous fluids with implications for subduction zone geochemistry. *Philosophical Transactions of the Royal Society of London*, 335(1638):365–375.

Ayres, M. and Harris, N. (1997). Ree fractionation and Nd-isotope disequilibrium during crustal anatexis: Constraints from Himalayan leucogranites. *Chem. Geology*, 139(1-4):249–269.

Batt, G., Kohn, B., Braun, J., Mcdougall, I., and Ireland, T. (1999). New insight into the dynamic development of the Southern Alps of New Zealand, from detailed thermochronological investigation of the Mataketake Range pegmatites. In Ring, U., Brandon, M., Lister, G., and Willet, S., editors, *Exhumation Processes: Brittle Faulting Ductile Flow and Erosion*, volume 154, pages 261–262. Geological Society of London Special Publication.

Bea, F. (1996). Residence of REE, Y, Thand U in Granites and Crustal Protoliths; Implications for the Chemistry of Crustal Melts. *Journal of Petrology*, 37(3):521.

Beaumont, C., Jamieson, R. A., Nguyen, M. H., and Lee, B. (2001). Himalayan tectonics explained by extrusion of a low-viscosity crustal channel coupled to focused surface denudation. *Nature*, 414:738–742.

Beaumont, C., Jamieson, R. A., Nguyen, M. H., and Medvedev, S. (2004). Crustal channel flows: 1. Numerical models with applications to the tectonics of the Himalayan-Tibetan Orogen. *Journal of Geophysical Research*, 109(B6):B06406.

Bindeman, I. N., Davis, A. M., and Drake, M. J. (1998). Ion microprobe study of plagioclase-basalt partition experiments at natural concentration levels of trace elements. *Geochimica Et Cosmochimica Acta*, 62(7):1175–1193.

Black, L., Kamo, S., Allen, C., Aleinikoff, J., Davis, D., Korsch, R., and Foudoulis, C.

(2003). TEMORA 1: a new zircon standard for Phanerozoic U-Pb geochronology. *Chemical Geology*, 200(1):155–170.

Bollinger, L., Avouac, J. P., Beyssac, O., Catlos, E. J., Harrison, T. M., Grove, M., Goffe, B., and Sapkota, S. (2004). Thermal structure and exhumation history of the Lesser Himalaya in central nepal. *Tectonics*, 23.

Bollinger, L., Henry, P., and Avouac, J. (2006). Mountain building in the Nepal Himalaya: Thermal and kinematic model. *Earth and Planetary Science Letters*, 244(1):58–71.

Booth, A. L., Zeitler, P. K., Kidd, W. S. F., Wooden, J., Liu, Y. P., Idleman, B., Hren, M., and Chamberlain, C. P. (2004). U-pb zircon constraints on the tectonic evolution of southeastern Tibet, Namche Barwa area. *Am. J. Science*, 304(10):889–929.

Brookfield, M. (1993). The Himalayan passive margin from Precambrian to Cretaceous. *Sedimentary Geology*, 84:1–35.

Brown, M. (1994). The generation, segregation, ascent and emplacement of granite magma - the migmatite to crustally derived granite connection in thickened orogens. *Earth Science Reviews*, 36(1-2):83–130.

Burchfield, B., Chen, Z., Hodges, K., Liu, Y., Royden, L., Deng, C., and Xu, J. (1992). The South Tibetan Detachment System, Himalayan orogen: Extension contemporaneous with and parallel to shortening in a collisional mountain belt. *Geological Society of America Special Paper*, 269:1–41.

Burchfield, B., Chen, Z., Royden, L., Liu, Y., and Deng, C. (1991). Extensional development of Gabo valley, southern Tibet. *Tectonophysics*, 194:187–193.

Burg, J., Brunel, M., Gapais, D., Chen, G., and Liu, G. (1984a). Deformation of

leucogranites of the crystalline Main Central Sheet in southern Tibet (China). *Journal of Structural Geology*, 6:535–542.

Burg, J. and Chen, G. (1984). Tectonics and structural zonation of southern Tibet, China. *Nature*, 311:219–223.

Burg, J., Guiraud, M., Chen, G., and Li, G. (1984b). Himalayan metamorphism and deformation in the northern himalayan belt (southern Tibet, China). *Earth and Planetary Science Letters*, 69:391–400.

Butera, K., Williams, I., Blevin, P., and Simpson, C. (2001). Zircon U–Pb dating of Early Palaeozoic monzonitic intrusives from the Goonumbla area. *New South Wales. Australian Journal of Earth Sciences*, 48:457–464.

Catlos, E., Harrison, T., Kohn, M., Ryerson, F., Manning, C., and Upreti, B. (2001). Geochronologic and thermobarometric constraints on the evolution of the Main Central Thrust, central Nepal Himalaya. *Journal of Geophysical Research*, 106:16177–16204.

Catlos, E., Harrison, T., Manning, C., Grove, M., Rai, S., Hubbard, M., and Upreti, B. (2002). Records of the evolution of the Himalayan orogen from in situ Th-Pb ion microprobe dating of monazite: Eastern neapal and western Garhwal. *Journal of Asian Earth Sciences*, 200:459–479.

Celerier, J. (2007). The thermal and structural evolution of the Kumaun and Garwhal Lesser Himalaya, India. PhD Thesis.

Cesare, B., Marchesi, C., Hermann, J., and Gomez-Pugnaire, M. (2003). Primary melt inclusions in andalusite from anatectic graphitic metapelites: Implications for the postion of the Al_2SiO_5 triple point. *Geology*, 31(7):573–576.

Chen, Z., Liu, Y., Hodges, K., Burchfield, B., Royden, L., and Deng, C. (1990).

The Kangmar Dome - A metamorphic core comples in southern Xizang (Tibet). *Science*, 250:1552–1556.

Cheng, J. aand Xu, G. (1987). Geological map of the Gerdake region at a scale of 1:1,000,000 and geological report. Technical report, Xizang Bureau of Geology and Mineral Resources.

Cherniak, D. and Watson, E. (2003). Diffusion in zircon. In Hanchar, J. and Hoskin, P., editors, *Reviews in Mineralogy and Geochemistry: Zircon*, volume 53, pages 113–143. Mineralogical Society of America.

Claoue-Long, J., Compston, W., Roberts, J., and Fanning, C. (1995). Two Carboniferous ages: a comparison of SHRIMP zircon dating with conventional zircon ages and $^{40}Ar/^{39}Ar$ analysis. In Berggren, W., Kent, D., Aubrey, M., and Hardenbol, J., editors, *Geochronology, Time Scales and Global Stratigraphic Correlation*, volume 54, pages 3–21. SEPM Special Publication.

Clemens, J. and GTR, D. (1998). Fluids, P-T paths and the fates of anatectic melts in the Earth's crust. *Lithos*, 44(1–2):21–36.

Copeland, P., Harrison, T. M., and Lefort, P. (1990). Age and cooling history of the manaslu granite - implications for himalayan tectonics. *J. Volcanology Geothermal Research*, 44(1-2):33–50.

Craw, D., Koons, P. O., Zeitler, P. K., and Kidd, W. S. F. (2005). Fluid evolution and thermal structure in the rapidly exhuming gneiss complex of Namche Barwa Gyala Peri, eastern Himalayan syntaxis. *J. Metamorphic Geology*, 23(9):829–845.

Crouzet, C., Dunkl, I., Paudel, L., Arkai, P., Rainer, T., Baglogh, K., and Appel, E. (2007). Temperature and age constraints on the metamorphism of the Tethyan HImalaya in Central Nepal: A multidisciplinary approach. *Journal of Asian Earth Sciences*, page doi:10.1016/j.jseaes.2006.07.014.

Crowley, T. and Burke, K., editors (1998). *Tectonic Boundary Conditions for Climate Reconstructions*. Oxford University Press.

Cumming, G. and Richards, J. (1975). Ore lead isotope ratios in a continuously changing Earth. *Earth and Planetary Science letters*, 28:155–171.

Davidson, C., Grujic, D., Hollister, L., and Schmid, S. M. (1997). Metamorphic reactions related to decompression and synkinematic intrusion of leucogranite, High Himalayan Crystallines, Bhutan. *Journal of Metamorphic Geology*, 15:593–612.

Debon, F., LeFort, P., Sheppard, S., and Sonet, J. (1986). The four plutonic belts of the Transhimalaya-Himalaya: A chemical, mineralogical , isotopic, and chronological synthesis along a Tibet-Nepal granite section. *Journal of Petrology*, 27(1):219–250.

DeCelles, P., Robinson, D., Quade, J., Copeland, P., Upreti, B., Ojha, T., , and Garzione, C. (2001a). Regional structure and stratigraphy of the Himalayan fold-thrust belt, farwestern Nepal. *Tectonics*, 20:487–509.

DeCelles, P., Robinson, D., Quade, J., Ojha, T., Garzione, C., Copeland, P., and Upreti, B. (2001b). Stratigraphy, structure, and tectonic evolution of the Himalayan fold-thrust belt in western Nepal. *Tectonics*, 20(4):487–509.

DeCelles, P. G., Gehrels, G. E., Quade, J., LaReau, B., and Spurlin, M. (2000). Tectonic implications of U-Pb zircon ages of the Himalayan orogenic belt in Nepal. *Science*, 288(5465):497–499.

DeCelles, P. G., Gehrels, G. E., Quade, J., Ojha, T. P., Kapp, P. A., and Upreti, B. N. (1998). Neogene foreland basin deposits, erosional unroofing, and the kinematic history of the Himalayan fold-thrust belt, western Nepal. *Geological Society of America Bulletin*, 110(1):2–21.

Deniel, C., Vidal, P., Fernandez, A., Lefort, P., and Peucat, J. J. (1987). Isotopic study of the manaslu granite (himalaya, nepal) - inferences on the age and source of himalayan leukogranites. *Contributions To Mineralogy Petrology*, 96:78–92.

Dewey, J., Cande, S., and Pitman, W. (1989). Tectoni evolution of the India-Eurasia collision zone. *Eclogae Geologicae Helvetiae*, 82:717–734.

Dewey, J. F. and Burke, K. C. A. (1973). Tibetan, variscan, and precambrian basement reactivation - products of continental collision. *J. Geology*, 81:683–692.

Dezes, P. J., Vannay, J. C., Steck, A., Bussy, F., and Cosca, M. (1999). Synorogenic extension; quantitative constraints on the age and displacement of the Zanskar shear zone (Northwest Himalaya). *Geological Society of America Bulletin*, 111(3):364–374.

Dong, G., Mo, X., Zhao, Z., Guo, T., Wang, L., and Chen, T. (2005). Geological constraints on magmatic underplating of the Gandese belt in the India-Eurasia collision: Evidence of SHRIMP 2 U-Pb dating. *Acta Geologica Sinica*, 79(6):801–808.

Dürr, S. (1996). Provenance of Xigaze fore-arc basin clastic rocks (Cretaceous, south Tibet). *Geological Society of America Bulletin*, 108(6):669–684.

Edwards, M. A. and Harrison, T. M. (1997). When did the roof collapse? Late Miocene north-south extension in the high Himalaya revealed by Th-Pb monazite dating of the Khula Kangri granite. *Geology*, 25:543–546.

Eggins, S. and Shelley, J. (2002). Compositional heterogeneity in NIST SRM 610–617 glasses. *Geostandards Newsletter*, 26:269–286.

Einsele, G., Liu, B., Durr, S., Liu, G., Lutebacher, H., Ratschbacher, L., Ricken, W., Wendt, J., Wetzel, A., Yu, G., and Zheng, H. (1994). The Xigaze fore-arc basin

- evolution and facies architecture (Cretaceous, Tibet). *Sedimentary Geology*, 90(1–2):1–32.

England, P., Le Fort, P., Molnar, P., and Pecher, A. (1992). Heat sources for Tertiary magmatism and anatexis in the Annapurna-Manaslu reigion of Central Nepal. *Journal of Geophysical Resarchical*, 97:2107–2128.

England, P. and Molnar, P. (1993). The interpretation of inverted metamorphic isograds using simple physical calculations. *Tectonics*, 12:145–157.

Ferry, J. and Watson, E. (2007). New thermodynamic models and revised calibrations for the Ti-in-zircon and Zr-in-rutile thermometers. Submitted.

Frost, B., Barnes, C., Collins, W., Arculus, R., Ellis, D., and Frost, C. (2001). A Geochemical Classification for Granitic Rocks. *Journal of Petrology*, 42(11):2033–2048.

Gansser, A. (1964). *The geology of the Himalayas*. Wiley Interscience, New York.

Garzanti, E. (1999). Stratigraphy and sedimentary history of the Nepal Tethys Himalaya passive margin. *Journal of Asian Earth Sciences*, 17:805–827.

Gehrels, G., DeCelles, P., Martin, A., Ojha, T., Pinhassi, G., and Upreti, B. (2003). Initiation of the Himalayan Orogen as an Early Paleozoic thin-skinned thrust belt. *GSA Today*, 13(9):4–10.

Gehrels, G., DeCelles, P., Ojha, T., and Upreti, B. (2006). Geologic and U-Th-Pb geochronolic evidence for early Paleozoic tectonism in the Kathmandu thrust sheet, central Nepal Himalaya. *Geological Society of America Bulletin*, 118(1-2):185–198.

Gingele, F. and De Deckker, P. (2005). Clay mineral, geochemical and Sr–Ndisotopic

fingerprinting of sediments in the Murray–Darling fluvial system, southeast Australia. *Australian Journal of Earth Sciences*, 52(6):965–974.

Glikson, A. (2006). Comment on "Zircon Thermometer Reveals Minimum Melting Conditions on Earliest Earth" 1. *Science*, 311:779a.

Godin, L. (2003). Structural evolution of the Tethyan sedimentary sequence in the Annapurna area, central Nepal Himalaya. *Journal of Asian Earth Sciences*, 22:307–328.

Godin, L., Brown, R., and Hanmer, S. (1999a). High strain zone in the hanging wall of the Annapurna detachment, central Nepal Himalaya. *Geological Society of America Special Paper*, 328:199–210.

Godin, L., Brown, R., Hanmer, S., and Parrish, R. (1999b). Back folds in the core of the Himalayan orogen: An alternative interpretation. *Geology*, 27(2):151–154.

Grevemeyer, I. and Flueh, E. (2000). Crustal underplating and its implications for subsidence and state of isostasy along the Ninetyeast Ridge hotspot trail. *Geophysical Journal Interantional*, 142:643–649.

Guillot, S., Hodges, K., Le, Fort, P., and Pecher, A. (1994). New constraints on the age of the Manaslu Leucogranite; evidence for episodic tectonic denudation in the central Himalayas. *Geology*, 22(6):559–562.

Guillot, S. and Lefort, P. (1995). Geochemical constraints on the bimodal origin of high himalayan leukogranites. *Lithos*, 35(3-4):221–234.

Harris, N., Ayres, M., and Massey, J. (1995). Geochemistry of granitic melts produced during the incongruent melting of muscovite - implications for the extraction of himalayan leukogranite magmas. *J. Geophysical Research-solid Earth*, 100:15767–15777.

Harris, N. and Inger, S. (1992). Trace element modelling of pelite-derived granites. *Contributions to Mineralogy and Petrology*, 110(1):46–56.

Harris, N. and Massey, J. (1994). Decompression and anatexis of Himalayan metapelites. *Tectonics*, 13(6):1537–1546.

Harris, N., Pearce, J., and Tindle, A. (1986). Geochemical chracteristics of collision-zone magmatism. In Coward, M. and Ries, A., editors, *Collision Tectonics*, volume 19, pages 67–81. Geological Society of London Special Publication.

Harrison, T. (2006). Did the Himalayan crystallines extrude from beneath the Tibetan Plateau? In Law, R., Searle, M., and Godin, L., editors, *Geological Society of London Special Paper: Channel flow, Ductile Extrusion and Exhumation of Lower-mid Crust in Continental Collision Zones*, volume 268 of *237–254*. Geological Society of London.

Harrison, T., Catlos, E., and Montel, J. (2002). U-th-pb dating of phosphate minerals. In *Reviews in Mineralogy and Geochemistry: Phosphates*, volume 48, pages 523–558. Mineralogical Society of America.

Harrison, T., Grove, M., Lovera, O., and Catlos, E. (1998a). A model for the origin of Himalayan anatexis and inverted metamorphism. *Journal of Geophysical Research*, 103:27,017–27,032.

Harrison, T., Grove, M., Lovera, O., Catlos, E., and D'Andrea, J. (1999a). The origin of Himalayan anatexis and inverted metamorphism: Models and constraints. *Journal of Asian Earth Sciences*, 17:755–772.

Harrison, T., Grove, M., Lovera, O., and Zeitler, P. (2005). Continuous Thermal Histories from Inversion of Closure Profiles. *Reviews in Mineralogy and Geochemistry*, 58(1):389–409.

Harrison, T., Heizler, M., Lovera, O., Chen, W., and Grove, M. (1994). A chlorine disinfectant for excess argon released from K-feldspar during step-heating. *Earth and Planetary Science letters*, 123:95–104.

Harrison, T., Lovera, O., and Grove, M. (1997a). New insights into the origin of two contrasing Himalayan granite belts. *Geology*, 25:899–902.

Harrison, T., Watson, E., and Aikman, A. (2007). Temperature specture of zircon crystallization in plutonic rocks. Accepted, Geology.

Harrison, T. and Zeitler, P. (2005). Fundamentals of Noble Gas Thermochronometry. *Reviews in Mineralogy and Geochemistry*, 58(1):123–149.

Harrison, T. M., An, Y., Grove, M., Lovera, O. M., Ryerson, F. J., and Zhou, X. (2000). The Zedong Window; a record of superposed Tertiary convergence in southeastern Tibet. *Journal of Geophysical Research*, 105(8):19,211–19,230.

Harrison, T. M., Grove, M., D, A. J., Catlos, E. J., and Lovera, O. M. (1999b). Models for the thermal and tectonic evolution of southern Tibet and the Himalaya. In *AGU 1999 fall meeting*, volume 80; 46, Suppl., pages 989–990. American Geophysical Union, Washington, DC, United States.

Harrison, T. M., Grove, M., Lovera, O. M., Catlos, E. J., and D, A. J. (1999c). The origin of Himalayan anatexis and inverted metamorphism; models and constraints. In *Geology of the Nepal Himalaya; recent advances*, volume 17; 5-6, pages 755–772. Pergamon, Oxford, United Kingdom.

Harrison, T. M., Grove, M., McKeegan, K. D., Coath, C. D., Lovera, O. M., and Fort, P. L. (1999d). Origin and episodic emplacement of the Manaslu intrusive complex, central himalaya. *J. Petrology*, 40(1):3–19.

Harrison, T. M., Mckeegan, K. D., and Lefort, P. (1995). Detection of inherited

monazite in the manaslu leukogranite by pb-208/th-232 ion microprobe dating - crystallization age and tectonic implications. *Earth Planetary Science Lett.*, 133:271–282.

Harrison, T. M., Ryerson, F. J., Le Fort, P., Yin, A., Lovera, O. M., and Catlos, E. (1997b). A Late Miocene-Pliocene origin for the Central Himalayan inverted metamorphism. *Earth and Planetary Science Letters*, 146:E1–E6.

Harrison, T. M. and Watson, E. B. (1983). Kinetics of zircon dissolution and zirconium diffusion in granitic melts of variable water-content. *Contributions To Mineralogy Petrology*, 84(1):66–72.

Harrison, T. M., Yin, A., and Ryerson, F. J. (1998b). Orographic evolution of the Himalaya and Tibetan Plateau. In *Tectonic boundary conditions for climate reconstructions*, volume 39;, pages 39–72. Oxford University Press, Oxford, United Kingdom.

Hauck, M. L., Nelson, K. D., Brown, L. D., Zhao, W., and Ross, A. R. (1998). Crustal structure of the Himalayan orogen at $\approx 90^\circ$ east longitude from Project INDEPTH deep reflection profiles. *Tectonics*, 17:481–500.

Heim, A. and Gansser, A. (1939). *Central Himalaya Geological Observations of Swiss Expedition*. Swiss.

Henderson, P. (1982). *Inorganic geochemistry*, page 367. Pergamon.

Hermann, J., Rubatto, D., and Trommsdorff, V. (2006). Sub-solidus Oligocene zircon formation in garnet peridotite during fast decompression and fluid infiltration (Duria, Central Alps). *Mineralogy and Petrology*, 88(1):181–206.

Hodges, K., Parrish, R., Housh, T., Lux, D., Burchfield, B., Royden, L., and Chen,

Z. (1992). Simultaneous Miocene extension and shortening in the Himalayan orogen. *Science*, 258:1466–1470.

Hodges, K., Parrish, R., and Searle, M. (1996). Tectonic evolution of the central Annapurna range, Nepalese Himalaya. *Tectonics*, 15:1264–1291.

Hollister, L. and Crawford, M. (1986). Melt enhanced deformation: a major tectonic process. *Geology*, 14:558–561.

Holtz, F., Johannes, W., Tamic, N., and Behrens, H. (2001). Maximum and minimum water contents of granitic melts generated in the crust: a reevaluation and implications. *Lithos*, 56(1):1–14.

Horn, I., Hinton, R., Jackson, S., and Longerich, H. (1997). Ultra-trace element analysis of NIST SRM 616 and 614 using laser ablation microprobe-inductively coupled plasma-mass spectrometry (LAM-ICP-MS): a comparison with secondary ion mass spectrometry (SIMS). *Geostand. Newsl*, 21(2):191–203.

Houseman, G. A., McKenzie, D. P., and Molnar, P. (1981). Convective instability of a thickened boundary layer and its relevance for the thermal evolution of continental convergent belts. *Journal of Geophysical Research*, 86(NB7):6115–6132.

Huang, W. and Wyllie, P. (1986). Phase relationships of gabbro-tonalite-granite-water at 15 kbar with applications to differentiation and anatexis. *American Mineralogist*, 71(3-4):301–316.

Hutton, J. (1788). On certain natural appearances of the ground on the hill of Arthur's Seat. *Transactions of the Royal sociaty of Edinburgh*, 1.

Ingebritsen, S. and Manning, C. (2002). Diffuse fluid flux through orogenic belts: Implications for the world ocean. *Proceedings of the National Academy of Sciences*, 99(14):9113.

Inger, S. (1994). Magmagenesis associated with extension in orogenic belts - examples from the himalaya and tibet. *Tectonophysics*, 238(1-4):183–197.

Inger, S. and Harris, N. (1993). Geochemical constraints on leucogranite magmatism in the Langtang valley, Nepal Himalaya. *Journal of Petrology*, 34(2):345–368.

Irvine, T. and Baragar, W. (1971). A guide to the chemical classification of the common volcanic rocks. *Canadian Journal of Earth Sciences*, 8(5):523–547.

Jamieson, R., Beaumont, C., Medvedev, S., and Nguyen, M. (2004). Crustal channel flows: 2. Numerical models with implications for metamorphism in the Himalayan-Tibetan orogen. *Journal of Geophysical Research*, 109(B6):B06407.

Johnson, M. (2002). Shortening budgets and the role of continental subduction during the India-Asia collision. *Earth Science Reviews*, 59(1-4):101–123.

Kapp, J., Harrison, T., Kapp, P., Grove, M., Lovera, O., and Ding, L. (2005). The Nyainqentanglha Shan: A window into the tectonic, thermal, and geochemical evolution of the Lhasa block, southern Tibet. *Journal of Geophysical Resarch*, 110:B08413.

Kennett, B., Engdahl, E., and Buland, R. (1995). Constraints on seismic velocities in the Earth from travel times. *Geophysical Journal Interantional*, 122:108–124.

Kennett, B. and Widiyantoro, S. (1999). A low seismic wavespeed anomaly beneath northwestern India: a seismic signature of the Deccan plume? *Earth and Planetary Science Letters*, 165(1):145–155.

Kennett, B., Widiyantoro, S., and van der Hilst, R. (1998). Joint seismic tomography for bulk sound and shear wave speed in the Earth's mantle. *Journal of Geophysical Research*, 103(B6):12469–12494.

Koester, E., Pawley, A., Luis, A., Fernandes, L., Porcher, C., and Soliani Jr., E. (2002). Experimental melting of cordierite gneiss and the petrogenesis of syntranscurrent peraluminous granites in Southern Brazil. *Journal of Petrology*, 43:1595–1616.

Koulakov, I., Tychkov, S., Bushenkova, N., and Vasilevsky, A. (2002). Structure and dynamics of the upper mantle beneath the Alpine-Himalayan orogenic belt, from teleseismic tomography. *Tectonophysics*, 358:77–96.

Larson, K., Burgmann, R., Bilham, R., and Freymueller, J. (1999). Kinematics of the India-Eurasia collsion zone from GPS. *Journal of Geophysical Research*, 104:1077–1093.

Le Breton, N. and Thompson, A. (1988). Fluid-absent (dehydration) melting of biotite in metapelites in the early stages of crustal anatexis. *Contributions to Mineralogy and Petrology*, 99(2):226–237.

Lee, J., Hacker, B., and Wang, Y. (2004). Evolution of North Himalayan gneiss domes: structural and metamorphic studies in Mabja Dome, southern tibet. *J. Struct. Geology*, 26(12):2297–2316.

Lee, J., Hacker, B. R., Dinklage, W. S., Wang, Y., Gans, P., Calvert, A., Wan, J. L., Chen, W. J., Blythe, A. E., and McClelland, W. (2000). Evolution of the Kangmar Dome, southern Tibet: Structural, petrologic, and thermochronologic constraints. *Tectonics*, 19(5):872–895.

Lee, J. and Whitehouse, M. (2007). Onset of mid-crustal extensional flow in southern Tibet: Evidence from U/Pb zircon ages. *Geology*, 35(1):45–48.

LeFort, P. (1975). Himalayas, the collided range. Present knowledge of the continental arc. *American Journal of Science*, 275(A):1–44.

LeFort, P. (1996). Evolution of the Himalaya. In Yin, A. and Harrison, T., editors, *The Tectonics of Asia*, pages 95–106. Cambridge University Press.

LeFort, P., Vuney, M., Deniel, C., and France-Lanord, C. (1987). Crustal generation of the Himalayan leucogranites. *Tectonophysics*, 134:39–57.

Liu, G. and Ensele, G. (1994). Sedimentary history of the Tethyan basin in the Tibetan Himalayas. *Geologische Rundschau*, 82:32–61.

Longerich, H., Jackson, S., and Gunther, D. (1996). Laser ablation inductively coupled plasma mass spectrometric transient signal data acquisition and analyte concentration calculation. *Journal of Analytical Atomic Spectrometry*, 11:899–904.

Lovera, O., Grove, M., and Harrison, T. (2002). Systematic analysis of K-feldspar 40Ar/39Ar step heating results II: relevance of laboratory argon diffusion properties to nature. *Geochimica et Cosmochimica Acta*, 66(7):1237–1255.

Lovera, O., Richter, F., and Harrison, T. (1989). $^{40}Ar/^{39}Ar$ thermochronology for slowly cooled samples having a distribution of diffusion domain sizes. *Journal of Geophysical Research*, 94:17,917–17,936.

Ludwig, K. (2001). Squid 1.02: A user manual. *Berkeley Geochronological Center Special Publication*, 2:19.

Lyell, C. (1830). *Principles of Geology.* John Murray, Albemarle-Street.

Makovsky, Y., Klemperer, S., Liyan, H., and Deyuan, L. (1996). Structural elements of the southern Tethyan Himalaya crust from wide-angle seismic data. *Tectonics*, 15(5):997–1005.

Maluski, H., Matte, P., Brunel, M., and Xiao, X. (1988). $^{40}Ar/^{39}Ar$ dating of metamorphic and plutonic events in the north and high Himalaya belts (southern Tibet - China). *Tectonics*, 7:799–326.

McCaig, A., Wayne, D., and Rosenbaum, J. (2000). Fluid expulsion and dilatancy pumping during thrusting in the Pyrenees: Pb and Sr isotope evidence. *Geological Society of America Bulletin*, 112(8):1199–1208.

McDonough, W. and Sun, S. (1995). The composition of the Earth. *Chem. Geol*, 120(3):223–253.

McDougall, I. and Harrison, T. (1988). *Geochronology and Thermochronology by the $^{40}Ar/^{39}Ar$ Method*. Oxford University Press, New York, first edition.

McNamara, D. E., Walter, W. R., Owens, T. J., and Ammon, C. J. (1997). Upper mantle velocity structure beneath the Tibetan Plateau from Pn travel time tomography. *J. Geophysical Research-solid Earth*, 102:493–505.

Meigs, A., Burbank, D., and Beck, R. (1995). Middle-Late Miocene (>10 Ma) formation of the Main Boundary Thrust in the western Himalaya. *Geology*, 23:423–426.

Miller, C., Thoni, M., Frank, W., Grasemann, B., Klotzli, U., Guntli, P., and Draganits, E. (2001). The early Palaeozoic magmatic event in the Northwest Himalaya, India: source, tectonic setting and age of emplacement. *Geological Magazine*, 138:237–251.

Mo, X., Dong, G., Zhao, Z., Guo, T., Wang, L., and Chen, T. (2005). Timing of magma mixing in the Gangdese magmatic belt during the India-Asia collision: Zircon SHRIMP U-Pb dating. *Acta Geologica Sinica*, 79(1):66–76.

Mo, X., Hou, Z., Niu, Y., Dong, G., Qu, X., Zhao, Z., and Yang, Z. (2007). Mantle contributions to crustal thickening during continental collision: Evidence from Cenozoic igneous rocks in southern Tibet. In press.

Mo, X., Zhao, Z., Deng, J., Flower, M., Yu, X., Lui, Z., Li, Y., Zhou, S., Dong, G.,

Zhu, D., and Wang, L. (2006). Petrology and geochemistry of postcollisional volcanic rocks from the Tibetan plateau: Implications for lithosphere heterogeneity and collision-induced asthenosphere flow. In Dilek, Y. and Pavlides, S., editors, *Postcollisional Tectonics and Magmatism in the Mediterranean Region and Asia*, volume 409. Geological Society of America.

Montel, J. M. (1993). A model for monazite/melt equilibrium and application to the generation of granitic magmas. *Chem. Geology*, 110(1-3):127–146.

Murphy, M. and Harrison, T. (1999). Relationship between leucogranites and the Qomolangma detachment in the Rongbuk Valley, south Tibet. *Geology*, 27(9):831–834.

Murphy, M. and Yin, A. (2003). Structural evolution and sequence of thrusting in the Tethyan fold-thrust belt and Indus-Yalu suture zone, southwest Tibet. *Geological Society of America Bulletin*, 115:21–34.

Murphy, M., Yin, A., Harrison, T., Durr, S., Chen, Z., Ryerson, F., Kidd, W., Wang, X., and Zhou, X. (1997). Did the Indo-Asia collision alone create the Tibetan plateau? *Geology*, 25(8):719–722.

Myrow, P. M., Hughes, N. C., Paulsen, T. S., Williams, I. S., Parcha, S. K., Thompson, K. R., Bowring, S. A., Peng, S. C., and Ahluwalia, A. D. (2003). Integrated tectonostratigraphic analysis of the Himalaya and implications for its tectonic reconstruction. *Earth and Planetary Science Letters*, 212(3-4):433–441.

Nabelek, P., Russ-Nabelek, C., and Denison, J. (1992). The generation and crystallization conditions of the Proterozoic Harney Peak Leucogranite, Black Hills, South Dakota, USA: Petrologic and geochemical constraints. *Contributions to Mineralogy and Petrology*, 110(2):173–191.

Nash, W. and Crecraft, H. (1985). Partition coefficients for trace elements in silicic magmas. *Geochimica et Cosmochimica Acta*, 49:2309–2322.

Nelson, K., Zhao, W., Brown, L., and etal. (1996). Partially molten middle crust beneath southern Tibet: Synthesis of project INDEPTH results. *Science*, 274(5293):1684–1688.

Norman, M., Griffinab, W., Pearsona, N., Garciac, M., and O'Reillya, S. (1998). Quantitative analysis of trace element abundances in glasses and minerals: a comparison of laser ablation inductively coupled plasma mass spectrometry, solution inductively coupled plasma mass spectrometry, proton microprobe and electron microprobe data. *Journal of Analytical Atomic Spectrometry*, 13:477–482.

Nutman, A. (2006). Comment on "Zircon Thermometer Reveals Minimum Melting Conditions on Earliest Earth" II. *Science*, 311:779b.

O'Brien, P. J. (2001). Subduction followed by collision: Alpine and Himalayan examples. *Phys. Earth Planetary Interiors*, 127:277–291.

Osborn, E. (1959). Role of oxygen pressure in the crystallization and differentiation of basaltic magma. *American Journal of Science*, 257(9):609.

Paces, J. and Miller, J. (1993). U–Pb ages of Duluth complex and related mafic intrusions, northeastern Minnesota: geochronological insights to physical, petrogenetic, palaeomagnetic, and tectonomagmatic processes associated with the 1· 1 Ga mid-continent rift system. *Journal of Geophysical Research*, 98:13997–14013.

Pan, G., Ding, J., Yao, D., and Wang, L. (2004). Geological map of Qinghai-Xiang (Tibet) Plateau and Adjacent Areas (1:1,500,000).

Patino Douce, A. and Beard, J. (1996). Effects of P, f (O_2) and Mg/Fe ratio on dehydration melting of model metagreywackes. *Journal of Petrology*, 37(999):1024.

Patino Douce, A. and Harris, N. (1998). Experimental Constraints on Himalayan Anatexis. *Journal of Petrology*, 39(4):689–710.

Patriat, P. and Achache, J. (1984). India-Eurasia collision chronology has implications for crustal shrtening an driving mechanisms of plates. *Nature*, 311:615–621.

Pearce, J., Harris, N., and Tindle, A. (1984). Trace Element Discrimination Diagrams for the Tectonic Interpretation of Granitic Rocks. *Journal of Petrology*, 25(4):956.

Pearce, N., Perkins, W., Westgate, J., Gorton, M., Jackson, S., Neal, C., and Chenery, S. (1997). A compilation of new and published major and trace element data for NIST SRM 610 and NIST SRM 612 glass reference materials. *Geostandards Newsletter*, 21(1):115–144.

Pecerillo, A. and Taylor, S. (1976). Geochemistry of Eocene calc-akaline volcanic rocks from the Kastamonu area, north Turkey. *Contributions to Mineralogy and Petrology*, 58:63–81.

Peto, P. (1976). An experimental investigation of melting relations involving muscovite and paragonite in the silica-saturated portion of the system K_2O-Na_2O-Al_2O_3-SiO_2-H_2O to 15 kb total pressure. *Progress in Experimental Petrology*, 3:41–45.

Pinet, C. and Jaupart, C. (1987). A thermal model for the distribution in space and time of the Himalayan granites. *Earth and Planetary Science Letters*, 84(1):87–99.

Powell, C. M. (1986). Continental underplating model for the rise of the tibetan plateau. *Earth Planetary Science Lett.*, 81:79–94.

Press, W. H., Teukolky, S. A., Vetterling, W. T., and Flannery, B. P. (1992). *Nu-*

merical Recipes, The Art of Scientific Computing. Cambridge University Press, Cambridge, England, second edition.

Prince, C., Harris, N., and Vance, D. (2001). Fluid-enhanced melting during prograde metamorphism. *J. Geological Soc.*, 158:233–241.

Quidelleur, X., Grove, M., Lovera, O., Harrison, T., and Yin, A. (1997). Thermal evolution and slip history of the Renbu Zedong Thrust, southeastern Tibet. *Journal of Geophysical Research*, 102(B2):2659–2679.

Quigley, M., Yu, L. J., Liu, X. H., Wilson, C. J. L., Sandiford, M., and Phillips, D. (2006). Ar-40/ar-39 thermochronology of the Kampa Dome, southern Tibet: Implications for tectonic evolution of the North Himalayan gneiss domes. *Tectonophysics*, 421(3-4):269–297.

Rapp, R. P. and Watson, E. B. (1986). Monazite solubility and dissolution kinetics - implications for the thorium and light rare-earth chemistry of felsic magmas. *Contributions To Mineralogy Petrology*, 94(3):304–316.

Ratschbacher, L., Frisch, W., Chen, C., and Pan, G. (1992). Deformation and motion along the southern margin of the Lhasa block (Tibet) prior and during the India-Asia collision. *Journal of Geodynamics*, 16(1):21–54.

Ratschbacher, L., Frisch, W., Liu, T., and Chen, C. (1994). Distributed deformation in southern and western Tibet during and after the India-Asia collision. *Journal of Geophysical Research*, 99:19,817–19,945.

Replumaz, A., Karason, H., van der Hilst, R. D., Besse, J., and Tapponnier, P. (2004). 4-d evolution of SE Asia's mantle from geological reconstructions and seismic tomography. *Earth Planetary Science Lett.*, 221:103–115.

Richards, A., Argles, T., Harris, N., Parrish, R., Ahmad, T., Darbyshire, F., and

Draganits, E. (2005). Himalayan architecture constrained by isotopic tracers from clastic sediments. *Earth and Planetary Science Letters*, 236(3-4):773–796.

Royden, L. H. (1993). The steady-state thermal structure of eroding orogenic belts and accretionary prisms. *J. Geophysical Research-solid Earth*, 98:4487–4507.

Rubatto, D. and Hermann, J. (2003). Zircon formation during fluid circulation in eclogites (Monviso, Western Alps): implications for Zr and Hf budget in subduction zones. *Geochimica et Cosmochimica Acta*, 67(12):2173–2187.

Rubatto, D. and Hermann, J. (2007). Experimental constraints on zircon/melt and zircon/garnet trace element partitioning and implication for the geochronology of crustal rocks. Submitted.

Sambridge, M. and Compston, W. (1994). Mixture modeling of multi-component data sets with application to ion-probe zircon ages. *Earth and Planetary Science letters*, 128:373–390.

Saxena, M. (1971). The crystalline axis of the Himalaya, Indian shield and continenetal drift. *Tectonophysics*, 12:433–447.

Schärer, U. (1984). The effect of initial ^{230}Th disequilibrium on young U-Pb ages: The Makalu case, Himalayas, the collided range. Present knowledge of the continental arc. *Earth and Planetary Science Letters*, 99:19817–19945.

Schärer, U., Ronghua, X., and Allègre, C. (1986). U-(Th)-Pb systematics and ages of Himalayan leucogranites, South Tibet. *Earth and Planetary Science letters*, 77:35–48.

Schelling, D. and Arita, K. (1991). Thrust tectonics, crustal shortening, and the structure of the far-eastern Nepal Himalaya. *Tectonics*, 10:851–862.

Searle, M. P., Parrish, R. R., Hodges, K. V., Hurford, A., Ayres, M. W., and Whitehouse, M. J. (1997). Shisha Pangma leucogranite, south Tibetan Himalaya: Field relations, geochemistry, age, origin, and emplacement. *J. Geology*, 105(3):295–317.

Shand, S. (1943). *The Eruptive Rocks*, page 444. John Wiley, New York, 2 edition.

Simons, F., Zielhuis, A., and van der Hilst, R. (1999). The deep structure of the Australian continent from surface wave tomography. *Lithos*, 48(1):7–43.

Singh, S. (2003). Conventional and SHRIMP U-Pb zircon dating of the Chor Granitoid, Himachal himalaya. *J. Geological Soc. India*, 62:614–626.

Spear, F. (1995). *Metamorphic phase equilibria and pressure-temperature-time paths*. Mineralogical Society of America Washington, DC.

Spell, T. and McDougall, I. (2003). Characterization and calibration of $^{40}Ar/^{39}Ar$ dating standards. *Chemical Geology*, 198(3-4).

Steiger, R. and Jager, E. (1977). Submission on geochronology - convention on use of decay constants in geochronology and cosmochronology. *Earth and Planetary Science letters*, 36(3):359–362.

Stern, C., Kligfield, R., Schelling, D., Virdi, N., Futa, K., Peterman, Z., and Amini, H. (1989). The Bhagirathi leucogranite of the High Himalaya (Garhwal India); age, petrogenesis and tectonic implications. *Geological Society of America Special Paper*, 232:Stern, C.R. and Kligfield, R. and Schelling, D. and Virdi, N.S. and Futa, K. and Peterman, Z.E. and Amini, H.

Streckeisen, A. and Le Maitre, R. (1979). A chemical approximation to the modal QAPF classification of the igneous rocks. *Neues Jahrbuch für Mineralogie, Abhandlungen*, 136:169–206.

Suess, E. (1875). *Die Entstehung der Alpen*. Braumuller.

Suppe, J., Chou, G., Hook, S., and McClay, K. (1992). *Thrust Tectonics*. Chapman and Hall.

Tetley, N., McDougall, I., and Heydegger, H. (1980). Thermal neutron interferences in the ^{40}ar/^{39}ar dating technique. *Journal of Geophysical Research*, 85:7201–7205.

Valley, J., Carvosie, A., Fu, B., Peck, W., and Wilde, S. (2006). Comment on "Heterogeneous Hadean Hafnium: Evidence of Continental Crust at 4.4 to 4.5 Ga". *Science*, 312:1139.

Vannay, J. and Spring, L. (1993). Geochemistry of the continental basalts within the Tethyan Himalaya of Lahul-Spiti and SE Zanskar (NW India). In Treloar, P. and Searle, M., editors, *Himalayan Tectonics*, volume 74, pages 237–249. Geological Society of London Special Publication.

Vannay, J. and Steck, A. (1995). Tectonic evolution of the High Himalaya in Upper Lahul (NW Himalaya, India). *Tectonics*, 14(2):253–263.

Watson, E. and Harrison, T. (2006). Response to Comments on "Zircon Thermometer Reveals Minimum Melting Conditions on Earliest Earth". *Science*, 311:779c.

Watson, E., Wark, D., and Thomas, J. (2006). Crystallization thermometers for zircon and rutile. *Contributions to Mineralogy and Petrology*, 151:413–433.

Watson, E. B. and Harrison, T. M. (1983). Zircon saturation revisited - temperature and composition effects in a variety of crustal magma types. *Earth Planetary Science Lett.*, 64(2):295–304.

Watson, E. B. and Harrison, T. M. (2005). Zircon thermometer reveals minimum melting conditions on earliest Earth. *Science*, 308(5723):841–844.

Watts, D. R. and Harris, N. B. W. (2005). Mapping granite and gneiss in domes

along the North Himalayan antiform with ASTER SWIR band ratios. *Geological Soc. Am. Bulletin*, 117(7-8):879–886.

Wiesmayr, G. and Grasemann, B. (2002). Eohimalayan fold and thrust belt: Implications for the geodynamic evolution of the NW-Himalaya (India). *Tectonics*, 21(6):doi:10.1029/2002TC001363.

Willett, S. and Beaumont, C. (1994). Subduction of Asian lithospheric mantle beneath Tibet inferred from models of continental collision. *Nature*, 369:642–645.

Williams, I. and Hergt, J. (2000). U-pb dating of Tasmanian dolerites: a cautionary tale of SHRIMP analysis of h-gh-U zircon. In Woodhead, J., Hergt, J., and Noble, W., editors, *Beyond 2000: New Frontiers in Isotope Geoscience*. Lorne.

Williams, I. S. (1998). U-Th-Pb geochronology by Ion Microprobe. In McKibben, M. A., 3rd, W. C. S., and Ridley, W. I., editors, *Applications of microanalytical techniques to understanding mineralizing processes*, volume 7, pages 1–35. Reviews in Economic Geology.

Yin, A. (2006). Cenozoic Evolution of the Himalayan Orogen as Constrained by Along-strike Variations ofStructural Geometry, Exhumation History, and Foreland Sedimentation. *Earth Science Reviews*, 76(1-2):1–134.

Yin, A. (2007). Construction of the Cenozoic Arunachal Himalaya by Thick-skinned Thrust Stacking of Indian Basement. in prep.

Yin, A., Dubey, C., Kelty, T., Gehrels, G., Chou, M., Grove, M., and Lovera, O. (2006). Structural evolution of the Arunchal Himalaya and implications for the asymmetric development of the Himalayan orogen. *Current Science*, 90(2):195–207.

Yin, A. and Harrison, T. (2000). Geologic evolution of the Himalayan-Tibetan orogen. *Annual Review of Earth and Planetary Sciences*, 28:211–280.

Yin, A., Harrison, T., Ryerson, F., Wenji, C., Kidd, W., and Copeland, P. (1994). Tertiary structural evolution of the Gangdese thrust system, southeastern Tibet. *Journal of Geophysical Research*, 99(B4):18,175–18,201.

Yin, A., Harrison, T. M., Murphy, M. A., Grove, M., Nie, S., Ryerson, F. J., Wang, X., and Chen, Z. (1999). Tertiary deformation history of southeastern and southwestern Tibet during the Indo-Asian collision. *Geological Society of America Bulletin*, 111(11):1644–1664.

Zeitler, P. K. (2006). Geochronological evidence for rates of geodynamic evolution in the Himalayan syntaxes. *Geochimica Et Cosmochimica Acta*, 70(18):A732–A732.

Zeitler, P. K. and Chamberlain, C. P. (1991a). Petrogenetic and tectonic significance of young leukogranites from the northwestern himalaya, pakistan. *Tectonics*, 10(4):729–741.

Zeitler, P. K. and Chamberlain, C. P. (1991b). Petrogenetic and tectonic significance of young leukogranites from the northwestern himalaya, pakistan. *Tectonics*, 10(4):729–741.

Zeitler, P. K., Chamberlain, C. P., and Smith, H. A. (1993). Synchronous anatexis, metamorphism, and rapid denudation at nanga-parbat (pakistan himalaya). *Geology*, 21(4):347–350.

Zeitler, P. K., Koons, P.O. M. Bishop, M., Chamberlain, C., Craw, D., Edwards, M., Hamidullah, S., Jan, M., Khan, M. A., Khattak, M. U. K., Kidd, W., Mackie, R., Meltzer, M., Park, S., Pecher, A., Poage, M., Sarker, G., Schneider, G., Seeber, S., and Shroder, J. (2001a). Crustal Reworking at Nanga Parbat, Pakistan: Evidence for erosional focusing of crustal strain. *GSA Today*, 11:4–8.

Zeitler, P. K., Koons, P. O., Bishop, M. P., Chamberlain, C. P., Craw, D., Edwards, M. A., Hamidullah, S., Jan, M. Q., Khan, M. A., Khattak, M. U. K., Kidd, W. S. F., Mackie, R. L., Meltzer, A. S., Park, S. K., Pecher, A., Poage, M. A., Sarker, G., Schneider, D. A., Seeber, L., and Shroder, J. F. (2001b). Crustal reworking at Nanga Parbat, Pakistan: Metamorphic consequences of thermal-mechanical coupling facilitated by erosion. *Tectonics*, 20(5):712–728.

Zhang, H. F., Harris, N., Parrish, R., Kelley, S., Zhang, L., Rogers, N., Argles, T., and King, J. (2004a). Causes and consequences of protracted melting of the mid-crust exposed in the North Himalayan antiform. *Earth Planetary Science Lett.*, 228(1-2):195–212.

Zhang, H. F., Harris, N., Parrish, R., Zhang, L., and Zhao, Z. (2004b). U-pb ages of Kude and Sajia leucogranites in Saffia dome from North Himalaya and their geological implications. *Chinese Science Bulletin*, 49(19):2087–2092.

Zhao, L. S. and Xie, J. K. (1993). Lateral variations in compressional velocities beneath the tibetan plateau from pn travel-time tomography. *Geophysical J. Int.*, 115:1070–1084.

Zhao, W. L. and Morgan, W. J. (1985). Uplift of tibetan plateau. *Tectonics*, 4:359–369.

Zhao, W. L. and Morgan, W. J. (1987). Injection of indian crust into tibetan lower crust - a two-dimensional finite-element model study. *Tectonics*, 6:489–504.

Zhu, B., Kidd, W. S. F., Rowley, D. B., Currie, B. S., and Shafique, N. (2005). Age of initiation of the India-Asia collision in the east-central himalaya. *J. Geology*, 113:265–285.

Analytical methods

.1 $^{40}Ar/^{39}Ar$ thermochronology

Samples dated in this study were collected in-situ. Samples were first reduced to gravel size using conventional crushing techniques and then *ca.* 1 kg was pulverised in a tungsten carbide mill. The resulting powders were sieved to a size at which few composite grains remained and only individual mineral grains could be seen in a binocular microscope. Samples containing micas/k-feldspar greater than *ca.* 100 μm in size were separated using standard heavy liquid and magnetic separation techniques, resulting separates were typically greater than 95% pure.

Samples were irradiated for 24 hours in positions X33 or X34 of the Australian Nuclear Science and technology Organization HIFAR reactor, Lucas Heights, NSW. Mineral separate aliquots of *ca.* 40 mg were wrapped in aluminium foil and packed into an aluminium can with a number of splits of the fluence monitor 92-176 sanidine (K-Ar age, 28.1 Ma, Spell and McDougall, 2003). The sample can was inverted 180° three times during the irradiation to minimise the effect of the large neutron flux gradient in the irradiation position. A Cd liner was used to minimise interference from thermal neutrons. Irradiation duration was chosen in order to achieve a $^{40}Ar/^{39}Ar$ ratio of *ca.* 20.

Upon return from the HIFAR reactor, samples were allowed to decay to safe radiation levels and were then unpacked and transferred into plastic vials. Sample weights (*ca.* 20 mg) were calculated to provide *ca.* 45 V of ^{40}Ar for analysis, and then wrapped in tin foil ready to load into the argon extraction line. Six aliquots (*ca.* 0.6 mg) of each fluence monitor were subject to total fusion and isotopically analysed in a VG 3600 gas source mass spectrometer equipped with a Daly/photomultiplier collector with an overall sensitivity of *ca.* 3.5 × 10-17 mol/mV. The ^{40}Ar/^{39}Ar determined for each fluence monitor enabled J, the irradiation parameter, to be calculated (McDougall and Harrison, 1988).

Samples were then step-heated in a double-vacuum resistance furnace, the temperature at the base of the tantalum crucible monitored with a thermocouple. The schedule of heating temperatures for each sample can be found in the data tables in *Appendix .1.* Following each temperature step, the gas released was exposed for *ca.* 12 minutes to Zr-Al getters to remove all volatiles. The purified argon was subsequently analysed in a mass spectrometer. Samples were isotopically analysed using a VG 1200 or VG 3600 gas source mass spectrometer. Measurement was made using an electron multiplier with a sensitivity of *ca.* 7.6 × 10-15 mol/mV. Interferences from argon isotopes produced by neutron interactions with Ca, K and Cl were corrected for using standard correction factors (Tetley et al., 1980). Decay constants and ^{40}K abundances were those recommended by the IUGS Subcommission for Geochronolgy (Steiger and Jager, 1977). All data treatment was via the software K-Ar Date and Noble 1.6. Final ages include uncertainties in the decay constant and the monitor age.

Data tables

.2 Geochemistry

SAMPLE	2004T263	2004T264	2004T265	0602005	0602008	0602009	0602010	0602011	0602012
LITHOLOGY	Leucogranite	Leucogranite	Leucogranite	Gneiss (GHC)	Leucogranite	Leucogranite	Leucogranite	Meta-granite	Orthogneiss
SiO_2	72.38	73.47	74.55	87.48	67.95	74.74	76.01	76.8	73.68
Al_2O_3	14.94	14.8	15.01	5.98	17	13.26	15.23	10.81	14.03
CaO	1.01	0.91	0.75	0.57	1.18	1.14	1.13	0.14	1.28
MgO	0.13	0.1	0.09	0.6	0.45	0.37	0.25	0.04	0.59
MnO	0.02	0.02	0.02	0.02	0.02	0.02	0.01	0.04	0.03
Na_2O	4.24	3.64	4.07	1.48	3.8	3.06	3.26	0.28	3.48
K_2O	5.37	4.86	3.95	0.94	6.75	3.99	1.92	8.3	3.96
TiO_2	0.11	0.08	0.07	0.29	0.22	0.18	0.1	0.12	0.2
P_2O_5	0.13	0.1	0.1	0.03	0.09	0.06	0.08	nd	0.11
SO_3	nd	nd	nd	nd	nd	nd	nd	nd	nd
Fe_2O_3	0.89	0.91	0.74	1.96	1.67	1.48	1	2.86	1.96
Total	99.22	98.87	99.53	99.34	99.14	98.31	98.99	99.41	99.35
Sc	4.6	3.9	4.9	4.8	4.9	5.4	4.9	2.4	7.4
V	62.7	61.5	61.3	71.1	68.8	68	69.5	43.8	73.3
Cr	7.2	8	8.4	17.5	12.9	12	9.1	6	24.1
Co	33.8	35.4	51.8	54.1	37.2	43.1	30.9	40.2	30.1
Ni	2.8	2.7	2.9	8.6	7.2	7	5.9	2.8	5.2
Cu	8	2.4	2	4.9	2.7	8.7	3	9.3	3.5
Ga	24.5	23.6	22.3	6.2	16.9	15.3	20.9	10	14.5
Rb	318.9	333.6	227.9	49.4	231.9	142.6	85.8	211.3	128.7
Sr	54.6	32.7	35.1	32.8	157.3	90.3	61.4	7	118.4
Y	9.3	8.1	15.4	14.1	30.2	11.1	7.6	30.9	25.4
Zr	43.6	33.8	49.4	491.2	112	83.7	46.6	152.5	77.3
Nb	9.8	11.6	17.1	4.8	8.7	7.1	6.1	10.2	8.4
Mo	0.5	0.6	0.6	0.7	0.7	1.3	0.6	0.5	0.9
Sn	10.6	12.6	12.3	2.1	4	10.8	8.9	1.4	1.7
Cs	15.2	15.8	8.7	3.5	5.9	7.7	3.3	2.7	2.6
Ba	180.9	90.7	54.9	112.5	1002.6	508.9	148.6	290.4	556.3
La	17.8	12	8.2	26.3	47.7	29.8	13.8	52.9	16.4
Ce	37	24.6	16.4	56.3	95.7	60.4	27.6	109.6	33.8
Pr	4.3	2.9	1.9	6	10.8	6.8	3.1	12.1	3.9
Nd	16.8	11	7.3	23.5	41.8	26.2	11.6	44.2	15.4
Sm	4.5	3.3	2.4	4.8	10	5.9	3	7.6	3.7
Eu	0.6	0.3	0.3	0.7	1.8	0.9	0.5	0.8	0.7
Gd	4.1	3.2	3.1	4.5	10	5.3	2.7	6.2	3.9
Tb	0.5	0.4	0.5	0.6	1.3	0.6	0.4	0.9	0.6
Dy	2.3	2.1	3.1	3.1	6.9	2.9	1.9	6	4.6
Ho	0.3	0.3	0.5	0.5	1.1	0.4	0.3	1.2	0.9
Er	0.7	0.6	1.2	1.4	2.5	1	0.7	3.2	2.8
Tm	nd	nd	0.1	0.2	0.3	0.1	nd	0.5	0.5
Yb	0.5	0.4	0.8	1.5	1.9	0.8	0.6	2.9	3.4
Lu	nd	nd	0.1	0.2	0.3	0.1	nd	0.4	0.5
Hf	2.7	2.4	3.6	15.2	4.4	3.7	2.8	6.2	3.5
Ta	2.5	2	5.7	1.4	1.2	1.5	1.5	1.8	1.5
Pb	71.9	66.7	57.3	31.5	146.3	155.3	60.4	3.3	9.7
Th	15.7	10.7	6.7	13.7	35.9	22.5	9.9	22.9	9.6
U	11.7	11.9	18.5	3	11.2	5.6	4.9	4.4	2.6

Table 1: Bulk geochemical data from the Arunachal and Tsona Leucogranites; see *Chapter 5* for discussion.

SAMPLE	0405008	0405011	0405013	0410007	0410008	0410009	0410010	0410012
LITHOLOGY	Granite	Granite	Granite	Granite	Granite	Granite	Granite	Granite
SiO_2	71.65	71.01	68.92	62.12	69.79	69.97	70.02	70.90
Al_2O_3	16.53	15.85	15.90	20.21	15.78	15.80	15.57	15.31
CaO	2.76	2.66	2.14	3.73	2.95	2.82	2.87	2.58
MgO	0.84	0.81	1.23	0.98	0.77	0.83	0.68	0.59
MnO	0.04	0.03	0.04	0.04	0.03	0.04	0.02	0.02
Na_2O	3.77	3.71	3.66	5.18	3.86	3.72	4.35	4.09
K_2O	2.97	3.01	3.11	3.18	2.71	2.87	2.89	2.81
TiO_2	0.28	0.27	0.36	0.32	0.29	0.28	0.24	0.24
P_2O_5	0.13	0.12	0.13	0.14	0.10	0.12	0.15	0.05
SO_3	0.01	nd	0.02	nd	nd	nd	nd	nd
Fe_2O_3	1.75	1.71	2.42	2.05	1.63	1.75	1.42	1.55
Total	100.71	99.16	97.92	97.95	97.90	98.19	98.19	98.12
Sc	5.4	5.1	6.6	5.4	4.7	5.2	4.3	4.4
V	69.9	69.5	82.9	-	-	-	-	-
Cr	14.4	17.1	44.9	-	-	-	-	-
Mn	223.2	173.6	226.5	-	-	-	-	-
Co	35.2	35.9	26.1	-	-	-	-	-
Ni	5.5	6.0	20.7	-	-	-	-	-
Cu	2.8	3.0	13.2	-	-	-	-	-
Ga	67.5	64.8	58.1	-	-	-	-	-
Rb	125.4	124.3	144.7	122.7	116.2	121.1	90.5	113.3
Sr	340.2	336.1	280.7	478.6	348.3	344.3	425.8	548.3
Y	6.2	6.2	7.7	7.0	5.5	5.8	7.8	5.4
Zr	124.3	116.6	121.7	128.6	97.5	107.0	113.4	60.3
Nb	5.2	4.8	7.5	6.3	4.6	5.3	4.6	4.5
Mo	0.4	0.4	0.6	-	-	-	-	-
Sn	3.8	3.5	5.8	3.6	3.0	4.0	2.8	3.4
Cs	9.0	10.3	6.3	9.0	5.7	5.7	3.8	4.0
Ba	436.7	438.8	368.9	610.3	353.7	419.9	460.6	647.2
La	30.0	27.0	26.5	36.9	25.8	31.1	36.2	8.6
Ce	61.4	54.3	54.5	74.9	52.6	63.9	74.9	17.1
Pr	6.5	5.8	5.7	8.0	5.6	6.7	7.9	1.9
Nd	22.9	20.5	19.1	31.1	21.7	25.9	30.3	7.1
Sm	4.6	4.2	4.1	5.7	4.1	4.7	5.5	1.4
Eu	1.1	1.0	0.9	1.4	1.0	1.1	1.3	0.6
Gd	3.5	2.9	3.1	3.7	2.8	3.2	3.5	1.3
Tb	0.3	0.3	0.4	0.4	0.3	0.3	0.3	0.2
Dy	1.5	1.4	1.6	1.5	1.2	1.3	1.5	1.0
Ho	-	-	-	0.2	0.2	0.2	0.3	0.2
Er	0.6	0.6	0.7	0.6	0.5	0.5	0.7	0.5
Tm	nd	nd	nd	nd	nd	nd	0.1	nd
Yb	0.5	0.5	0.7	0.6	0.5	0.5	0.8	0.5
Lu	nd	nd	0.1	nd	nd	nd	0.1	nd
Hf	-	-	-	4.2	3.7	4.5	4.2	3.3
Ta	1.0	0.9	1.1	0.8	0.9	1.3	0.9	1.2
W	309.3	324.9	183.3	-	-	-	-	-
Pb	41.5	42.7	33.3	53.1	42.9	45.3	47.4	84.2
Th	12.2	11.4	12.9	15.0	10.5	12.6	15.5	4.7
U	2.8	1.8	4.4	3.6	2.0	2.5	3.5	2.3

Table 2: Bulk geochemical data from the Dala Granitoids; see *Chapter 5* for discussion.

SAMPLE	0310019	0310021	0310037	0310038	0310008	0310013	0310015	0310029	0310034	0310039
LITHOLOGY	Granite	Granite	Granite	Granite	Pelite	Pelite	Pelite	Pelite	Pelite	Pelite
SiO_2	74.29	75.12	71.85	74.14	66.03	74.32	68.43	67.75	72.74	73.42
Al_2O_3	14.72	12.90	15.78	15.54	17.22	11.22	13.24	13.84	13.33	12.47
CaO	1.02	0.55	0.61	0.36	1.09	0.98	1.94	1.50	1.02	0.70
MgO	0.03	0.04	0.03	0.02	0.91	1.10	1.68	1.46	1.06	1.00
MnO	0.01	0.06	0.01	0.14	0.18	0.07	0.28	0.22	0.03	0.10
Na_2O	5.65	2.87	4.47	4.15	1.43	2.58	2.80	2.48	3.92	1.69
K_2O	2.04	6.04	5.06	2.36	4.02	1.34	1.33	2.56	1.89	2.62
TiO_2	0.04	0.07	0.05	0.03	0.78	0.64	0.63	0.79	0.41	0.56
P_2O_5	0.04	0.12	0.03	0.02	0.13	0.13	0.10	0.14	0.06	0.06
SO_3	0.01	0.02	0.03	0.01	0.01	0.02	0.03	0.07	0.02	0.02
Fe_2O_3	0.30	1.27	0.17	1.03	3.93	4.50	7.42	6.75	3.74	3.98
Total	98.15	99.08	98.08	97.79	95.74	96.91	97.89	97.54	98.20	96.61
Be	9.1	3.8	12.1	17.0	3.2	3.5	3.6	6.7	5.1	6.0
Sc	2.0	7.7	2.0	1.5	13.0	9.4	11.5	12.7	9.6	10.9
V	39.1	37.2	39.7	37.5	108.3	81.2	111.0	131.1	68.1	113.3
Cr	10.9	9.0	13.2	12.2	66.8	50.5	50.5	61.1	22.2	52.4
Co	34.0	52.1	49.7	46.9	20.4	25.3	51.5	43.9	33.9	55.4
Ni	3.4	1.9	3.3	4.3	14.8	19.1	13.8	20.4	7.9	16.7
Cu	7.7	3.1	4.9	2.6	16.3	8.1	27.9	11.1	3.6	7.5
Ga	25.1	26.8	52.5	22.1	64.4	23.4	18.7	27.7	30.9	32.3
Rb	90.9	378.1	240.2	164.9	144.3	86.6	91.0	201.4	133.3	165.2
Sr	128.5	74.9	128.3	29.6	152.9	174.5	202.2	237.4	55.1	111.1
Y	3.7	35.6	1.5	14.1	26.4	21.6	24.8	28.2	39.2	27.4
Zr	20.9	49.7	8.7	28.7	240.2	355.1	180.9	221.4	222.0	258.1
Nb	3.0	11.0	3.6	5.4	14.0	10.8	10.0	13.8	14.2	10.5
Mo	0.4	0.4	0.4	0.5	0.8	0.6	0.8	1.6	0.7	0.5
Sn	4.4	6.9	6.7	8.4	6.8	4.4	4.0	5.6	21.4	5.9
Cs	31.4	7.2	14.4	3.9	8.0	6.6	13.8	55.0	6.1	49.3
Ba	161.6	180.0	576.6	49.1	715.1	200.5	130.0	235.2	244.1	295.9
La	6.6	8.5	4.1	2.4	43.3	27.4	29.5	40.5	50.7	29.1
Ce	13.9	20.5	8.7	4.4	90.0	54.5	60.3	82.9	98.0	59.0
Pr	1.5	2.4	0.9	0.4	10.1	6.2	6.7	9.5	10.5	6.6
Nd	5.8	8.9	3.5	1.4	38.3	24.8	27.0	37.3	38.8	25.9
Sm	1.6	3.1	0.9	0.6	6.7	4.8	5.1	6.9	7.4	4.9
Eu	0.3	0.2	0.3	nd	1.4	1.0	1.4	1.5	1.3	1.0
Gd	1.4	3.6	0.8	0.8	5.4	4.3	4.8	5.7	6.9	4.5
Tb	0.2	0.8	nd	0.2	0.8	0.6	0.7	0.8	1.1	0.7
Dy	0.8	6.2	0.4	1.9	5.2	3.9	4.5	5.1	6.9	4.5
Ho	0.1	1.3	nd	0.4	1.0	0.8	0.9	1.0	1.4	1.0
Er	0.3	4.0	0.1	1.0	2.8	2.3	2.7	2.9	4.2	2.9
Tm	nd	0.7	nd	0.2	0.4	0.4	0.4	0.5	0.6	0.4
Yb	0.2	5.1	nd	1.1	2.6	2.7	2.7	3.1	4.4	2.9
Lu	nd	0.7	nd	0.1	0.4	0.4	0.4	0.5	0.6	0.4
Hf	1.9	3.7	1.6	3.1	7.2	9.7	6.3	6.9	7.4	8.2
Ta	1.0	2.2	2.0	1.9	1.4	1.2	1.6	1.7	2.2	1.5
Pb	80.4	33.9	137.9	75.3	19.6	21.8	23.8	32.3	17.3	30.4
Th	3.4	14.1	1.8	2.2	15.9	11.1	10.9	13.4	34.0	11.0
U	1.6	5.5	1.1	3.1	3.4	2.2	2.1	2.5	6.4	3.3

Table 3: Bulk geochemical data from the Yala-Xiangbo Granitoids and Yala-Xiangbo Pelites; see *Chapter 5* for discussion.

SAMPLE	0410004	0410019	0410024	0410026	0410027	0410028	0410033	0410036	0410037	0410041
LITHOLOGY	Mafic	Mafic	Mafic	Mafic	Mafic	Mafic	Mafic	Mafic	Mafic	Mafic
SiO_2	48.35	47.87	55.78	43.75	54.23	54.67	47.2	43.73	47.1	49.92
Al_2O_3	16.14	11.5	17.81	2.18	13.62	16.39	15.36	13.59	16.7	13.09
CaO	0.63	7.96	5.75	2.33	7.97	4.67	11.19	5.79	12.07	10.1
MgO	8.7	4.35	2.74	39.99	8.95	4.6	6.96	6.71	7.91	5.97
MnO	0.13	0.26	0.17	0.13	0.14	0.15	0.17	0.2	0.14	0.19
Na_2O	2.49	2.47	3.94	nd	3.6	6.31	2.21	2.78	1.79	2.58
K_2O	0.4	0.93	2.77	nd	0.64	0.2	0.19	0.07	0.02	0.02
TiO_2	2.79	3.37	0.59	0.04	0.31	0.62	1.17	2.96	0.74	2.24
P_2O_5	0.33	0.44	0.41	nd	0.02	0.04	0.1	0.54	0.06	0.22
SO_3	nd	0.59	nd	0.04	nd	nd	0.2	0.52	0.24	nd
Fe_2O_3	13.41	17.97	6.58	8.48	7.7	8.68	10.89	14.26	8.6	12.48
Total	93.36	97.71	96.54	96.96	97.19	96.34	95.64	91.14	95.37	96.8
Sc	27.5	45.6	11.6	15.2	41.4	32.1	49.2	28.6	36.6	40.8
V	-	-	-	-	-	-	-	-	-	-
Cr	-	-	-	-	-	-	-	-	-	-
Co	-	-	-	-	-	-	-	-	-	-
Ni	-	-	-	-	-	-	-	-	-	-
Cu	-	-	-	-	-	-	-	-	-	-
Ga	-	-	-	-	-	-	-	-	-	-
Rb	12.3	29.7	75.6	nd	3.4	1.3	4.6	1.9	0.5	nd
Sr	91.6	157.8	371.1	0.3	68.1	96.7	207.7	496.8	221.2	568.2
Y	30	62.5	19.2	1.2	7.8	11.8	24.5	28.3	15.3	31.8
Zr	208.3	262.1	116.5	0.2	11.6	23.4	59.3	175	41.3	133
Nb	13.8	25.1	6	nd	0.1	0.1	3.5	38.1	3.9	8.7
Mo	-	-	-	-	-	-	-	-	-	-
Sn	2.4	2.6	1.4	0.9	0.9	0.9	1.4	1.9	1.2	1.9
Cs	1.6	0.9	1.5	nd	0.4	0.2	1.8	1.8	0.2	nd
Ba	86.3	289.2	370.9	0.2	17.7	10.3	71.4	103	9.9	5.7
La	21.2	25.2	22.4	nd	0.4	0.7	6.4	30.1	4.8	10.9
Ce	48.2	52	41.4	nd	1.2	2	13.3	60.8	9.9	25.2
Pr	6.1	6.7	4.6	nd	0.2	0.4	1.7	7.5	1.3	3.6
Nd	27	31.3	18.7	nd	1.3	2.3	8.5	32.4	5.9	17.2
Sm	6.4	8.2	3.7	nd	0.6	1	2.5	7	1.7	4.9
Eu	1.6	2.4	1.2	nd	0.2	0.4	0.9	2.2	0.7	1.7
Gd	6.6	10.2	3.4	nd	0.9	1.5	3.4	6.8	2.3	5.9
Tb	1	1.7	0.5	nd	0.2	0.3	0.6	1	0.4	0.9
Dy	6.1	11.4	3.3	0.2	1.4	2.1	4.3	5.8	2.7	6.2
Ho	1.1	2.4	0.7	nd	0.3	0.5	0.9	1.1	0.6	1.3
Er	3.1	7.1	2.2	0.2	0.9	1.4	2.9	3	1.8	3.4
Tm	0.4	1	0.3	nd	0.1	0.2	0.4	0.4	0.2	0.5
Yb	2.8	7	2.4	0.2	1	1.4	2.9	2.6	1.7	3.2
Lu	0.4	1	0.4	nd	0.2	0.2	0.4	0.4	0.2	0.4
Hf	5.4	6.9	3.2	0.2	0.7	1	1.9	4.3	1.3	3.8
Ta	1	1.6	0.5	0.1	0.3	0.1	0.4	2.6	0.3	0.7
Pb	5.9	8.3	7.7	2.6	2.5	2.5	4.4	4.5	3.9	5.5
Th	5.3	6.2	6.3	nd	nd	nd	1.2	3	1.1	1.8
U	0.9	1	1.4	nd	nd	nd	0.2	0.7	0.2	0.4

Table 4: Bulk geochemical data from mafic bodies outcropping within the Tethyan Himalaya; see *Chapter 5* for discussion.

SAMPLE	0405005	0410005	0410084	0410086	0310014
LITHOLOGY	Metabasite	Metabasite	Metabasite	Metabasite	Metabasite
SiO_2	46.54	50.35	50.61	51.14	44.96
Al_2O_3	13.61	13.61	13.21	15.32	14.27
CaO	13.39	7.68	9.55	10.45	9.90
MgO	9.33	4.52	5.05	6.55	7.16
MnO	0.19	0.18	0.16	0.25	0.16
Na_2O	1.59	3.1	3.1	0.97	0.78
K_2O	0.02	1.39	1.13	0.29	0.01
TiO_2	0.91	4.04	3.41	1.17	1.33
P_2O_5	0.06	0.31	0.43	0.12	0.13
SO_3	nd	0.03	0.01	0.4	0.01
Fe_2O_3	10.27	12.38	11.37	11.89	11.14
Total	95.9	97.58	98.04	98.55	89.85
Be	-	-	-	-	1.2
Sc	50.9	29.2	25.7	42.6	41.8
V	-	-	-	-	293.3
Cr	-	-	-	-	179.2
Co	-	-	-	-	46.5
Ni	-	-	-	-	87.7
Cu	-	-	-	-	120.2
Ga	-	-	-	-	13.0
Rb	nd	40.4	33.1	7.7	0.3
Sr	123.9	335.5	410.9	97.5	297.9
Y	15.9	32.1	32.5	23.8	24.4
Zr	38	230.8	247.6	70.3	63.6
Nb	2.2	15.6	24.6	2.1	6.3
Mo	-	-	-	-	0.9
Sn	1.3	2.8	2.7	2.8	3.5
Cs	nd	2.8	3.6	15.9	nd
Ba	2.7	311.7	115	56.5	2.0
La	2.2	25.8	27.2	4.2	6.3
Ce	5.7	55.5	59.5	10.5	13.8
Pr	0.9	7.1	7.9	1.6	1.9
Nd	4.9	31.1	35.6	8.1	9.4
Sm	1.7	7.2	8.2	2.6	2.8
Eu	0.7	2.1	2.6	1.1	1.1
Gd	2.5	7.2	8	3.6	3.8
Tb	0.4	1	1.1	0.6	0.6
Dy	3	6.5	6.9	4.3	4.4
Ho	0.6	1.2	1.3	0.9	0.9
Er	1.8	3.3	3.4	2.7	2.7
Tm	0.3	0.5	0.4	0.4	0.4
Yb	1.8	3	2.9	2.6	2.5
Lu	0.3	0.4	0.4	0.4	0.4
Hf	1.4	6.4	6.7	2.7	1.9
Ta	0.3	1.4	1.9	0.5	0.5
Pb	7.3	8.5	9.6	11.7	6.7
Th	0.2	6.5	3.8	1.4	0.6
U	nd	1.1	0.8	0.4	0.1

Table 5: Bulk geochemical data from metabasites outcropping within the Tethyan Himalaya; see *Chapter 5* for discussion.

.3 $^{40}Ar/^{39}Ar$ thermochronology

Temp (C)	^{36}Ar (mol)	^{37}Ar (mol)	^{38}Ar (mol)	^{39}Ar (mol)	^{40}Ar (mol)	%^{40}Ar*	^{40}Ar*/^{39}Ar$_K$	Cum. %^{39}Ar	Age (Ma)	$\pm 1\sigma$ (Ma)
1400	5.99E-16	1.50E-14	1.22E-15	6.934E-15	2.827E-13	37.9	15.48	19.95	11.98	0.34
1400	5.82E-16	3.79E-15	1.21E-15	6.841E-15	2.771E-13	38.0	15.42	39.65	11.93	0.26
1400	4.54E-16	8.80E-15	9.47E-16	5.538E-15	2.183E-13	38.9	15.37	55.58	11.89	0.30
1400	4.55E-16	7.37E-15	1.01E-15	5.779E-15	2.355E-13	43.2	17.62	72.22	13.63	0.31
1400	3.99E-16	8.26E-15	8.53E-16	4.927E-15	1.946E-13	39.7	15.72	86.39	12.17	0.31
1400	3.74E-16	8.15E-15	8.23E-16	4.729E-15	1.833E-13	40.2	15.59	100.00	12.07	0.28
Total	2.86E-15	5.14E-14	6.06E-15	3.475E-14	1.392E-12	-	15.86	-	12.27	0.30

Data corrected for mass spectrometer discrimination, line blanks, and for the decay of ^{37}Ar and ^{39}Ar during and after irradiation. Amounts of ^{39}Ar are derived from the measured sensitivity of the mass spectrometer. Absolute isotope amounts may have uncertainties of $\sim$10%. Totals are the %^{39}Ar weighted means of the analyses. Correction factors: $(^{40}\mathrm{Ar}/^{39}\mathrm{Ar})_K = 0.024$; $(^{36}\mathrm{Ar}/^{37}\mathrm{Ar})_{Ca} = 0.00035$; $(^{39}\mathrm{Ar}/^{37}\mathrm{Ar})_{Ca} = 0.000786$. J = 4.3048E-4

Table 6: ^{40}Ar/^{39}Ar data from biotite separated from sample 0310008 of the Yala-Xiangbo pelites.

Temp (C)	^{36}Ar (mol)	^{37}Ar (mol)	^{38}Ar (mol)	^{39}Ar (mol)	^{40}Ar (mol)	%^{40}Ar*	^{40}Ar*/^{39}Ar$_K$	Cum. %^{39}Ar	Age (Ma)	$\pm 1\sigma$ (Ma)
1400	1.44E-16	1.95E-14	9.14E-16	5.547E-15	1.327E-13	69.3	16.63	22.92	13.04	0.14
1400	1.33E-16	1.94E-18	7.81E-16	4.703E-15	1.162E-13	66.1	16.34	42.41	12.81	0.15
1400	1.20E-16	1.94E-18	7.76E-16	4.712E-15	1.121E-13	68.4	16.27	61.93	12.75	0.17
1400	1.29E-16	1.94E-18	7.73E-16	4.647E-15	1.149E-13	66.7	16.49	81.19	12.93	0.17
1400	1.23E-16	1.95E-18	7.60E-16	4.540E-15	1.106E-13	67.0	16.32	100.00	12.80	0.17
Total	6.49E-16	1.95E-14	4.00E-15	2.415E-14	5.865E-13	-	16.42	-	12.87	0.16

Data corrected for mass spectrometer discrimination, line blanks, and for the decay of ^{37}Ar and ^{39}Ar during and after irradiation. Amounts of ^{39}Ar are derived from the measured sensitivity of the mass spectrometer. Absolute isotope amounts may have uncertainties of $\sim$10%. Totals are the %^{39}Ar weighted means of the analyses. Correction factors: $(^{40}\mathrm{Ar}/^{39}\mathrm{Ar})_K = 0.024$; $(^{36}\mathrm{Ar}/^{37}\mathrm{Ar})_{Ca} = 0.00035$; $(^{39}\mathrm{Ar}/^{37}\mathrm{Ar})_{Ca} = 0.000786$. J = 4.3611E-4

Table 7: ^{40}Ar/^{39}Ar data from biotite separated from sample 0310011 of the Yala-Xiangbo pelites.

Temp (C)	^{36}Ar (mol)	^{37}Ar (mol)	^{38}Ar (mol)	^{39}Ar (mol)	^{40}Ar (mol)	%^{40}Ar*	^{40}Ar*/^{39}Ar$_K$	Cum. %^{39}Ar	Age (Ma)	$\pm 1\sigma$ (Ma)
1400	1.20E-16	1.67E-14	6.23E-16	3.890E-15	9.641E-14	64.8	16.13	25.29	13.39	0.22
1400	1.02E-16	9.76E-17	5.24E-16	3.244E-15	8.119E-14	62.9	15.74	46.45	13.07	0.21
1400	9.49E-17	1.94E-18	4.00E-16	2.420E-15	6.540E-14	57.0	15.41	62.24	12.80	0.21
1400	8.82E-17	1.94E-18	4.79E-16	2.982E-15	7.190E-14	63.7	15.35	81.70	12.75	0.19
1400	8.91E-17	1.94E-18	4.50E-16	2.805E-15	6.917E-14	61.8	15.25	100.00	12.66	0.20
Total	4.94E-16	1.68E-14	2.48E-15	1.534E-14	3.841E-13	-	15.6	-	12.97	0.21

Data corrected for mass spectrometer discrimination, line blanks, and for the decay of ^{37}Ar and ^{39}Ar during and after irradiation. Amounts of ^{39}Ar are derived from the measured sensitivity of the mass spectrometer. Absolute isotope amounts may have uncertainties of $\sim$10%. Totals are the %^{39}Ar weighted means of the analyses. Correction factors: $(^{40}\mathrm{Ar}/^{39}\mathrm{Ar})_K = 0.024$; $(^{36}\mathrm{Ar}/^{37}\mathrm{Ar})_{Ca} = 0.00035$; $(^{39}\mathrm{Ar}/^{37}\mathrm{Ar})_{Ca} = 0.000786$. J = 4.6188E-4

Table 8: ^{40}Ar/^{39}Ar data from biotite separated from sample 0310012 of the Yala-Xiangbo Granitoids.

Temp (C)	^{36}Ar (mol)	^{37}Ar (mol)	^{38}Ar (mol)	^{39}Ar (mol)	^{40}Ar (mol)	%^{40}Ar*	^{40}Ar*/^{39}Ar$_K$	Cum. %^{39}Ar	Age (Ma)	$\pm 1\sigma$ (Ma)
650	4.78E-16	4.47E-17	-	9.660E-16	1.601E-13	11.7	19.44	0.66	16.61	2.53
725	2.48E-16	2.69E-16	-	2.907E-15	1.227E-13	40.1	16.92	2.67	14.47	0.42
775	3.33E-16	4.48E-17	-	4.386E-15	1.716E-13	42.5	16.62	5.68	14.21	0.29
815	6.03E-16	4.78E-17	-	6.170E-15	2.832E-13	36.9	16.96	9.93	14.50	0.24
850	1.20E-15	4.81E-17	-	1.772E-14	6.511E-13	45.4	16.70	22.13	14.28	0.18
880	5.65E-16	4.81E-17	-	3.020E-14	6.629E-13	74.5	16.35	42.91	13.98	0.05
915	2.28E-16	4.82E-17	-	2.522E-14	4.766E-13	85.5	16.15	60.26	13.82	0.10
965	3.05E-16	4.82E-17	-	2.112E-14	4.327E-13	78.8	16.14	74.80	13.81	0.13
1050	4.32E-16	4.83E-17	-	1.453E-14	3.662E-13	64.8	16.33	84.80	13.97	0.14
1150	2.94E-16	2.84E-16	-	1.697E-14	3.674E-13	76.0	16.46	96.48	14.08	0.08
1150	8.77E-17	6.54E-16	-	2.517E-15	6.491E-14	59.9	15.44	98.22	13.21	0.34
1250	1.32E-16	2.16E-15	-	1.256E-15	5.755E-14	32.3	14.80	99.08	12.66	0.54
1350	3.35E-16	4.55E-17	-	1.337E-15	1.226E-13	19.2	17.64	100.00	15.08	1.09
Total	5.24E-15	3.79E-15	-	1.453E-13	3.940E-12	-	16.4	-	14.02	0.16

Data corrected for mass spectrometer discrimination, line blanks, and for the decay of ^{37}Ar and ^{39}Ar during and after irradiation. Amounts of ^{39}Ar are derived from the measured sensitivity of the mass spectrometer. Absolute isotope amounts may have uncertainties of ∼10%. Totals are the %^{39}Ar weighted means of the analyses. Correction factors: $(^{40}\mathrm{Ar}/^{39}\mathrm{Ar})_K = 0.024$; $(^{36}\mathrm{Ar}/^{37}\mathrm{Ar})_{Ca} = 0.00035$; $(^{39}\mathrm{Ar}/^{37}\mathrm{Ar})_{Ca} = 0.000786$. J = 4.7594E-4

Table 9: ^{40}Ar/^{39}Ar data from muscovite separated from sample 0310012 of the Yala-Xiangbo Granitoids.

Temp (C)	^{36}Ar (mol)	^{37}Ar (mol)	^{38}Ar (mol)	^{39}Ar (mol)	^{40}Ar (mol)	%^{40}Ar*	^{40}Ar*/^{39}Ar$_K$	Cum. %^{39}Ar	Age (Ma)	$\pm1\sigma$ (Ma)
650	1.46E-16	6.03E-17	-	1.553E-15	6.637E-14	34.7	14.85	0.79	11.44	0.23
725	2.56E-16	3.39E-17	-	4.699E-15	1.512E-13	49.8	16.02	3.19	12.33	0.27
760	2.25E-16	1.42E-16	-	5.358E-15	1.514E-13	55.8	15.76	5.92	12.13	0.15
800	4.01E-16	1.67E-16	-	7.904E-15	2.500E-13	52.3	16.55	9.94	12.74	0.13
830	5.66E-16	3.89E-17	-	9.737E-15	3.268E-13	48.6	16.31	14.91	12.55	0.22
860	9.71E-16	6.76E-16	-	1.463E-14	5.311E-13	45.8	16.62	22.36	12.79	0.13
880	6.39E-16	3.89E-17	-	2.067E-14	5.330E-13	64.3	16.58	32.89	12.76	0.09
900	3.41E-16	9.27E-16	-	2.029E-14	4.360E-13	76.5	16.45	43.23	12.66	0.06
925	3.23E-16	3.95E-17	-	1.897E-14	4.071E-13	76.2	16.37	52.90	12.60	0.07
955	4.22E-16	3.96E-17	-	1.870E-14	4.390E-13	71.3	16.73	62.43	12.88	0.06
995	4.54E-16	1.61E-16	-	1.630E-14	4.028E-13	66.4	16.40	70.74	12.62	0.09
1045	5.82E-16	3.96E-17	-	2.142E-14	5.322E-13	67.4	16.75	81.65	12.89	0.07
1100	3.54E-16	3.97E-17	-	2.305E-14	4.888E-13	78.3	16.61	93.40	12.78	0.05
1165	1.14E-16	3.97E-17	-	6.912E-15	1.493E-13	77.1	16.65	96.92	12.82	0.14
1230	1.60E-16	3.73E-17	-	2.532E-15	8.823E-14	46.1	16.07	98.21	12.37	0.36
1350	4.38E-16	3.74E-17	-	3.512E-15	1.883E-13	31.1	16.65	100.00	12.81	0.26
Total	6.39E-15	2.52E-15	-	1.962E-13	5.142E-12	-	16.50	-	12.70	0.10

Data corrected for mass spectrometer discrimination, line blanks, and for the decay of ^{37}Ar and ^{39}Ar during and after irradiation. Amounts of ^{39}Ar are derived from the measured sensitivity of the mass spectrometer. Absolute isotope amounts may have uncertainties of ∼10%. Totals are the %^{39}Ar weighted means of the analyses. Correction factors: $(^{40}\mathrm{Ar}/^{39}\mathrm{Ar})_K = 0.024$; $(^{36}\mathrm{Ar}/^{37}\mathrm{Ar})_{Ca} = 0.00035$; $(^{39}\mathrm{Ar}/^{37}\mathrm{Ar})_{Ca} = 0.000786$. J = 4.2818E-04

Table 10: ^{40}Ar/^{39}Ar data from muscovite separated from sample 0310019 of the Yala-Xiangbo Granitoids.

Temp (C)	^{36}Ar (mol)	^{37}Ar (mol)	^{38}Ar (mol)	^{39}Ar (mol)	^{40}Ar (mol)	%^{40}Ar*	^{40}Ar*/^{39}Ar$_K$	Cum. %^{39}Ar	Age (Ma)	$\pm1\sigma$ (Ma)
450	2.16E-16	5.86E-19	1.23E-16	5.154E-16	1.591E-13	59.9	184.91	0.06	157.69	7.26
450	1.26E-16	3.45E-19	8.91E-17	4.207E-16	4.432E-14	15.9	16.70	0.10	14.83	2.83
500	1.75E-16	5.86E-19	2.31E-16	1.282E-15	1.022E-13	49.4	39.36	0.24	34.74	1.51
500	3.62E-16	1.32E-16	3.34E-16	1.669E-15	1.236E-13	13.4	9.89	0.42	8.79	0.89
550	8.05E-17	3.51E-19	5.73E-16	3.848E-15	6.513E-14	63.3	10.72	0.84	9.53	0.23
600	9.68E-17	3.51E-19	8.91E-16	5.676E-15	1.158E-13	75.2	15.34	1.46	13.61	0.20
600	8.30E-17	2.58E-16	1.08E-15	7.000E-15	1.026E-13	76.0	11.14	2.22	9.90	0.11
650	8.20E-17	1.14E-16	1.42E-15	9.237E-15	1.406E-13	82.6	12.58	3.23	11.17	0.09
650	8.62E-17	3.52E-19	1.79E-15	1.185E-14	1.604E-13	83.9	11.36	4.51	10.09	0.09
700	8.37E-17	1.54E-16	2.13E-15	1.387E-14	1.928E-13	87.0	12.10	6.02	10.75	0.07
700	1.01E-16	1.53E-16	2.72E-15	1.773E-14	2.333E-13	87.0	11.44	7.95	10.17	0.05
750	7.93E-17	7.67E-18	2.81E-15	1.858E-14	2.455E-13	90.3	11.93	9.97	10.60	0.05
750	1.01E-16	2.52E-16	3.61E-15	2.381E-14	3.081E-13	90.1	11.67	12.57	10.37	0.05
800	7.89E-17	3.36E-16	3.47E-15	2.304E-14	2.957E-13	91.9	11.80	15.07	10.49	0.09
800	9.44E-17	6.95E-16	4.15E-15	2.735E-14	3.471E-13	91.8	11.65	18.05	10.35	0.30
850	5.78E-17	6.09E-19	4.00E-15	2.620E-14	3.319E-13	94.7	11.99	20.90	10.65	0.07
850	1.24E-16	3.52E-16	5.18E-15	3.413E-14	4.432E-13	91.6	11.89	24.61	10.57	0.05
900	6.59E-17	1.07E-16	3.96E-15	2.600E-14	3.304E-13	93.9	11.94	27.44	10.61	0.08
900	1.65E-16	3.50E-16	5.04E-15	3.265E-14	4.350E-13	88.6	11.80	30.99	10.49	0.06
950	1.84E-15	2.95E-16	3.70E-15	2.234E-14	8.073E-13	32.6	11.79	33.42	10.47	0.24
950	1.80E-16	2.06E-16	4.36E-15	2.868E-14	3.994E-13	86.5	12.05	36.54	10.70	0.08
950	2.84E-16	1.77E-16	4.33E-15	2.886E-14	4.335E-13	80.5	12.08	39.68	10.74	0.12
1000	6.89E-17	6.32E-19	1.75E-15	1.155E-14	1.710E-13	87.9	13.02	40.94	11.57	0.09
1000	1.87E-16	6.33E-19	2.74E-15	1.798E-14	2.807E-13	80.1	12.51	42.90	11.11	0.12
1050	1.06E-16	6.33E-19	2.13E-15	1.434E-14	2.156E-13	85.2	12.81	44.46	11.38	0.14
1050	2.55E-16	2.54E-16	2.91E-15	1.942E-14	3.247E-13	76.7	12.81	46.57	11.38	0.12
1050	5.37E-16	4.16E-17	3.73E-15	2.408E-14	4.747E-13	66.4	13.10	49.19	11.63	0.18
1100	1.50E-16	9.07E-19	1.59E-15	1.079E-14	1.902E-13	76.6	13.50	50.36	11.99	0.21
1100	3.00E-16	9.08E-19	2.79E-15	1.814E-14	3.447E-13	74.2	14.10	52.34	12.52	0.15
1100	6.13E-16	5.01E-16	3.90E-15	2.519E-14	5.351E-13	66.1	14.03	55.08	12.46	0.17
1100	1.03E-15	6.70E-16	4.78E-15	3.025E-14	7.254E-13	57.9	13.89	58.37	12.33	0.15
1100	1.39E-15	9.14E-19	4.94E-15	3.057E-14	8.328E-13	50.7	13.81	61.69	12.27	0.22
1100	1.87E-15	9.18E-19	5.34E-15	3.353E-14	1.022E-12	45.7	13.93	65.34	12.37	0.21
1100	2.59E-15	2.46E-16	5.50E-15	3.380E-14	1.259E-12	39.1	14.55	69.02	12.92	0.24
1100	4.40E-15	2.68E-16	7.35E-15	4.392E-14	1.940E-12	32.9	14.51	73.80	12.88	0.41
1200	1.35E-16	6.55E-19	2.76E-15	1.846E-14	3.126E-13	87.1	14.76	75.81	13.10	0.09
1230	2.67E-16	6.98E-16	5.50E-15	3.613E-14	5.941E-13	86.6	14.23	79.74	12.64	0.09
1260	2.76E-16	9.36E-19	8.65E-15	5.725E-14	9.046E-13	90.8	14.35	85.96	12.74	0.09
1290	3.12E-16	2.54E-16	1.03E-14	6.805E-14	1.057E-12	91.1	14.16	93.37	12.57	0.07
1320	2.85E-16	9.37E-19	7.35E-15	4.901E-14	7.611E-13	88.8	13.79	98.70	12.25	0.16
1350	3.09E-16	4.32E-16	1.81E-15	1.167E-14	2.391E-13	61.7	12.63	99.97	11.22	0.24
1450	1.42E-17	1.58E-18	7.17E-17	2.744E-16	8.882E-15	52.8	17.09	100.00	15.17	7.92
Total	1.97E-14	6.96E-15	1.42E-13	9.192E-13	1.801E-11	-	13.25	-	11.77	0.15

Data corrected for mass spectrometer discrimination, line blanks, and for the decay of ^{37}Ar and ^{39}Ar during and after irradiation. Amounts of ^{39}Ar are derived from the measured sensitivity of the mass spectrometer. Absolute isotope amounts may have uncertainties of ∼10%. Totals are the %^{39}Ar weighted means of the analyses. Correction factors: $(^{40}\mathrm{Ar}/^{39}\mathrm{Ar})_K = 0.025$; $(^{36}\mathrm{Ar}/^{37}\mathrm{Ar})_{Ca} = 0.00035$; $(^{39}\mathrm{Ar}/^{37}\mathrm{Ar})_{Ca} = 0.000786$. J = 4.9398E-4

Table 11: ^{40}Ar/^{39}Ar data from K-feldspar separated from sample 0310019 of the Yala-Xiangbo Granitoids.

Temp (C)	^{36}Ar (mol)	^{37}Ar (mol)	^{38}Ar (mol)	^{39}Ar (mol)	^{40}Ar (mol)	%^{40}Ar*	^{40}Ar*/^{39}Ar$_K$	Cum. %^{39}Ar	Age (Ma)	$\pm 1\sigma$ (Ma)
1400	1.87E-16	1.24E-14	8.01E-16	4.927E-15	1.312E-13	58.7	15.66	23.47	12.05	0.21
1400	1.61E-16	1.93E-18	6.13E-16	3.668E-15	1.044E-13	54.3	15.44	40.98	11.88	0.18
1400	1.62E-16	1.93E-15	6.98E-16	4.236E-15	1.134E-13	57.9	15.50	61.19	11.92	0.16
1400	1.55E-16	6.83E-17	6.53E-16	3.905E-15	1.056E-13	56.6	15.32	79.83	11.79	0.53
1400	1.71E-16	1.93E-18	6.97E-16	4.226E-15	1.154E-13	56.0	15.30	100.00	11.77	0.24
Total	8.36E-16	1.44E-14	3.46E-15	2.096E-14	5.700E-13	-	15.46	-	11.89	0.26

Data corrected for mass spectrometer discrimination, line blanks, and for the decay of ^{37}Ar and ^{39}Ar during and after irradiation. Amounts of ^{39}Ar are derived from the measured sensitivity of the mass spectrometer. Absolute isotope amounts may have uncertainties of $\sim$10%. Totals are the %^{39}Ar weighted means of the analyses. Correction factors: $(^{40}\mathrm{Ar}/^{39}\mathrm{Ar})_K = 0.024$; $(^{36}\mathrm{Ar}/^{37}\mathrm{Ar})_{Ca} = 0.00035$; $(^{39}\mathrm{Ar}/^{37}\mathrm{Ar})_{Ca} = 0.000786$. J = 4.2777E-4

Table 12: ^{40}Ar/^{39}Ar data from biotite separated from sample 0310029 of the Yala-Xiangbo pelites.

Temp (C)	^{36}Ar (mol)	^{37}Ar (mol)	^{38}Ar (mol)	^{39}Ar (mol)	^{40}Ar (mol)	%^{40}Ar*	^{40}Ar*/^{39}Ar$_K$	Cum. %^{39}Ar	Age (Ma)	$\pm 1\sigma$ (Ma)
650	1.67E-16	3.93E-17	-	1.433E-15	7.161E-14	31.1	15.52	0.97	11.96	0.63
750	3.09E-16	3.94E-17	-	5.996E-15	1.938E-13	52.7	17.02	5.04	13.12	0.16
800	3.36E-16	7.72E-17	-	7.858E-15	2.335E-13	57.3	17.02	10.38	13.12	0.12
840	9.25E-16	4.20E-17	-	1.315E-14	5.004E-13	45.2	17.20	19.30	13.25	0.13
865	5.44E-16	4.20E-17	-	1.848E-14	4.769E-13	66.0	17.04	31.85	13.13	0.10
885	2.00E-16	4.21E-17	-	1.744E-14	3.521E-13	82.9	16.73	43.69	12.89	0.05
910	1.65E-16	4.21E-17	-	1.566E-14	3.099E-13	83.9	16.61	54.32	12.80	0.07
945	2.27E-16	4.22E-17	-	1.458E-14	3.101E-13	78.0	16.59	64.21	12.78	0.06
990	3.06E-16	4.22E-17	-	1.151E-14	2.838E-13	67.9	16.74	72.03	12.90	0.08
1050	4.90E-16	4.44E-17	-	1.380E-14	3.781E-13	61.5	16.84	81.40	12.98	0.15
1120	4.55E-16	4.45E-17	-	2.127E-14	4.969E-13	72.7	16.98	95.84	13.08	0.09
1200	1.29E-16	6.13E-16	-	4.922E-15	1.202E-13	68.2	16.65	99.18	12.83	0.16
1270	1.80E-16	4.19E-17	-	1.077E-15	7.139E-14	25.4	16.85	99.91	12.98	0.64
1350	3.80E-16	2.22E-17	-	1.349E-16	1.133E-13	0.9	7.57	100.00	5.84	13.63
Total	4.81E-15	1.18E-15	-	1.473E-13	3.912E-12	-	16.84	-	12.97	0.12

Data corrected for mass spectrometer discrimination, line blanks, and for the decay of ^{37}Ar and ^{39}Ar during and after irradiation. Amounts of ^{39}Ar are derived from the measured sensitivity of the mass spectrometer. Absolute isotope amounts may have uncertainties of ∼10%. Totals are the %^{39}Ar weighted means of the analyses. Correction factors: $(^{40}\mathrm{Ar}/^{39}\mathrm{Ar})_K = 0.024$; $(^{36}\mathrm{Ar}/^{37}\mathrm{Ar})_{Ca} = 0.00035$; $(^{39}\mathrm{Ar}/^{37}\mathrm{Ar})_{Ca} = 0.000786$. J = 4.2867E-04

Table 13: ^{40}Ar/^{39}Ar data from muscovite separated from sample 0310029 of the Yala-Xiangbo pelites.

Temp (C)	^{36}Ar (mol)	^{37}Ar (mol)	^{38}Ar (mol)	^{39}Ar (mol)	^{40}Ar (mol)	%^{40}Ar*	^{40}Ar*/^{39}Ar$_K$	Cum. %^{39}Ar	Age (Ma)	$\pm1\sigma$ (Ma)
1400	1.44E-16	1.82E-18	1.06E-15	6.104E-15	1.388E-13	69.3	15.77	15.77	12.57	0.17
1400	1.40E-16	2.73E-16	1.03E-15	5.883E-15	1.340E-13	69.0	15.72	30.97	12.53	0.11
1400	1.25E-16	6.82E-15	8.68E-16	5.054E-15	1.160E-13	68.5	15.74	44.02	12.55	0.18
1400	1.62E-16	2.79E-15	1.33E-15	7.649E-15	1.680E-13	71.6	15.73	63.78	12.54	0.11
1400	1.96E-16	4.28E-15	1.64E-15	9.508E-15	2.074E-13	72.2	15.76	88.34	12.56	0.09
1400	9.76E-17	1.94E-18	7.93E-16	4.511E-15	1.002E-13	71.1	15.81	100.00	12.60	0.16
Total	8.64E-16	1.42E-14	6.72E-15	3.871E-14	8.643E-13	-	15.75	-	12.56	0.13

Data corrected for mass spectrometer discrimination, line blanks, and for the decay of ^{37}Ar and ^{39}Ar during and after irradiation. Amounts of ^{39}Ar are derived from the measured sensitivity of the mass spectrometer. Absolute isotope amounts may have uncertainties of $\sim$10%. Totals are the %^{39}Ar weighted means of the analyses. Correction factors: $(^{40}\mathrm{Ar}/^{39}\mathrm{Ar})_K = 0.024$; $(^{36}\mathrm{Ar}/^{37}\mathrm{Ar})_{Ca} = 0.00035$; $(^{39}\mathrm{Ar}/^{37}\mathrm{Ar})_{Ca} = 0.000786$. J = 4.4354E-4

Table 14: ^{40}Ar/^{39}Ar data from biotite separated from sample 0310033 of the Yala-Xiangbo pelites.

Temp (C)	^{36}Ar (mol)	^{37}Ar (mol)	^{38}Ar (mol)	^{39}Ar (mol)	^{40}Ar (mol)	%^{40}Ar*	^{40}Ar*/^{39}Ar$_K$	Cum. %^{39}Ar	Age (Ma)	$\pm 1\sigma$ (Ma)
1400	1.01E-16	1.11E-14	7.14E-16	4.398E-15	9.874E-14	70.9	15.95	22.99	12.87	0.22
1400	8.50E-17	1.94E-18	5.84E-16	3.691E-15	8.360E-14	69.9	15.82	42.33	12.76	0.17
1400	8.90E-17	1.94E-18	5.88E-16	3.612E-15	8.371E-14	68.5	15.87	61.25	12.80	0.16
1400	8.38E-17	1.43E-16	5.24E-16	3.239E-15	7.586E-14	67.3	15.76	78.21	12.71	0.22
1400	1.00E-16	1.94E-18	6.66E-16	4.159E-15	9.704E-14	69.3	16.18	100.00	13.05	0.19
Total	4.59E-16	1.12E-14	3.08E-15	1.910E-14	4.389E-13	-	15.93	-	12.84	0.19

Data corrected for mass spectrometer discrimination, line blanks, and for the decay of ^{37}Ar and ^{39}Ar during and after irradiation. Amounts of ^{39}Ar are derived from the measured sensitivity of the mass spectrometer. Absolute isotope amounts may have uncertainties of $\sim$10%. Totals are the %^{39}Ar weighted means of the analyses. Correction factors: $(^{40}\mathrm{Ar}/^{39}\mathrm{Ar})_K = 0.024$; $(^{36}\mathrm{Ar}/^{37}\mathrm{Ar})_{Ca} = 0.00035$; $(^{39}\mathrm{Ar}/^{37}\mathrm{Ar})_{Ca} = 0.000786$. J = 4.4862E-4

Table 15: ^{40}Ar/^{39}Ar data from biotite separated from sample 0310034 of the Yala-Xiangbo pelites.

Temp (C)	^{36}Ar (mol)	^{37}Ar (mol)	^{38}Ar (mol)	^{39}Ar (mol)	^{40}Ar (mol)	%^{40}Ar*	^{40}Ar*/^{39}Ar$_K$	Cum. %^{39}Ar	Age (Ma)	$\pm1\sigma$ (Ma)
650	9.95E-16	4.20E-17	-	1.170E-15	3.176E-13	7.4	20.14	0.93	16.22	1.82
700	3.12E-16	5.91E-16	-	2.085E-15	1.232E-13	25.1	14.83	2.58	11.96	0.49
750	3.23E-16	2.78E-16	-	4.546E-15	1.688E-13	43.3	16.09	6.19	12.98	0.24
790	5.13E-16	4.35E-17	-	7.164E-15	2.690E-13	43.4	16.29	11.88	13.14	0.27
830	1.21E-15	4.64E-17	-	1.095E-14	5.371E-13	33.4	16.40	20.57	13.23	0.24
860	1.58E-15	4.64E-17	-	2.597E-14	8.951E-13	47.7	16.43	41.19	13.25	0.11
885	5.44E-16	4.65E-17	-	2.543E-14	5.716E-13	71.5	16.08	61.37	12.97	0.07
915	4.19E-16	4.66E-17	-	2.152E-14	4.732E-13	73.5	16.17	78.46	13.04	0.08
945	4.36E-16	4.71E-17	-	1.622E-14	3.915E-13	66.8	16.13	91.33	13.00	0.13
985	4.97E-16	4.72E-17	-	1.092E-14	3.264E-13	54.8	16.38	100.00	13.20	0.12
Total	6.82E-15	1.24E-15	-	1.260E-13	4.073E-12	-	16.26	-	13.11	0.15

Data corrected for mass spectrometer discrimination, line blanks, and for the decay of ^{37}Ar and ^{39}Ar during and after irradiation. Amounts of ^{39}Ar are derived from the measured sensitivity of the mass spectrometer. Absolute isotope amounts may have uncertainties of $\sim$10%. Totals are the %^{39}Ar weighted means of the analyses. Correction factors: $(^{40}\mathrm{Ar}/^{39}\mathrm{Ar})_K = 0.024$; $(^{36}\mathrm{Ar}/^{37}\mathrm{Ar})_{Ca} = 0.00035$; $(^{39}\mathrm{Ar}/^{37}\mathrm{Ar})_{Ca} = 0.000786$. J = 4.4862E-04

Table 16: ^{40}Ar/^{39}Ar data from muscovite separated from sample 0310034 of the Yala-Xiangbo pelites.

Temp (C)	^{36}Ar (mol)	^{37}Ar (mol)	^{38}Ar (mol)	^{39}Ar (mol)	^{40}Ar (mol)	%^{40}Ar*	^{40}Ar*/^{39}Ar$_K$	Cum. %^{39}Ar	Age (Ma)	$\pm1\sigma$ (Ma)
437	2.67E-15	2.20E-16	1.60E-15	7.374E-15	1.305E-12	39.6	70.08	0.04	704.01	12.53
437	6.34E-16	1.50E-16	6.34E-16	3.569E-15	2.004E-13	6.5	3.66	0.06	44.44	14.83
487	8.25E-16	7.71E-18	1.55E-15	9.685E-15	3.933E-13	37.9	15.40	0.11	179.98	5.41
487	4.95E-16	1.59E-16	2.13E-15	1.462E-14	1.741E-13	15.8	1.89	0.19	23.05	3.22
541	3.14E-16	2.38E-16	5.37E-15	3.823E-14	2.662E-13	64.8	4.52	0.39	54.64	0.68
541	2.72E-16	3.98E-16	9.92E-15	7.057E-14	1.650E-13	50.2	1.17	0.76	14.36	0.32
590	3.52E-16	9.84E-16	2.02E-14	1.437E-13	3.944E-13	72.8	2.00	1.52	24.39	0.31
590	2.62E-16	1.02E-15	3.09E-14	2.206E-13	3.469E-13	76.2	1.20	2.69	14.67	0.05
640	3.17E-16	1.29E-15	4.49E-14	3.230E-13	5.381E-13	81.2	1.35	4.40	16.54	0.08
640	2.09E-16	1.58E-15	6.26E-14	4.530E-13	6.216E-13	88.4	1.21	6.80	14.84	0.04
691	2.80E-16	1.77E-15	7.45E-14	5.405E-13	7.756E-13	87.7	1.26	9.66	15.40	0.08
691	1.67E-16	2.28E-15	1.05E-13	7.601E-13	1.001E-12	93.3	1.23	13.69	15.02	0.03
750	2.00E-16	2.45E-15	1.05E-13	7.634E-13	1.038E-12	92.6	1.26	17.73	15.40	0.03
750	1.59E-16	3.38E-15	1.32E-13	9.622E-13	1.269E-12	94.5	1.25	22.83	15.25	0.02
800	1.55E-16	3.95E-15	1.05E-13	7.602E-13	1.023E-12	93.8	1.26	26.85	15.44	0.04
800	1.41E-16	4.22E-15	1.18E-13	8.610E-13	1.148E-12	94.6	1.26	31.41	15.43	0.03
850	1.42E-16	3.81E-15	8.51E-14	6.194E-13	8.480E-13	93.3	1.28	34.69	15.64	0.07
850	1.41E-16	4.31E-15	9.80E-14	7.141E-13	9.688E-13	94.0	1.28	38.48	15.60	0.06
900	1.80E-16	3.57E-15	7.03E-14	5.108E-13	7.248E-13	91.0	1.29	41.18	15.80	0.04
900	1.89E-16	3.65E-15	8.46E-14	6.152E-13	8.644E-13	91.9	1.29	44.44	15.80	0.08
950	2.88E-16	3.20E-15	6.55E-14	4.761E-13	7.235E-13	86.7	1.32	46.96	16.12	0.09
950	2.85E-16	3.47E-15	9.17E-14	6.657E-13	9.745E-13	89.7	1.31	50.49	16.07	0.07
950	4.26E-16	3.13E-15	9.77E-14	7.122E-13	1.094E-12	87.0	1.34	54.26	16.33	0.05
1000	3.82E-16	1.89E-15	4.79E-14	3.499E-13	6.174E-13	80.4	1.42	56.11	17.35	0.12
1000	3.77E-16	2.30E-15	7.15E-14	5.201E-13	8.441E-13	85.3	1.39	58.87	16.94	0.06
1050	5.26E-16	2.35E-15	6.33E-14	4.613E-13	8.467E-13	80.4	1.48	61.31	18.03	0.06
1050	6.55E-16	3.25E-15	8.72E-14	6.331E-13	1.152E-12	81.9	1.49	64.66	18.23	0.10
1050	9.95E-16	3.94E-15	1.05E-13	7.614E-13	1.499E-12	79.2	1.56	68.69	19.06	0.09
1100	5.30E-16	2.81E-15	4.79E-14	3.481E-13	7.335E-13	77.6	1.63	70.54	19.97	0.12
1100	5.45E-16	3.29E-15	6.68E-14	4.867E-13	9.599E-13	82.0	1.62	73.11	19.77	0.10
1100	7.10E-16	3.92E-15	7.77E-14	5.627E-13	1.133E-12	80.3	1.62	76.10	19.76	0.09
1100	9.10E-16	3.76E-15	7.09E-14	5.151E-13	1.119E-12	74.9	1.63	78.82	19.88	0.06
1100	9.86E-16	3.20E-15	6.09E-14	4.413E-13	1.034E-12	70.8	1.66	81.16	20.27	0.06
1100	1.42E-15	2.66E-15	5.89E-14	4.267E-13	1.144E-12	62.5	1.68	83.42	20.47	0.15
1100	2.16E-15	2.42E-15	5.71E-14	4.105E-13	1.351E-12	52.1	1.71	85.59	20.93	0.23
1100	4.66E-15	3.03E-15	7.14E-14	5.115E-13	2.275E-12	39.0	1.73	88.30	21.19	0.21
1200	2.85E-16	8.53E-16	1.48E-14	1.067E-13	3.028E-13	71.4	2.03	88.87	24.71	0.38
1230	4.91E-16	1.73E-15	2.45E-14	1.770E-13	5.028E-13	70.4	2.00	89.81	24.39	0.12
1260	7.81E-16	3.16E-15	4.03E-14	2.965E-13	8.408E-13	71.8	2.04	91.38	24.84	0.20
1290	1.19E-15	3.92E-15	6.56E-14	4.732E-13	1.302E-12	72.2	1.99	93.88	24.25	0.19
1320	1.33E-15	3.67E-15	7.85E-14	5.678E-13	1.506E-12	73.0	1.94	96.89	23.64	0.12
1350	9.40E-16	3.00E-15	5.62E-14	4.073E-13	1.063E-12	73.0	1.91	99.05	23.25	0.17
1450	6.31E-15	5.28E-15	2.60E-14	1.802E-13	2.179E-12	14.3	1.73	100.00	21.11	1.78
Total	3.53E-14	1.10E-13	2.61E-12	1.888E-11	3.926E-11	-	1.50	-	18.39	0.12

Data corrected for mass spectrometer discrimination, line blanks, and for the decay of ^{37}Ar and ^{39}Ar during and after irradiation. Amounts of ^{39}Ar are derived from the measured sensitivity of the mass spectrometer. Absolute isotope amounts may have uncertainties of ~10%. Totals are the %^{39}Ar weighted means of the analyses. Correction factors: $(^{40}\mathrm{Ar}/^{39}\mathrm{Ar})_K = 0.024$; $(^{36}\mathrm{Ar}/^{37}\mathrm{Ar})_{Ca} = 0.00035$; $(^{39}\mathrm{Ar}/^{37}\mathrm{Ar})_{Ca} = 0.000786$. J = 6.8108E-03

Table 17: ^{40}Ar/^{39}Ar data from K-feldspar separated from sample 0405008 of the Dala Granitoids.

Temp (C)	^{36}Ar (mol)	^{37}Ar (mol)	^{38}Ar (mol)	^{39}Ar (mol)	^{40}Ar (mol)	%^{40}Ar*	^{40}Ar*/^{39}Ar$_K$	Cum. %^{39}Ar	Age (Ma)	$\pm1\sigma$ (Ma)
437	1.72E-15	2.86E-16	3.00E-15	1.151E-14	3.146E-12	83.8	229.01	0.07	1709.32	9.37
437	4.18E-16	2.55E-18	6.99E-16	4.344E-15	1.669E-13	26.0	9.98	0.10	120.06	8.05
487	9.79E-16	3.11E-16	4.45E-15	2.426E-14	2.515E-12	88.5	91.73	0.25	884.23	3.35
487	1.93E-16	7.38E-17	2.51E-15	1.722E-14	1.265E-13	54.6	4.01	0.36	49.19	2.05
541	6.07E-16	3.51E-16	8.68E-15	5.856E-14	1.497E-12	87.9	22.48	0.72	260.00	1.08
541	1.77E-16	3.73E-16	9.60E-15	6.835E-14	1.742E-13	69.1	1.76	1.15	21.78	0.36
590	5.25E-16	1.13E-15	2.34E-14	1.653E-13	1.347E-12	88.2	7.19	2.18	87.30	0.32
590	1.60E-16	1.11E-15	2.60E-14	1.875E-13	3.111E-13	83.4	1.38	3.34	17.13	0.08
640	3.33E-16	1.88E-15	3.97E-14	2.863E-13	8.822E-13	88.1	2.72	5.12	33.46	0.23
640	1.46E-16	1.82E-15	4.49E-14	3.264E-13	4.865E-13	89.5	1.34	7.16	16.53	0.04
691	2.47E-16	2.34E-15	5.32E-14	3.853E-13	8.453E-13	90.3	1.98	9.56	24.48	0.06
691	1.09E-16	2.44E-15	5.80E-14	4.216E-13	6.078E-13	93.1	1.34	12.18	16.62	0.03
750	1.99E-16	3.21E-15	5.84E-14	4.249E-13	7.992E-13	91.4	1.72	14.82	21.26	0.14
750	8.97E-17	3.63E-15	6.30E-14	4.594E-13	6.637E-13	94.4	1.36	17.68	16.89	0.04
800	1.09E-16	4.08E-15	5.33E-14	3.896E-13	6.332E-13	93.5	1.52	20.11	18.81	0.08
800	9.23E-17	4.72E-15	5.90E-14	4.309E-13	6.254E-13	94.1	1.37	22.79	16.90	0.05
850	1.17E-16	4.21E-15	4.78E-14	3.493E-13	5.627E-13	92.5	1.49	24.96	18.44	0.04
850	9.00E-17	4.89E-15	5.46E-14	3.988E-13	5.858E-13	93.9	1.38	27.45	17.08	0.05
900	1.10E-16	4.45E-15	4.16E-14	3.050E-13	4.873E-13	91.9	1.47	29.35	18.18	0.07
900	1.17E-16	4.98E-15	4.99E-14	3.649E-13	5.554E-13	92.3	1.40	31.62	17.39	0.06
950	1.62E-16	4.75E-15	3.82E-14	2.774E-13	4.810E-13	88.8	1.54	33.34	19.05	0.08
950	1.96E-16	5.02E-15	4.91E-14	3.558E-13	5.981E-13	89.0	1.50	35.56	18.51	0.09
950	3.00E-16	4.34E-15	5.34E-14	3.903E-13	7.257E-13	86.6	1.61	37.99	19.91	0.05
1000	2.84E-16	3.87E-15	2.70E-14	1.973E-13	4.715E-13	81.3	1.94	39.22	24.00	0.09
1000	2.90E-16	3.38E-15	4.14E-14	3.034E-13	6.601E-13	86.0	1.87	41.10	23.13	0.08
1050	4.39E-16	5.57E-15	4.38E-14	3.174E-13	8.302E-13	83.5	2.19	43.08	26.98	0.14
1050	5.94E-16	4.02E-15	6.73E-14	4.891E-13	1.258E-12	85.2	2.19	46.12	27.06	0.11
1050	9.40E-16	5.36E-15	1.00E-13	7.262E-13	2.017E-12	85.4	2.37	50.64	29.26	0.07
1100	4.53E-16	3.60E-15	5.66E-14	4.109E-13	1.176E-12	87.8	2.51	53.20	31.00	0.08
1100	5.85E-16	5.39E-15	8.33E-14	6.067E-13	1.664E-12	88.8	2.44	56.98	30.04	0.05
1100	8.44E-16	6.79E-15	1.05E-13	7.632E-13	2.122E-12	87.4	2.43	61.73	29.99	0.06
1100	8.91E-16	6.33E-15	9.91E-14	7.235E-13	2.037E-12	86.3	2.43	66.23	29.96	0.09
1100	9.68E-16	5.43E-15	8.65E-14	6.289E-13	1.908E-12	84.2	2.56	70.15	31.53	0.09
1100	1.37E-15	4.84E-15	8.47E-14	6.176E-13	2.077E-12	79.9	2.69	73.99	33.10	0.20
1100	2.03E-15	3.76E-15	8.17E-14	5.905E-13	2.276E-12	73.0	2.81	77.67	34.67	0.23
1100	3.77E-15	4.49E-15	1.10E-13	7.916E-13	3.475E-12	67.4	2.96	82.59	36.43	0.15
1200	1.62E-16	1.34E-15	2.11E-14	1.527E-13	5.516E-13	90.7	3.28	83.54	40.29	0.30
1230	2.54E-16	1.88E-15	3.49E-14	2.520E-13	8.932E-13	90.9	3.22	85.11	39.66	0.11
1260	4.19E-16	3.31E-15	6.41E-14	4.633E-13	1.596E-12	91.6	3.16	88.00	38.83	0.09
1290	6.65E-16	4.26E-15	1.14E-13	8.227E-13	2.776E-12	92.2	3.11	93.12	38.31	0.07
1320	6.33E-16	3.90E-15	1.11E-13	8.040E-13	2.663E-12	92.3	3.05	95.56	37.61	0.06
1350	6.01E-16	3.55E-15	1.08E-13	7.852E-13	2.549E-12	92.3	3.00	98.00	36.90	0.05
1450	4.36E-15	4.38E-15	4.47E-14	3.207E-13	2.236E-12	42.0	2.93	100.00	36.06	0.47
Total	2.71E-14	1.42E-13	2.22E-12	1.607E-11	5.140E-11	-	2.68	-	33.00	0.12

Data corrected for mass spectrometer discrimination, line blanks, and for the decay of ^{37}Ar and ^{39}Ar during and after irradiation. Amounts of ^{39}Ar are derived from the measured sensitivity of the mass spectrometer. Absolute isotope amounts may have uncertainties of ~10%. Totals are the %^{39}Ar weighted means of the analyses. Correction factors: $(^{40}\mathrm{Ar}/^{39}\mathrm{Ar})_K = 0.024$; $(^{36}\mathrm{Ar}/^{37}\mathrm{Ar})_{Ca} = 0.00035$; $(^{39}\mathrm{Ar}/^{37}\mathrm{Ar})_{Ca} = 0.000786$. J = 6.8959E-03

Table 18: ^{40}Ar/^{39}Ar data from K-feldspar separated from sample 0405011 of the Dala Granitoids.

.4 U-Th-Pb geochronology

Sample	$\frac{^{206}Pb}{^{238}U}$	$\pm 1\sigma\%$	$\frac{^{207}Pb}{^{206}Pb}$	$\pm 1\sigma\%$	$^{206}Pb_c\%$	U_{ppm}	Th_{ppm}	**Age (Ma)**	$\pm$**2**σ **(Ma)**
410003	0.041	2.5	0.064	5.2	0.80	302	212	205	7
410003	0.047	1.0	0.050	2.6	0.32	360	605	210	5
410003	0.093	1.2	0.051	2.2	0.18	812	492	231	10
410003	0.110	3.1	0.048	2.9	1.04	240	155	236	11
410003	0.097	1.0	0.050	2.9	0.52	317	250	245	11
410003	0.137	1.4	0.049	3.4	0.24	139	132	328	16
410003	0.038	4.1	0.052	2.9	1.55	316	202	336	9
410003	0.088	1.2	0.054	1.2	0.04	1263	450	355	5
410003	0.088	0.9	0.053	1.5	0.00	920	792	357	5
410003	0.092	0.6	0.054	1.5	0.11	651	79	376	9
410003	0.065	9.8	0.054	1.8	0.81	1217	133	376	17
410003	0.114	0.5	0.055	0.9	0.05	1638	165	386	5
410003	0.105	1.1	0.057	2.7	0.88	170	143	473	12
410003	0.122	1.1	0.059	2.6	1.66	148	73	517	13
410003	0.248	1.4	0.056	1.5	0.06	347	73	554	28
410003	0.241	0.9	0.059	1.8	0.25	233	43	564	27
410003	0.137	0.6	0.061	1.3	0.10	553	32	564	14
410003	0.243	1.2	0.058	1.4	0.05	405	6	570	28
410003	0.152	0.6	0.058	1.5	0.10	387	100	580	9
410003	0.130	1.0	0.063	2.9	0.65	182	144	593	15
410003	0.150	1.1	0.060	1.2	0.00	610	391	623	9
410003	0.144	1.2	0.065	2.6	1.10	118	42	631	16
410003	0.162	1.7	0.055	3.7	0.40	58	64	638	14
410003	0.282	0.6	0.061	1.2	0.12	460	163	649	32
410003	0.158	0.7	0.063	1.5	0.41	304	159	659	16
410003	0.148	1.4	0.063	2.9	0.10	92	11	659	18
410003	0.105	1.9	0.059	1.1	0.16	1039	61	693	20
410003	0.064	8.2	0.064	2.9	0.11	159	79	704	19
410003	0.395	0.6	0.066	1.0	0.05	400	78	842	40
410003	0.209	0.6	0.070	1.3	0.43	317	123	914	22
410003	0.448	0.9	0.080	7.1	0.97	138	49	1027	47
410003	0.281	2.5	0.077	0.9	0.00	436	68	1067	16
410003	0.507	1.0	0.075	1.1	0.18	240	211	1119	51
410003	0.289	0.8	0.080	1.5	0.01	170	292	1126	29
410003	0.322	1.4	0.082	2.5	0.40	64	45	1153	33
410003	0.487	2.0	0.080	0.9	0.06	375	202	1166	48
410003	0.272	0.9	0.079	1.7	0.20	125	107	1183	31
410003	0.255	1.6	0.080	2.9	1.60	39	10	1185	28
410003	0.574	1.1	0.079	1.7	0.02	84	53	1214	58
410003	0.317	1.1	0.087	1.4	0.15	140	117	1266	33
410003	0.362	0.9	0.099	1.2	0.46	159	222	1555	40
410003	0.768	1.4	0.097	0.5	0.02	637	72	1581	39
410003	0.909	1.7	0.102	1.0	0.01	123	56	1687	55
410003	0.443	0.4	0.107	0.6	0.07	426	7	1736	30
410003	1.859	0.5	0.239	0.3	0.02	335	125	3117	63
410006	0.074	1.5	0.053	2.4	0.55	469	339	195	9
410006	0.048	1.7	0.054	3.1	0.28	185	51	236	6
410006	0.063	1.2	0.047	4.0	0.39	177	110	240	5
410006	0.052	1.0	0.051	2.6	0.73	293	185	246	6
410006	0.106	1.5	0.055	3.6	0.08	151	127	249	12
410006	0.054	1.0	0.053	2.8	0.37	260	162	268	7
410006	0.101	3.9	0.051	1.0	0.26	2339	952	272	12
410006	0.127	0.7	0.054	1.7	0.20	579	112	306	14
410006	0.153	0.8	0.052	1.8	0.15	482	148	314	14
410006	0.057	0.7	0.053	1.8	0.42	544	252	322	7

continues next page...

Sample	$\frac{^{206}Pb}{^{238}U}$	$\pm 1\sigma\%$	$\frac{^{207}Pb}{^{206}Pb}$	$\pm 1\sigma\%$	$^{206}Pb_c\%$	U_{ppm}	Th_{ppm}	**Age (Ma)**	$\pm 2\sigma$ **(Ma)**
410006	0.094	0.9	0.053	1.8	0.08	540	380	336	5
410006	0.098	0.7	0.052	1.9	0.05	450	117	376	6
410006	0.111	2.3	0.059	2.2	0.25	164	36	489	12
410006	0.119	0.8	0.059	1.9	0.22	198	66	541	13
410006	0.121	0.7	0.058	1.6	0.04	285	7	544	13
410006	0.144	1.1	0.057	2.4	0.24	180	183	548	9
410006	0.245	1.1	0.060	2.4	0.21	138	50	549	26
410006	0.243	7.9	0.070	8.9	1.28	10	22	557	38
410006	0.118	0.6	0.059	1.4	0.31	426	115	557	13
410006	0.253	1.0	0.060	2.1	0.41	171	30	561	25
410006	0.122	1.0	0.061	2.3	0.36	134	50	565	14
410006	0.248	1.3	0.060	2.8	1.05	104	62	568	26
410006	0.151	0.8	0.058	2.2	0.21	196	59	572	10
410006	0.173	2.8	0.061	1.7	0.00	334	5	589	9
410006	0.141	1.9	0.062	3.7	1.29	40	59	597	18
410006	0.150	0.5	0.062	1.2	0.24	423	142	621	15
410006	0.172	0.6	0.061	1.1	0.09	730	414	652	9
410006	0.296	0.8	0.060	1.6	0.70	242	158	660	30
410006	0.290	2.1	0.060	1.2	0.07	487	92	675	33
410006	0.197	2.7	0.065	2.0	0.21	179	140	691	12
410006	0.217	1.4	0.063	2.3	0.00	116	86	695	13
410006	0.315	5.1	0.064	2.7	0.67	90	37	720	33
410006	0.211	0.5	0.068	1.3	0.14	422	231	740	11
410006	0.207	0.7	0.066	1.1	0.07	466	124	798	12
410006	0.212	3.7	0.078	3.2	2.11	100	34	800	18
410006	0.124	6.8	0.069	1.8	0.33	317	43	860	14
410006	0.411	1.4	0.068	1.0	0.05	408	299	902	41
410006	0.205	1.2	0.073	1.0	0.10	352	183	912	22
410006	0.423	2.0	0.070	1.7	0.00	454	118	947	45
410006	0.418	2.7	0.072	1.2	0.07	336	53	975	45
410006	0.229	1.7	0.074	3.5	1.48	27	12	1012	33
410006	0.242	0.8	0.076	1.5	0.55	134	57	1073	27
410006	0.504	0.9	0.075	1.6	0.73	140	106	1079	51
410006	0.309	1.2	0.073	0.7	0.00	745	87	1081	16
410006	0.572	0.7	0.076	1.0	0.01	271	408	1140	47
410006	0.281	0.6	0.079	1.1	0.15	223	143	1198	30
410006	0.369	1.7	0.092	2.8	0.16	62	40	1472	75
410006	0.466	1.3	0.097	1.0	0.03	240	140	1526	24
410006	0.394	0.7	0.102	1.1	0.13	112	65	1634	40
410006	0.401	0.4	0.102	0.6	0.07	442	102	1650	30
410006	0.267	0.8	0.095	1.4	0.82	101	203	1699	44
410006	0.391	0.7	0.108	1.0	0.05	130	128	1766	37
410006	0.440	0.5	0.123	0.7	0.00	209	88	1998	33
410006	0.600	2.1	0.126	0.6	0.00	369	186	2080	27
410006	0.488	2.6	0.172	1.7	0.21	46	79	2560	42
410006	0.702	0.8	0.218	0.9	0.44	67	26	2947	46
410016	0.106	1.6	0.053	4.0	1.45	121	120	249	12
410016	0.076	0.3	0.051	1.0	0.06	2436	1501	253	3
410016	0.144	4.6	0.103	0.7	1.07	1595	182	366	18
410016	0.092	0.8	0.060	2.3	0.28	314	229	460	8
410016	0.147	0.5	0.078	0.5	0.15	2398	309	527	13
410016	0.123	1.0	0.060	1.3	0.20	506	116	543	13
410016	0.135	0.3	0.060	0.8	0.06	1167	160	560	14
410016	0.168	0.5	0.086	1.7	0.83	1851	760	615	9
410016	0.150	0.5	0.065	1.5	0.30	713	167	629	14
410016	0.288	1.6	0.062	3.0	0.47	68	25	666	32
410016	0.330	1.6	0.065	0.7	0.07	954	135	736	35
410016	0.190	0.8	0.069	0.8	0.13	881	53	833	20
410016	0.228	1.0	0.074	1.3	0.13	775	604	896	21

continues next page...

Sample	$\frac{^{206}Pb}{^{238}U}$	$\pm 1\sigma\%$	$\frac{^{207}Pb}{^{206}Pb}$	$\pm 1\sigma\%$	$^{206}Pb_c\%$	U_{ppm}	Th_{ppm}	**Age (Ma)**	$\pm 2\sigma$ **(Ma)**
410016	0.419	2.5	0.069	1.3	0.00	564	161	906	42
410016	0.211	0.9	0.069	1.4	0.09	225	65	942	24
410016	0.448	1.8	0.074	1.1	0.17	265	74	1023	48
410016	0.238	1.9	0.073	1.8	0.89	122	55	1038	26
410016	0.464	2.8	0.075	0.7	0.17	675	86	1064	44
410016	0.264	1.5	0.087	4.5	0.74	901	467	1079	24
410016	0.536	1.6	0.075	0.9	0.18	371	147	1108	50
410016	0.524	2.1	0.076	1.0	0.06	255	118	1119	48
410016	0.365	0.8	0.077	0.7	0.11	953	66	1132	39
410016	0.215	0.5	0.079	1.7	0.03	486	299	1159	21
410016	0.292	2.8	0.077	3.3	0.91	40	46	1188	32
410016	0.318	1.1	0.079	2.2	0.00	73	63	1202	26
410016	0.287	0.7	0.080	1.2	0.03	184	643	1207	30
410016	0.567	2.5	0.079	1.3	0.08	143	95	1216	54
410016	0.630	0.7	0.079	1.1	0.13	190	183	1228	56
410016	0.655	1.2	0.086	0.9	0.04	265	139	1355	49
410016	0.380	0.5	0.095	0.9	0.13	237	315	1459	34
410016	0.388	0.5	0.104	0.6	0.34	771	71	1658	31
410016	0.878	1.6	0.104	0.4	0.04	953	746	1693	38
410016	0.448	0.5	0.107	0.9	0.10	320	115	1736	37
410016	0.837	4.0	0.109	0.4	0.07	903	164	1774	41
410016	0.316	0.3	0.117	0.4	0.18	1172	338	1892	26
410016	0.857	1.9	0.119	0.7	0.00	228	96	1920	50
410016	1.033	1.4	0.124	0.5	0.07	353	358	2012	48
410016	0.367	3.8	0.126	1.1	0.24	161	71	2020	39
410016	0.901	0.9	0.140	1.8	0.05	567	92	2223	75
410016	0.566	2.1	0.171	0.3	0.02	741	102	2568	25
410016	0.319	1.9	0.182	0.6	0.18	518	174	2661	31
410016	0.681	0.3	0.197	0.4	0.01	543	314	2805	26
410016	1.740	1.5	0.237	0.7	0.10	133	42	3112	68
410016	0.932	0.6	0.245	0.5	0.01	923	47	3156	28
410016	0.824	0.4	0.246	0.6	0.03	380	265	3157	35
410016	0.789	0.4	0.247	0.4	0.01	337	243	3158	29
410016	1.698	2.6	0.249	0.8	0.04	449	188	3178	71
410029	0.050	0.8	0.066	3.6	1.96	425	321	205	5
410029	0.045	1.5	0.053	4.0	0.00	107	116	214	6
410029	0.052	2.6	0.055	3.2	0.48	156	158	218	6
410029	0.047	1.3	0.056	4.3	2.19	129	96	223	8
410029	0.064	0.9	0.050	2.6	0.00	437	373	231	4
410029	0.048	1.0	0.051	3.5	0.49	204	200	235	6
410029	0.049	1.1	0.052	3.0	0.63	177	83	245	6
410029	0.048	1.6	0.051	3.1	0.67	152	86	248	6
410029	0.052	1.2	0.051	2.5	1.01	280	213	255	6
410029	0.058	1.2	0.054	3.2	0.10	126	77	292	8
410029	0.091	0.6	0.052	1.5	0.06	811	43	302	4
410029	0.087	0.9	0.054	2.5	0.35	263	157	306	5
410029	0.123	0.8	0.065	0.9	0.18	792	253	493	11
410029	0.147	1.4	0.057	1.8	0.35	409	176	518	8
410029	0.128	1.1	0.060	2.6	0.74	81	54	528	14
410029	0.115	1.1	0.059	1.6	0.20	252	213	544	13
410029	0.125	1.0	0.064	2.2	0.45	107	113	548	14
410029	0.121	0.8	0.058	1.2	0.16	371	66	549	13
410029	0.110	1.0	0.059	2.2	0.51	114	128	559	14
410029	0.119	1.4	0.061	3.3	0.82	47	1	564	16
410029	0.164	0.9	0.057	2.5	0.21	137	2	565	10
410029	0.117	0.6	0.059	1.4	0.13	303	69	572	14
410029	0.118	1.3	0.057	3.2	1.08	56	49	575	16
410029	0.125	0.9	0.062	2.1	0.09	140	83	576	15
410029	0.112	0.4	0.060	1.0	0.01	511	134	576	14

continues next page...

Sample	$\frac{^{206}Pb}{^{238}U}$	$\pm 1\sigma\%$	$\frac{^{207}Pb}{^{206}Pb}$	$\pm 1\sigma\%$	$^{206}Pb_c\%$	U_{ppm}	Th_{ppm}	**Age (Ma)**	$\pm 2\sigma$ **(Ma)**
410029	0.120	2.8	0.060	7.0	0.20	12	6	578	23
410029	0.062	7.6	0.062	2.2	1.36	405	123	580	10
410029	0.124	0.7	0.059	1.7	0.37	217	58	584	14
410029	0.172	1.3	0.061	1.6	0.00	908	69	605	8
410029	0.116	1.7	0.060	4.1	0.92	35	28	616	19
410029	0.132	0.9	0.062	2.3	0.71	111	106	616	15
410029	0.163	2.4	0.060	5.1	0.00	428	54	619	9
410029	0.148	1.9	0.069	5.4	0.34	246	99	635	14
410029	0.199	2.4	0.062	4.5	0.00	458	113	701	10
410029	0.168	1.2	0.068	1.6	0.22	136	30	770	19
410029	0.220	1.1	0.072	2.2	0.00	133	34	817	15
410029	0.181	1.3	0.070	0.9	0.22	357	52	935	23
410029	0.216	3.0	0.069	1.9	0.67	82	43	949	24
410029	0.208	0.8	0.074	0.9	0.07	518	167	1003	24
410029	0.273	1.6	0.079	1.5	0.23	198	223	1007	17
410029	0.227	0.7	0.074	1.4	0.42	136	35	1039	25
410029	0.229	0.6	0.075	1.3	0.00	172	117	1069	27
410029	0.265	1.2	0.078	1.4	0.01	99	47	1221	32
410029	0.355	2.0	0.077	4.1	0.61	18	31	1239	40
410029	0.395	1.4	0.103	1.4	0.35	47	43	1679	45
410029	0.386	0.5	0.102	0.7	0.01	194	66	1684	32
410029	0.418	0.4	0.106	0.7	0.01	708	227	1689	30
410029	0.380	1.4	0.114	0.7	0.18	211	82	1833	37
410029	0.696	0.7	0.186	0.7	0.07	93	48	2710	36
410029	0.674	0.4	0.202	0.4	0.04	335	130	2836	27
410029	0.782	5.2	0.208	0.4	0.05	516	192	2885	25
410031	0.053	0.8	0.054	2.1	0.88	249	135	267	6
410031	0.052	0.5	0.052	1.4	0.42	703	566	275	6
410031	0.056	1.5	0.051	4.0	0.55	73	73	286	8
410031	0.062	1.2	0.052	3.1	0.23	113	81	317	8
410031	0.063	1.3	0.054	3.3	1.10	89	61	345	9
410031	0.072	1.4	0.056	3.5	1.64	66	29	373	11
410031	0.100	0.7	0.061	1.6	0.42	222	87	482	11
410031	0.109	0.6	0.060	1.4	0.31	704	112	500	23
410031	0.105	1.6	0.061	3.6	0.67	151	72	506	24
410031	0.106	0.9	0.058	2.0	0.09	133	67	521	13
410031	0.263	1.5	0.060	2.8	0.28	308	208	529	24
410031	0.174	1.6	0.059	2.0	0.00	263	198	543	9
410031	0.117	0.8	0.061	2.1	0.15	132	63	549	13
410031	0.264	1.4	0.059	2.9	0.32	192	94	552	25
410031	0.239	6.8	0.063	7.0	0.32	155	241	556	27
410031	0.121	1.3	0.059	3.0	0.03	157	97	556	27
410031	0.114	1.1	0.061	2.5	0.28	161	61	558	26
410031	0.111	0.8	0.058	2.0	0.80	127	24	559	13
410031	0.115	0.7	0.059	1.6	0.60	218	32	561	13
410031	0.121	0.5	0.059	1.1	0.07	370	226	567	14
410031	0.120	0.3	0.058	0.7	0.02	1036	176	568	14
410031	0.276	1.1	0.062	2.3	0.00	322	226	593	28
410031	0.285	2.1	0.061	3.9	0.60	98	58	595	28
410031	0.274	1.2	0.058	2.5	0.67	253	262	608	27
410031	0.193	0.6	0.055	1.2	0.00	757	175	613	9
410031	0.127	1.4	0.060	2.4	0.62	118	81	618	15
410031	0.137	8.1	0.060	1.8	0.36	138	34	627	15
410031	0.127	1.2	0.064	2.8	0.18	57	25	655	18
410031	0.141	1.1	0.068	1.5	0.21	324	34	668	16
410031	0.155	1.9	0.054	4.6	3.15	66	18	689	34
410031	0.155	0.9	0.077	4.0	1.26	92	36	747	18
410031	0.357	3.4	0.068	4.2	0.06	796	147	758	33
410031	0.161	1.0	0.072	1.5	0.21	134	27	780	19

continues next page...

Sample	$\frac{^{206}Pb}{^{238}U}$	$\pm 1\sigma\%$	$\frac{^{207}Pb}{^{206}Pb}$	$\pm 1\sigma\%$	$^{206}Pb_c\%$	U_{ppm}	Th_{ppm}	**Age (Ma)**	$\pm 2\sigma$ **(Ma)**
410031	0.176	3.4	0.068	2.2	0.24	184	21	802	38
410031	0.280	0.4	0.075	1.8	0.03	453	173	969	15
410031	0.387	4.6	0.076	3.5	0.31	80	50	980	50
410031	0.431	0.8	0.072	2.0	0.12	405	48	981	45
410031	0.211	1.0	0.073	2.0	0.44	57	28	1016	26
410031	0.365	2.2	0.076	1.3	0.00	244	170	1103	18
410031	0.243	1.7	0.075	1.4	0.23	97	49	1108	28
410031	0.389	0.8	0.078	1.6	0.29	144	195	1164	21
410031	0.291	0.5	0.082	1.4	0.22	192	134	1201	29
410031	0.278	1.2	0.088	0.9	0.08	190	64	1346	31
410031	0.501	1.6	0.100	1.5	0.00	134	330	1622	28
410031	0.299	1.1	0.145	1.6	1.36	35	5	2168	40
410031	0.547	0.5	0.136	0.9	0.03	258	117	2176	27
410031	0.938	2.3	0.197	1.7	0.00	25	25	2745	60

All errors are 1σ unless otherwise stated. Uranium and Thorium contents were calibrated against zircon standard SL13, all other measurements calibrated against zircon standard FC1. $^{206}Pb/^{238}U$ and $^{207}Pb/^{206}Pb$ ratios are uncorrected for common Pb. Apparent ages were calculated using a ^{204} correction assuming a common Pb composition of $^{207}Pb/^{206}Pb$=0.836±0.015, $^{208}Pb/^{206}Pb$=2.065±0.1 and $^{206}Pb/^{204}Pb$=18.703±1, and decay constants from (Steiger and Jager, 1977)

Table 19: Results of zircon U-Pb dating of detrital populations from samples of the Triassic metasediments outcropping in the eastern Himalaya. See *Chapter 2* for discussion.

Sample	$\frac{^{206}Pb}{^{238}U}$	$\pm 1\sigma\%$	$\frac{^{207}Pb}{^{206}Pb}$	$\pm 1\sigma\%$	$^{206}Pb_c\%$	U_{ppm}	Th_{ppm}	**Age (Ma)**	$\pm$**2**σ **(Ma)**	Ti_{ppm}	$\pm 2\sigma_{ppm}$	**T°C**	$\pm 2\sigma$**°C**
2004T263	0.005	1.9	0.047	2.1	0.35	4291	204	18.9	0.2	8.46	0.51	726	14.5
2004T263	0.008	1.3	0.045	1.8	0.19	4324	223	19.4	0.3	9.59	0.58	737	14.8
2004T263	0.005	2.5	0.048	2.3	0.17	3333	133	19.5	0.2	6.51	0.39	705	13.8
2004T263	0.007	1.4	0.047	2.3	1.52	3044	121	19.5	0.3	10.64	0.64	746	15.0
2004T263	0.009	2.0	0.046	1.6	0.27	5131	284	19.5	0.3	8.19	0.52	724	14.8
2004T263	0.008	1.2	0.046	1.9	0.34	5520	307	19.8	0.3	7.59	0.46	717	14.3
2004T263	0.007	0.8	0.059	4.8	2.15	6815	304	19.8	0.3	10.01	0.60	741	14.8
2004T263	0.005	1.3	0.046	2.0	0.33	4365	175	20.0	0.2	8.81	0.51	730	14.2
2004T263	0.008	0.8	0.046	1.5	0.31	6399	248	20.1	0.3	10.27	0.60	743	14.6
2004T263	0.006	2.2	0.047	1.5	0.17	8037	538	20.1	0.1	9.98	0.60	741	14.9
2004T263	0.007	0.5	0.047	1.6	0.23	5232	270	20.3	0.3	7.20	0.43	713	14.0
2004T263	0.010	1.6	0.046	1.4	0.47	7132	478	20.3	0.3	9.39	0.54	736	14.3
2004T263	0.006	3.4	0.046	1.2	0.17	12726	926	20.4	0.1	13.70	0.79	769	15.2
2004T263	0.006	1.3	0.047	1.6	0.00	7204	460	20.5	0.1	9.21	0.53	734	14.3
2004T263	0.008	1.3	0.047	1.3	0.21	8859	420	20.5	0.3	12.06	0.70	758	14.9
2004T263	0.006	2.5	0.046	2.2	0.41	2932	136	20.6	0.2	6.14	0.38	700	14.0
2004T263	0.008	1.1	0.047	1.6	0.30	5305	246	20.7	0.3	11.39	0.64	753	14.5
2004T263	0.006	1.4	0.046	2.5	0.07	7607	351	20.7	0.1	12.31	0.73	760	15.2
2004T263	0.006	1.3	0.046	1.8	0.22	5120	230	20.8	0.2	7.76	0.45	719	14.0
2004T263	0.008	1.7	0.047	1.7	0.35	7287	373	20.8	0.3	12.31	0.73	760	15.2
2004T263	0.006	1.0	0.047	1.4	0.23	8830	473	20.9	0.1	30.24	2.29	849	21.2
2004T263	0.007	2.3	0.045	1.3	0.08	10081	507	21.0	0.1	14.11	0.81	772	15.3
2004T263	0.006	1.5	0.047	1.1	0.12	13584	869	21.2	0.1	18.48	1.09	798	16.3
2004T263	0.007	1.5	0.047	1.4	0.00	9399	435	21.6	0.1	12.06	0.70	758	14.9
2004T263	0.010	2.1	0.049	1.1	1.07	10221	3940	21.6	0.4	11.26	0.64	751	14.6
2004T263	0.005	0.8	0.048	2.9	0.40	4498	234	21.8	0.3	19.30	1.14	802	16.3
2004T263	0.006	1.0	0.047	1.0	0.05	18182	601	21.9	0.1	7.47	0.43	716	13.8
2004T263	0.005	0.5	0.046	1.4	0.09	10039	636	22.4	0.2	19.26	1.12	802	16.2
2004T263	0.005	1.8	0.049	2.7	0.28	6990	336	23.8	0.3	13.93	0.78	771	14.9
2004T263	0.137	0.7	0.062	1.5	0.46	399	108	478.7	4.1	-	-	-	-
2004T263	0.134	2.7	0.056	1.3	0.00	373	188	497.2	4.6	-	-	-	-
2004T263	0.153	1.0	0.058	1.4	0.16	287	68	498.0	5.1	-	-	-	-
2004T263	0.144	1.2	0.056	1.1	0.12	483	86	501.5	4.0	-	-	-	-
2004T263	0.143	1.6	0.058	1.2	0.00	434	184	512.7	4.3	-	-	-	-
2004T263	0.149	1.1	0.058	1.2	0.10	392	323	512.8	4.6	-	-	-	-
2004T263	0.145	1.6	0.058	1.1	0.12	480	412	515.7	4.2	-	-	-	-
2004T263	0.153	1.4	0.058	1.5	0.02	231	175	520.6	5.3	-	-	-	-
2004T263	0.152	3.1	0.058	0.6	0.00	2930	1191	528.2	3.2	-	-	-	-
2004T263	0.184	2.9	0.058	0.7	0.00	995	369	554.5	3.8	-	-	-	-

continues next page...

Sample	$\frac{^{206}Pb}{^{238}U}$	$\pm 1\sigma\%$	$\frac{^{207}Pb}{^{206}Pb}$	$\pm 1\sigma\%$	$^{206}Pb_c\%$	U_{ppm}	Th_{ppm}	**Age (Ma)**	$\pm 2\sigma$ **(Ma)**	Ti_{ppm}	$\pm 2\sigma_{ppm}$	**T°C**	$\pm 2\sigma$**°C**
2004T263	0.188	2.0	0.064	0.6	0.02	1234	513	639.8	4.4	-	-	-	-
2004T263	0.173	2.0	0.061	0.9	0.14	577	173	665.7	5.1	-	-	-	-
2004T264	0.004	1.0	0.054	3.4	0.72	4121	62	18.5	0.3	1.87	0.19	612	17.3
2004T264	0.005	3.0	0.046	1.7	0.40	5789	92	18.5	0.1	0.48	0.12	529	31.5
2004T264	0.005	2.4	0.048	2.0	0.31	4906	72	18.5	0.2	0.78	0.16	557	29.3
2004T264	0.005	0.9	0.047	2.5	0.44	3553	105	18.7	0.2	3.70	0.25	660	13.8
2004T264	0.007	0.6	0.046	1.2	0.17	10210	419	19.1	0.3	12.06	0.67	758	14.6
2004T264	0.006	0.6	0.047	1.7	0.09	5894	225	19.3	0.3	7.77	0.46	719	14.2
2004T264	0.007	1.0	0.046	1.7	0.49	5453	200	19.3	0.3	10.74	0.63	747	14.8
2004T264	0.009	1.3	0.047	1.3	0.26	8195	137	19.3	0.3	0.53	0.15	535	36.7
2004T264	0.005	1.4	0.070	3.9	2.40	3985	57	19.4	0.2	0.53	0.11	535	27.2
2004T264	0.006	1.6	0.047	2.0	0.00	4881	304	19.5	0.2	5.62	0.33	693	13.5
2004T264	0.008	0.7	0.049	1.1	0.87	10497	550	19.7	0.3	9.38	0.60	735	15.3
2004T264	0.006	2.5	0.047	2.0	0.19	4681	183	19.8	0.2	8.14	0.46	723	13.9
2004T264	0.004	1.3	0.047	1.9	0.33	5436	305	19.9	0.2	5.32	0.33	688	13.9
2004T264	0.006	2.3	0.045	2.1	0.24	6062	200	19.9	0.2	7.31	0.43	714	13.9
2004T264	0.006	0.7	0.047	2.0	0.31	4451	180	19.9	0.2	6.09	0.36	699	13.6
2004T264	0.007	0.4	0.046	1.1	0.26	12876	616	19.9	0.3	12.39	0.69	760	14.7
2004T264	0.006	1.0	0.047	1.8	0.15	5752	353	20.1	0.2	8.49	0.48	727	13.9
2004T264	0.007	0.8	0.046	2.0	1.36	5066	81	20.2	0.2	0.55	0.11	537	26.9
2004T264	0.009	0.9	0.047	1.2	0.16	12801	676	20.3	0.3	7.96	0.47	721	14.1
2004T264	0.006	4.2	0.046	1.2	0.11	11970	191	20.4	0.1	0.99	0.14	571	20.6
2004T264	0.007	2.9	0.047	1.2	0.00	11381	466	20.4	0.1	12.06	0.67	758	14.6
2004T264	0.006	1.7	0.045	1.2	0.00	12640	718	20.4	0.1	9.03	0.53	732	14.5
2004T264	0.010	0.8	0.047	1.0	0.11	13516	721	20.5	0.3	8.40	0.55	726	15.3
2004T264	0.006	2.2	0.047	1.5	0.12	8291	512	20.6	0.1	15.58	0.92	782	15.8
2004T264	0.006	5.7	0.046	1.2	0.00	12328	215	20.6	0.1	0.67	0.12	548	23.9
2004T264	0.010	0.6	0.047	1.0	0.15	12388	667	20.7	0.3	5.25	0.35	687	14.3
2004T264	0.010	0.3	0.047	1.0	0.02	12851	660	20.8	0.3	8.14	0.49	723	14.4
2004T264	0.005	0.7	0.047	1.3	0.00	10995	553	21.0	0.2	11.51	0.67	754	14.9
2004T264	0.005	0.6	0.050	2.2	0.75	6413	109	21.1	0.2	-	-	-	-
2004T264	0.007	1.7	0.049	3.6	0.07	10363	215	21.3	0.1	0.55	0.14	538	33.9
2004T264	0.006	0.4	0.051	1.3	0.63	9148	177	22.0	0.2	0.55	0.11	538	26.2
2004T264	0.007	0.9	0.047	1.0	0.14	14750	297	23.9	0.2	0.64	0.11	546	23.4
2004T264	0.007	1.8	0.047	2.0	0.23	2983	83	25.4	0.2	3.55	0.26	657	14.5
2004T264	0.005	1.2	0.048	2.7	0.50	2211	62	25.5	0.3	3.70	0.23	660	13.0
2004T264	0.142	1.7	0.059	1.7	0.41	213	60	500.6	5.3	-	-	-	-
2004T264	0.140	2.7	0.057	0.7	0.00	1157	226	503.2	3.2	-	-	-	-
2004T264	0.148	2.6	0.058	0.8	0.00	850	107	503.6	3.4	-	-	-	-

continues next page...

Sample	$\frac{^{206}Pb}{^{238}U}$	$\pm 1\sigma\%$	$\frac{^{207}Pb}{^{206}Pb}$	$\pm 1\sigma\%$	$^{206}Pb_c\%$	U_{ppm}	Th_{ppm}	**Age (Ma)**	$\pm$**2**σ **(Ma)**	Ti_{ppm}	$\pm 2\sigma_{ppm}$	**T°C**	$\pm 2\sigma$**°C**
2004T264	0.155	1.6	0.057	0.6	0.00	1481	897	507.2	3.4	-	-	-	-
2004T264	0.155	1.5	0.057	0.6	0.00	1702	408	514.2	3.3	-	-	-	-
2004T264	0.150	4.0	0.058	0.3	0.07	4151	788	516.1	3.6	-	-	-	-
2004T264	0.205	3.1	0.071	0.6	0.16	1175	311	727.4	5.0	-	-	-	-
2004T264	0.289	0.3	0.066	0.6	0.05	847	1135	822.9	6.0	-	-	-	-
2004T264	0.243	1.8	0.067	0.9	0.05	408	146	836.5	6.9	-	-	-	-
2004T264	0.365	1.4	0.078	0.4	0.00	1191	795	1163.9	9.5	-	-	-	-
2004T264	0.386	1.1	0.095	0.7	0.00	289	117	1530.0	11.4	-	-	-	-
2004T265	0.005	2.7	0.049	2.6	0.00	2979	11	16.0	0.2	9.29	3.42	735	74.0
2004T265	0.005	2.1	0.049	2.4	0.49	3649	8	16.3	0.1	1.21	0.13	584	16.9
2004T265	0.005	1.3	0.049	2.7	0.35	2588	8	17.0	0.2	0.97	0.12	570	18.6
2004T265	0.005	2.5	0.048	1.4	0.00	9622	680	17.2	0.1	11.44	0.67	753	14.9
2004T265	0.005	1.6	0.056	2.0	1.81	3688	28	17.5	0.1	22.70	1.50	819	18.2
2004T265	0.005	2.1	0.046	1.8	0.00	5953	257	17.6	0.1	8.90	0.50	731	13.9
2004T265	0.004	2.6	0.050	3.4	0.35	1871	42	18.0	0.2	5.00	0.33	683	14.1
2004T265	0.006	1.7	0.048	1.4	0.22	9174	463	18.5	0.1	-	-	-	-
2004T265	0.003	4.0	0.056	4.5	4.33	2940	13	18.6	0.3	-	-	-	-
2004T265	0.004	2.5	0.054	3.3	1.22	4365	11	18.7	0.3	-	-	-	-
2004T265	0.006	1.2	0.052	1.6	1.23	6463	338	18.8	0.4	10.83	0.64	748	14.9
2004T265	0.005	1.8	0.048	2.1	0.26	6576	45	18.8	0.2	3.03	0.21	646	13.8
2004T265	0.006	2.1	0.051	1.4	0.53	7059	42	19.2	0.1	-	-	-	-
2004T265	0.004	2.3	0.057	1.8	2.26	6440	28	19.5	0.2	-	-	-	-
2004T265	0.005	0.6	0.050	1.4	0.45	9703	51	20.4	0.2	3.25	0.20	651	12.9
2004T265	0.007	1.4	0.048	2.1	0.26	10812	63	20.8	0.1	0.92	0.12	567	19.6
2004T265	0.005	0.6	0.049	2.1	0.74	8372	47	21.0	0.2	-	-	-	-
2004T265	0.005	2.6	0.050	1.4	0.00	11119	99	21.3	0.2	1.69	0.19	606	18.4
2004T265	0.008	2.9	0.049	1.1	0.31	12282	92	21.8	0.1	2.75	0.20	639	14.0
2004T265	0.006	1.6	0.050	0.9	0.51	18184	129	22.3	0.2	2.10	0.16	620	13.8
2004T265	0.007	4.1	0.053	1.4	0.96	18367	147	22.8	0.1	3.86	0.28	664	14.8
2004T265	0.007	1.0	0.051	0.9	0.68	19239	231	23.1	0.2	7.54	0.49	717	14.9
2004T265	0.005	2.0	0.058	4.0	1.62	6849	60	23.3	0.3	-	-	-	-
2004T265	0.007	3.7	0.047	1.0	0.16	18112	206	23.5	0.2	5.80	0.39	695	14.6
2004T265	0.011	2.0	0.049	1.1	0.17	8578	109	23.6	0.2	2.97	0.21	644	13.7
2004T265	0.010	0.7	0.050	1.2	0.32	23044	292	23.7	0.1	5.50	0.31	691	13.0
2004T265	0.012	3.9	0.050	2.6	0.43	33777	515	24.6	0.1	6.40	0.38	703	13.7
2004T265	0.007	2.3	0.049	1.1	0.60	22761	242	24.9	0.3	-	-	-	-
2004T265	0.010	2.0	0.050	0.8	0.36	18959	197	25.2	0.2	5.02	0.31	684	13.6
2004T265	0.062	4.1	0.064	0.8	0.04	1738	159	221.7	1.4	-	-	-	-
2004T265	0.113	4.1	0.068	1.2	0.17	415	119	373.6	3.1	-	-	-	-

continues next page...

Sample	$\frac{^{206}Pb}{^{238}U}$	$\pm 1\sigma\%$	$\frac{^{207}Pb}{^{206}Pb}$	$\pm 1\sigma\%$	$^{206}Pb_c\%$	U_{ppm}	Th_{ppm}	**Age (Ma)**	$\pm 2\sigma$ **(Ma)**	Ti_{ppm}	$\pm 2\sigma_{ppm}$	**T°C**	$\pm 2\sigma$**°C**
2004T265	0.141	2.0	0.059	0.8	0.00	749	81	492.1	3.5	-	-	-	-
2004T265	0.153	2.8	0.060	0.8	0.00	728	83	555.5	3.8	-	-	-	-
2004T265	0.228	1.1	0.068	0.7	0.03	642	486	733.8	5.4	-	-	-	-
2004T265	0.225	3.1	0.066	0.8	0.07	532	258	752.4	5.8	-	-	-	-
2004T265	0.248	2.4	0.067	0.5	0.02	1039	556	825.3	5.5	-	-	-	-
2004T265	0.230	2.7	0.066	0.9	0.00	319	191	828.3	6.6	-	-	-	-
2004T265	0.250	2.7	0.066	0.7	0.01	772	443	839.8	5.6	-	-	-	-
2004T265	0.301	0.4	0.067	0.4	0.02	1850	1349	873.8	5.6	-	-	-	-
2004T265	0.226	4.5	0.072	0.7	0.03	1305	80	975.0	7.0	-	-	-	-

All errors are 1σ unless otherwise stated. Uranium and Thorium contents were calibrated against zircon standard SL13, all other measurements calibrated against zircon standard FC1. ^{206}Pb/^{238}U and ^{207}Pb/^{206}Pb ratios are uncorrected for common Pb. Apparent ages were calculated using a ^{204} correction assuming a common Pb composition of ^{207}Pb/^{206}Pb=0.836±0.015, ^{208}Pb/^{206}Pb=2.065±0.1 and ^{206}Pb/^{204}Pb=18.703±1, and decay constants from (Steiger and Jager, 1977)

Table 20: Results of U-Pb dating and Ti-thermometry of zircons from the Tsona Leucogranites. See *Chapter 4* for discussion.

Sample	$\frac{^{206}Pb}{^{238}U}$	$\pm 1\sigma\%$	$\frac{^{207}Pb}{^{206}Pb}$	$\pm 1\sigma\%$	$^{206}Pb_c\%$	U_{ppm}	Th_{ppm}	**Age (Ma)**	$\pm$**2**σ **(Ma)**	Ti_{ppm}	$\pm 2\sigma_{ppm}$	**T°C**	$\pm 2\sigma$**°C**
0602005	0.175	0.6	0.067	0.9	0.03	359	183	831.2	10.8	6.62	0.38	706	13.4
0602005	0.195	1.2	0.082	5.9	0.97	1650	1202	887.7	11.1	12.79	0.73	763	14.9
0602005	0.156	1.8	0.072	1.0	0.16	300	190	952.0	11.4	18.64	1.04	799	15.7
0602005	0.377	2.3	0.073	0.9	0.09	309	371	952.6	13.9	20.36	1.57	808	20.0
0602005	0.396	1.8	0.070	0.3	0.01	2892	215	955.4	12.1	-	-	-	-
0602005	0.199	1.2	0.071	0.3	0.01	2522	515	957.0	8.1	6.27	0.37	702	13.6
0602005	0.207	1.5	0.071	0.6	0.04	607	100	965.4	10.9	10.10	0.65	742	15.5
0602005	0.204	1.1	0.071	1.0	0.07	255	114	973.1	12.9	5.01	0.31	684	13.5
0602005	0.201	1.1	0.072	1.2	0.04	352	96	980.4	12.4	12.79	0.72	763	14.9
0602005	0.208	1.2	0.075	1.6	0.00	264	355	1004.3	13.9	9.71	0.57	738	14.6
0602005	0.228	0.4	0.073	1.0	-0.12	220	195	1065.1	14.5	12.89	0.71	764	14.7
0602005	0.474	1.7	0.079	0.8	0.14	347	243	1137.6	16.4	5.54	0.34	692	13.8
0602005	0.246	1.1	0.078	0.5	-0.02	731	965	1148.1	11.2	17.04	0.95	790	15.5
0602005	0.256	0.4	0.079	0.8	0.06	246	173	1150.0	14.8	12.56	0.70	761	14.6
0602005	0.184	0.4	0.080	0.7	0.00	487	505	1195.0	11.0	17.75	1.04	794	16.0
0602005	0.414	1.5	0.086	0.4	0.02	1114	297	1334.0	14.9	6.05	0.34	699	13.2
0602005	0.555	2.1	0.089	1.0	0.17	165	58	1361.6	21.5	42.38	2.38	886	18.2
0602005	0.307	1.0	0.090	0.3	0.02	1766	292	1422.0	8.5	8.58	0.49	728	14.1
0602005	0.270	2.5	0.094	0.8	0.37	227	128	1446.0	16.5	12.54	0.74	761	15.3
0602005	0.335	1.0	0.092	0.2	0.00	1969	1239	1470.1	7.6	22.88	1.29	819	16.3
0602005	0.316	1.1	0.098	0.5	0.02	514	131	1577.0	11.5	7.76	0.48	719	14.6
0602005	0.264	0.8	0.098	0.5	0.04	548	264	1588.0	11.1	6.99	0.39	710	13.5
0602005	0.363	0.7	0.099	0.5	0.02	420	289	1613.4	11.9	7.67	0.46	718	14.2
0602005	0.317	0.6	0.100	0.6	0.00	701	360	1623.0	13.1	4.39	0.27	673	13.2
0602005	0.403	0.4	0.101	0.3	0.00	770	147	1635.0	8.9	6.83	0.39	708	13.5
0602005	0.380	1.5	0.100	0.5	-0.04	386	274	1635.4	11.9	12.21	0.69	759	14.7
0602005	0.376	1.4	0.103	0.3	0.01	875	309	1669.7	9.0	12.76	0.73	763	15.0
0602005	0.353	1.5	0.106	0.7	0.29	194	225	1674.0	16.4	8.42	0.49	726	14.2
0602005	0.329	1.7	0.105	0.5	0.25	329	150	1684.0	15.6	5.04	0.31	684	13.7
0602005	0.384	1.0	0.105	0.6	0.08	257	143	1700.0	14.1	8.61	0.50	728	14.1
0602005	0.389	0.5	0.105	0.4	0.03	725	218	1704.9	10.1	4.29	0.27	672	13.5
0602005	0.712	2.1	0.105	0.6	0.15	327	175	1710.8	23.4	6.44	0.40	704	14.2
0602005	0.349	1.0	0.106	0.5	0.04	413	327	1725.0	12.9	7.06	0.45	711	14.5
0602005	0.373	0.8	0.107	0.4	0.10	565	264	1731.0	12.0	4.72	0.30	679	13.8
0602008	0.010	1.8	0.048	1.5	0.00	11087	254	20.6	0.2	3.74	0.24	661	13.3
0602008	0.009	2.1	0.046	1.4	0.21	12117	100	20.7	0.2	2.64	0.19	636	13.5
0602008	0.005	3.5	0.051	1.3	0.88	8870	156	20.9	0.2	9.99	0.64	741	15.5
0602008	0.005	1.7	0.046	0.9	0.07	20880	598	22.6	0.2	5.38	0.31	689	13.2
0602008	0.006	1.4	0.047	0.9	0.06	20307	229	22.9	0.2	2.46	0.22	631	15.8

continues next page...

Sample	$\frac{^{206}Pb}{^{238}U}$	$\pm 1\sigma\%$	$\frac{^{207}Pb}{^{206}Pb}$	$\pm 1\sigma\%$	$^{206}Pb_c\%$	U_{ppm}	Th_{ppm}	**Age (Ma)**	$\pm$**2**σ **(Ma)**	Ti_{ppm}	$\pm 2\sigma_{ppm}$	**T°C**	$\pm 2\sigma$**°C**
0602008	0.006	0.5	0.048	0.8	0.23	19376	266	23.2	0.2	5.64	0.32	693	13.1
0602008	0.012	1.7	0.048	0.9	0.00	26116	278	23.4	0.3	4.99	0.30	683	13.3
0602008	0.006	0.7	0.048	0.8	0.07	20835	204	23.8	0.2	2.65	0.21	636	14.6
0602008	0.006	0.4	0.047	0.7	0.06	27653	361	24.3	0.2	3.28	0.22	652	13.3
0602008	0.005	1.3	0.051	4.0	0.99	787	6	25.2	0.4	2.24	0.18	624	14.9
0602008	0.007	0.3	0.048	1.7	0.54	10448	102	25.2	0.3	1.99	0.16	617	14.5
0602008	0.015	2.7	0.048	0.7	0.20	36267	625	25.6	0.3	12.09	0.79	758	16.2
0602008	0.110	1.3	0.057	0.5	0.02	3674	1217	511.0	5.9	7.29	0.41	714	13.6
0602008	0.293	1.9	0.068	1.1	0.14	288	131	738.8	11.1	-	-	-	-
0602008	0.298	1.6	0.066	0.9	0.05	731	204	745.1	10.4	-	-	-	-
0602008	0.188	0.8	0.066	0.5	0.04	1184	1109	805.0	9.5	12.74	0.72	763	14.9
0602008	0.187	0.8	0.066	0.4	0.01	2081	1403	817.0	8.4	9.12	0.52	733	14.2
0602008	0.336	2.8	0.066	0.4	0.03	1697	942	828.6	11.0	4.93	0.28	682	12.8
0602008	0.357	2.0	0.066	0.4	0.00	2120	2181	829.4	11.6	-	-	-	-
0602008	0.174	1.2	0.067	0.8	0.07	461	282	830.5	10.5	3.27	0.21	651	13.1
0602008	0.326	1.4	0.066	1.1	0.00	397	119	831.6	12.4	-	-	-	-
0602008	0.179	0.6	0.067	0.9	0.07	351	200	841.2	11.0	2.76	0.19	639	13.3
0602009	0.004	0.8	0.045	2.2	0.39	4072	91	19.0	0.2	2.49	0.19	632	14.5
0602009	0.008	0.5	0.048	1.6	0.48	5709	75	19.2	0.3	1.96	0.16	616	14.5
0602009	0.004	1.3	0.048	1.8	0.10	5104	32	20.0	0.2	0.74	0.11	554	21.4
0602009	0.004	0.6	0.047	1.3	0.05	9714	216	20.2	0.2	6.15	0.39	700	14.4
0602009	0.004	0.8	0.057	3.1	0.78	11288	111	20.5	0.2	2.04	0.16	618	14.1
0602009	0.005	0.8	0.047	1.6	0.22	5930	101	20.5	0.2	2.97	0.19	644	13.1
0602009	0.009	4.0	0.059	2.0	1.92	12838	355	20.6	0.3	4.04	0.25	667	13.3
0602009	0.009	4.3	0.047	1.4	0.27	11281	127	20.6	0.3	3.74	0.24	661	13.2
0602009	0.009	3.3	0.048	1.6	0.18	8428	84	20.7	0.2	3.47	0.25	656	14.5
0602009	0.009	3.1	0.048	1.4	0.21	9946	172	20.9	0.3	4.33	0.26	672	13.2
0602009	0.005	1.0	0.047	1.1	0.08	14183	222	21.1	0.2	3.07	0.22	647	13.8
0602009	0.005	0.7	0.049	1.2	0.21	10297	152	21.3	0.2	2.54	0.19	633	14.3
0602009	0.009	1.3	0.047	1.6	-0.06	6959	186	21.5	0.3	3.91	0.24	665	13.2
0602009	0.010	1.0	0.047	1.4	0.18	10391	205	21.6	0.2	-	-	-	-
0602009	0.005	0.3	0.047	1.2	0.10	9670	162	22.2	0.2	2.92	0.20	643	13.5
0602009	0.012	0.6	0.050	2.3	0.72	2929	100	22.9	0.3	4.54	0.26	676	12.7
0602009	0.012	0.9	0.047	1.2	0.40	12737	258	23.3	0.3	4.47	0.26	675	12.9
0602009	0.005	0.5	0.047	1.8	0.37	4428	57	23.5	0.2	2.29	0.19	626	15.3
0602009	0.015	1.3	0.059	1.7	1.40	17039	290	25.3	0.4	10.17	0.65	742	15.5
0602009	0.016	2.5	0.051	2.2	0.29	2118	32	40.4	0.6	3.26	0.22	651	13.4
0602009	0.053	0.5	0.056	1.2	0.43	1152	171	157.3	2.7	4.99	0.30	683	13.3
0602009	0.046	0.8	0.057	0.7	0.02	2459	52	224.4	2.5	2.94	0.20	644	13.7

continues next page...

Sample	$\frac{^{206}Pb}{^{238}U}$	$\pm 1\sigma\%$	$\frac{^{207}Pb}{^{206}Pb}$	$\pm 1\sigma\%$	$^{206}Pb_c\%$	U_{ppm}	Th_{ppm}	**Age (Ma)**	$\pm$**2**σ **(Ma)**	Ti_{ppm}	$\pm 2\sigma_{ppm}$	**T°C**	$\pm 2\sigma$**°C**
0602009	0.142	1.6	0.056	0.6	0.04	3297	70	365.8	4.7	6.77	0.40	708	13.7
0602009	0.145	3.0	0.073	0.6	0.79	2144	191	400.4	4.9	-	-	-	-
0602009	0.099	1.1	0.056	0.5	0.03	2391	53	477.5	5.6	7.05	0.42	711	14.1
0602009	0.185	0.6	0.058	0.9	0.11	637	383	481.5	9.2	5.27	0.32	688	13.5
0602009	0.178	2.7	0.059	1.5	0.16	417	265	496.1	7.1	-	-	-	-
0602009	0.190	1.1	0.057	0.7	-0.02	864	888	503.1	9.7	5.72	0.34	694	13.4
0602009	0.207	0.4	0.058	0.7	0.10	875	803	506.2	9.8	7.94	0.49	721	14.6
0602009	0.104	0.6	0.058	1.7	-0.06	173	142	513.0	7.4	8.47	0.48	727	14.0
0602009	0.103	1.7	0.058	0.8	0.05	1278	245	513.3	6.0	5.60	0.33	693	13.4
0602009	0.277	2.3	0.063	0.9	0.06	672	490	691.8	9.8	-	-	-	-
0602010	0.007	0.8	0.049	2.4	1.57	2733	10	16.6	0.3	0.99	0.13	572	19.2
0602010	0.006	0.9	0.051	2.8	-0.95	1958	12	17.1	0.3	1.43	0.15	595	16.9
0602010	0.004	0.7	0.047	2.0	0.00	4334	11	18.5	0.2	1.19	0.13	583	17.5
0602010	0.004	1.1	0.048	2.2	0.00	3531	13	19.5	0.2	0.80	0.14	559	24.4
0602010	0.004	0.9	0.049	4.2	0.25	3210	17	19.8	0.2	0.53	0.12	535	30.5
0602010	0.004	0.5	0.048	2.0	0.37	4404	29	20.3	0.2	0.53	0.12	535	31.0
0602010	0.008	0.6	0.067	4.3	2.02	4543	35	20.6	0.3	4.82	0.28	681	13.1
0602010	0.004	1.2	0.046	1.8	0.09	4867	52	21.4	0.2	2.48	0.20	632	14.9
0602010	0.009	1.5	0.045	1.4	-0.08	6200	178	21.9	0.3	8.20	0.46	724	13.8
0602010	0.009	0.5	0.047	1.4	0.33	5549	151	21.9	0.3	6.83	0.45	709	14.9
0602010	0.005	0.9	0.047	1.3	0.14	9047	113	22.8	0.2	0.70	0.11	551	22.1
0602010	0.010	0.5	0.047	1.1	0.04	9373	141	22.9	0.3	7.16	0.40	712	13.5
0602010	0.005	0.7	0.046	1.5	0.06	6288	130	23.0	0.2	5.41	0.32	690	13.3
0602010	0.010	0.7	0.046	2.6	0.29	7549	222	23.2	0.3	5.12	0.29	685	13.0
0602010	0.010	0.5	0.046	1.3	0.08	11296	409	23.3	0.3	10.95	0.61	749	14.3
0602010	0.005	1.6	0.046	1.6	0.00	5446	49	23.4	0.2	4.25	0.27	671	13.4
0602010	0.010	1.1	0.046	2.3	0.16	11284	185	23.4	0.3	-	-	-	-
0602010	0.010	0.3	0.047	1.0	-0.02	12409	495	23.8	0.4	12.03	0.67	758	14.6
0602010	0.010	3.3	0.050	2.7	1.07	6750	85	24.0	0.3	5.61	0.32	693	13.1
0602010	0.010	1.1	0.047	1.8	0.24	6085	56	24.1	0.3	4.12	0.29	669	14.3
0602010	0.011	1.6	0.047	1.1	0.19	14182	252	24.4	0.4	3.86	0.23	664	12.9
0602010	0.011	2.2	0.046	1.4	0.12	9782	198	24.4	0.3	5.95	0.34	697	13.2
0602010	0.014	0.8	0.049	0.9	0.22	19562	690	26.3	0.3	7.56	0.44	717	14.0
0602010	0.014	0.7	0.047	1.1	0.38	14002	279	26.7	0.3	3.37	0.23	654	13.9
0602010	0.021	0.6	0.057	2.0	0.21	1742	54	55.0	1.0	3.32	0.23	653	13.9
0602010	0.027	0.4	0.053	1.0	0.08	3336	125	71.8	1.2	10.36	0.59	744	14.4
0602010	0.032	1.9	0.056	1.1	0.12	2553	16	95.9	1.6	3.01	0.19	645	12.7
0602010	0.027	1.1	0.081	0.7	0.17	9059	507	126.6	1.5	6.38	0.37	703	13.4
0602010	0.103	2.3	0.065	1.1	0.00	1002	174	323.4	4.4	3.76	0.23	662	13.0

continues next page...

Sample	$\frac{^{206}Pb}{^{238}U}$	$\pm 1\sigma\%$	$\frac{^{207}Pb}{^{206}Pb}$	$\pm 1\sigma\%$	$^{206}Pb_c\%$	U_{ppm}	Th_{ppm}	**Age (Ma)**	$\pm$**2**σ **(Ma)**	Ti_{ppm}	$\pm 2\sigma_{ppm}$	**T°C**	$\pm 2\sigma$**°C**
0602010	0.159	0.3	0.058	0.4	0.13	4265	50	386.3	7.0	15.52	0.90	781	15.5
0602010	0.157	3.4	0.058	1.3	0.10	566	179	455.0	6.3	3.77	0.28	662	14.7
0602010	0.112	1.1	0.057	0.4	0.01	3003	368	523.3	5.9	2.65	0.18	636	13.4
0602010	0.107	7.1	0.072	12.6	1.95	1375	682	534.5	8.6	9.45	0.58	736	14.9
0602010	0.326	1.2	0.066	0.7	0.15	960	428	804.1	11.3	1.88	0.15	613	14.4
0602010	0.341	0.3	0.066	0.7	0.05	517	288	819.3	15.0	3.77	0.23	662	12.8
0602010	0.376	2.8	0.067	0.3	0.05	5375	2601	820.0	11.4	26.39	1.49	834	16.8
0602010	0.169	0.7	0.067	0.8	0.00	453	205	827.5	10.3	4.64	0.28	678	13.4
0602010	0.372	1.8	0.073	0.8	0.08	498	305	978.6	14.8	11.88	0.69	756	14.9
0602010	0.450	6.9	0.072	2.5	0.00	311	119	1020.4	52.5	-	-	-	-
0602010	0.564	0.9	0.095	1.1	1.05	149	82	1316.1	22.3	-	-	-	-
0602011	0.299	2.6	0.067	0.7	0.03	495	256	711.3	4.7	7.39	0.43	715	13.9
0602011	0.285	1.8	0.069	1.0	0.18	410	185	728.1	5.4	6.07	0.38	699	14.0
0602011	0.339	1.5	0.065	0.9	0.15	291	153	814.7	6.5	5.71	0.40	694	15.1
0602011	0.340	1.9	0.067	0.6	0.01	701	457	821.9	5.1	11.00	0.60	749	14.2
0602011	0.352	2.3	0.066	0.6	0.04	755	559	822.8	5.2	8.55	0.50	727	14.2
0602011	0.364	1.5	0.066	0.7	0.03	542	332	823.1	5.7	6.17	0.35	700	13.2
0602011	0.370	1.8	0.067	0.6	0.06	757	489	825.1	5.3	7.40	0.41	715	13.4
0602011	0.326	1.4	0.068	0.7	0.00	765	430	828.4	11.8	7.23	0.40	713	13.5
0602011	0.325	0.7	0.067	0.6	0.07	630	355	828.9	14.3	4.41	0.26	674	13.0
0602011	0.347	1.2	0.066	0.8	0.07	697	421	832.4	12.0	5.17	0.30	686	13.2
0602011	0.182	0.3	0.067	0.6	0.02	718	412	833.4	9.8	6.53	0.37	705	13.5
0602011	0.349	2.0	0.067	0.8	0.00	429	256	834.8	6.6	6.74	0.37	707	13.3
0602011	0.342	1.6	0.066	0.7	0.04	486	296	836.8	5.7	5.95	0.34	697	13.2
0602011	0.362	1.1	0.067	0.7	0.03	568	369	837.7	5.7	5.46	0.31	690	13.1
0602011	0.370	1.4	0.067	0.7	0.09	620	423	840.2	5.6	7.95	0.47	721	14.2
0602011	0.323	3.7	0.067	0.5	0.02	632	420	840.7	5.0	7.73	0.45	719	14.0
0602011	0.348	5.0	0.067	0.6	0.03	984	660	841.2	13.3	6.97	0.38	710	13.2
0602011	0.366	1.4	0.066	0.6	0.00	690	506	847.6	5.5	6.93	0.40	710	13.6
0602012	0.196	3.6	0.067	0.7	0.38	710	106	745.0	10.6	-	-	-	-
0602012	0.231	2.1	0.067	1.3	0.31	162	133	796.7	8.4	-	-	-	-
0602012	0.232	3.0	0.067	1.7	0.11	545	137	797.1	5.9	-	-	-	-
0602012	0.254	1.3	0.068	0.9	0.10	319	69	804.9	6.7	-	-	-	-
0602012	0.247	2.4	0.066	1.0	0.06	295	115	812.3	7.1	-	-	-	-
0602012	0.247	2.3	0.067	1.3	0.07	320	128	814.2	6.8	-	-	-	-
0602012	0.249	1.3	0.068	1.9	0.37	70	114	816.7	12.4	-	-	-	-
0602012	0.249	2.1	0.067	0.6	0.03	751	55	819.3	5.7	3.00	0.19	645	12.8
0602012	0.242	2.3	0.066	1.3	0.00	165	149	823.4	8.8	-	-	-	-
0602012	0.319	2.3	0.067	0.2	0.00	6823	78	826.0	5.3	-	-	-	-

continues next page...

Sample	$\frac{^{206}Pb}{^{238}U}$	$\pm1\sigma\%$	$\frac{^{207}Pb}{^{206}Pb}$	$\pm1\sigma\%$	$^{206}Pb_c\%$	U_{ppm}	Th_{ppm}	**Age (Ma)**	**$\pm2\sigma$ (Ma)**	Ti_{ppm}	$\pm2\sigma_{ppm}$	**T°C**	**$\pm2\sigma$°C**
0602012	0.246	1.5	0.066	0.8	0.08	390	172	829.3	6.6	-	-	-	-
0602012	0.246	2.7	0.068	2.1	0.00	129	120	832.6	9.4	-	-	-	-
0602012	0.248	1.7	0.067	1.5	0.00	123	72	837.7	9.9	-	-	-	-
0602012	0.267	1.8	0.067	0.6	0.00	808	147	838.9	5.9	-	-	-	-
0602012	0.258	1.7	0.068	1.0	0.00	246	80	839.4	7.7	-	-	-	-
0602012	0.254	3.0	0.067	1.0	0.11	287	57	840.0	7.3	17.69	0.99	794	15.5
0602012	0.251	1.4	0.066	1.2	0.14	196	65	841.9	8.1	-	-	-	-
0602012	0.246	1.5	0.066	1.1	0.09	226	203	842.3	8.1	-	-	-	-
0602012	0.269	2.2	0.066	0.4	0.00	1614	78	845.2	5.4	-	-	-	-
0602012	0.261	1.9	0.067	0.7	0.02	625	328	846.3	6.2	-	-	-	-
0602012	0.265	2.1	0.067	0.6	0.02	847	27	848.0	5.8	-	-	-	-
0602012	0.269	0.7	0.067	1.0	0.15	255	168	850.1	7.7	-	-	-	-
0602012	0.256	1.9	0.067	0.5	0.07	876	24	851.1	5.8	-	-	-	-
0602012	0.253	1.9	0.065	1.9	0.00	74	108	851.5	12.9	-	-	-	-
0602012	0.252	2.0	0.067	1.2	0.13	192	114	852.4	8.3	-	-	-	-
0602012	0.267	1.6	0.068	0.8	0.04	442	152	853.2	6.7	-	-	-	-
0602012	0.259	1.7	0.066	0.6	0.06	629	214	853.6	6.1	10.70	0.60	747	14.3
0602012	0.277	0.4	0.066	0.9	0.00	345	110	856.2	7.1	-	-	-	-
0602012	0.271	2.1	0.067	1.1	0.00	202	92	857.8	8.5	10.44	0.59	745	14.3
0602012	0.266	1.1	0.067	0.9	-0.08	338	108	862.3	7.1	13.23	0.77	766	15.2
0602012	0.264	1.5	0.069	1.3	0.16	145	75	865.6	9.4	22.19	1.24	816	16.2
0602012	0.272	1.3	0.066	0.5	0.02	849	141	866.8	6.0	-	-	-	-
0602012	0.259	1.4	0.067	1.6	0.43	101	82	871.1	10.8	-	-	-	-
0602012	0.283	1.0	0.068	0.6	0.03	638	184	871.1	6.2	-	-	-	-
0602012	0.288	1.0	0.065	1.0	-0.09	259	68	876.4	7.6	-	-	-	-
0602012	0.285	1.5	0.070	0.9	0.00	281	124	926.4	8.2	-	-	-	-
0602012	0.471	0.8	0.093	0.6	0.04	317	270	1481.0	11.8	-	-	-	-

All errors are 1σ unless otherwise stated. Uranium and Thorium contents were calibrated against zircon standard SL13, all other measurements calibrated against zircon standard FC1. $^{206}Pb/^{238}U$ and $^{207}Pb/^{206}Pb$ ratios are uncorrected for common Pb. Apparent ages were calculated using a ^{204} correction assuming a common Pb composition of $^{207}Pb/^{206}Pb$=0.836±0.015, $^{208}Pb/^{206}Pb$=2.065±0.1 and $^{206}Pb/^{204}Pb$=18.703±1, and decay constants from (Steiger and Jager, 1977)

Table 21: Results of U-Pb dating and Ti-thermometry of zircons from the Arunachal Leucogranites and Arunachal Crystallins. See *Chapter 4* for discussion.

Sample	$\frac{^{206}Pb}{^{238}U}$	$\pm 1\sigma\%$	$\frac{^{207}Pb}{^{206}Pb}$	$\pm 1\sigma\%$	$^{206}Pb_c\%$	U_{ppm}	Th_{ppm}	**Age (Ma)**	$\pm 2\sigma$ **(Ma)**	Ti_{ppm}	$\pm 2\sigma_{ppm}$	**T°C**	$\pm 2\sigma$**°C**
0310012	0.063	2.6	-	-	0.54	110	67	396.2	9.9	-	-	-	-
0310012	0.009	1.4	-	-	0.08	6082	198	58.2	0.9	-	-	-	-
0310012	0.008	1.8	-	-	0.09	2867	43	48.7	0.9	-	-	-	-
0310012	0.008	4.4	-	-	0.32	1067	45	53.5	2.4	-	-	-	-
0310012	0.006	8.0	-	-	0.89	1689	15	36.0	2.9	-	-	-	-
0310012	0.010	2.4	-	-	0.78	1754	129	66.1	1.6	-	-	-	-
0310012	0.007	4.2	-	-	0.75	449	24	43.3	1.8	-	-	-	-
0310012	0.033	2.9	-	-	0.34	197	94	211.1	6.0	-	-	-	-
0310012	0.006	2.2	-	-	0.16	1110	147	41.6	0.9	-	-	-	-
0310012	0.008	3.3	-	-	0.33	2352	165	51.2	1.7	-	-	-	-
0310012	0.006	3.4	-	-	0.10	2137	12	37.3	1.3	-	-	-	-
0310012	0.007	3.2	-	-	0.33	407	44	42.5	1.4	-	-	-	-
0310012	0.007	1.9	-	-	0.44	2122	44	44.1	0.8	-	-	-	-
0310012	0.007	2.6	-	-	0.12	583	71	42.0	1.1	-	-	-	-
0310012	0.008	2.1	-	-	0.04	2372	28	50.9	1.1	-	-	-	-
0310012	0.007	3.1	-	-	0.77	566	37	42.1	1.3	-	-	-	-
0310012	0.007	2.8	-	-	1.30	2786	336	47.9	1.4	-	-	-	-
0310012	0.006	1.9	-	-	0.36	1604	57	41.0	0.8	-	-	-	-
0310012	0.004	2.8	-	-	0.91	2165	27	27.6	0.8	-	-	-	-
0310012	0.006	6.2	-	-	0.25	1590	34	36.1	2.2	-	-	-	-
0310012	0.006	2.8	-	-	0.09	1988	34	39.7	1.1	-	-	-	-
0310012	0.006	2.7	-	-	0.35	642	62	38.7	1.1	-	-	-	-
0310012	0.007	2.6	-	-	0.20	2127	100	42.4	1.1	-	-	-	-
0310012	0.158	2.4	-	-	9.65	772	64	944.8	21.2	-	-	-	-
0310012	0.007	1.7	-	-	0.15	2442	126	42.6	0.7	-	-	-	-
0310016	0.007	1.0	0.050	2.6	0.96	3120	18	21.3	0.3	-	-	-	-
0310016	0.008	0.5	0.061	2.8	2.44	5922	52	26.8	0.2	-	-	-	-
0310016	0.012	0.9	0.050	2.6	1.35	1939	10	36.4	0.5	-	-	-	-
0310016	0.015	2.3	0.077	22.7	2.76	5373	93	41.7	0.7	-	-	-	-
0310016	0.015	3.4	0.049	1.8	0.61	4996	26	42.1	0.5	-	-	-	-
0310016	0.011	2.1	0.046	1.2	0.24	5056	81	42.2	0.3	-	-	-	-
0310016	0.015	1.4	0.052	1.5	0.89	4177	23	43.1	0.6	-	-	-	-
0310016	0.016	1.8	0.051	2.6	0.83	7093	65	43.6	0.6	-	-	-	-
0310016	0.016	0.6	0.052	1.4	0.55	6130	62	45.4	0.6	-	-	-	-
0310016	0.014	1.6	0.093	3.6	5.55	13866	342	48.5	0.3	-	-	-	-
0310016	0.016	1.3	0.049	1.3	0.35	6623	39	48.7	0.6	-	-	-	-
0310016	0.020	1.2	0.054	2.3	0.79	9742	347	49.4	0.6	-	-	-	-
0310016	0.016	2.2	0.107	6.0	7.55	7480	210	50.8	0.7	-	-	-	-
0310016	0.021	3.2	0.069	1.2	2.96	11385	198	52.8	0.6	-	-	-	-

continues next page...

Sample	$\frac{^{206}Pb}{^{238}U}$	$\pm 1\sigma\%$	$\frac{^{207}Pb}{^{206}Pb}$	$\pm 1\sigma\%$	$^{206}Pb_c\%$	U_{ppm}	Th_{ppm}	**Age (Ma)**	$\pm$**2**σ **(Ma)**	Ti_{ppm}	$\pm 2\sigma_{ppm}$	**T°C**	$\pm 2\sigma$**°C**
0310016	0.017	8.5	0.071	3.6	3.50	7505	157	66.1	0.8	-	-	-	-
0310019	0.003	1.6	-	-	5.90	5500	138	20.6	0.3	-	-	-	-
0310019	0.003	2.5	-	-	9.07	3642	78	18.2	0.5	-	-	-	-
0310019	0.004	1.5	-	-	0.36	12714	2438	25.9	0.4	-	-	-	-
0310021	0.013	1.4	0.047	2.0	0.48	1800	38	41.5	0.7	-	-	-	-
0310021	0.015	0.9	0.048	1.4	0.94	3446	69	45.4	0.7	-	-	-	-
0310021	0.014	2.2	0.048	1.6	0.09	4346	120	45.8	0.7	-	-	-	-
0310021	0.017	0.6	0.047	1.2	0.14	6545	160	46.0	0.7	-	-	-	-
0310021	0.065	0.2	0.056	0.7	0.05	2600	81	203.8	3.1	-	-	-	-
0310021	0.070	2.2	0.056	0.8	0.06	1813	123	227.2	3.4	-	-	-	-
0310021	0.106	1.9	0.057	0.7	0.07	2036	94	285.1	4.5	-	-	-	-
0310021	0.105	1.9	0.056	0.7	0.10	2304	111	285.2	4.3	-	-	-	-
0310021	0.094	2.8	0.057	0.5	0.03	3591	151	291.0	4.5	-	-	-	-
0310021	0.123	0.8	0.056	0.6	0.09	2918	138	317.0	4.8	-	-	-	-
0310021	0.128	0.8	0.057	0.5	0.02	2941	170	374.2	5.7	-	-	-	-
0310021	0.133	0.4	0.057	0.6	0.04	2997	189	378.0	5.8	-	-	-	-
0310021	0.139	2.3	0.067	0.6	1.55	2223	93	387.1	5.7	-	-	-	-
0310021	0.142	3.6	0.057	0.4	0.09	2871	272	399.1	7.3	-	-	-	-
0310021	0.155	2.2	0.055	0.4	0.01	4767	65	412.1	6.4	-	-	-	-
0310021	0.142	5.1	0.057	0.4	0.03	4026	77	422.3	7.1	-	-	-	-
0310021	0.164	1.0	0.057	0.4	0.03	3561	86	422.6	6.6	-	-	-	-
0310021	0.150	4.7	0.056	0.3	0.05	4356	129	423.1	7.8	-	-	-	-
0310021	0.152	1.0	0.057	0.8	0.03	2231	193	424.1	6.3	-	-	-	-
0310021	0.154	0.8	0.056	0.4	0.01	4103	106	428.0	6.6	-	-	-	-
0310021	0.153	2.4	0.057	0.3	0.00	4582	359	435.8	7.0	-	-	-	-
0310021	0.139	3.3	0.057	0.4	0.05	3561	95	437.9	6.9	-	-	-	-
0310021	0.200	2.6	0.057	0.4	0.04	3220	146	441.2	6.9	-	-	-	-
0310021	0.178	1.9	0.056	0.4	0.03	8819	143	463.7	8.4	-	-	-	-
0310021	0.185	1.0	0.066	0.5	1.20	2594	245	468.6	6.8	-	-	-	-
0310021	0.170	0.6	0.058	0.7	0.08	1184	358	470.7	7.2	-	-	-	-
0310021	0.170	0.3	0.057	0.4	0.01	3429	228	475.5	7.5	-	-	-	-
0310021	0.143	1.0	0.057	0.7	0.06	785	101	476.0	7.3	-	-	-	-
0310021	0.159	1.3	0.061	1.1	0.35	1514	347	476.5	6.9	-	-	-	-
0310021	0.153	1.0	0.058	0.8	0.03	788	224	477.7	7.3	-	-	-	-
0310021	0.167	1.4	0.057	0.4	0.03	3493	161	484.0	7.9	-	-	-	-
0310021	0.178	2.3	0.057	0.3	0.01	4246	73	495.7	7.9	-	-	-	-
0310021	0.207	0.9	0.057	0.6	0.06	4274	240	497.0	7.6	-	-	-	-
0310021	0.196	1.0	0.057	0.3	0.05	4951	187	498.8	7.9	-	-	-	-
0310021	0.196	1.7	0.058	0.4	0.02	3095	254	507.3	8.2	-	-	-	-

continues next page...

Sample	$\frac{^{206}Pb}{^{238}U}$	$\pm 1\sigma\%$	$\frac{^{207}Pb}{^{206}Pb}$	$\pm 1\sigma\%$	$^{206}Pb_c\%$	U_{ppm}	Th_{ppm}	**Age (Ma)**	$\pm$**2**σ **(Ma)**	Ti_{ppm}	$\pm 2\sigma_{ppm}$	**T°C**	$\pm 2\sigma$**°C**
0310021	0.198	0.5	0.057	0.4	0.03	3334	271	509.6	8.1	-	-	-	-
0310021	0.177	0.7	0.057	0.7	0.07	1201	291	512.8	7.9	-	-	-	-
0310021	0.204	2.1	0.057	0.3	0.00	5731	404	541.8	8.6	-	-	-	-
0310021	0.204	1.8	0.057	0.3	0.01	5299	209	542.0	8.6	-	-	-	-
0310021	0.255	0.8	0.057	0.3	0.00	4914	430	569.9	9.1	-	-	-	-
0310021	0.241	2.6	0.057	0.2	0.00	11882	486	570.7	8.3	-	-	-	-
0310021	0.402	0.7	0.080	0.3	0.00	1969	105	1193.0	13.9	-	-	-	-
0310021	0.569	0.3	0.098	0.5	0.00	389	160	1559.3	20.9	-	-	-	-
0310037	0.007	2.2	0.049	2.0	0.84	5025	89	19.3	0.3	-	-	-	-
0310037	0.007	1.8	0.048	1.1	0.76	9377	174	19.3	0.3	-	-	-	-
0310037	0.005	2.4	0.060	1.8	2.61	5015	91	19.4	0.2	-	-	-	-
0310037	0.007	2.6	0.048	1.6	0.81	4969	84	19.6	0.3	-	-	-	-
0310037	0.005	2.9	0.085	2.0	5.24	6558	223	20.3	0.2	-	-	-	-
0310037	0.008	1.6	0.051	1.3	0.50	7020	124	20.6	0.3	-	-	-	-
0310037	0.009	0.5	0.059	1.4	2.44	5517	69	20.7	0.3	-	-	-	-
0310037	0.005	3.5	0.051	1.8	0.14	7714	145	21.0	0.2	-	-	-	-
0310038	0.010	5.5	0.049	1.5	0.76	7822	141	40.2	1.5	0.11	0.15	457	141.6
0310038	0.012	1.4	0.047	0.8	-	-	-	43.8	0.7	-	-	-	-
0310038	0.011	2.6	0.047	0.9	0.04	16083	295	43.9	0.7	0.15	0.15	472	108.1
0310038	0.014	2.5	0.048	0.6	0.32	20161	318	46.4	1.5	0.17	0.15	475	102.1
0310038	0.014	0.3	0.046	1.4	-	-	-	46.5	0.8	0.70	0.20	551	37.9
0310038	0.019	1.7	0.051	1.1	-	-	-	47.1	2.4	0.37	0.15	515	51.9
0310038	0.014	2.2	0.048	0.8	0.09	23359	392	47.8	0.9	0.26	0.15	497	70.0
0310038	0.018	1.5	0.048	1.2	-	-	-	47.9	0.8	0.08	0.15	444	183.7
0310038	0.014	0.5	0.048	0.8	0.21	16662	386	48.3	0.9	0.43	0.16	524	45.9
0310038	0.017	0.9	0.049	2.8	-	-	-	48.6	1.1	-	-	-	-
0310038	0.016	0.7	0.047	1.1	-	-	-	48.6	0.7	-	-	-	-
0310038	0.014	0.5	0.047	0.8	0.09	19124	431	49.0	0.9	0.29	0.15	504	62.7
0310038	0.015	1.8	0.050	0.8	0.57	15537	341	49.4	1.7	0.13	0.15	464	125.4
0310038	0.017	0.7	0.047	0.5	-	-	-	51.1	0.7	-	-	-	-
0310038	0.020	3.5	0.046	1.3	0.26	11620	277	54.1	2.1	0.41	0.16	521	49.7
0310038	0.019	1.1	0.047	0.6	0.02	24858	406	55.3	1.0	1.10	0.17	578	22.6
0310038	0.019	0.5	0.049	0.6	0.25	26627	640	56.7	1.0	0.33	0.16	509	57.6
0310038	0.023	1.3	0.047	0.6	0.10	18625	453	57.7	1.9	0.30	0.15	504	62.1

continues next page...

Sample	$\frac{^{206}Pb}{^{238}U}$	$\pm 1\sigma\%$	$\frac{^{207}Pb}{^{206}Pb}$	$\pm 1\sigma\%$	$^{206}Pb_c\%$	U_{ppm}	Th_{ppm}	**Age (Ma)**	**$\pm 2\sigma$ (Ma)**	Ti_{ppm}	$\pm 2\sigma_{ppm}$	**T°C**	**$\pm 2\sigma$°C**

All errors are 1σ unless otherwise stated. Uranium and Thorium contents were calibrated against zircon standard SL13, all other measurements calibrated against zircon standard FC1. ^{206}Pb/^{238}U and ^{207}Pb/^{206}Pb ratios are uncorrected for common Pb. Apparent ages were calculated using a ^{204} correction assuming a common Pb composition of ^{207}Pb/^{206}Pb=0.836±0.015, ^{208}Pb/^{206}Pb=2.065±0.1 and ^{206}Pb/^{204}Pb=18.703±1, and decay constants from (Steiger and Jager, 1977)

Table 22: Results of U-Pb dating and Ti thermometry of zircons from the Yala-Xiangbo Granitoids. See *Chapter 4* for discussion.

Sample	$\frac{^{206}Pb}{^{238}U}$	$\pm 1\sigma\%$	$\frac{^{207}Pb}{^{206}Pb}$	$\pm 1\sigma\%$	$^{206}Pb_c\%$	U_{ppm}	Th_{ppm}	**Age (Ma)**	$\pm$**2**σ **(Ma)**	Ti_{ppm}	$\pm 2\sigma_{ppm}$	**T°C**	$\pm 2\sigma$**°C**
0310015	0.011	1.1	0.050	3.1	1.57	1525	5	33.7	0.5	-	-	-	-
0310015	0.013	1.5	0.991	1.7	0.32	723	698	41.8	0.7	-	-	-	-
0310015	0.018	1.6	0.369	2.4	0.79	415	180	63.2	1.3	-	-	-	-
0310015	0.073	1.7	0.052	0.9	0.08	2808	1501	225.5	2.5	-	-	-	-
0310015	0.078	1.7	0.051	4.4	1.46	101	83	233.7	5.4	-	-	-	-
0310015	0.080	1.8	0.068	2.8	1.17	1675	166	243.9	4.5	-	-	-	-
0310015	0.077	1.9	0.072	3.1	0.52	929	23	257.1	3.2	-	-	-	-
0310015	0.097	2.3	0.063	5.2	1.61	46	22	275.5	7.8	-	-	-	-
0310015	0.143	0.4	0.060	0.8	0.13	1472	488	465.8	5.5	-	-	-	-
0310015	0.160	0.9	0.059	0.8	0.03	1200	284	482.4	5.8	-	-	-	-
0310015	0.155	1.3	0.070	0.8	0.06	1035	111	483.5	6.0	-	-	-	-
0310015	0.159	3.1	0.059	1.0	0.21	805	86	516.6	6.2	-	-	-	-
0310015	0.159	4.4	0.056	4.1	0.08	884	38	517.4	7.4	-	-	-	-
0310015	0.182	2.4	0.101	0.8	0.11	903	86	521.9	6.6	-	-	-	-
0310015	0.149	1.4	0.060	2.3	0.24	134	38	522.9	13.7	-	-	-	-
0310015	0.175	1.9	0.060	1.1	0.03	501	89	532.8	7.0	-	-	-	-
0310015	0.184	1.2	0.058	0.8	0.06	1339	123	534.6	6.3	-	-	-	-
0310015	0.186	1.6	0.059	1.2	0.05	830	174	550.1	6.7	-	-	-	-
0310015	0.195	1.4	0.059	0.7	0.04	1471	213	552.6	6.6	-	-	-	-
0310015	0.186	1.5	0.061	0.9	0.23	895	23	565.6	6.8	-	-	-	-
0310015	0.276	1.2	0.068	0.9	0.15	540	233	768.0	10.1	-	-	-	-
0310015	0.281	7.1	0.068	5.8	0.04	478	27	774.5	22.2	-	-	-	-
0310015	0.242	1.8	0.072	1.1	0.25	451	174	785.7	10.3	-	-	-	-
0310015	0.311	1.9	0.077	1.9	0.09	548	120	954.5	11.6	-	-	-	-
0310015	0.334	1.5	0.075	1.0	0.06	334	38	1007.6	14.5	-	-	-	-
0310015	0.382	0.9	0.078	0.9	0.12	342	208	1074.7	14.5	-	-	-	-
0310015	0.293	0.5	0.078	0.9	0.28	514	426	1079.0	12.0	-	-	-	-
0310015	0.390	0.7	0.077	1.1	0.31	230	81	1090.3	15.4	-	-	-	-
0310015	0.415	0.6	0.096	0.9	0.41	282	85	1494.0	17.2	-	-	-	-
0310015	0.680	2.2	0.112	0.7	0.14	281	101	1837.5	23.5	-	-	-	-
0310029	0.060	1.4	0.082	1.4	0.02	947	93	223.4	4.8	8.91	0.34	731	11.3
0310029	0.068	1.0	0.051	1.1	0.01	869	695	235.3	5.2	-	-	-	-
0310029	0.058	1.0	0.052	1.8	0.15	515	361	263.2	5.0	-	-	-	-
0310029	0.072	4.1	0.072	1.1	0.45	584	22	279.5	6.0	360.77	6.69	1198	17.4
0310029	0.122	3.6	0.058	0.8	0.05	969	118	439.0	9.7	8.27	0.34	725	11.5
0310029	0.129	3.1	0.058	1.5	0.06	217	63	489.2	11.1	-	-	-	-
0310029	0.156	0.4	0.063	1.1	0.14	494	38	551.0	12.2	-	-	-	-
0310029	0.158	1.5	0.057	0.7	0.01	744	209	558.3	12.7	6.41	0.33	703	12.5
0310029	0.172	2.2	0.067	0.7	0.09	573	104	675.3	15.2	-	-	-	-

continues next page...

Sample	$\frac{^{206}Pb}{^{238}U}$	$\pm 1\sigma\%$	$\frac{^{207}Pb}{^{206}Pb}$	$\pm 1\sigma\%$	$^{206}Pb_c\%$	U_{ppm}	Th_{ppm}	**Age (Ma)**	$\pm 2\sigma$ **(Ma)**	Ti_{ppm}	$\pm 2\sigma_{ppm}$	**T°C**	$\pm 2\sigma$**°C**
0310029	0.205	0.6	0.067	0.7	0.09	770	112	676.3	17.3	-	-	-	-
0310029	0.184	3.5	0.062	1.4	0.11	167	130	679.2	15.9	16.11	0.41	785	10.7
0310029	0.214	4.0	0.078	0.7	0.16	398	989	728.9	17.6	13.57	0.38	769	10.7
0310029	0.219	1.1	0.069	0.5	0.05	1004	222	745.3	16.9	14.81	0.40	777	10.7
0310029	0.255	4.9	0.069	0.6	0.03	523	277	929.5	21.3	-	-	-	-
0310029	0.270	1.4	0.070	0.9	0.02	555	227	967.0	19.1	-	-	-	-
0310029	0.304	2.8	0.071	0.5	0.01	651	285	979.5	21.8	13.18	0.38	766	10.7
0310029	0.330	1.9	0.074	0.4	0.03	832	354	1057.8	22.8	-	-	-	-
0310029	0.336	3.1	0.079	0.9	0.04	187	391	1166.3	28.6	9.96	0.35	741	11.1
0310029	0.416	0.7	0.100	0.5	0.03	413	190	1615.0	31.0	3.39	0.31	654	17.0
0310029	0.257	3.6	0.100	0.4	0.06	1051	131	1624.0	26.6	-	-	-	-
0310029	0.411	4.0	0.104	0.8	0.36	132	193	1657.0	37.2	12.74	0.37	763	10.8
0310029	0.449	2.1	0.102	0.5	0.00	354	102	1669.0	30.7	7.85	0.33	720	11.6
0310029	0.552	2.1	0.121	0.4	0.01	381	214	1977.0	32.7	-	-	-	-
0310029	0.783	3.1	0.236	0.2	0.03	735	460	3088.0	44.6	15.70	0.42	782	10.8
0310034	0.114	3.3	0.058	0.8	0.27	1225	209	390.9	8.3	-	-	-	-
0310034	0.133	0.7	0.057	1.0	0.05	729	186	440.8	8.4	-	-	-	-
0310034	0.149	0.8	0.057	0.8	0.12	960	543	457.0	8.6	-	-	-	-
0310034	0.143	2.3	0.057	2.2	0.88	148	102	470.4	9.5	5.63	0.34	693	13.7
0310034	0.152	0.3	0.058	0.9	0.02	687	242	488.6	9.4	-	-	-	-
0310034	0.162	4.3	0.057	0.8	0.03	902	276	491.5	9.5	5.09	0.31	685	13.6
0310034	0.157	1.8	0.058	1.5	0.59	270	70	492.6	9.5	-	-	-	-
0310034	0.201	0.9	0.057	0.3	0.03	6130	1850	496.3	10.4	-	-	-	-
0310034	0.157	1.6	0.058	1.0	0.06	587	162	507.9	9.7	10.14	0.35	742	11.0
0310034	0.153	0.5	0.058	1.3	0.32	347	99	509.1	9.8	-	-	-	-
0310034	0.165	1.6	0.058	0.9	0.16	804	448	518.3	9.8	-	-	-	-
0310034	0.165	0.9	0.057	0.9	0.20	661	168	519.6	9.8	-	-	-	-
0310034	0.180	0.3	0.057	1.2	0.03	963	479	519.7	10.4	-	-	-	-
0310034	0.163	1.0	0.058	1.1	0.12	557	232	519.9	9.8	6.07	0.32	699	12.7
0310034	0.175	1.5	0.057	0.5	0.08	2282	345	521.7	10.1	-	-	-	-
0310034	0.177	0.5	0.057	0.7	0.02	1336	421	522.3	10.2	-	-	-	-
0310034	0.172	0.8	0.057	0.6	0.03	3263	759	522.8	10.1	-	-	-	-
0310034	0.167	0.8	0.057	1.0	0.10	624	241	524.6	9.9	-	-	-	-
0310034	0.169	0.6	0.058	1.1	0.06	482	159	524.8	10.1	7.03	0.32	711	12.0
0310034	0.182	0.8	0.057	0.4	0.04	3363	1412	527.3	10.4	-	-	-	-
0310034	0.194	0.1	0.057	0.3	0.02	5701	1448	531.1	10.8	2.33	0.30	627	21.9
0310039	0.112	1.8	0.059	1.4	0.11	342	80	398.3	7.6	5.25	0.32	687	13.5
0310039	0.144	2.0	0.059	0.7	0.04	1368	133	477.2	9.6	13.83	0.39	770	10.7
0310039	0.110	2.1	0.059	1.6	0.34	338	76	534.9	10.3	7.37	0.33	715	11.8

continues next page...

Sample	$\frac{^{206}Pb}{^{238}U}$	$\pm 1\sigma\%$	$\frac{^{207}Pb}{^{206}Pb}$	$\pm 1\sigma\%$	$^{206}Pb_c\%$	U_{ppm}	Th_{ppm}	**Age (Ma)**	$\pm 2\sigma$ **(Ma)**	Ti_{ppm}	$\pm 2\sigma_{ppm}$	**T°C**	$\pm 2\sigma$**°C**
0310039	0.187	0.6	0.058	1.5	0.02	216	66	560.0	11.3	9.66	0.34	738	11.1
0310039	0.196	4.0	0.061	1.7	0.10	1250	42	594.4	13.7	7.03	0.33	711	12.0
0310039	0.181	2.5	0.062	0.9	0.05	937	70	663.5	10.2	5.98	0.32	698	12.8
0310039	0.224	2.0	0.079	1.0	1.83	605	88	813.4	14.2	300.66	6.66	1165	17.4
0310039	0.307	2.0	0.076	0.5	0.14	711	349	1096.9	21.4	9.55	0.34	737	11.1
0310039	0.266	3.5	0.077	1.5	0.02	1889	152	1124.0	60.4	16.11	0.41	785	10.7
0310039	0.558	0.7	0.121	1.4	0.03	214	112	1908.7	25.6	8.69	0.34	729	11.3
0310039	0.660	0.8	0.124	0.4	0.02	410	168	2017.2	19.5	8.10	0.41	723	12.8
0310039	0.591	1.8	0.167	1.1	0.02	234	108	2531.0	39.0	4.34	0.31	673	14.7
0310039	0.624	3.2	0.193	0.6	0.07	288	25	2773.0	36.0	2.99	0.30	645	18.4
0310039	0.988	2.6	0.312	0.6	0.04	143	51	3531.0	40.5	11.09	0.36	750	10.9

All errors are 1σ unless otherwise stated. Uranium and Thorium contents were calibrated against zircon standard SL13, all other measurements calibrated against zircon standard FC1. ^{206}Pb/^{238}U and ^{207}Pb/^{206}Pb ratios are uncorrected for common Pb. Apparent ages were calculated using a ^{204} correction assuming a common Pb composition of ^{207}Pb/^{206}Pb=0.836±0.015, ^{208}Pb/^{206}Pb=2.065±0.1 and ^{206}Pb/^{204}Pb=18.703±1, and decay constants from (Steiger and Jager, 1977)

Table 23: Results of U-Pb dating and Ti thermometry of zircons from the Yala-Xiangbo pelites. See *Chapter 4* for discussion.

Sample	Th/U	$\%^{206}Pb^*$	$\%^{208}Pb^*$	$\frac{^{206}Pb}{^{238}U}$	$\pm 1\sigma$	$\frac{^{208}Pb}{^{232}Th}$	$\pm 1\sigma$	**6/38 Age (Ma)**	**$\pm 1\sigma$ (Ma)**	**8/32 Age (Ma)**	**$\pm 1\sigma$ (Ma)**
0310015	8.47	97.3	97.7	0.00194	0.00004	0.00083	0.00001	12.5	0.2	16.8	0.2
0310015	17.36	95.1	97.7	0.00209	0.00005	0.00084	0.00001	13.5	0.3	16.9	0.2
0310015	7.34	98.7	98.6	0.00436	0.00009	0.00183	0.00003	28.0	0.6	37.0	0.5
0310015	9.34	97.2	97.8	0.00205	0.00004	0.00086	0.00001	13.2	0.3	17.3	0.2
0310015	8.15	98.4	98.5	0.00244	0.00004	0.00103	0.00001	15.7	0.3	20.7	0.3
0310015	10.04	96.4	97.4	0.00196	0.00004	0.00086	0.00001	12.7	0.2	17.4	0.3
0310016	3.50	97.5	95.0	0.00277	0.00010	0.00191	0.00002	17.9	0.7	38.6	0.4
0310016	2.74	97.8	94.5	0.00321	0.00018	0.00189	0.00002	20.7	1.2	38.2	0.4
0310016	3.36	95.1	90.0	0.00277	0.00020	0.00190	0.00002	17.9	1.3	38.3	0.5
0310016	1.57	97.6	89.9	0.00457	0.00007	0.00204	0.00003	29.4	0.4	41.2	0.7
0310016	4.28	95.6	92.6	0.00470	0.00005	0.00197	0.00004	30.2	0.4	39.7	0.7
0310016	8.97	90.6	88.5	0.00420	0.00006	0.00118	0.00002	27.0	0.4	23.8	0.4
0310016	2.60	97.0	92.2	0.00455	0.00006	0.00200	0.00003	29.3	0.4	40.5	0.7
0310016	2.44	96.2	89.6	0.00459	0.00006	0.00203	0.00003	29.6	0.4	41.0	0.5
0310016	3.81	96.8	93.9	0.00459	0.00005	0.00195	0.00002	29.5	0.4	39.4	0.5
0310016	4.57	96.1	93.9	0.00454	0.00010	0.00196	0.00004	29.2	0.6	39.5	0.7
0310016	3.49	96.0	91.9	0.00463	0.00006	0.00196	0.00003	29.8	0.4	39.7	0.5
0310016	3.15	96.6	92.3	0.00463	0.00010	0.00198	0.00004	29.8	0.7	39.9	0.8
0310016	3.24	96.5	92.5	0.00465	0.00007	0.00200	0.00003	29.9	0.5	40.5	0.7
0310016	3.05	97.1	93.2	0.00456	0.00011	0.00197	0.00005	29.3	0.7	39.7	1.0
0310016	4.92	96.4	94.7	0.00454	0.00012	0.00195	0.00006	29.2	0.8	39.4	1.2
0310016	3.83	96.8	93.9	0.00465	0.00007	0.00199	0.00003	29.9	0.5	40.2	0.6
0310016	1.83	98.4	94.0	0.00457	0.00012	0.00203	0.00006	29.4	0.7	41.1	1.2
0310019	14.17	94.0	96.3	0.00306	0.00013	0.00088	0.00003	19.7	0.8	17.7	0.5
0310019	14.36	94.6	96.6	0.00316	0.00015	0.00094	0.00003	20.4	1.0	19.1	0.6
0310019	13.46	94.5	96.7	0.00285	0.00019	0.00091	0.00005	18.4	1.2	18.3	0.9
0310019	14.82	94.9	97.1	0.00284	0.00014	0.00089	0.00004	18.3	0.9	18.0	0.8
0310019	4.84	98.5	97.6	0.00260	0.00009	0.00089	0.00004	16.8	0.6	18.0	0.8
0310019	9.94	70.4	74.6	0.00279	0.00009	0.00089	0.00002	18.0	0.6	17.9	0.3
0310019	4.18	97.3	95.1	0.00276	0.00008	0.00091	0.00003	17.8	0.5	18.4	0.6
0310019	9.56	94.2	95.6	0.00267	0.00014	0.00094	0.00003	17.2	0.9	19.0	0.7
0310019	9.91	93.4	94.6	0.00285	0.00007	0.00093	0.00003	18.4	0.5	18.7	0.6
0310019	9.89	95.8	96.3	0.00281	0.00008	0.00084	0.00002	18.1	0.5	16.9	0.4
0310019	8.95	96.3	96.5	0.00327	0.00010	0.00089	0.00002	21.0	0.6	17.9	0.4
0310019	7.17	97.0	96.7	0.00253	0.00008	0.00087	0.00003	16.3	0.5	17.7	0.6
0310019	14.24	95.2	97.0	0.00291	0.00011	0.00082	0.00003	18.7	0.7	16.6	0.6
0310019	2.66	98.3	95.2	0.00257	0.00008	0.00083	0.00002	16.5	0.5	16.7	0.4
0310019	5.62	95.9	94.6	0.00256	0.00006	0.00089	0.00001	16.5	0.4	18.1	0.3
0310021	5.57	99.0	99.2	0.00122	0.00002	0.00077	0.00001	7.9	0.2	15.5	0.2

continues next page...

Sample	Th/U	$\%^{206}Pb^*$	$\%^{208}Pb^*$	$\frac{^{206}Pb}{^{238}U}$	$\pm1\sigma$	$\frac{^{208}Pb}{^{232}Th}$	$\pm1\sigma$	**6/38 Age (Ma)**	**$\pm1\sigma$ (Ma)**	**8/32 Age (Ma)**	**$\pm1\sigma$ (Ma)**
0310021	26.10	97.1	99.2	0.00183	0.00004	0.00080	0.00001	11.8	0.3	16.1	0.2
0310021	24.51	99.1	99.7	0.00435	0.00007	0.00188	0.00002	28.0	0.5	37.9	0.4
0310021	27.95	97.1	99.2	0.00204	0.00004	0.00084	0.00001	13.1	0.2	17.0	0.2
0310021	26.09	98.2	99.5	0.00178	0.00004	0.00076	0.00001	11.5	0.3	15.4	0.3
0310021	34.26	96.4	99.1	0.00244	0.00004	0.00093	0.00001	15.7	0.3	18.7	0.2
0310021	18.47	99.3	99.7	0.00436	0.00008	0.00182	0.00003	28.0	0.5	36.8	0.5
0310021	8.55	98.3	98.5	0.00194	0.00003	0.00083	0.00001	12.5	0.2	16.8	0.2
0310021	8.55	96.9	97.3	0.00201	0.00004	0.00084	0.00002	12.9	0.3	17.0	0.3
0310021	19.90	98.9	99.6	0.00427	0.00005	0.00181	0.00003	27.5	0.3	36.6	0.6
0310021	24.17	97.5	99.2	0.00206	0.00004	0.00081	0.00001	13.3	0.3	16.3	0.2
0310021	318.33	94.1	99.8	0.00699	0.00034	0.00223	0.00004	44.9	2.2	45.0	0.8
0310021	22.89	99.3	99.8	0.00434	0.00012	0.00182	0.00004	27.9	0.8	36.7	0.8
0310021	27.34	98.0	99.4	0.00194	0.00007	0.00078	0.00002	12.5	0.4	15.8	0.4
0310021	21.77	99.1	99.7	0.00428	0.00008	0.00176	0.00003	27.5	0.5	35.6	0.6
0310021	2.97	97.8	94.8	0.00456	0.00008	0.00195	0.00002	29.3	0.5	39.3	0.5
0310021	3.27	95.7	90.7	0.00469	0.00007	0.00197	0.00004	30.2	0.4	39.8	0.7
0310021	5.16	96.0	93.7	0.00519	0.00013	0.00194	0.00007	33.4	0.8	39.2	1.4
0310037	20.92	89.6	95.2	0.00226	0.00006	0.00081	0.00001	14.5	0.4	16.3	0.2
0310037	4.74	95.5	93.2	0.00201	0.00003	0.00088	0.00001	12.9	0.2	17.7	0.2
0310037	3.73	95.5	91.7	0.00201	0.00003	0.00089	0.00001	12.9	0.2	18.0	0.3
0310037	6.70	94.6	94.0	0.00207	0.00004	0.00087	0.00001	13.4	0.2	17.7	0.2
0310037	3.07	96.0	91.1	0.00203	0.00003	0.00090	0.00001	13.1	0.2	18.1	0.2
0310037	5.89	96.1	95.2	0.00202	0.00004	0.00087	0.00001	13.0	0.2	17.6	0.3
0310037	8.08	94.7	95.2	0.00207	0.00003	0.00088	0.00001	13.4	0.2	17.7	0.2
0310037	10.07	94.6	95.8	0.00209	0.00004	0.00087	0.00001	13.5	0.2	17.5	0.3
0310037	7.80	95.4	95.5	0.00202	0.00003	0.00086	0.00001	13.0	0.2	17.4	0.2
0310037	5.90	94.5	93.2	0.00180	0.00004	0.00076	0.00002	11.6	0.3	15.4	0.3
0310037	7.02	95.9	95.6	0.00211	0.00003	0.00086	0.00001	13.6	0.2	17.4	0.3
0310037	7.43	96.0	96.0	0.00205	0.00004	0.00087	0.00001	13.2	0.2	17.6	0.3
0310037	5.46	96.6	95.2	0.00203	0.00003	0.00085	0.00001	13.1	0.2	17.1	0.2
0310037	7.51	92.9	92.5	0.00207	0.00003	0.00084	0.00001	13.3	0.2	16.9	0.2
0310037	5.66	96.7	95.6	0.00203	0.00004	0.00086	0.00002	13.1	0.2	17.4	0.4
0310037	8.35	96.3	96.7	0.00202	0.00003	0.00087	0.00002	13.0	0.2	17.5	0.3
0310037	9.68	92.7	94.2	0.00205	0.00005	0.00088	0.00003	13.2	0.3	17.7	0.5
0310038	23.75	79.0	90.6	0.00558	0.00010	0.00185	0.00002	35.9	0.7	37.3	0.5
0310038	33.45	71.2	89.3	0.00591	0.00010	0.00188	0.00003	38.0	0.6	38.0	0.6
0310038	27.70	67.3	86.0	0.00295	0.00009	0.00102	0.00002	19.0	0.6	20.5	0.3
0310038	35.79	71.6	90.3	0.00557	0.00021	0.00183	0.00006	35.8	1.3	36.9	1.2

continues next page...

Sample	Th/U	$\%^{206}Pb^*$	$\%^{208}Pb^*$	$\frac{^{206}Pb}{^{238}U}$	$\pm 1\sigma$	$\frac{^{208}Pb}{^{232}Th}$	$\pm 1\sigma$	**6/38 Age (Ma)**	**$\pm 1\sigma$ (Ma)**	**8/32 Age (Ma)**	**$\pm 1\sigma$ (Ma)**

All errors are 1σ unless otherwise stated. Measurements calibrated against monazite standard FT554 (45±1 Ma). Apparent ages were calculated using a ^{207} correction assuming a common Pb composition of ^{207}Pb/^{206}Pb=0.836±0.015, ^{208}Pb/^{206}Pb=2.065±0.1 and ^{206}Pb/^{204}Pb=18.703±1, and decay constants from (Steiger and Jager, 1977)

Table 24: Results of U-Th-Pb dating of monazites from the Yala-Xiangbo Granitoids and Yala-Xiangbo pelites. See *Chapter 4* for discussion.

.5 Sr-Nd isotopes

Sample	Lithology	Sm_{ppm}	Nd_{ppm}	$^{147}Sm/^{144}Nd$	$^{143}Nd/^{144}Nd$	2σ	Rb_{ppm}	Sr_{ppm}	$^{87}Rb/^{86}Sr$	$^{87}Sr/^{86}Sr$	2σ
0602008	AL	10.6	46	0.1398	0.51188	0.000011	279.4	190.5	4.294	0.824754	0.000013
0602009	AL	7.2	32.9	0.133	0.511856	0.000009	169.5	108	4.5826	0.799797	0.000017
0602010	AL	3.2	12.8	0.151	0.511861	0.000011	99.1	66.3	4.3621	0.804067	0.000014
T263	TL	4.6	17.2	0.1612	0.51196	0.000009	408.9	64.2	18.547	0.764508	0.000024
T264	TL	3.6	12.1	0.1779	0.511972	0.000009	436	36.7	34.5645	0.766703	0.000013
T265	TL	3	9.8	0.1877	0.511918	0.000013	289.6	43.4	19.4479	0.782315	0.000016
0602005	AC_{GHC}	5.5	27.5	0.1212	0.511785	0.000007	69.8	40.7	5.0497	0.876757	0.000016
0602011	AC_{MG}	11.6	66	0.1067	0.511861	0.000016	343.5	11.9	91.5567	1.709545	0.000023
0602012	AC_{ZG}	3.4	13.7	0.1485	0.512013	0.000016	149.4	134.4	3.2308	0.752523	0.000012
0405008	DG	4.5	22.5	0.1207	0.511998	0.000008	125.4	340.2	7.8590	0.718534	0.000015
0405011	DG	3.9	19.2	0.1217	0.511971	0.000008	124.3	336.1	7.8330	0.718602	0.000016
0405013	DG	4.2	20.1	0.1248	0.51209	0.000008	144.7	280.7	5.6192	0.717773	0.000017
0410007	DG	5.7	29.4	0.1177	0.511957	0.000014	122.7	478.6	11.2989	0.717999	0.000021
0410008	DG	6.1	29.9	0.1229	0.511934	0.00001	116.2	348.3	8.6757	0.71858	0.000008
0410009	DG	5.8	31.4	0.1118	0.511934	0.00001	121.1	344.3	8.2361	0.718523	0.000012
0410010	DG	6.8	35.8	0.1142	0.511958	0.000014	90.5	425.8	13.6286	0.717663	0.000029
0410012	DG	1.8	8.5	0.1258	0.512059	0.000004	113.3	548.3	14.0162	0.716476	0.000010
0310019	YX_G	2.5	10.4	0.1426	0.512066	0.000007	151.5	128.5	2.4565	0.715531	0.000018
0310021	YX_G	3	8.5	0.2138	0.512228	0.000006	630.2	74.9	0.3472	0.808553	0.000017
0310037	YX_G	1.1	4.1	0.1567	0.512117	0.000012	400.3	128.3	0.9284	0.715601	0.000012
0310038	YX_G	1.7	4.6	0.223	0.511985	0.000103	274.9	29.6	0.3120	0.729187	0.000021
0310008	YX_P	7.8	44.8	0.105	0.512291	0.000007	240.5	152.9	1.8420	0.718011	0.000016
0310013	YX_P	5.1	26.7	0.1154	0.512201	0.000007	144.3	174.5	3.5038	0.719065	0.000012
0310015	YX_P	4.8	23.8	0.1213	0.512294	0.000005	151.7	202.2	3.8598	0.716368	0.000016
0310029	YX_P	6.4	34.2	0.1135	0.512281	0.000009	275.4	237.4	2.4966	0.715313	0.000016
0310034	YX_P	4.8	25.4	0.1154	0.511981	0.000008	222.2	55.1	0.7279	0.845424	0.000019
0310039	YX_P	5.5	30.9	0.1074	0.512145	0.000008	275.4	111.1	1.1691	0.718509	0.000013
0310014	TM_M	3	9.9	0.1808	0.512935	0.000005	0.6	297.9	1436.8000	0.708029	0.000014

Table 25: Isotopic data

[blank page]

[blank page]

[blank page]